CORA Cork Open Research Archive
Cartlann Taighde Oscailte Chorcaí

Title	Monolithically integrated, high coherence frequency comb generation through on-chip gain switching
Authors	McCarthy, John T.
Publication date	2023
Original Citation	McCarthy, J. T. 2023. Monolithically integrated, high coherence frequency comb generation through on-chip gain switching. PhD Thesis, University College Cork.
Type of publication	Doctoral thesis
Rights	© 2023, John T. McCarthy. - https://creativecommons.org/licenses/by-nc-nd/4.0/
Download date	2026-10-27 19:29:01
Item downloaded from	https://hdl.handle.net/10468/15921



UCC
University College Cork, Ireland
Coláiste na hOllscoile Corcaigh

Monolithically Integrated, High Coherence Frequency Comb Generation through On-Chip Gain Switching

John McCarthy
PhD
115371331



NATIONAL UNIVERSITY OF IRELAND, CORK

School of Physics

Thesis submitted for the degree of Doctor of Philosophy

August 2023

Head of School: Prof. Paul Callanan

Supervisors: Prof. Frank Peters
Mr. Brian Corbett

Research supported by Science Foundation Ireland

Contents

List of Figures iv
List of Tables xiii
Abbreviations xiv
Acknowledgements xv
Abstract xvi

1 Introduction **1**
1.1 Optical Communications 1
1.2 WDM and Co-WDM 2
1.3 Comb Generation Methods 4
1.4 Injection locking 7
1.5 Thesis Motivation 8
1.6 Thesis Outline 10

2 Simulations **12**
2.1 Chapter Overview 12
2.2 Laser Modelling 12
2.2.1 Fabry Pérot Profile 14
2.2.2 Slotted Fabry Pérot Profile 17
2.2.3 Pitted Fabry Pérot 18
2.3 Gain Switching 21
2.3.1 The Rate Equations 21
2.3.2 Gain Switched Current 23
2.3.3 Gain Switched Frequency Combs 26
2.3.4 Frequency Response of Gain Switched Combs 27
2.3.5 Bias Current Response 29
2.4 Comb Line Filtering 30
2.5 Chapter Conclusion 33

3 Device Fabrication Process **34**
3.1 Chapter Overview 34
3.2 Epitaxial Structure 34
3.3 Mask Design 35
3.4 DC Fabrication 36
3.4.1 Ridge Lithography 36
3.4.2 Deep Lithography 37
3.4.3 Deep and Shallow Etches 38
3.4.4 Isolation Lithography 40
3.4.5 Oxide Open Lithography 42
3.4.6 Metal Lithography 43
3.4.7 Final Steps 43
3.5 Chapter Conclusion 44

4 Introduction to Device Characterisation and Features **45**
4.1 Chapter Overview 45

4.2 Characterisation . . . 45
4.3 Fabry Pérot Laser Diodes . . . 46
4.4 Etched Facets . . . 48
4.5 A FP laser with an added defect . . . 49
4.6 U-bend Lasers . . . 52
4.7 Slotted Fabry Pérot Lasers . . . 54
4.8 Pitted Fabry Pérot Lasers . . . 56
4.9 Chapter Conclusion . . . 57

5 Comb Generation Techniques 59
5.1 Chapter Overview . . . 59
5.2 Combs through Primary-Secondary Coupling . . . 59
5.2.1 Example 1: Slotted Fabry Pérot Lasers . . . 60
5.2.1.1 Device Design . . . 60
5.2.1.2 DC Characterisation . . . 61
5.2.1.3 Comb Generation . . . 64
5.2.2 Example 2: Pitted Fabry Pérot Lasers . . . 65
5.2.2.1 Device Design . . . 65
5.2.2.2 DC Characterisation . . . 66
5.2.2.3 Comb Generation . . . 67
5.2.2.4 Frequency Response . . . 68
5.3 Combs through Bidirectional Coupling . . . 71
5.3.1 Device Design . . . 72
5.3.2 Device Characterisation . . . 73
5.4 Combs Through Mutual Coupling . . . 75
5.4.1 Device Design . . . 75
5.4.2 DC Characterisation . . . 76
5.4.3 Comb Generation . . . 77
5.4.3.1 Primary-Secondary Coupling . . . 77
5.4.3.2 Mutual Coupling . . . 78
5.4.4 Comb Generation at RO Frequency . . . 80
5.5 Chapter Conclusion . . . 81

6 Comb Frequency Response Through Asymmetric and Non-Asymmetric Gain Switching Techniques. 83
6.1 Chapter Overview . . . 83
6.2 Device Design . . . 83
6.3 DC Characterisation . . . 84
6.4 Primary-Secondary Coupling . . . 86
6.4.1 Comb Generation . . . 88
6.4.2 ESA Analysis . . . 91
6.5 Mutual Coupling . . . 92
6.5.1 Comb Generation: Example One . . . 92
6.5.2 Comb Generation: Example Two . . . 95
6.5.2.1 Induction of a Spectral Bulge . . . 100
6.6 Analysis of Comb Quality . . . 102
6.7 Chapter Conclusion . . . 104

7 Comb Line Filtering **106**
7.1 Chapter Overview . . . 106
7.2 Device Design . . . 107
7.3 Theoretical Approach . . . 109
7.4 Device Characterisation . . . 110
7.4.1 DC Characterisation of the SM Laser . . . 110
7.4.2 DC Characterisation of the FP Laser and Injection Locking 112
7.5 Comb Generation . . . 113
7.6 Comb Filtering . . . 114
7.7 Chapter Conclusion . . . 116

8 Comb Generation Without Additional Optical Injection **118**
8.1 Chapter Overview . . . 118
8.2 Device Design . . . 119
8.3 Device characterisation . . . 120
8.3.1 RF Characterisation . . . 122
8.4 Effects of Bias Current . . . 124
8.4.1 RF Amplifier at 4V . . . 124
8.4.2 RF Amplifier at 8V . . . 125
8.5 Chapter Conclusion . . . 127

9 Conclusion and Future Work **128**
9.1 Chapter Overview . . . 128
9.2 Thesis Conclusion . . . 128
9.3 Future Work . . . 132
9.3.1 Power Enhancement: Example 1 . . . 132
9.3.2 Power Enhancement: Example 2 . . . 133
9.3.3 Power Enhancement: Example 3 . . . 134
9.3.4 De-Multiplexer . . . 135
9.3.5 De-multiplexing Network . . . 137
9.3.6 Comb Enhancement Through a High Speed Fabrication Process . . . 137
9.3.7 Micro-Transfer Printing . . . 139

References **143**

List of Figures

1.1 Illustration of internet users from 2013 - 2023 [1]. 1
1.2 Illustration of channels in an optical network separated by 50 GHz. 3
1.3 Illustration of channels in an optical network where the channels are generated by a comb source. This allows for smaller separation between channels and so the bandwidth can be reclaimed. 3
1.4 Schematic of a comb based optical network. A comb is injected into a de-multiplexer which splits the comb lines into separate modulators. Here data is incorporated before the comb lines are recombined and transmitted. 4
1.5 (a) Damped harmonic of the carrier and photon densities when device is biased abruptly. (b) Gain-switched carrier and photon density pulse train. 5
1.6 Spectra measured from an on-chip FP laser biased at (red) 50 mA and (blue) a 50 mA bias current that is modulated with a high power RF signal. 5
1.7 Plot of a frequency comb generated through gains witching. . . 6
1.8 Spectra of the secondary FP laser (blue) before and (red) after it is injection locked with the SM primary laser. 8

2.1 Illustration of the inputs and outputs of a multi-port scattering junction. 13
2.2 Illustration of a two port junction with the scattering and transmission inputs and outputs. 13
2.3 (blue) Reflection profile and (red) Transmission profile of a FP laser 600 μm in length. 15
2.4 (a) Reflection profile and (b) Transmission profile of a FP laser for a cavity length ranging from 400 - 800 μm 16
2.5 Illustration of the varying effective refractive indices created by etching slots into the ridge of a laser. 17
2.6 Diagram of a single cavity device separated into a gain and slotted mirror section. 18
2.7 (a) Reflections caused by the 7 slots with an interslot separation of 87 μm and (b) Transmission profile of a 1300 μm cavity with 7 slots and an interslot separation of 87 μm. 18
2.8 Transmission profile of the SFP laser as the optical path length of the device is varied. 19
2.9 Illustration of the varying reflective defects created by etching pits into the ridge of a laser. 19
2.10 Diagram of a single cavity device separated into a gain and pitted mirror section. 19
2.11 (a) Reflections caused by the 8 pits with an interpit separation of 77 μm and (b) Transmission profile of a 1300 μm cavity with 8 pits and an interpit separation of 77 μm. 20

2.12 Transmission profile of the PFP laser as the optical path length of the device is varied. 20
2.13 (a) Bias current of 50 mA being switched on in the time domain. (b) the corresponding carrier and photon densities of the biased laser. 22
2.14 (a) Carrier concentration and (b) Photon concentration of a diode laser as the bias current is swept from 30 - 100 mA. 23
2.15 Frequency of the relaxation oscillations as bias current of the diode laser is swept from 30 - 100 mA. 23
2.16 (a) Sinusoidal current as the bias current is varied from 0 - 100 mA. (b) Sinusoidal current as the V_{rf} is varied from 0 - 8 V. . . 25
2.17 (a) Sinusoidal current biasing a laser in the time domain. (b) Resulting carrier and photon densities of the gain switched laser. 25
2.18 (a) Period of gain switched carrier and photon concentration. (b) Fast fourier transform of the gain switched photon density period in (a). 26
2.19 Comb simulation achieved using *Equation* 2.24. The simulation demonstrates 7 comb lines within 10 dB of the maximum comb giving a comb quality of Δf_{10} = 36 GHz. 27
2.20 The effects of the modulation frequency on the gain switched photon density for bias currents of (a) 50 mA, (b) 75 mA and (c) 100 mA. 28
2.21 The effects of the modulation frequency on the gain switched comb for bias currents of (a) 50 mA, (b) 75 mA and (c) 100 mA. The equivalent ROFs are depicted by the dotted red line. 28
2.22 Plot illustrating how a gain switched comb varies with bias current. 29
2.23 Schematic of a comb based optical network. 30
2.24 (a) Transmission profile of a ring laser. (b) transmission profile of a ring laser as the optical path length is adjusted. 31
2.25 (a) Simulated comb with frequency spacing of 5 GHz. (b) Corresponding ring transmission mode. 31
2.26 (a) Illustration of the generated comb, the ring transmission profile and the resulting filtered comb line. (b) Illustration of the different comb lines being filtered through changing the optical path length of the ring laser. 32

3.1 (a) Quad mask showing the layers used to fabricate PICs. (b) Quarter wafer design showing the overlapping layers. 36
3.2 Resolution features in microns as seen on (a) the mask layer image and (b) microscope image after development of the ridge lithography. 37
3.3 (a) Schematic showing the EPI wafer with the defined SiO_2 ridge hard mask. (b) The SiO_2 ridge hard mask as viewed under a microscope. 37

3.4 (a) Schematic showing the EPI wafer with the defined SiO_2 ridge hard mask and Si_3N_4 deep hard mask. (b) The SiO_2 ridge hard mask and etched Si_3N_4 hard mask as viewed under a microscope. 38
3.5 Reflectance fringes measure as the Oxford Cobra ICP Etcher etches the EPI layers. 39
3.6 (a) Schematic showing the EPI wafer after the deep regions are etched. (b) Microscope View. 40
3.7 (a) Schematic showing the EPI wafer after the deep and shallow regions are defined and etched. (b) Microscope View of (top) top of ridge and (bottom) bottom of the deep etched region. 41
3.8 (a) Schematic showing the EPI wafer after the isolation etch. (b) Microscope View of isolation etch. 41
3.9 (a) Schematic showing the EPI wafer after the Oxide etch. (b) Microscope View of Oxide etch. 42
3.10 (a) Schematic showing the EPI wafer after the metal liftoff. (b) Microscope View of metal liftoff. 43
3.11 (a) Schematic showing finalised laser structure. (b) Microscope View of a laser. 44

4.1 Image of characterisation setup. 46
4.2 Illustration of deep and shallow etched waveguides. 47
4.3 Illustration of the mask layout of a deep and shallow etched FP laser. 47
4.4 (a) Measured LIV curves and (b) measured spectra of a shallow and deep etched FP. 47
4.5 Top and side view schematics of a FP laser with an etched facet and a metal etched facet. 49
4.6 (a) LI curves of a FP laser with a cleaved facet, etched facet and metal etched facet. (b) Spectra of FP with etched facet and metal etched facet biased at 80 mA. 49
4.7 Top and side view schematics of a FP laser with a shallow and a deep slot etched into the ridge. 50
4.8 Lasing spectra of a FP with a single deep and shallow slot etched into the ridge. 50
4.9 Transmission profile for a FP laser with a cavity length of (a) 750 μm and (b) 250 and 500 μm 51
4.10 FFT of spectra attained for a FP laser with (a) a shallow slot etched into the ridge and (b) a deep slot etched into the ridge. . 52
4.11 Single and double deep etched ubend lasers. 52
4.12 (a) LIV and (b) spectra of two Ubend lasers, one wih a deep etch at both sides of the bend and the other with a deep etch at one side of the bend. 53
4.13 FFT of the spectra attained from a Ubend laser with a deep etch on (a) the outside of the bend and (b) both sides of the bend. . 54

4.14 (a) Measured threshold current for both Ubend structures for different curvature of radius. (b) Measured power at 100 mA for both Ubend structures for different curvature of radius. 54
4.15 (a) Mask schematic and (b) side view illustration of a SFP laser. 55
4.16 (a) LIV curves of a SFP laser. (b) Different single mode spectra attained from a SFP laser. 56
4.17 (a) Mask schematic and (b) side view illustration of a PFP laser. 56
4.18 (a) LIV curves of a PFP laser. (b) Different single mode spectra attained from a PFP laser. 57

5.1 Block diagram of the experimental setup used to generate combs. 60
5.2 (a) Mask schematic and (b) side view illustration of the integrated primary-secondary laser. 61
5.3 LIV characteristics of the primary laser as current is swept through the gain section. 62
5.4 (top) SMSR and (bottom) lasing wavelength of the primary laser as current is swept across both laser sections. 62
5.5 Plot of the SMSR of the primary laser achieved at different wavelengths. 63
5.6 (a) LIV curves and (b) spectra of the FP secondary laser. 63
5.7 (a) Spectra of the secondary laser before and after the primary laser is biased and injection locking occurs. (b) Different injection locked spectra achieved at each lasing mode of the primary laser. 64
5.8 Frequency comb generated at an frequency of 5 GHz. 65
5.9 Example of frequency combs generated at an frequency of 5 GHz at different wavelengths. 65
5.10 a) Mask schematic and (b) side view illustration of the integrated primary-secondary laser. 66
5.11 LIV characteristics of the primary laser as current is swept across the gain section for different bias currents through the mirror section. 67
5.12 top) SMSR and (bottom) lasing wavelength of the primary laser as current is swept across both laser sections. 67
5.13 Plot of the SMSR of the primary laser achieved at each of the lasing wavelengths. 68
5.14 (a) Different injection locked spectra achieved at each lasing mode of the primary laser (b) Example of a comb generated at 1552nm at a gain switched frequency of 4.5 GHz. 68
5.15 Example of frequency combs generated at an frequency of 4.5 GHz at different wavelengths. 69
5.16 Combs generated at gain switched frequencies ranging from 3.8 - 8 GHz. 69
5.17 Spectrum of the FP laser biased at 45 mA illustrating the lasing modes and the sidebands caused by the lasers RO frequency. . . 70

5.18 Spectra of the SM primary laser when the gain and mirror sections are biased at 125 and 30 mA respectively. 71
5.19 Combs measured at a gain switched frequency of 2.3, 2.5 and 2.7 GHz. 71
5.20 Side view illustration of device. 72
5.21 LIV curves measured from (a) the primary and (b) the secondary lasers. 73
5.22 Spactra measured from (a) the primary laser and (b) the secondary laser. 74
5.23 (a) Injection locked spectra and (b) Combs measured through the left and right cleaved facet. 74
5.24 (a) Top view and (b) side view of the PIC schematic. 75
5.25 LIV characteristics of (a) the FP laser and (b) the SM laser as current is swept through the gain section for different bias currents through the slotted section. 76
5.26 Spectra of (a) the FP laser biased at 50 mA and (b) the SM laser after biasing the gain and mirror sections at 75 and 100 mA respectively. 77
5.27 (a) Spectrum attained while the SM laser is injection locked to the FP laser while the laser are asymmetrically biased in a primary-secondary configuration. (b) Frequency comb generated at 6.80 GHz while the device is operating under this primary-secondary configuration. 78
5.28 (a) SMSR and (b) lasing wavelength of the device as the current is varied through the gain and FP sections. 78
5.29 (a) Plot of the SMSR achieved at each lasing wavelength. (b) Examples of single mode spectra attained at six different wavelengths 79
5.30 (a) Spectrum attained while the SM laser and FP laser are operating in a mutually coupled configuration. (b) Frequency comb generated at 6.80 GHz while the device is operating in this mutually coupled configuration. 79
5.31 (Red) Comb attained through primary-secondary coupling with a modulation frequency equivalent to the FP laser's RO frequency. (Blue) Comb attained through mutual coupling with a modulation frequency equivalent to the FP laser's RO frequency. 81

6.1 (a) Top view and (b) side view of the PIC schematic. 84
6.2 LIV curves of (a) FP laser and (b) SM laser as the current is swept across the gain section for different bias currents through the mirror section. 85
6.3 Spectra measured from the FP laser as current is swept from 20 - 150 mA. 85
6.4 (a) SMSR and (b) lasing wavelength measured from the SM laser as current is swept from 0 - 200 mA across both the gain and mirror sections. 85

6.5 The SMSR achieved at each lasing wavelength of the SM laser. . 86
6.6 (a) SMSR and (b) lasing wavelength measured from the PIC as current is swept from 0 - 200 mA across both the gain and mirror sections, while the FP is biased at 26 mA. 87
6.7 The SMSR achieved at each lasing wavelength of the primary-secondary PIC. 88
6.8 (a) A colour plot depicting the spectra of the device as current was swept through the gain section for bias currents of 35 and 26 mA through the mirror and FP sections respectively. (b) The equivalent SMSR and lasing wavelength. 88
6.9 Colour plot depicting the generated combs as the gain switched frequency was swept from 4.5-10.5 GHz, while the PIC operates in an asymmetric bias regime. 89
6.10 Plot of the lasing mode of the SM laser demonstrating the side peaks caused by the lasers RO frequency. 89
6.11 (a) Plot of the full spectra of the PIC while gain switched at 2.5 GHz using the low resolution ANDO OSA. (b) close up of the lasing spectra of the PIC while gain switched at 2.5 GHz using the high resolution APEX OSA. 90
6.12 Combs generated through the asymmetric bias method at approximately (a) 2×RO Frequency, (b) 3×RO Frequency and (c) 4×RO Frequency of the SM laser. 90
6.13 Colour plot depicting the measured ESA from the generated combs as the gain switched frequency was swept from 4.5-10.5 GHz. . 91
6.14 Electrical spectra corresponding to the generated combs gain switched at approximately (a) 2×RO Frequency, (b) 3×RO Frequency and (c) 4×RO Frequency of the SM laser. 91
6.15 (a) SMSR and (b) lasing wavelength measured from the PIC as current is swept from 0 - 150 mA across the gain section and 0 - 55 mA across the mirror sections, while the FP is biased at 50 mA. 92
6.16 The SMSR achieved at each lasing wavelength of the mutually coupled PIC. 93
6.17 Spectra of the coupled system (a) before and (b) after the FP laser is gain switched at 5 GHz. 93
6.18 Combs measured through the high resolution APEX OSA as the gain switched frequency is swept from 5 - 7.5 GHz. 93
6.19 Combs generated at (a) 5.36 GHz, (b) 5.60 GHz, (c) 6.42 GHz and (d) 7.20 GHz. 94
6.20 Colour plot demonstrating the ESA analysis of the PIC. The plot also measures extra narrow peaks at regions corresponding to the RO frequency of the single mode and Fabry-Pérot lasers. . . 95
6.21 Electrical spectra of combs generated at (a) 5.36 GHz, (b) 5.60 GHz, (c) 6.42 GHz and (d) 7.20 GHz. 96
6.22 Spectra of the coupled system (a) before and (b) after the FP laser is gain switched at 5 GHz. 97

6.23 Combs measured as the gain switched frequency is swept from 5 - 11 GHz. 97
6.24 Combs generated through the non-asymmetric bias method at (a) 2×RO, (b) 3×RO and (c) 4×RO frequency of the SM laser. . 98
6.25 Comb generated through the non-asymmetric bias method at 2×ROF of the FP laser. 98
6.26 Colour plot demonstrating the ESA analysis of the PIC. The plot also measures extra narrow peaks at regions corresponding to the integer multiples of the RO frequency of the SM and FP lasers. Illustrations of the locking ranges are also included. . . . 99
6.27 Electrical spectra of combs generated through the non-asymmetric bias method at (a) 2×RO, (b) 3×RO and (c) 4×RO frequency of the SM laser. 99
6.28 High resolution spectra of the mutually coupled system showing the side peaks caused by the PICs RO frequency. 100
6.29 The gain switched optical spectra of the mutually coupled system when gain switched at the apparent RO and double RO frequency of the coupled system. 101
6.30 The gain switched electrical spectra of the mutually coupled system when gain switched at the apparent RO and double RO frequency of the coupled system. 101
6.31 Measurement of the SNR of a generated comb. This is a measurement in dB between the maximum power of the comb and the maximum power of the noise level. 102
6.32 The measured SNR of combs generated from a primary-secondary configuration as the gain switched frequency is swept from 4.5 - 10.5 GHz. 103
6.33 The measured SNR of the frequency combs generated through mutual coupling in *Sections* 6.5.1 and 6.5.2. 103

7.1 (a) Schematic of the PIC design and (b) SEM image of the fabricated PIC. 107
7.2 (a) Approximation of the transmission profile of a ring laser. (b) Simulation of the injected comb and transmission profile of the ring, and the filtered comb output of the ring laser. 110
7.3 (a) LIV curves attained from the SM laser as current was swept across the gain section for different currents through the mirror section. 111
7.4 (a) SMSR and (b) lasing wavelength of the SM section of the device as the current is varied through the gain and mirror sections of the device. 111
7.5 Plot illustrating the measured SMSR of the laser for each lasing wavelength. 112
7.6 (a) LIV curve of the FP laser. (b) Spectra of the FP laser when biased at the lasers threshold current and at twice threshold current. 112

7.7 Examples of the injection locked spectra between the primary SM and secondary FP lasers measured through *Port B* via fiber coupling. 113
7.8 (a) Comb measured through *Port A* compared to *Port B*. (b) Comb measured through *Port C* compared to *Port B*. 114
7.9 (a) LIV curves and (b) free running spectra of the ring laser. . . 115
7.10 (a) Individual comb lines filtered by the ring laser and (b) plotted against the comb measured through *Port C*. 116
7.11 Colour plot illustrating the growth and suppression of individual comb lines as the current through the ring resonator is increased. 116
7.12 Schematic of a comb based optical network. 117

8.1 (a)Top view and (b) side view of device schematic. 119
8.2 (a) LIV measurements as current is swept through the mirror section for different bias currents through the gain section (b) example of a single mode spectrum attained at 1549.5 nm. . . . 120
8.3 SMSR (top) and lasing wavelength (bottom) of the device as the current is varied through the gain and mirror sections. 121
8.4 (a) Colour plot showing the power of the spectra as current was swept across the mirror section. (b) SMSR and lasing wavelength of the device as the current was swept across the mirror section. 121
8.5 Comb attained through gain switching (a) the gain section and (b) the mirror section. 122
8.6 Frequency response of the generated combs. 123
8.7 Comb attained through gain switching at (a) 1 GHz, (b) 5 GHz and (c) 10 GHz. 123
8.8 (a) High resolution image of the single mode spectrum with the RO sidebands. (b) The generated comb at a frequency equivalent to the RO frequency measured from the sidebands. 123
8.9 (a) Colour plot showing the power of the spectra as the gain switched current was swept across the mirror section. (b) SMSR and lasing wavelength of the device as the gain switched current was swept across the mirror section. 125
8.10 Analysis of the peak lasing wavelength while the gain switched current through the mirror section is (a) 50 mA, (b) 115 mA and (c) 225 mA. 125
8.11 (a) Colour plot showing the power of the spectra as the gain switched current was swept across the mirror section. (b) SMSR and lasing wavelength of the device as the gain switched current was swept across the mirror section. 126
8.12 Analysis of the peak lasing wavelength while the RF current through the mirror section is (a) 50 mA, (b) 150 mA and (c) 186 mA. . 126

9.1 Optimum combs generated through different coupling techniques and devices. 131
9.2 (a)Top view and (b) side view of device schematic. 132
9.3 (a)Top view and (b) side view of device schematic. 133

9.4 Top view of device schematic. 134
9.5 Schematic of a comb based optical network. 135
9.6 Schematic of a PIC that can generate combs and filter out two individual comb lines. 135
9.7 Schematic of a PIC that can generate combs and filter out two individual comb lines. 136
9.8 Schematic of a PIC that can generate combs and filter out four individual comb lines. 137
9.9 (a) Deep etched waveguide deposited with a layer of SiO_2. (b) BCB is deposited. 138
9.10 (a) BCB etched back and SiO_2 deposited. (b) Oxide open etch created and metal contact pad deposited. 139
9.11 (a) Full μTP epistructure depicting the active region, the release layer and the Native substrate. (b) The fabricated device sitting on the release layer that has been etched down to the substrate. (c) The fabricated device and the release layer encapsulated in PR. 140
9.12 The encapsulated polymer is shaped into a grid like structure and the release layer is undercut. The grid polymer now acts as tethers holding the device in position. 140
9.13 The encapsulated polymer is shaped into a grid like structure and the release layer is undercut. The grid polymer now acts as tethers holding the device in position. 141
9.14 Schematic of device where the comb source is confined by a metal etched facet and an etched facet. 141
9.15 Plots of how the generated comb changes as the bias across the angled waveguide contact decreases. 142

List of Tables

2.1 Parameter definitions and values 16
2.2 Parameter definitions and values. 22
2.3 Parameter definitions and values 24
2.4 Parameter definitions and values 26
2.5 Parameter definitions and values 27

3.1 Layers of epitaxial structure 35

Abbreviations

WDM	Wavelength Division Multiplexing
CoCs	Coherent Optical Combs
CoWDM	Coherent Wavelength Division Multiplexing
FSR	Free Spectral Range
SMSR	Side Mode Suppression Ratio
RF	Radio Frequency
DC	Direct Current
AC	Alternating Current
ILF	Integrated Laser Filter
FP	Fabry Perot
SM	Single Mode
QW	Quantum Well
MQW	Multi-Quantum Well
DFB	Distributed Feedback Laser
DBR	Distributed Bragg Reflector
GS	Ground-Signal
GSG	Ground-Signal-Ground
PECVD	Plasma-Enhanced Chemical Vapour Deposition
TLM	Transfer Length Measurement
TLS	Tunable Laser Source
PIC	Photonic Integrated Circuit
SFP	Slotted Fabry Perot
PFP	Pitted Fabry Perot
CF	Cleaved Facet
EF	Etched Facet
MEF	Metal Etched Facet
WG	Waveguide
RO	Relaxation Oscillation
ROF	Relaxation Oscillation Frequency
MTP	Micro-Transfer Printing

Acknowledgements

I would like to thank my supervisor Frank Peters and my co-supervisors Brian Corbett and Bryan Kelleher for giving me the opportunity to discover the field of integrated photonics and for their help throughout my PhD.

I would also like to thank my parents Angela and Ted for their support and encouragement over the last 26 years.

I am grateful to the housemates I've had over the past four years, Kevin, Jack, Megan, Louise (and Michael), Pablo and Sorcha. You have all put up with my ever present spectre and my long occupations of the sitting room whenever a new *Legend of Zelda* game was released.

Mary, you kept me grounded when I broke my ribs by making me row you across that lake. Rita, you made me realise how much of this I can write in an hour.

I'm thankful to Dario, Kevin and Colum for our weekly Wednesday crosswords, I always looked forward to them.

Finally I will like to thank Eoin, Julie, Kamille and Salvador. Our Friday events always cheered me up regardless of how the week went.

I gratefully acknowledge the funding received towards my PhD from Science foundation of Ireland (SFI). And many thanks go to the people of Tyndall National Institute and University College Cork (UCC) for making my PhD a pleasant experience.

Abstract

As the number of internet users continuous to increase, methods of developing new forms of communication networks are being widely considered. Optical frequency comb sources have the potential to reduce or eliminate the spectrally inefficient guard bands that are currently used to prevent cross-talk between adjacent channels. With their common laser source and fixed phase relation, frequency combs can offer to not only to replace the hundreds of lasers being used to generate hundreds of channels, but also reduce the present day separation between channels.

This thesis demonstrates on-chip frequency combs that are generated through gain switching. Simulation analysis is carried out to investigate the effects of experimental parameters on the quality of gain switched combs and extensive experimental analysis is carried out to examine the experimental conditions required to enhance the quality of these combs. Typically a two laser design is used where a gain switched Fabry–Pérot laser is phase locked to a single mode laser creating a primary-secondary configuration. Different coupling techniques were investigated and developed, with stable combs being generated as a result of bidirectional coupling, and greater comb enhancement being demonstrated using mutually coupled techniques. Utilising both the combs generated through mutual coupling and the knowledge of on-chip, stable, bidirectionally coupled combs, the conditions required to generate an enhanced comb with additional comb lines are developed. Methods of on-chip comb line filtering are demonstrated for the purpose of future de-multiplexing systems. Finally, a new method of frequency comb generation through on-chip gain switching, without the previously required additional optical injection, is analysed and developed.

The versatile design and ease of integration of these comb sources shows great promise for future generation designs and optical networks.

I, John McCarthy, certify that this thesis is my own work and I have not obtained a degree in this university or elsewhere on the basis of the work submitted in this thesis.

John McCarthy

Chapter 1

Introduction

1.1 Optical Communications

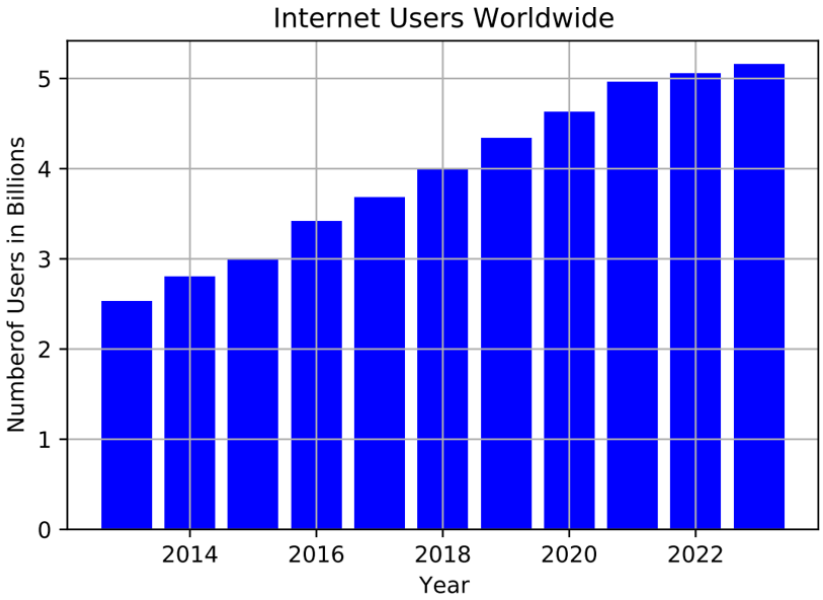


Figure 1.1: Illustration of internet users from 2013 - 2023 [1].

Laser diodes were first demonstrated in the early 1960's through the use of a pulsed ruby laser [2] and with the development of optical fibers in the second half of the 20^{th} century, the growth of fiber optic communications has become a major driving force for the research and development of optical technologies. With the successful transmission of the first data packet between two computers in 1969, the internet was officially developed on the first of January 1983. By the turn of the century, 30 years after the invention of low-loss fibers, more than 300 million km of optical fibers have been deployed worldwide [3].

Today it is estimated that approximately 60% of the worlds population uses the internet [4] which is vast in comparison to the 6.8% of internet users recorded in 2000 [5]. *Figure* 1.1 illustrates the growth of internet users from 2013 - 2023 with the number of internet users doubling from 2.5 billion users in 2013 to 5 billion users in 2021 in the space of eight years.

Along with the ever increasing user base, there is an ever increasing demand for bandwidth intensive services. In today's day and age, almost every household is familiar with one or more of the various available streaming services (Netflix, Disney +, Prime Video), as well as the many social medias made available (Meta, TikTok). The optical channels used to transmit this data is limited to the regions of low loss in an optical fiber, more specifically the O-band (original) located around a wavelength of 1310 nm and the S, C and L-bands (short, centre and long) located around 1550 nm. Since the development of optical fibers in the 1970's vast improvements have been made to these transmission windows reducing the loss to as low as 0.25 dB/km [6], [7].

1.2 WDM and Co-WDM

Wavelength Division Multiplexing (WDM) networks are widely used for long distance optical transmitters [8], [9]. Such a network is made up of a series of optical channels where each channel is generated by an independent laser. Each laser is modulated with data before being combined with the other modulated channels and transmitted along an optical fiber. Modern networks employ hundreds of these single channel lasers, each with its own distinct wavelength (or frequency) to prevent cross-talk between channels which would corrupt the transmitted data. Laser channels experience instability in the lasing wavelength/frequency (a frequency jitter) and so guard bands are used to separate channels and prevent overlap. Guard bands are empty regions of frequency space that separate the individual channels, the idea is that these regions are large enough that if one channel is to experience a jitter, then the adjacent channel isn't effected or corrupted by the jitter. Modern day separations between adjacent channels range from 50 - 100 GHz (0.4-0.8 nm) [10] which is illustrated in *Figure* 1.2. The result is that these guard bands are spectrally inefficient and, with more and more people seeking internet access, the available bandwidth is becoming more and more limited.

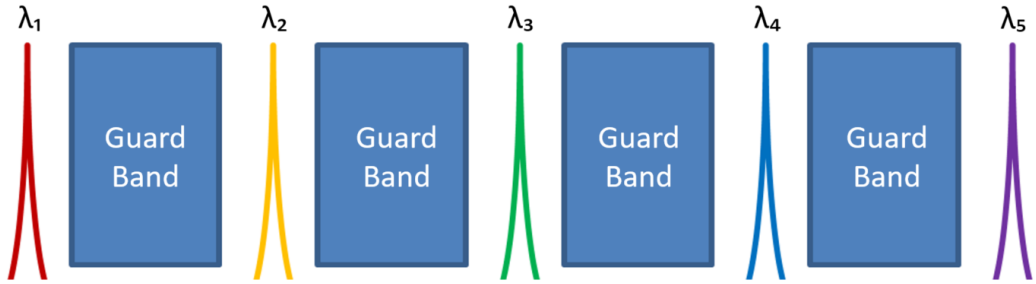


Figure 1.2: Illustration of channels in an optical network separated by 50 GHz.

Coherent optical combs (CoCs) can potentially reduce or eliminate the use of these guard bands. CoCs generate many different wavelengths of light, all separated by a fixed frequency. As a result, if one comb line jitters than all comb lines jitter and so there is no cross-talk between comb lines. Since a frequency comb is generated from one source, then there is also a great reduction in the carbon footprint of using a single laser to generate multiple channels as oppose to the hundreds of lasers currently used to generate hundreds of channels.

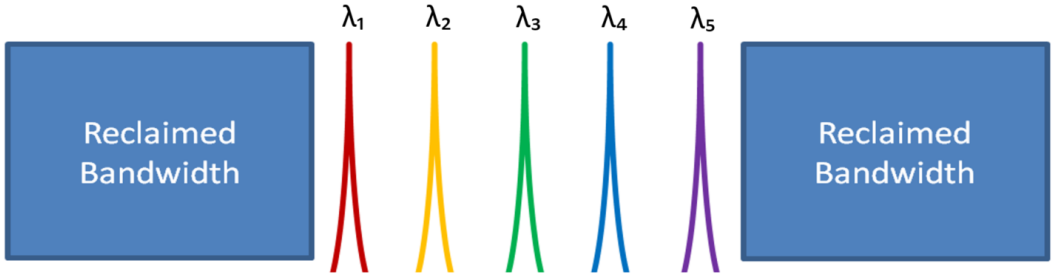


Figure 1.3: Illustration of channels in an optical network where the channels are generated by a comb source. This allows for smaller separation between channels and so the bandwidth can be reclaimed.

Coherent wavelength division multiplexing (Co-WMD) utilises the CoC to transfer data through each of the individual comb lines. Such an optical network would require a comb source to generate the frequency comb and define the separation between comb lines. A de-multiplexer would be utilised to separate out the individual comb lines into separate transmitters (optical fibers, waveguides), modulators would be used to incorporate data to each channel/comb line before the comb lines are recombined by a multiplexer and transmitted along the optical network. An illustration of such a Co-WDM is illustrated in *Figure* 1.4

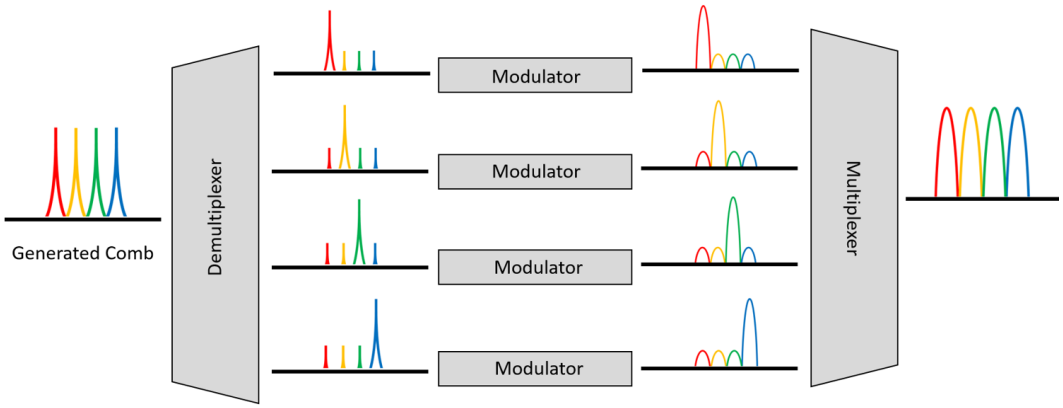


Figure 1.4: Schematic of a comb based optical network. A comb is injected into a de-multiplexer which splits the comb lines into separate modulators. Here data is incorporated before the comb lines are recombined and transmitted.

1.3 Comb Generation Methods

In the decades that followed the demonstrations of lasers and optical fibers, several methods of comb generation were developed from semiconductor devices, each with their own advantages and disadvantages.

Using mode-locked lasers is a conventional approach of generating optical frequency combs where modes of a multi-mode laser phase lock, resulting in a pulsed optical output [11]. The advantage of mode-locked lasers is their ability to generate multiple comb lines over a large bandwidth, however the spacing between their adjacent comb lines is fixed and determined by the the length of the lasers cavity [12]. Thus, a different device is required for each desired comb with a specific frequency spacing. Another disadvantage is the relatively large optical linewidth of the individual comb lines generated from passively mode-locked lasers. This can be as high as a few MHz which negatively impacts the rate at which data is transferred [12]. Optical injection locking of active mode-locked lasers has been demonstrated to improve this disadvantage [13], [14].

An alternative method of comb generation (which is the method used in this thesis) is through a technique called gain switching. This technique was first developed in the late 80s [15], [16] and the idea was simple, modulate the bias current of a laser with a high powered RF signal that rapidly, and continuously, turns the laser on and off. This takes advantage of the relaxation oscillation phenomenon which occurs when a laser is biased abruptly. When a laser is biased abruptly it undergoes a transient response in the carrier and

photon concentrations with damped oscillations before reaching a steady state. When the device is gain switched using the sinusoidal current that results from the RF modulated current, the first pulse of the relaxation oscillation is continuously excited creating a pulse train in the time domain. This is illustrated in *Figure* 1.5.

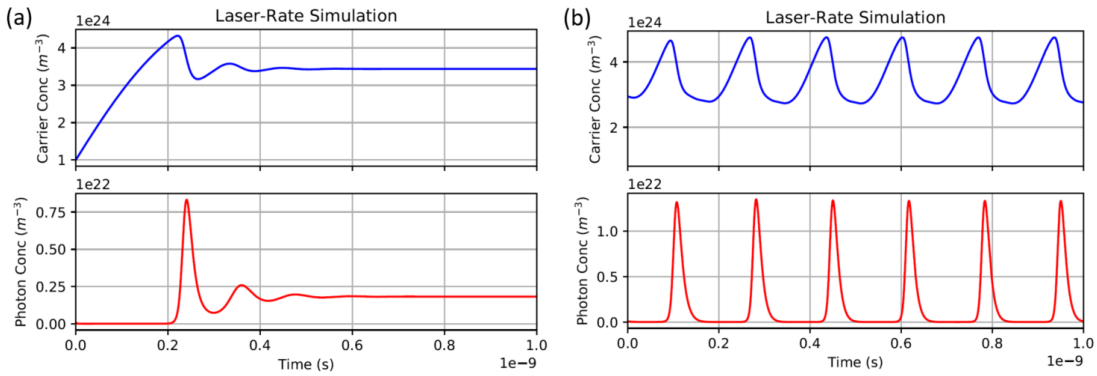


Figure 1.5: (a) Damped harmonic of the carrier and photon densities when device is biased abruptly. (b) Gain-switched carrier and photon density pulse train.

One of the main drawbacks of a gain switching during it's development was the large temporal jitter and chirp that exists across the generated pulse. This results in a broad spectral bulge as opposed to individual comb lines [17]. This is demonstrated by the plotted spectra in *Figure* 1.6 where a single sectioned Fabry–Pérot (FP) laser is biased at 50 mA (red) and is then gain switched (blue).

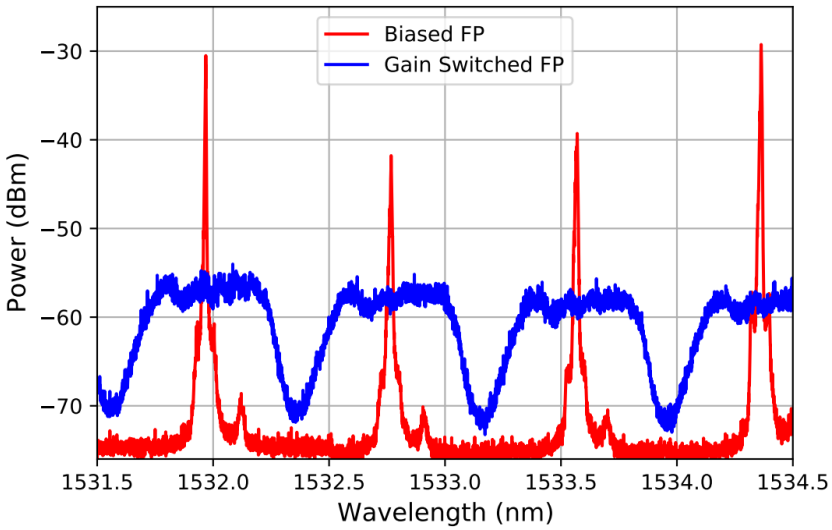


Figure 1.6: Spectra measured from an on-chip FP laser biased at (red) 50 mA and (blue) a 50 mA bias current that is modulated with a high power RF signal.

This issue was overcome in the 90s through the use of additional optical injection [18] which improved the quality of the generated pulses. Eventually on-chip gain switched combs were demonstrated through the technique of on-chip injection locking [19]. An example of a gain switched comb generated through on-chip injection locking is plotted in *Figure* 1.7.

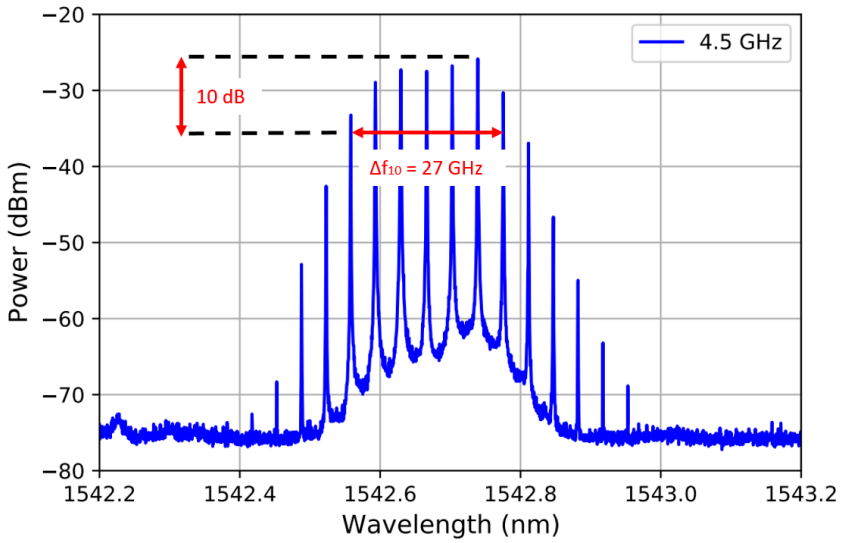


Figure 1.7: Plot of a frequency comb generated through gains witching.

While comb generation through gain switching offers less generated comb lines than those generated through mode-locking, the frequency spacing between comb lines are directly equivalent to the frequency of the gain switched current. Therefore this comb generation method offers more flexible combs than those produced through mode-locked lasers.

The quality of the combs generated in this thesis are defined by Δf_{10}, which is the frequency span of the generated comb lines that can be measured to a point 10 dB below the maximum power of the comb while plotted in dBm. This is demonstrated in *Figure* 1.7 where 7 comb lines are detectable 10 dB below the power of the maximum comb line. The comb is generated with a frequency spacing between comb lines of 4.5 GHz and so the quality of the comb is given as $\Delta f_{10} = 27$ GHz. A higher value of Δf_{10} indicates a higher quality comb, and it is the objective of this thesis to generate a comb with a high value of Δf_{10}.

1.4 Injection locking

As mentioned in the last section, the current method of on-chip comb generation is achieved through on-chip injection locking. The phenomena of injection locking was first realised by the Dutch scientist Huygens in the 1600s when he observed that two pendulum clocks would synchronise if they were placed on the same beam [20]. Optical injection locking is a technique whereby a laser (typically known as the master or primary laser) injects light into another laser (slave or secondary) and the light generated from the secondary laser phase locks to that of the primary laser. This technique is referred to as a primary-secondary configuration throughout this thesis. This phenomenon was first theorised in 1965 [21] and demonstrated experimentally a year later [22].

Since the development of lasers, the tendency for the emitted light to reflect back on itself has posed a challenge. This light, that is reflected back into the laser itself, can proceed to destabilise or even disable the functionality of the laser. An optical isolator was developed based on the Faraday effect which rotates the polarisation of incident light through the isolator which causes the reflective light to be cut off [23], [24]. So, typical off-chip primary-secondary configurations utilise these isolators between the two lasers so that no light is reflected back into the primary laser that would perturb the system. However, relating this to on-chip PICs, the scalability of on-chip isolators remains an issue and are not yet compatible with any semiconductor technology [25].

On-chip phase coupling between integrated lasers has been previously demonstrated in [26] and [27] with very different configurations and design types. In both of these cases, the biasing of the lasers was also highly asymmetric, thereby approximating a primary-secondary configuration and so an integrated isolator isn't required. On-chip gain switched comb generation has been demonstrated using this technique [19] by injection locking a secondary FP laser with a primary single mode (SM) laser and gain switching the secondary laser. This resulted in an optical frequency comb. The use of injection locking has resulted in favourable effects which include noise suppression, linewidth reduction [19], [28] and enhanced modulation bandwidth [29]. An example of the spectra of a FP laser before and after it is injection locked with a SM primary laser is demonstrated in *Figure* 1.8.

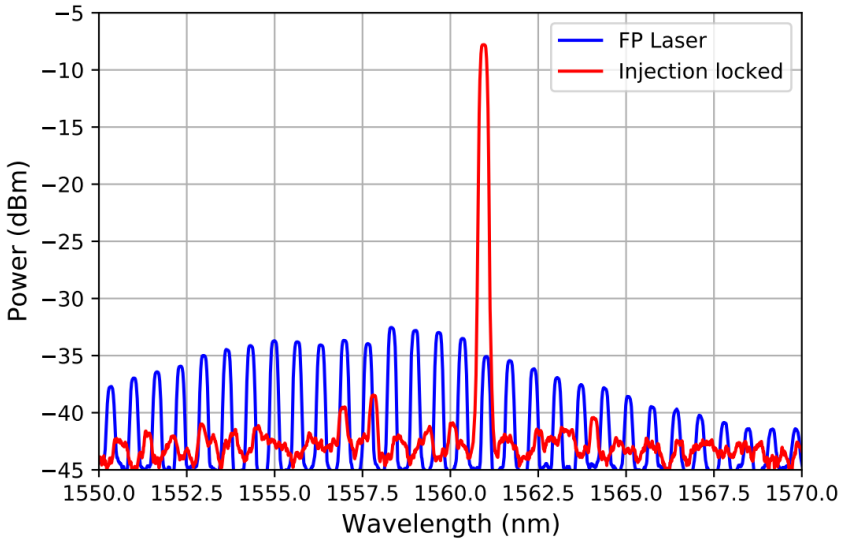


Figure 1.8: Spectra of the secondary FP laser (blue) before and (red) after it is injection locked with the SM primary laser.

1.5 Thesis Motivation

This chapter gives a brief introduction to fiber optic communications and the issues and limitations of today's day and age as more and more people seek to connect through the worldwide web. The need for next generation technologies that could help reclaim the limited bandwidth are becoming more and more necessary with optical comb sources being viewed as a realistic replacement to the hundreds of lasers that are in use today. Each of these hundreds of lasers are used to generate a channel which fill up the limited bandwidth, in part due to the spectrally inefficient guardbands that separate these channels to prevent cross-talk in the likely event of a jittering channel. Optical frequency comb sources have the potential to reduce or even eliminate these guardbands and reclaim bandwidth. As all comb lines originate from a single source, one laser could replace multiple lasers and be used to generate a number of channels (comb lines). The fixed phase relation between comb lines means that if one comb line jitters than all comb lines from that source will jitter, meaning there is no cross talk between adjacent carriers and so the frequency separation between channels can be decreased to below today's standards. This would lead to the development of Co-WDM where a comb source is integrated with a WDM network. Such a network would require a comb source to generate a number of channels, a de-multiplexer to separate these channels into different modulators where data is incorporated, finally a multiplexer would be used to recombine these channels before they are

transmitted. There are a few methods of generating such frequency combs, two that are mentioned in this chapter are combs through mode locked lasers and combs through gain switching. Gain switching was the method of comb generation selected for this thesis due to its flexibility in terms of the combs free spectral range (FSR) and general ease in terms of integration.

Previous work on gain switched combs carried out in this research group resulted in the development of on-chip gain switched combs. Several device designs were created, typically made up of two lasers operating in a primary-secondary configuration where one laser was gain switched to generate a comb. The effects of this optical injection was analysed and phase noise was shown to increase with gain switching and decrease when the gain switched laser was injection locked to a low linewidth primary laser. Optical combs with linewidths in the region of 300 kHz were demonstrated with a comb line spacing of up to 10 GHz [19]. While this work was valuable, the limit to the bandwidth of the combs generated through gain switching means that improvements can always be made, and thus this is the primary motivation for this thesis.

In this thesis, different methods of comb enhancement were investigated and developed. Simulations were carried out to investigate the experimental effects of the gain switched current on generated combs. Previous methods of gain switching were replicated through injection locked gain switched lasers and building on this, new forms of coupling were realised. The notoriously unstable bidirectional coupling that occurs on bench-top experiments due to the lack of optical isolators don't have the same detrimental effects for on-chip circuits. Instead, stable combs are found to propagate along gain switched PICs without disrupting the operation of the lasers themselves. The previous on-chip, primary-secondary coupling through the asymmetric biasing of two lasers were discarded in favour of non-asymmetric biasing techniques which greatly improved the Side Mode Suppression Ratio (SMSR) of the single mode phase locked lasers, and greatly enhanced the bandwidth of the resulting generated combs.

The use of integrated ring lasers were demonstrated to selectively filter the individual comb lines generated by a gain switched PIC. This paves the way for the use of an array of ring lasers to form a de-multiplexing network for next generation Co-WDM optical networks. Finally, a new method of achieving gain switched combs was realised using a two section, single cavity laser without

the previous additional forms of optical injection. This realised device was more flexible in terms of the range of bias currents at which combs could be generated which allowed for currents with higher RF effects to be analysed.

Based of the above techniques, next generation PICs were designed, demonstrating numerous methods of gain switched comb enhancement.

1.6 Thesis Outline

This thesis is comprised of nine chapters including the *Introduction* and *Conclusion* which illustrate in detail the development of the gain switched frequency combs throughout this project.

Chapter 1 introduces the concept of fiber optics and discusses the limitations of today's optical networks. WDM networks are introduced and the development of comb sources for Co-WDM networks are suggested as an alternative optical network that could reduce the number of lasers used and reclaim the limited bandwidth. Different comb generation methods are introduced and the method of gain switching is the technique chosen for this thesis.

Chapter 2 demonstrates the simulations analysed and utilised throughout this project. The use of reflection profiles are used to simulate the transmitted modes generated by the different lasers used throughout this thesis. Designs of on-chip FP lasers are demonstrated and designs of single mode lasers are illustrated by including reflective defects along portions of the FP ridge. The rate equations are introduced and utilised to demonstrate how gain switched combs are effected by experimental parameters like bias current and the amplitude of the gain switched current. Finally, the transmission profile of a ring laser is used to demonstrate how ring laser could be used as an integrated laser filter (ILF) and filter out the individual lines of a comb.

Chapter 3 focuses of the fabrication process of the devices utilised in this thesis. The standard lithography techniques and etch steps of each device feature is described in detail.

Chapter 4 introduces the characterisation setup used throughout this project and the experimental effects of the features described in *Chapter 3* are analysed. Starting with a FP confined with two cleaved facets, the characterisation effects of etched facets and metal etched facets are analysed. The effects of a reflective defect along the ridge of a FP are demonstrated, as

well as the effects of bends on curved waveguides.

Chapter 5 sets the stage of how different coupling techniques are used to generate gain switched combs. Starting with previous primary-secondary asymmetric bias coupling, non-asymmetric bias combs are realised and enhanced. On-chip bidirectional combs are generated and are demonstrated to propagate throughout the PIC without effecting the lasers functionality.

Chapter 6 demonstrates the effects of the gain switched frequency on the combs generated through non-asymmetrically biased means. The effects of the gain switched frequency on these combs are greatly effected by each lasers relaxation oscillation (RO) frequency, and when the gain switched frequency is an integer multiple of the laser's RO frequency, a comb is generated with a frequency spacing equivalent to that laser's RO frequency.

Chapter 7 demonstrates on-chip, how a ring laser can be used as an effective ILF to filter out individual comb lines. This PIC is designed with a large number of test structures, so that each laser can be characterised independently and as a system. The PIC demonstrates coherent combs through bidirectional coupling and comb line filtering through injecting the comb into a ring laser.

Chapter 8 introduces a new form of gain switched device that is capable of generation combs without an additional form of optical injection. The design of the device allows for comb generation through high bias currents and thus the generated combs can take advantage of higher RF effects as a result of gain switching through sinusoidal currents with greater amplitudes. This greatly enhances the bandwidth of the generated combs.

Chapter 9 concludes the work carried out as a part of this thesis and gives examples of next generation devices. The goal of the next generation devices is to increase the bandwidth and power of on-chip gain switched combs. Optical amplifiers, mutually coupled lasers and full de-multiplexing systems are described for future objectives.

Chapter 2

Simulations

2.1 Chapter Overview

This chapter introduces a model describing the spectra of photonic integrated circuits and gain switched combs. The first goal was to simulate the lasing wavelengths of a Fabry Pérot (FP) ridge laser using transmission matrices and, building on this, introducing different reflections to filter specific wavelengths over others. The designs simulated in this chapter are the primary designs used in the later experimental chapters.

Furthermore the concept of gain switching is introduced and a mathematical model is formed from the lasers rate equations. Methods of attaining the optimum parameters of gain switched combs are demonstrated by adjusting experimental variables. The concept of de-multiplexers are also relayed as well as methods of comb line filtering using injection locked ring lasers.

2.2 Laser Modelling

In terms of designing a laser, it is important to determine the wavelengths at which it lases. The transmission matrix method can be used to provide a one dimensional model of a laser's reflection and transmission, and thus can provide the wavelengths supported in the laser cavity [30]. To describe the transmission matrix method, it is first useful to introduce scattering matrices. Scattering matrices can be used to describe the behaviour of complex laser cavities by associating each series of elements into a given number of ports, usually inputs and outputs.

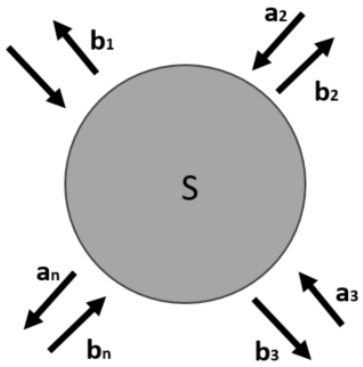


Figure 2.1: Illustration of the inputs and outputs of a multi-port scattering junction.

If the outputs are linearly related to the inputs, then a matrix can be formed to describe the outputs as a combination of the inputs.

This relation is so given:

$$b_i = \sum_j S_{ij} a_j \tag{2.1}$$

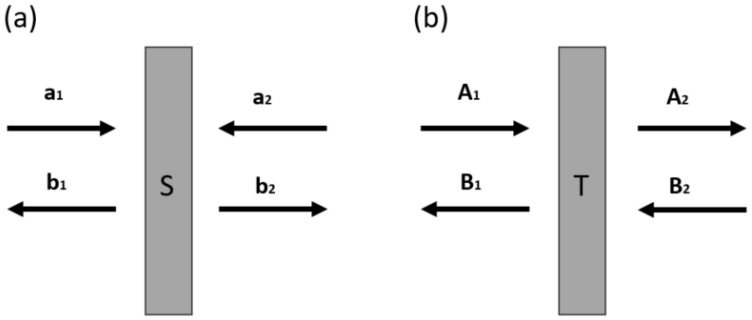


Figure 2.2: Illustration of a two port junction with the scattering and transmission inputs and outputs.

In the case of a two port system *Equation* 2.1 becomes:

$$\begin{bmatrix} b_1 \\ b_2 \end{bmatrix} = \begin{bmatrix} S_{11} & S_{12} \\ S_{21} & S_{22} \end{bmatrix} \times \begin{bmatrix} a_1 \\ a_2 \end{bmatrix} \tag{2.2}$$

and the corresponding transmission matrix can be given by:

$$\begin{bmatrix} a_1 \\ b_1 \end{bmatrix} = \begin{bmatrix} T_{11} & T_{12} \\ T_{21} & T_{22} \end{bmatrix} \times \begin{bmatrix} a_2 \\ b_2 \end{bmatrix} \tag{2.3}$$

The scattering and transmission matrices are therefore related by [30]:

$$\mathbf{S} = \frac{1}{T_{11}} \begin{bmatrix} T_{21} & det(\mathbf{T}) \\ 1 & -T_{12} \end{bmatrix} \tag{2.4}$$

$$\mathbf{T} = \frac{1}{S_{21}} \begin{bmatrix} 1 & -S_{22} \\ S_{11} & -det(\mathbf{S}) \end{bmatrix} \tag{2.5}$$

For the purpose of devices used in this project, the scattering and transmission matrices used refer to the matrix to describe a reflective interface and the matrix to describe the propagation through a waveguide of length L.

The matrices for a reflective interface and waveguide are given as:

$$\mathbf{S}_r = \begin{bmatrix} r & t \\ t & -r \end{bmatrix} \tag{2.6}$$

$$\mathbf{S}_{wg} = \begin{bmatrix} 0 & e^{-j\phi} \\ e^{-j\phi} & 0 \end{bmatrix} \tag{2.7}$$

respectively, where $\phi = 2\pi nL/\lambda$, r and t are the reflection and transmission coefficients respectively and n and L are respectively the refractive index and length of the waveguide.

The corresponding Transmission matrices for a reflective interface and waveguide are therefore:

$$\mathbf{T}_r = \frac{1}{t} \begin{bmatrix} 1 & r \\ r & 1 \end{bmatrix} \tag{2.8}$$

$$\mathbf{T}_{wg} = \begin{bmatrix} e^{j\phi} & 0 \\ 0 & e^{-j\phi} \end{bmatrix} \tag{2.9}$$

2.2.1 Fabry Pérot Profile

A semiconductor Fabry Pérot (FP) laser consists of two reflective surfaces (cleaved facets) separated by a waveguide. The transmission matrix that describes a FP can thus be determined by multiplying the matrices of each

cleaved facet and the waveguide.

$$T_{FP} = T_{CF} \cdot T_{WG} \cdot T_{CF} = \frac{1}{t}\begin{bmatrix} 1 & r \\ r & 1 \end{bmatrix} \cdot \begin{bmatrix} e^{j\phi} & 0 \\ 0 & e^{-j\phi} \end{bmatrix} \cdot \frac{1}{t}\begin{bmatrix} 1 & -r \\ -r & 1 \end{bmatrix} \tag{2.10}$$

The reflection and transmission profiles of the FP can be determined by S_{11}^2 and S_{21}^2 respectively.

$$S_{11}^2 = \left(\frac{T_{FP}(2,1)}{T_{FP}(1,1)}\right)^2 = -r_1 - \frac{r_2 t_1^2 e^{-2j\phi}}{1 - r_1 r_2 e^{-2j\phi}} \tag{2.11}$$

$$S_{21}^2 = \left(\frac{1}{T_{FP}(1,1)}\right)^2 = \frac{t_1 t_2 e^{-2j\phi}}{1 - r_1 r_2 e^{-2j\phi}} \tag{2.12}$$

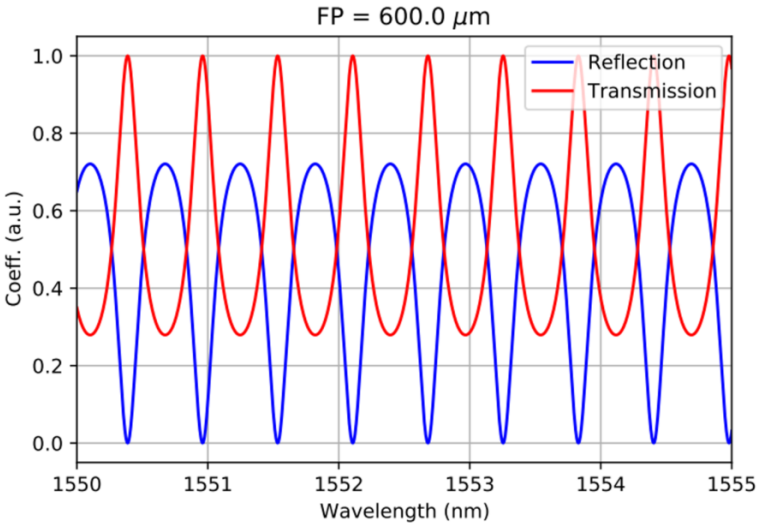


Figure 2.3: (blue) Reflection profile and (red) Transmission profile of a FP laser 600 μm in length.

The reflection and transmission coefficients can be related to the effective refractive index using:

$$r = \frac{n_1 - n_2}{n_1 + n_2} \tag{2.13}$$

In the case of a FP, the cleaved facet offers reflection between the laser cavity and air, and so $n_1 = 1$ and $n_2 = n_{(InP)}$. in order to simulate the reflection and transmission profiles of a laser, the following parameters are assumed:

Table 2.1: Parameter definitions and values

Name	Symbol	Value
Waveguide Length	L	600 μm
refractive index	n	3.5

And so both S_{11}^2 and S_{21}^2 can be plotted as shown in *Figure* 2.3.

Figure 2.3 demonstrates multiple modes being supported in the FP laser cavity, which is the nature of a FP Laser spectrum. The resonant wavelengths of the FP exists when the transmission is maximum and the reflection minimum. The separation between adjacent modes, and therefore lasing wavelengths, is dependent on the device length. This is demonstrated in *Figure* 2.4.

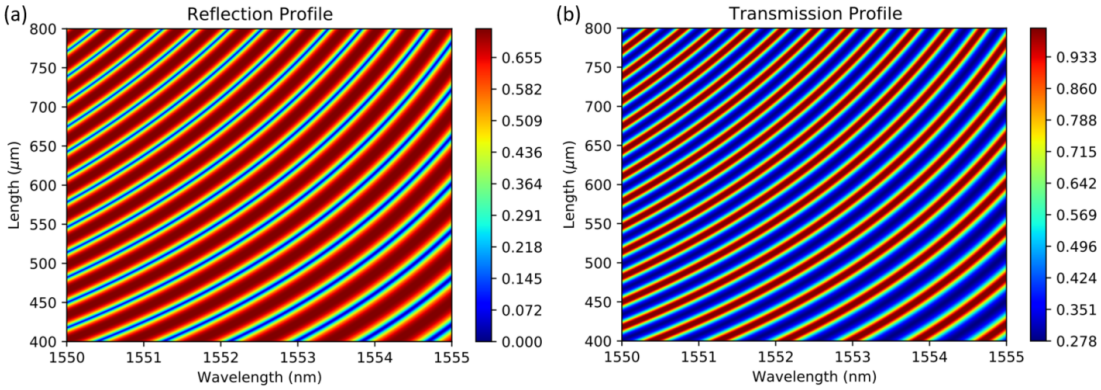


Figure 2.4: (a) Reflection profile and (b) Transmission profile of a FP laser for a cavity length ranging from 400 - 800 μm .

This simulation demonstrates how the separation between adjacent reflection/transmission modes decrease with an increasing cavity length. This is consistent with the free spectral range (FSR) of a laser cavity given by [31] where:

$$FSR(\nu) = \Delta\nu = \frac{c}{2nL} \tag{2.14}$$

Where c is the speed of light, n is the refractive index and L is the length of the cavity. The relation to FSR(λ) can be derived by:

$$\Delta\nu = \frac{c}{\lambda_1} - \frac{c}{\lambda_2} = \frac{c}{2nL} \tag{2.15}$$

Simplifying this further,

$$FSR(\lambda) = \Delta\lambda = \lambda_2 - \lambda_1 = \frac{\lambda_1\lambda_2}{2nL} \tag{2.16}$$

Which demonstrates that the FSR(λ) is inversely proportional to the length of the cavity.

2.2.2 Slotted Fabry Pérot Profile

The primary lasers used in later chapters are single mode lasers, which are lasers with a side mode suppression ratio (SMSR) grater than 30 dB. An SMSR is the difference in power measured in dB between the the primary and secondary lasing modes. This can be achieved by etching slots along the ridge of the FP laser. This in turn creates regions of varying effective refractive index and therefore these slots act as reflective defects along the ridge of the laser creating a Slotted Fabry Pérot (SFP) laser [32].

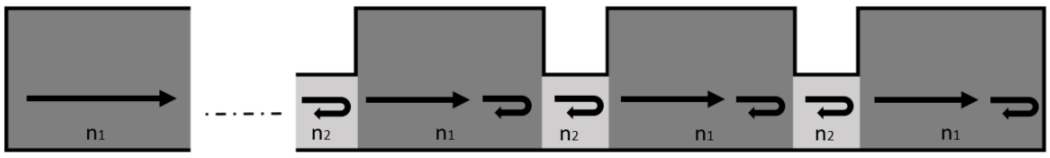


Figure 2.5: Illustration of the varying effective refractive indices created by etching slots into the ridge of a laser.

A profile describing the reflections of this slotted section of a laser can be derived using transmission matrices. One slot period, made up of the slot and interslot, can be described by the transmission matrix of the waveguide of the interslot $T_{WG_{IS}}$, interface between the interslot and slot $T_{R_{IS}}$, the waveguide of the slot T_{WG_S} and the interface between the slot and the interslot T_{R_S}. Therefore the transmission matrix of the entire slotted region of N slots can be given by:

$$T_{Slots} = \left(T_{WG_{IS}} T_{R_{IS}} T_{WG_S} T_{R_S}\right)^N \tag{2.17}$$

Deriving the S_{11} from this can give a description of the reflection profile of the slotted region. Transmission and reflection coefficients of the slot, t_s and r_s, are assumed to be $\sqrt{0.817}$ and $\sqrt{0.033}$ [30].

A typical cavity design that utilises these slots in later chapters to create a single mode spectra is illustrated in *Figure* 2.6. The slot length is assumed to be 1 μm, which is the limiting resolution of lithography, and the interslot region is set to 87 μm.

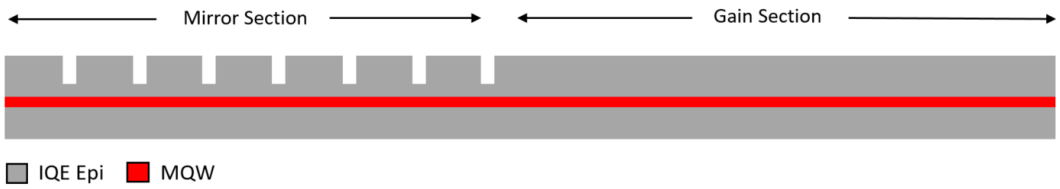


Figure 2.6: Diagram of a single cavity device separated into a gain and slotted mirror section.

Figure 2.7 demonstrates the modes reflected by 7 slots with an interslot separation of 87 μm as illustrated in *Figure 2.6*. These slots are etched into a portion of a 1300 μm ridge known as the mirror section, while the remaining portion of the ridge is known as the gain section. This gives the transmission lasing modes plotted in *Figure* 2.7. As opposed to the transmission profile of a FP laser, the maximum value of transmission peaks are no longer constant, but are instead suppressed by the larger modes created by the slots' reflection.

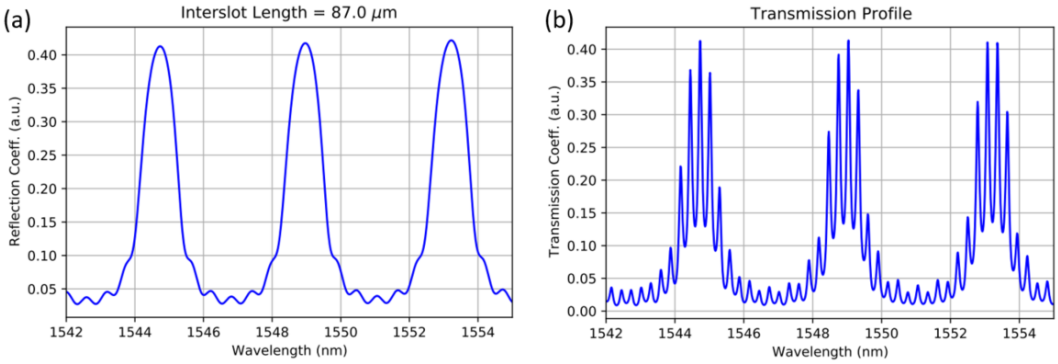


Figure 2.7: (a) Reflections caused by the 7 slots with an interslot separation of 87 μm and (b) Transmission profile of a 1300 μm cavity with 7 slots and an interslot separation of 87 μm.

The resulting laser has the potential to lase at any of the regions created by the supermodes, however whether or not they lase depends on the position of the smaller modes within. The position of these modes can be adjusted by changing the optical path length of the cavity through current injection [33]. This shift is illustrated in *Figure* 2.8.

What results is a single mode laser than can be tuned through current injection.

2.2.3 Pitted Fabry Pérot

An alternative method of creating reflections along the ridge of a laser is by etching small deep pits through the ridge. The repeated interfaces results in

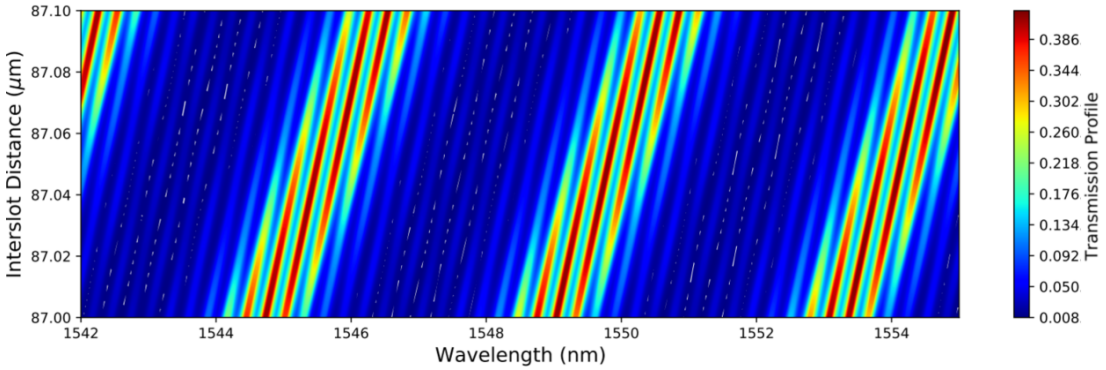


Figure 2.8: Transmission profile of the SFP laser as the optical path length of the device is varied.

additional reflections creating a Pitted Fabry Pérot (PFP) [34].

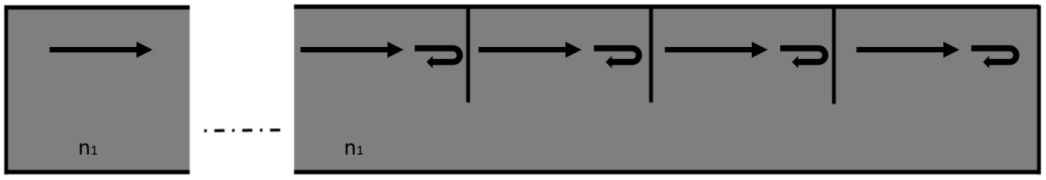


Figure 2.9: Illustration of the varying reflective defects created by etching pits into the ridge of a laser.

The transmission matrix of one pit period can be determined by multiplying the transmission matrix of the pit interface reflection T_{R_P}, and the waveguide of the interpit $T_{WG_{IP}}$. And so the transmission matrix of the entire pitted region of N pits can be given by:

$$T_{Pits} = (T_{R_P} T_{WG_{IP}})^N \tag{2.18}$$

Again, deriving the S_{11} from this can determine the reflection profile caused by these reflective defects. This was carried out for another typical laser design used in later chapters. This laser is depicted in *Figure* 2.10 where the mirror section is made up of 8 pits with an interpit separation of 77 μm.

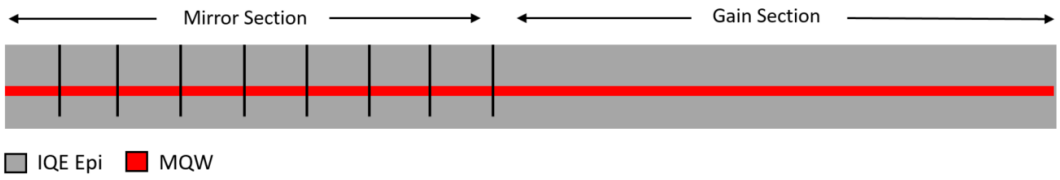


Figure 2.10: Diagram of a single cavity device separated into a gain and pitted mirror section.

Figure 2.11 demonstrates the reflection by 8 pits with an interpit separation of 77 μm. Again these are etched into a portion of a 1300 μm ridge which will act as a mirror section and the remaining portion of the ridge will act as a gain section. Plots of the resulting transmission profile of the device is shown in *Figure* 2.11.

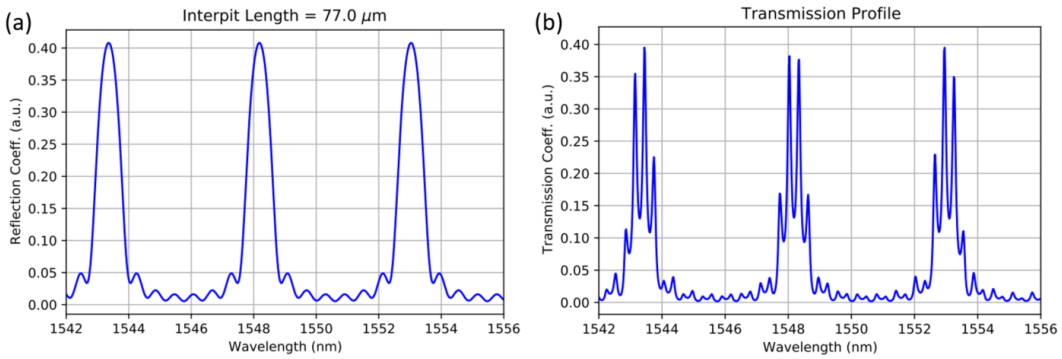


Figure 2.11: (a) Reflections caused by the 8 pits with an interpit separation of 77 μm and (b) Transmission profile of a 1300 μm cavity with 8 pits and an interpit separation of 77 μm.

Again the position of the lasing modes can be varied through current injection with an illustration of this depicted in *Figure* 2.12

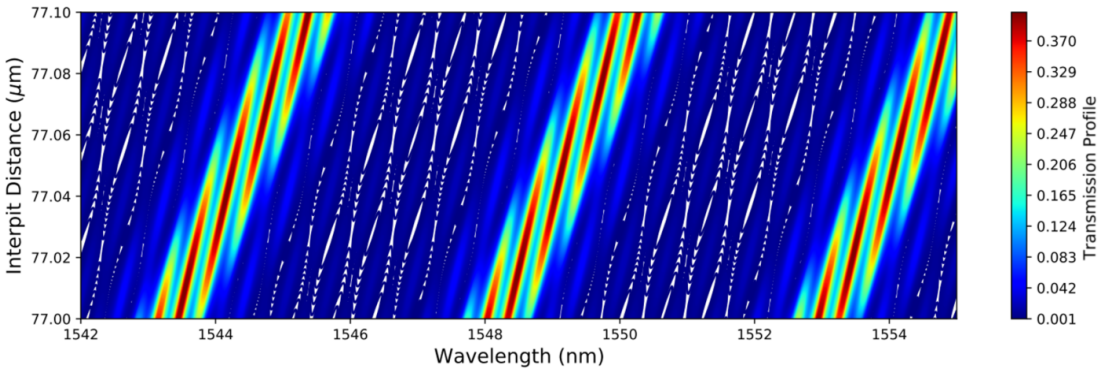


Figure 2.12: Transmission profile of the PFP laser as the optical path length of the device is varied.

2.3 Gain Switching

2.3.1 The Rate Equations

To understand how gain switching results in generating optical combs, one must first understand the relaxation oscillation phenomena for a semiconductor laser. Due to the interplay between carriers and photons, the laser does not initially operate in a steady state when it is switched on. Instead, when biased abruptly, it experiences a spike in carrier and photon densities with damped oscillations before reaching a steady state.

The dynamics of the carrier and photon densities, represented by $N(t)$ and $S(t)$ respectively, are given by the equations [35]:

$$\frac{dN}{dt} = \frac{I(t)}{eV} - R(N) - \frac{v_g g(N) S(t)}{1 + \epsilon S(t)} + F_N(t) \tag{2.19}$$

$$\frac{dS}{dt} = \left(\frac{\Gamma v_g g(N)}{1 + \epsilon S(t)} - \frac{1}{\tau_p} \right) S(t) + \beta \Gamma B N^2(t) + Y_S(t) + F_S(t) \tag{2.20}$$

Where $I(t)$ is the time varying injection current, e is the electron charge, V is the volume of the active region, v_g is the group velocity, $g(N)$ is the material gain, ϵ is the non linear gain coefficient, Γ is the optical confinement factor, τ_p is the photon lifetime, β is the fraction of the spontaneous emission coupled into the lasing mode. $Y_s(t)$ is a term used to describe external optical injection when it is considered. $F_N(t)$ and $F_S(t)$ represent additional Langevin noises from different sources. The recombination rate is given by [35]:

$$R(N) = AN + BN^2 + CN^3 \tag{2.21}$$

Where A, B and C are the non-radiative, the spontaneous and the Auger recombination coefficients respectively. The material gain, $g(N)$, is described by [35]:

$$g(N) = \frac{dg}{dN}(N - N_{tr}) \tag{2.22}$$

Where $\frac{dg}{dN}$ is the differential gain and N_{tr} is the carrier density at transparency.

Using the values provided in *Table 2.2* [36], the relaxation oscillations, with a step function input, of a diode laser can be plotted for a fixed current of 50 mA.

As mentioned earlier, when a laser is biased abruptly, the resulting carrier and photon concentrations undergo a transient response with damped oscillations

Table 2.2: Parameter definitions and values.

Name	Symbol	Value
Electron charge	e	1.602×10^{19} C
Volume of active region	V	1.53×10^{-17} m^3
Group velocity	v_g	8.5×10^{7} m s^{-1}
Material gain	$g(N)$	-
Non-linear gain coeff.	ϵ	1.97×10^{-23} m^3
Optical confinement factor	Γ	0.04
Photon lifetime	τ_p	2.2×10^{-12} s
Frac. of spontaneous emission	β	5.5×10^{-6}
External optical injection	$Y_s(t)$	Not considered
Langevin Noise	$F_N(t)$	-
Langevin Noise	$F_S(t)$	-
Non-radiative coeff.	A	3×10^{8} s^{-1}
Spontaneous coeff.	B	1.5×10^{-16} m^3 s^{-1}
Angular recombination coeff.	C	1×10^{-42} m^6 s^{-1}
Differential gain	$\frac{dg}{dN}$	4.4×10^{-20} m^2
Carrier density at transparency	N_{tr}	1×10^{24} m^{-3}

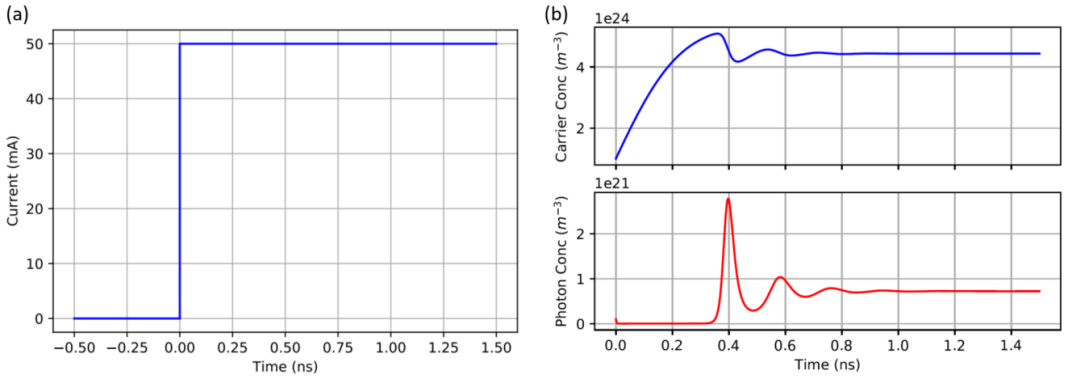


Figure 2.13: (a) Bias current of 50 mA being switched on in the time domain. (b) the corresponding carrier and photon densities of the biased laser.

before eventually reaching a steady state.

The value and frequency of these relaxation oscillations can vary a lot when changing certain parameters. In an experimental setting, the most common variable parameter would be the bias current of the laser. *Figure* 2.14 demonstrates how the carrier and photon densities vary as a function of time, from a bias current of 30 - 100 mA.

As the carrier and photon concentration values defined in *Equations* 2.19 and 2.20 are proportional to the bias current, the steady increase in peak value as the current is swept from 30 - 100 mA is expected. However, what is interesting to note is how the frequency of the relaxation oscillations also

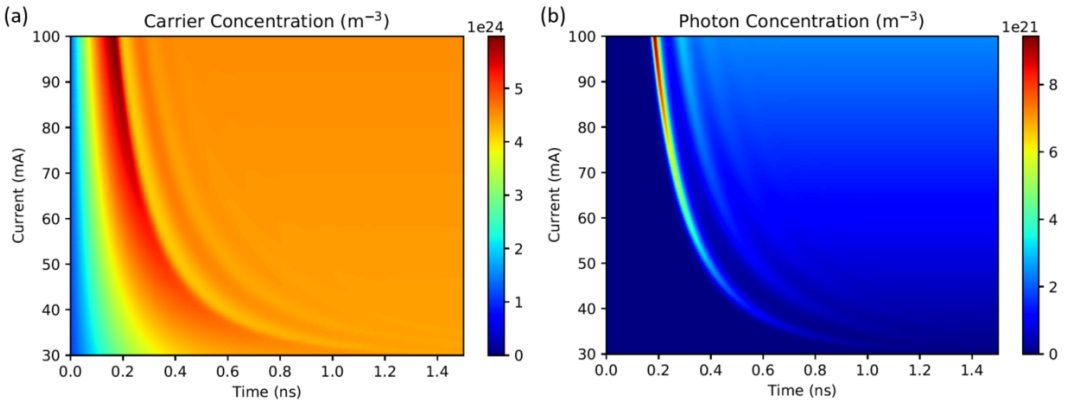


Figure 2.14: (a) Carrier concentration and (b) Photon concentration of a diode laser as the bias current is swept from 30 - 100 mA.

changes with the bias current. This frequency can be extracted from *Figure* 2.14 and is plotted in *Figure* 2.15.

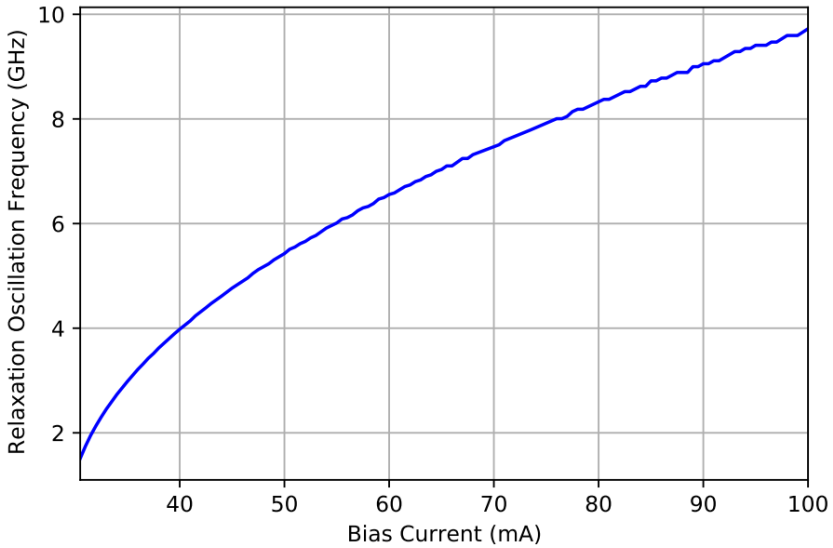


Figure 2.15: Frequency of the relaxation oscillations as bias current of the diode laser is swept from 30 - 100 mA.

The relaxation oscillation frequency (ROF) of a laser varies non-linearly with current, and in this case the ROF of the laser ranges from 1.8 - 9.8 GHz as the bias current is swept from 30 - 100 mA.

2.3.2 Gain Switched Current

The technique of gain switching, involves operating a laser in the initial non-linear regime of the relaxation oscillation phenomena demonstrated in *Figure* 2.13. In other words, we want to continuously excite the first peak of

the carrier and photon densities, creating a pulse train in the time domain. This is carried out by modulating the bias current with a strong radio frequency (RF) signal, effectively creating a sinusoidal current that rapidly turns the laser on and off throughout time and hence the first peak of the carrier and photon concentrations are continuously excited.

The input RF signal is treated as first passing an RC circuit, where the output signal is the voltage across the capacitor. This output voltage across the capacitor is used as the input signal to the rate equations.

The expression for $I(t)$ becomes [35]:

$$I(t) = I_{bias} + A_{loss}\left(\frac{Z_C V_{rf}}{R_C(Z_0 + Z_C)}\right)\sin(2\pi f t) \tag{2.23}$$

Treating the laser as a capacitor, the impedance of the capacitor is given by $Z_C = 1/j\omega C$ where C is the capacitance and $\omega = 2\pi f$. A_{loss} is a loss coefficient accounting for the frequency dependent electrical cable attenuation, V_{rf} is the root-mean square (RMS) voltage value of the signal generator applied to an ideal 50 Ω load, Z_0 = 50 Ω which is the generator output impedance. R_C represents the resistance of the laser.

When simulating the gain switched current, the following parameters are assumed.

Table 2.3: Parameter definitions and values

Name	Symbol	Value
Loss coeff.	A_{loss}	0.5
Resistance	R_C	15 Ω
Capacitance	C	500 fF

Figure 2.16 demonstrates how the sinusoidal current changes by adjusting the two experimental parameters, the bias current and the amplitude of the RF signal (V_{rf}). For a varying bias current the V_{rf} is assumed to be 1 V, and for a varying V_{rf} the bias current is assumed to be 30 mA.

What is apparent from *Figure* 2.16 and logical from *Equation* 2.23, is that there is a linear response in the value of the sinusoidal current as the bias current is increased from 0 - 100 mA. The minimum value of the sinusoidal current also increases linearly, which suggests there will be a point where the minimum value of the sinusoidal current no longer falls below the lasers threshold current, and therefore gain switching will no longer be possible.

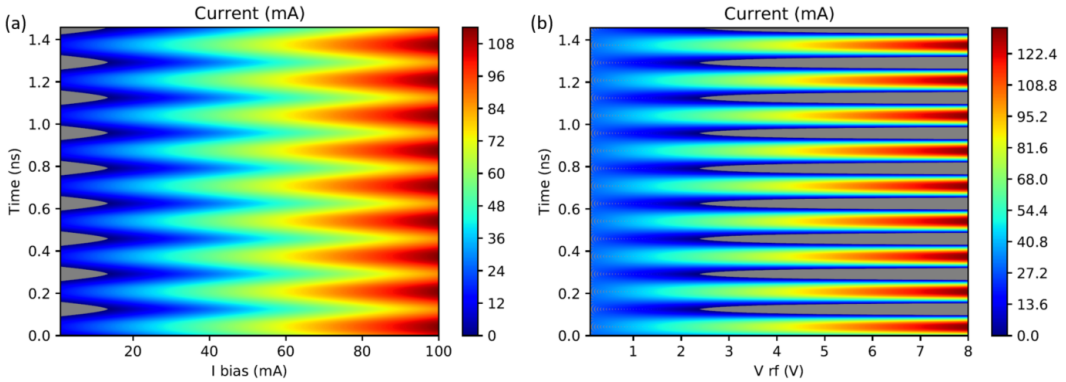


Figure 2.16: (a) Sinusoidal current as the bias current is varied from 0 - 100 mA. (b) Sinusoidal current as the V_{rf} is varied from 0 - 8 V.

The effect of the V_{rf} on the sinusoidal voltage is also demonstrated in *Figure* 2.16. The effect being an increase in the amplitude of the sinusoidal current as the V_{rf} is increased from 0 - 8 V. This increase in amplitude of the sinusoidal current can be used to compensate for the fore mentioned limitation of the bias current. In other words at higher biases, the V_{rf} can be increased to ensure that the minimum value of the sinusoidal current falls below threshold current, and so gain switching can occur.

This sinusoidal current can be introduced to the rate equations (*Equation* 2.19 and 2.20) to demonstrate how this effects the carrier and photon densities. The bias current is assumed to be 30 mA and the V_{rf} is assumed to be 1 V at a gain switched frequency of 6 GHz.

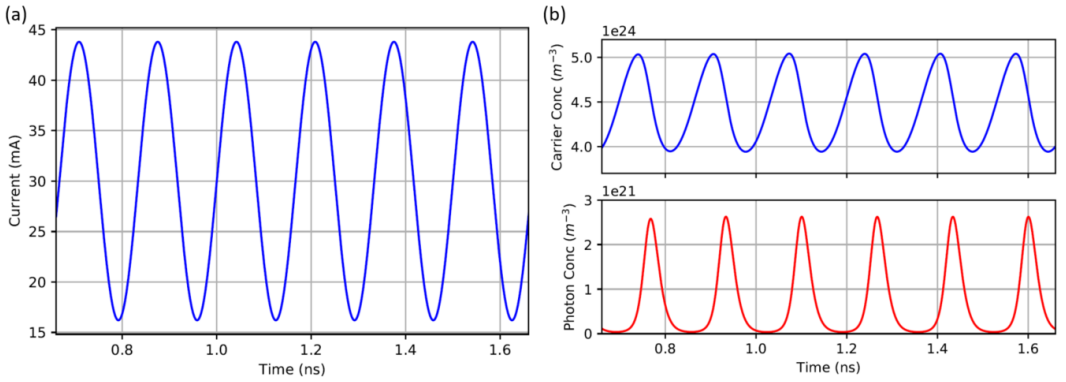


Figure 2.17: (a) Sinusoidal current biasing a laser in the time domain. (b) Resulting carrier and photon densities of the gain switched laser.

The sinusoidal current results in the device rapidly being switched on and off (gain switched). This allows for the first pulse of the carrier and photon densities relaxation oscillations to be excited continuously, effectively creating a pulse train in the time domain as demonstrated in *Figure* 2.17.

2.3.3 Gain Switched Frequency Combs

From here it is possible to simulate the generated frequency comb by first converting the pulse train of the photon density in the time domain to the frequency domain, which is possible by taking the fast fourier transform of the time trace.

This is demonstrated in *Figure* 2.18.

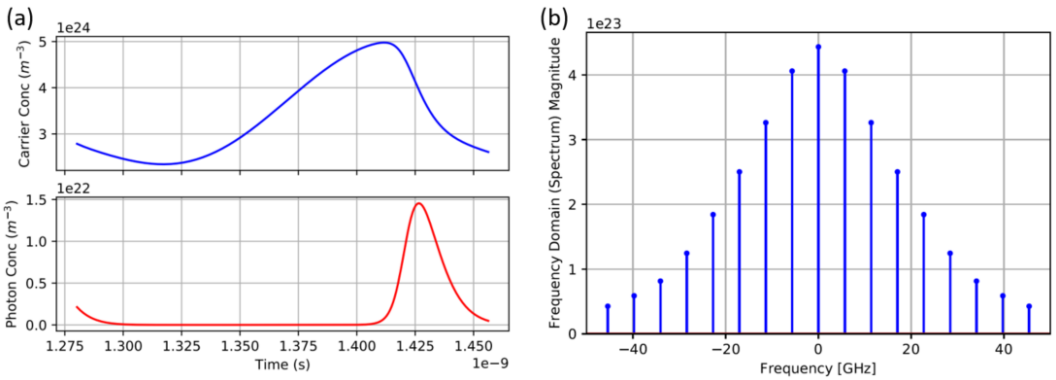


Figure 2.18: (a) Period of gain switched carrier and photon concentration. (b) Fast fourier transform of the gain switched photon density period in (a).

In *Figure* 2.18 optical pulses are attained in the frequency domain at a frequency spacing equivalent to the sinusoidal current. However, to simulate a comb, the frequency domain spectrum magnitude (the photon density) needs to be converted to power.

The photon density of the laser can be converted to power (mW) using [35]:

$$P(t) = 1000 \times \eta_f \frac{h f_0 V}{\Gamma \tau_p} S(t) \tag{2.24}$$

Where η_f is the in-fiber external quantum efficiency and f_0 is the emission frequency of the laser. These values are assumed to be:

Table 2.4: Parameter definitions and values

Name	Symbol	Value
External quantum efficiency	η_f	0.2
Emission Frequency	f_0	200×10^{12} Hz

This results in a simulated comb with a comb line separation of 6 GHz equivalent to the gain switched frequency of the RF current.

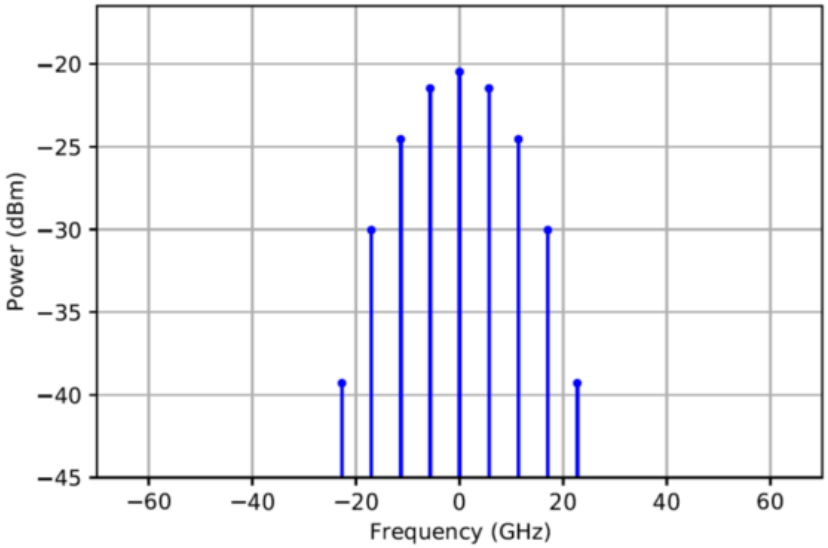


Figure 2.19: Comb simulation achieved using *Equation* 2.24. The simulation demonstrates 7 comb lines within 10 dB of the maximum comb giving a comb quality of $\Delta f_{10} = 36$ GHz.

2.3.4 Frequency Response of Gain Switched Combs

Now that a comb has been simulated, one can now go about determining the optimum parameters to generate a good quality comb, that is a comb with multiple comb lines. The main advantage of gain switched combs is the ability to easily adjust the frequency spacing of the comb lines by adjusting the frequency of the sinusoidal current. However, the range of possible frequencies is not infinite, but is largely dependent on the physical characteristics of the laser like capacitance and resistance. These parameters are assumed to be fixed and correspond with the values of the laser used in the experiment chapters.

Table 2.5: Parameter definitions and values

Name	Symbol	Value
Resistance	R	15 Ω
Capacitance	C	500 fF

The resulting combs from such a device will be generated in the low GHz range, typically from 1 - 10 GHz. However the optimum frequency of a gain switched device is known to occur at a gain switched frequency corresponding to that of the lasers ROF [12]. *Figure* 2.15 demonstrates how the ROF of a laser can be varied with current, so this can be demonstrated by attaining the frequency response of the photon density at different bias currents and

converting the results to the corresponding comb.

The effects of the modulation frequency on the gain switched photon density is demonstrated in *Figure* 2.20 for bias currents of 50, 75 and 100 mA.

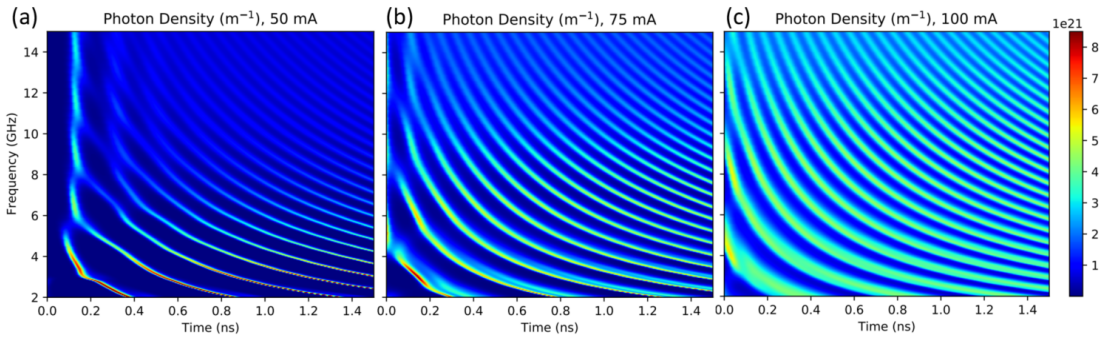


Figure 2.20: The effects of the modulation frequency on the gain switched photon density for bias currents of (a) 50 mA, (b) 75 mA and (c) 100 mA.

What is evident from *Figure* 2.20 is that the peak value of the photon density varies with current and frequency. As mentioned earlier, the ability of the gain switched device to generate combs is largely dependant on the minimum value of the sinusoidal current and whether or not it falls below the devices threshold current, therefore the degrading peak photon density for higher currents is expected. The optimum photon density peaks also occur at approximately the ROF of the device, however this is more apparent when *Figure* 2.20 is converted to the corresponding comb lines.

Using *Equation* 2.24, The corresponding combs are plotted in *Figure* 2.21

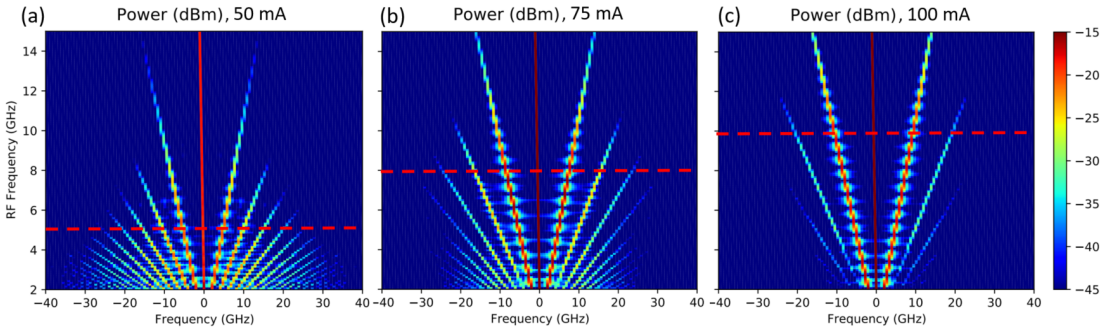


Figure 2.21: The effects of the modulation frequency on the gain switched comb for bias currents of (a) 50 mA, (b) 75 mA and (c) 100 mA. The equivalent ROFs are depicted by the dotted red line.

The main advantage of gain switched combs is the ability to generate combs at different frequencies by varying the frequency of the gain switched current. This is demonstrated here with the optimum bandwidth of the comb

depending on a different gain switched frequency for each bias current. *Figure* 2.13 gives the ROF of the device at currents of 50, 75 and 100 mA which are 5.5, 8 and 9.5 GHz respectively. These frequency values are consistent with the gain switched frequency at which the optimum combs are generated.

2.3.5 Bias Current Response

The effects of bias current on a generated comb can also be demonstrated. A comb is simulated at a gain switched frequency of 6 GHz and a current is swept from 25 - 150 mA. The result is plotted in *Figure* 2.22.

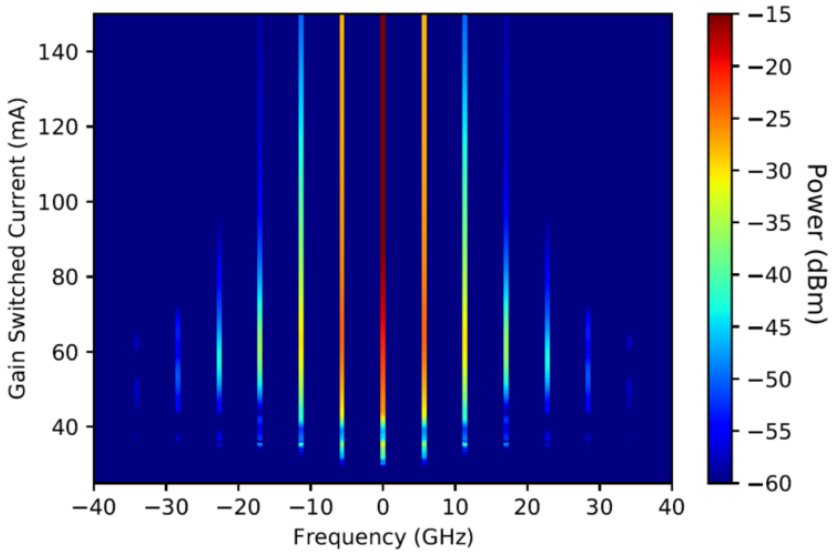


Figure 2.22: Plot illustrating how a gain switched comb varies with bias current.

The frequency separation of the generated comb is 6 GHz and again, from *Figure* 2.15, the bias current at which the ROF of the device is equivalent to the frequency of this comb occurs at 55 mA, which is consistent with the optimum comb generated here. Also, this plot demonstrates how the comb degrades as the current increases. Again this is due to the minimum value no longer falling below the threshold current as is illustrated in *Figure* 2.16(a). Therefore, as the current increases the gain switched effects will degrade until a point where a comb can no longer occur.

2.4 Comb Line Filtering

A comb based optical transmitter would not only need to generate comb lines, but also be integrated with a de-multiplexer. This would be used to divide the individual comb lines into waveguides with separate modulators which would incorporate data before the comb lines are recombined and transmitted. The main challenge in utilising an optical frequency comb source (OFCS) in such networks, is the difficulty in de-multiplexing closely spaced comb lines [37].

Modern day wavelength division multiplexing (WDM) systems employ de-multiplexers based on arrayed waveguide gratings (AWG) which is depicted in *Figure* 2.23. However, these de-multiplexers don't have the resolution to separate comb lines with a frequency spacing under 50 GHz [38], due to the difficulty of de-multiplexing the comb while retaining relative coherence between the optical carriers [39].

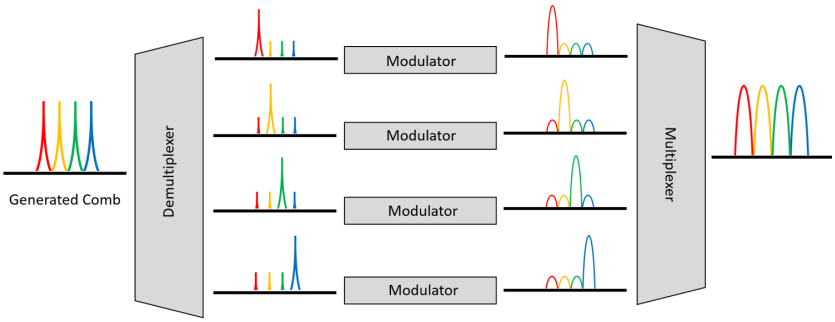


Figure 2.23: Schematic of a comb based optical network.

Later in this thesis, a ring laser is integrated on-chip with a comb source with the purpose of filtering out the individual comb lines. The idea is to use an injection locked ring laser as an integrated laser filter (ILF). Using injection locked lasers as coherent de-multiplexers has been previously demonstrated [39], while it has also been shown that further improvements in the mode suppression during de-multiplexing can be made with higher Q laser cavities [40–42].

An illustration of a ring's transmission profile is given in *Figure* 2.24 [30]. This example demonstrates a ring laser with a high Q factor and free spectral range of approximately 66 GHz. This figure also demonstrates how this transmission profile is effected as the optical path length changes.

The objective is to inject a comb into this ring and using current injection, change the optical path length of the ring to filter out individual comb lines.

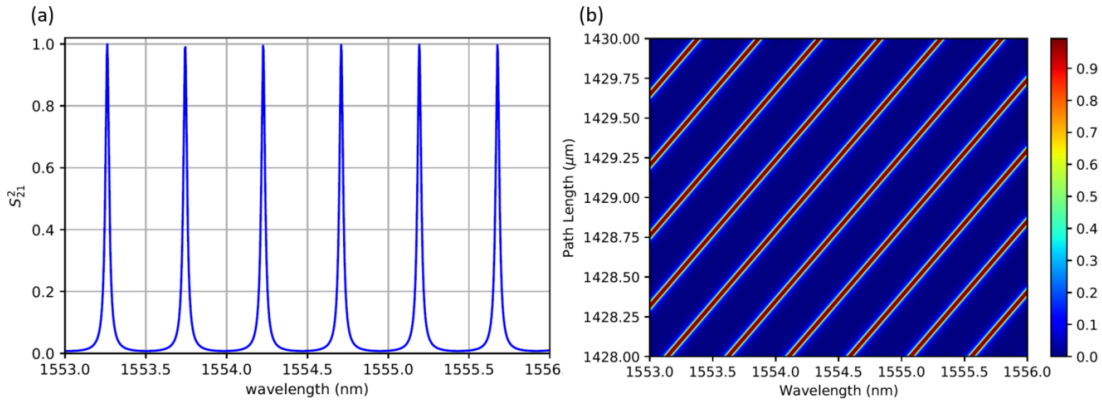


Figure 2.24: (a) Transmission profile of a ring laser. (b) transmission profile of a ring laser as the optical path length is adjusted.

Using a simulated comb from *Section* 2.3.3 and converting it to the wavelength domain, one could simulate this filtering. The simulated comb is demonstrated in *Figure* 2.25 as well as the corresponding ring laser mode required to filter the individual comb lines. The comb is simulated using a frequency spacing of 5 GHz with a bandwidth of 50 GHz. This ensures that the ring free spectral range of 66 GHz is large enough to ensure that no more than one comb line will be filtered at once.

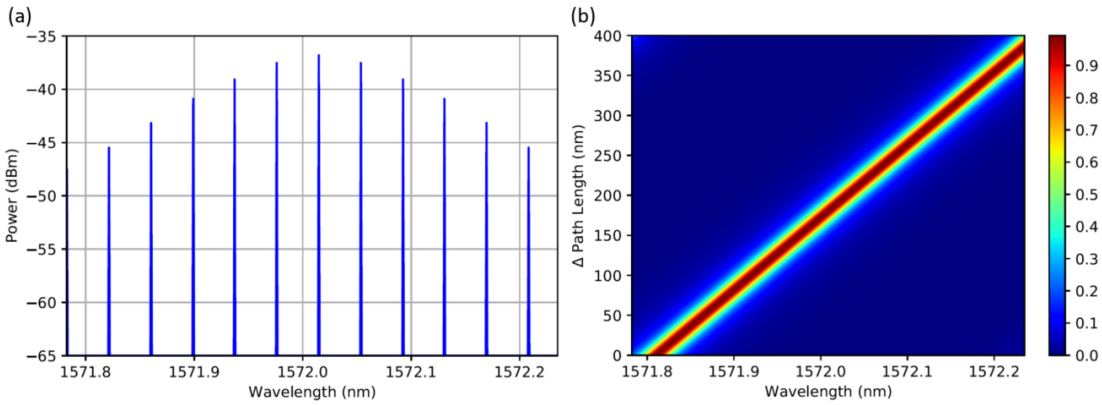


Figure 2.25: (a) Simulated comb with frequency spacing of 5 GHz. (b) Corresponding ring transmission mode.

The objective is to pass the comb through the ring laser and allow the injection locked ring to filter out one comb line at a time and use current injection to adjust the position of the rings transmission mode along the wavelength domain. This is depicted in *Figure* 2.26.

The high Q-factor of the ring laser allows for the injection locking of individual comb lines. As the position of the ring's transmission is adjusted, each comb is suppressed sufficiently before the next comb line is transmitted, therefore

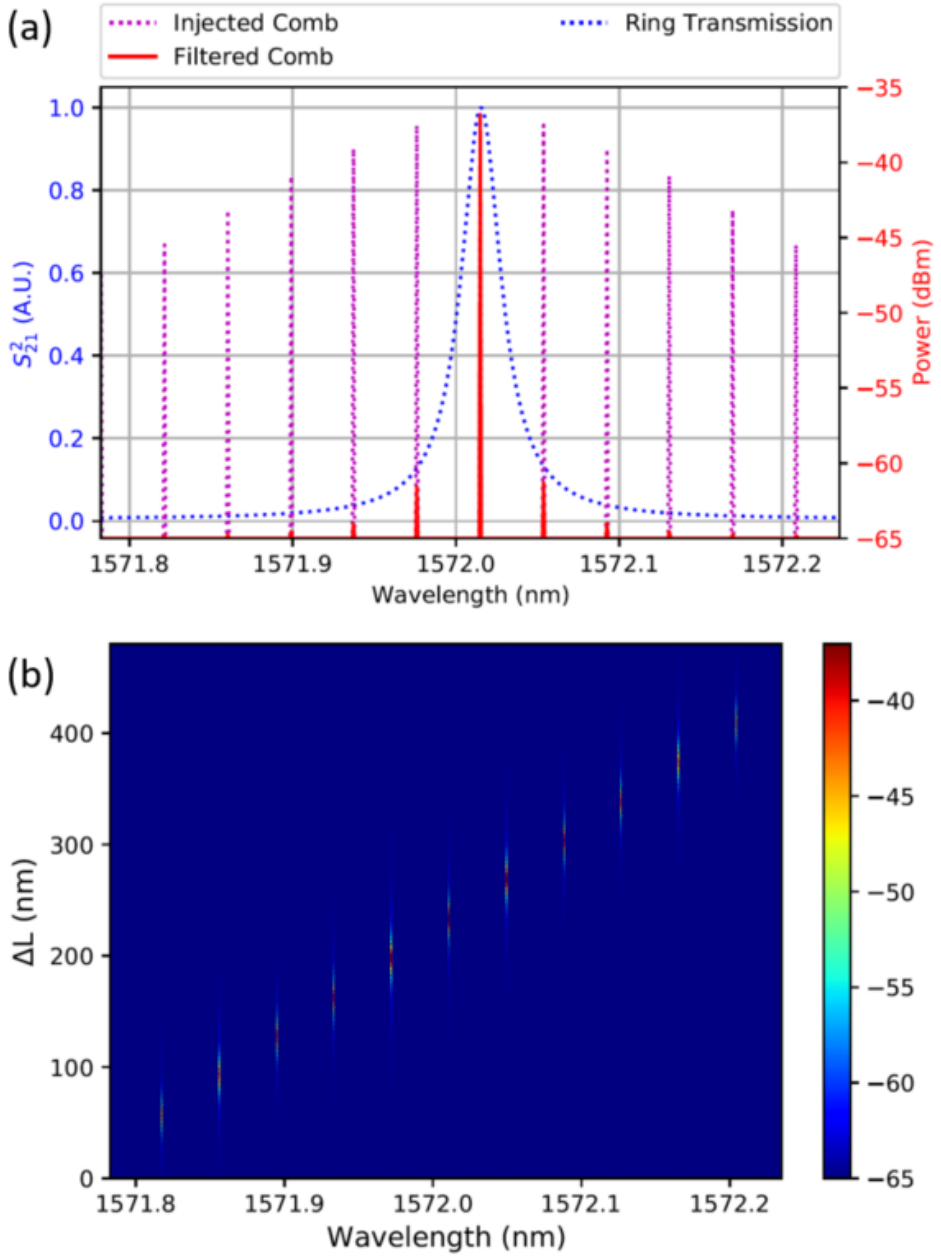


Figure 2.26: (a) Illustration of the generated comb, the ring transmission profile and the resulting filtered comb line. (b) Illustration of the different comb lines being filtered through changing the optical path length of the ring laser.

allowing for the selective or tunable filtering of a comb.

A full comb based optical network would include an array of ring lasers which would be used to fully de-multiplex the comb lines and separate them into different waveguides with separate modulators before being recombined and transmitted.

2.5 Chapter Conclusion

This chapter introduces the models and designs of the lasers that will be used in future chapters. Using the transmission matrix method, models of the emission spectra of a simple FP laser is demonstrated along with design features like slots and pits that can be used to warp this transmission spectrum into a single mode spectrum. That fabrication methods of achieving the etch depth for these features are described in more detail in *Chapter 3*.

Theoretical analysis behind the technique of gain switching is also carried out using the rate equations used to describe the carrier and photon densities of the laser. The effects of a gain switched sinusoidal current on these densities are analysed and the generation of a gain switched comb is demonstrated. The effects of current and frequency on the quality of a gain switched comb were investigated and optimum combs were achieved when the frequency of the gain switched current is equivalent to the ROF of the gain switched laser. This is analysed experimentally from *Chapter 5* on-wards.

Finally the concept of using a ring laser as an ILF to filter out individual comb lines is introduced. An illustration of the transmission profile of a ring laser is used to describe how an individual comb line can be filtered while the other comb lines are suppressed. An active ring laser would allow for the position of the rings transmission modes to be adjusted along the wavelength domain by adjusting current injection. And so, plots illustrating this ring transmission tuning and resulting comb filtering are given. This is demonstrated experimentally in *Chapter 7*.

Chapter 3

Device Fabrication Process

3.1 Chapter Overview

The previous chapter demonstrated theoretically that single mode spectra of a laser could be achieved by etching defects into a portion of the ridge of the laser. In this chapter, the fabrication process and techniques use to create these lasers and defects are described [36], [43], [44], [45].

In this chapter, the fabrication of a typical DC process will be presented. Starting with the epitaxyal structure of the lasers, the fabrication process will be presented referring to each layer of the structure.

3.2 Epitaxial Structure

The fabrication process is carried out using commercially available lasing material designed for the emission at 1550 nm, purchased from International Quantum Epitaxy (IQE). A table depicting the epitaxial structure is given below. This lasing material consists of 5 compressively strained 6 nm wide AlGaInAs quantum wells on an n-doped InP substrate. The upper p-doped cladding consists of a 0.2 μm of InGaAs cap layer, which is followed by 0.05 μm of InGaAsP, lattice matched to 1.62 μm of InP. The layers from top to bottom forms a PIN junction, with zinc and silicon used as P and N dopants.

Table 3.1: Layers of epitaxial structure

Layer No.	Material	Thickness (μm)	Dopant	C-V level (cm^{-3})
16	$GaIn_{(0.53)}As$	0.2	Zinc	$>$ 1.5e19
15	$GaIn_{(0.53)}As_{(0.62)}P$	0.05	Zinc	$>$ 3.00e18
14	InP	0.1	Zinc	$>$ 1.5e18
13	InP	1.5	Zinc	1.00e18
12	$GaIn_{(0.53)}As_{(0.33)}P$	0.02	Zinc	1.00e18
11	InP	0.05	Zinc	7.00e17
10	$(Al_{(0.9)}Ga)In_{(0.53)}As$	0.06	Zinc	4.00e17
9	$(Al_{(0.72to0.9)}Ga)In_{(0.53)}As$	0.06	Undoped	
8	$(Al_{(0.44)}Ga)In_{(0.49)}As$	0.01	Undoped	
7	$5 \times (Al_{(0.24)}Ga)In_{(0.71)}As$	0.006	Undoped	
6	$5 \times (Al_{(0.44)}Ga)In_{(0.49)}As$	0.01	Undoped	
5	$(Al_{(0.72to0.9)}Ga)In_{(0.53)}As$	0.06	Undoped	
4	$(Al_{(0.9)}Ga)In_{(0.53)}As$	0.06	Silicon	1.00e18
3	$(Al_{(0.86to0.9)}Ga)In_{(0.53)}As$	0.01	Silicon	1.00e18
2	InP		Silicon	1.00e18
1	InP		Silicon	3.00e18
Substrate				

3.3 Mask Design

A fabrication run is carried out on one quarter of a 2 inch wafer and consists of many devices separated into different bars which fill up the quarter wafer. The devices in this project are separated into different mask layers, one for each lithography step. The mask layers used account for the lithography for three different etch depts (shallow, deep and isolation), as well a layer to define the oxide opening along the ridge of a laser, and the metal lithography for the devices contact pads.

The mask layers are designed using an in-house software called PICDraw. The software allows the user to draw each layer of the PIC designs in separate bars and distribute these bars into a quarter of a 2 inch mask. *Figure* 3.1 gives the individual mask layers designed as well as all the layers overlapping.

This mask design is then sent to Compugraphics where the mask plate is manufactured.

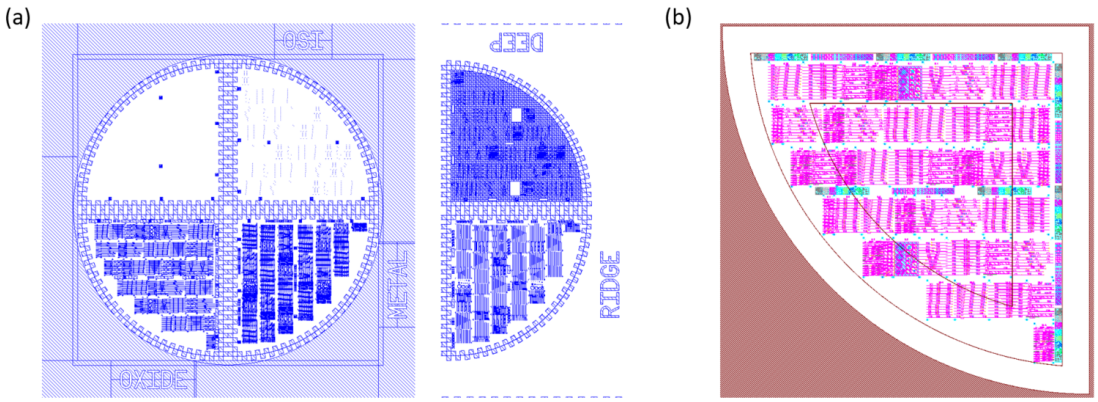


Figure 3.1: (a) Quad mask showing the layers used to fabricate PICs. (b) Quarter wafer design showing the overlapping layers.

3.4 DC Fabrication

This section will focus on the fabrication process for the devices used in this project. Illustrations will be used to describe each lithography step as well as the following etches required to shape the laser.

3.4.1 Ridge Lithography

The first step in fabrication is to deposit 600 - 700 nm of SiO_2 on an epitaxial (EPI) quarter wafer. This is deposited using plasma enhanced chemical vapor deposition (PECVD) at a deposition rate of 25 nm min^{-1}. The thickness of the SiO_2 is measured using a NanoSpec from Nanometrics. This measures the thickness of the SiO_2 film using reflectometry, which is a technique used to determine the thickness of a film by measuring the interference effects of the material.

After this, the sample is prepared for the ridge lithography by first depositing a layer of hexamethyldisilizane (HMDS) which is used as adhesion between the photoresist (PR) and EPI. The PR used is S1805 which is a positive PR and is spun on the sample at 4000 revolutions per minute (rpm) for 50 seconds. This ensures that the thickness of the PR is uniform. The sample is then baked at 115°C for 180 seconds.

Next the sample is placed into an MA6 Mask Aligner where it is exposed to UV light for 3 seconds at a vacuum contact. The sample is then developed in MF319 developer for approximately 45 seconds. This ensures an appropriate resolution for the ridges of the device. The resolution can be determined by

viewing the resolution marks under a microscope as shown in *Figure* 3.2. These resolution marks demonstrate the features achieved at that lithography step in microns. A good resolution is considered to be about 1 μm, which is achieved here.

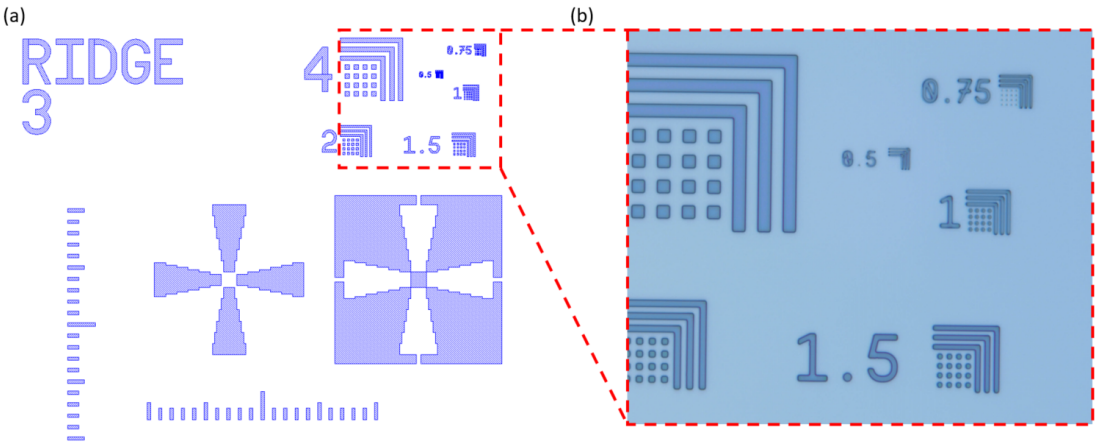


Figure 3.2: Resolution features in microns as seen on (a) the mask layer image and (b) microscope image after development of the ridge lithography.

The next step is to define the hard mask for the ridge by etching the exposed SiO_2. This is carried out using the SPTS Synapse Etcher and the available etch recipe for SiO_2. The final step in defining the ridges is by placing the sample in PR remover 1165 to remove the remaining PR. The ridge hard mask is now defined as shown in *Figure* 3.3.

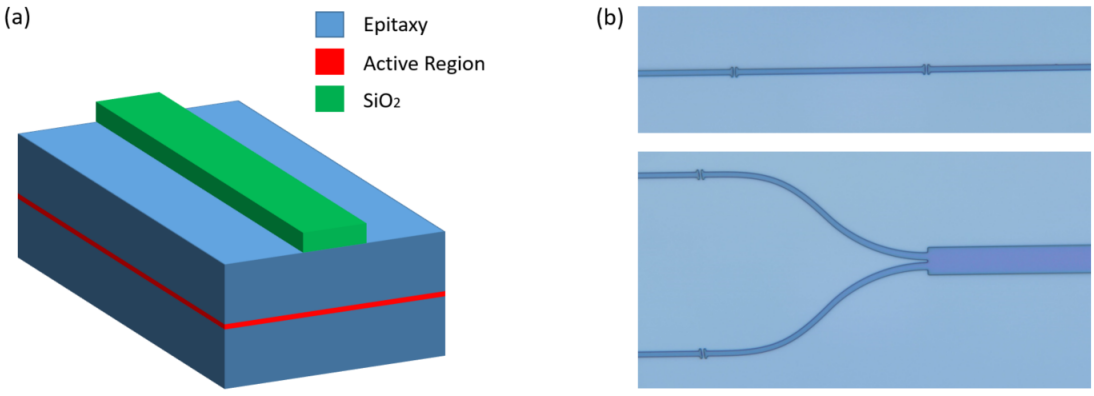


Figure 3.3: (a) Schematic showing the EPI wafer with the defined SiO_2 ridge hard mask. (b) The SiO_2 ridge hard mask as viewed under a microscope.

3.4.2 Deep Lithography

The primary shape of the device ridges are shallow etched, however for regions with sharp bends, deep etched slots and other reflective structures

where optical confinement is required, deep etched regions are created. Therefore, the second lithography step is used to define the hard mask for the deep etched regions. Using the PECVD, 350 - 400 nm of Si_3N_4 is deposited onto the wafer. Again the sample is prepared for lithography by first depositing a layer of HMDS on the sample. The etch rate of Si_3N_4 is slower and can etch the PR, so this time a thicker PR is used, S1828, and is spun on the sample at 4000 rpm for 50 seconds. Again the sample is baked at 115 °C for 180 seconds before the UV exposure. The MA6 mask aligner is set to a hard contact because strong resolution is not required for the deep etched regions and the exposure time is set to 21 seconds to account for the thicker PR. After UV exposure the sample is developed using MF319, exposing the deep etched regions.

The exposed Si_3N_4 is etched using the SPTS Synapse Etcher creating the hard mask for the deep etched regions on top of the hard mask defining the laser ridges. The PR is removed using 1165 and an illustration of the wafer at this fabrication stage is illustrated in *Figure* 3.4.

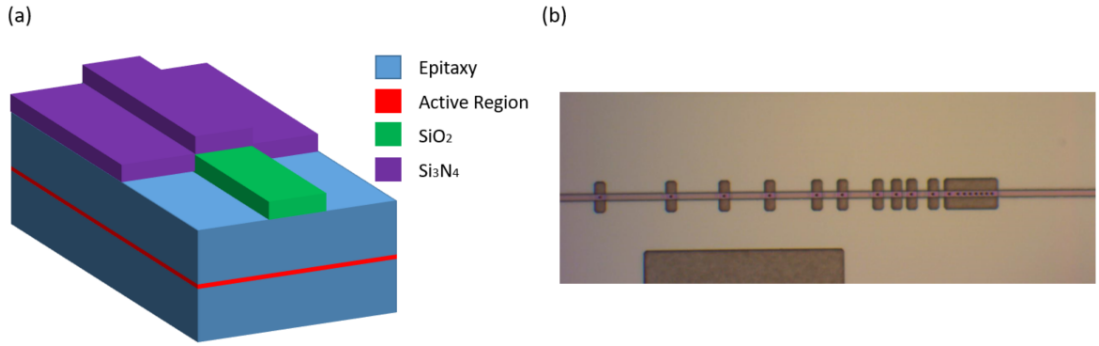


Figure 3.4: (a) Schematic showing the EPI wafer with the defined SiO_2 ridge hard mask and Si_3N_4 deep hard mask. (b) The SiO_2 ridge hard mask and etched Si_3N_4 hard mask as viewed under a microscope.

3.4.3 Deep and Shallow Etches

At this stage of the fabrication process the hard masks for the deep and shallow regions have been defined. The deep and shallow etches are used to shape the ridges of the laser where the shallow etched ridges are etched to a layer in the EPI above the quantum wells, and the deep etched regions are etched to a layer of the EPI below the quantum wells. These etches of the EPI are carried out using an Oxford Cobra ICP Etcher. The Oxford Cobra ICP Etcher is capable of measuring the reflectance of the exposed EPI layers as it etches through them and this measured reflectance is comparable to the

changing refractive index of the EPI layers. The Reflectance profile of the full EPI layers can be determined before etching the fabrication wafer by etching a small sample of the EPI wafer, and thus it is possible to accurately control the etch depths of the fabrication EPI wafer.

Cleaving off a piece of the leftover EPI wafer and etching it with the Oxford Cobra ICP Etcher, resulted in the reflectance profile depicted in *Figure* 3.5 as each layer was etched away. The layers refer to those mentioned in *Table* 3.1.

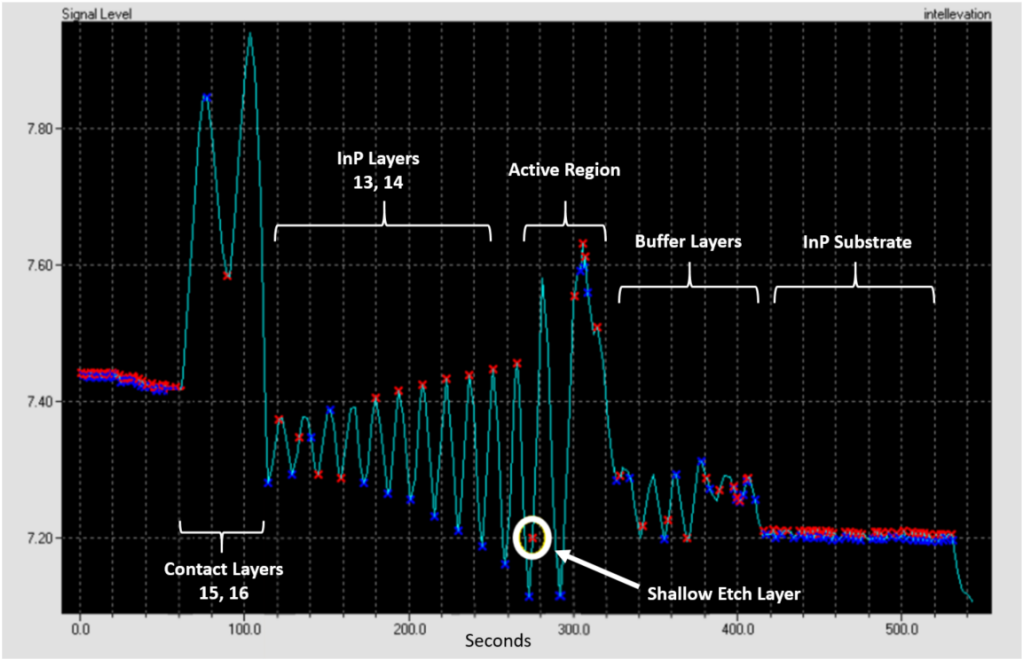


Figure 3.5: Reflectance fringes measure as the Oxford Cobra ICP Etcher etches the EPI layers.

The changing reflectance fringes occur due to the changing refractive index of the EPI layers, and so an etch rate of each layer of the material can be determined. The first two peaks in *Figure* 3.5, represents the two top contact layers (15 and 16) being etched away. The following ten peaks represents the reflectance caused by the Oxford etcher etching through the InP layers (12 and 13). The next peak is the reflectance caused by layer 12, which is the etch stop layer for a shallow etched ridge. The peaks following this represent the active region and buffer layers respectively.

The first etch step is to etch the deep regions at a depth that is the difference between the shallow and deep etch depths. This parameter is approximately 1 μm, which is deep enough to ensure the deep etch depth falls below the active region after the later shallow etch is carried out. The wafer is placed into the Oxford Cobra ICP Etcher and the target laser is fixed on the exposed deep etch

region. The wafer is etched until approximately peak 9-10 which is 1 μm into the EPI layers. This is illustrated in *Figure* 3.6.

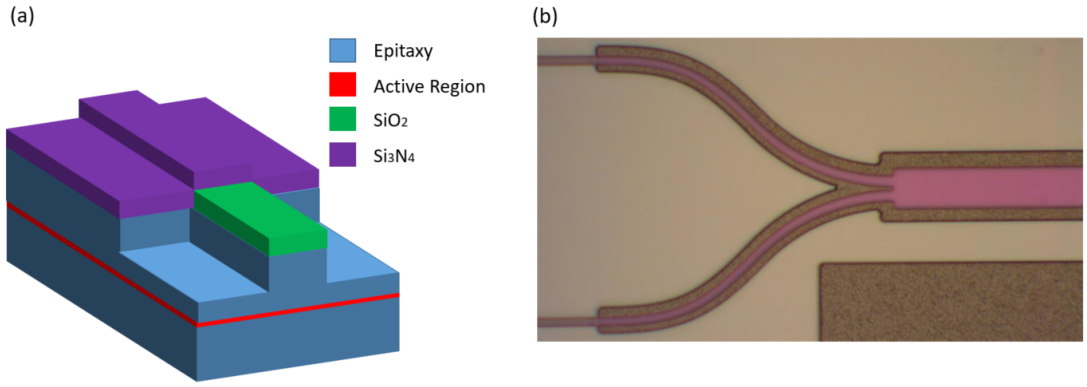


Figure 3.6: (a) Schematic showing the EPI wafer after the deep regions are etched. (b) Microscope View.

After this the Si_3N_4 hard mask is removed using the SPTS Synapse Etcher, exposing the SiO_2 hard mask defining the ridges of the device. Again the EPI wafer is placed into the Oxford Cobra ICP Etcher but his time the target laser is focused on the regions that will be shallow etched. The EPI layers are etched until peak 13 in *Figure* 3.5 which represents the etch stop layer just above the active region for the shallow regions. Because the deep etch regions are also exposed, these regions are also etched by an additional 1.8 μm to a layer below the active region.

After this etch step the remaining SiO_2 hard mask defining the ridges of the device are etched away using a wet chemical etch called buffering oxide etch (BOE). This is illustrated in *Figure* 3.7

3.4.4 Isolation Lithography

Between different sections of devices, electrical isolation is desired when biasing the laser sections. Therefore an isolation etch is required and is achieved by removing the top two contact layers of the EPI (layers 12, 13) between different sections of the ridge laser.

Using the PECVD, 250 nm of SiO_2 are deposited on the EPI wafer. As usual HMDS is deposited on the surface before S1828 PR is spun on at 4000 rpm for 50 seconds and the sample is baked at 115 $^\circ$ for 180 seconds. The sample is aligned to the isolation mask layer using the MA6 mask aligner and, using a hard contact, the sample is exposed to UV light for 21 seconds. Again the

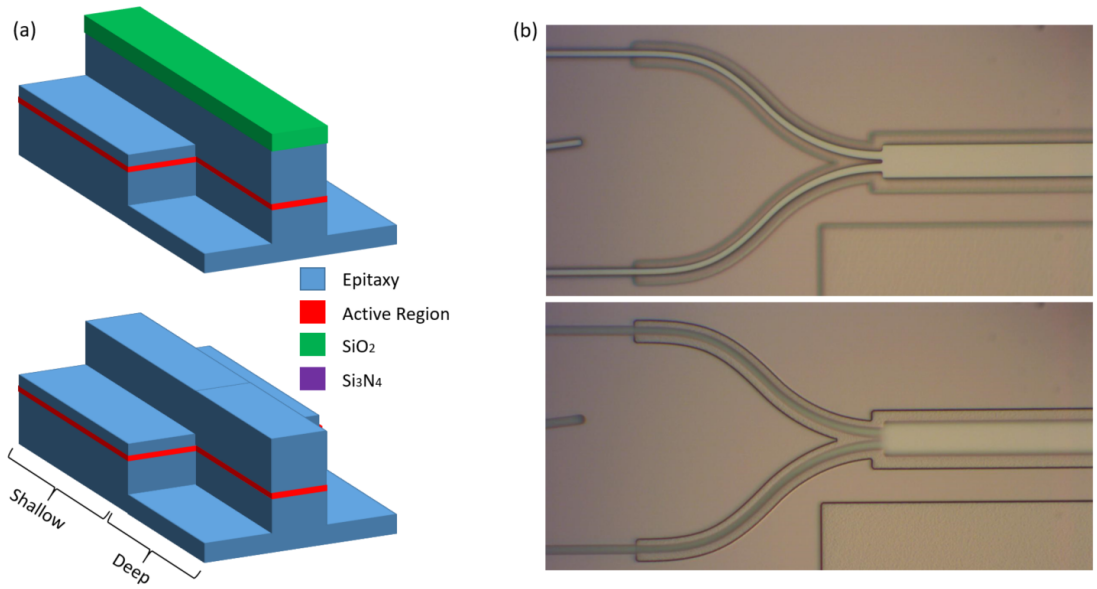


Figure 3.7: (a) Schematic showing the EPI wafer after the deep and shallow regions are defined and etched. (b) Microscope View of (top) top of ridge and (bottom) bottom of the deep etched region.

sample is developed using MF319 for approximately 50 seconds. Like before, the exposed SiO_2 is etched using the SPTS Synapse Etcher creating the hard mask for the isolation etch. The remaining PR is removed using 1165.

The EPI wafer is placed in the Oxford Cobra ICP Etcher, however the exposed regions of the hard mask may be too small for the laser target to detect. It is important at this point to refer back to *Figure* 3.5 and take note that the time to etch through the first two layers took 55 seconds. Therefore, if the laser target can't detect the exposed EPI, then the etch process is turned on for 55 seconds. After the etch is complete, the SiO_2 hard mask is removed using BOE. This is illustrated in *Figure* 3.8

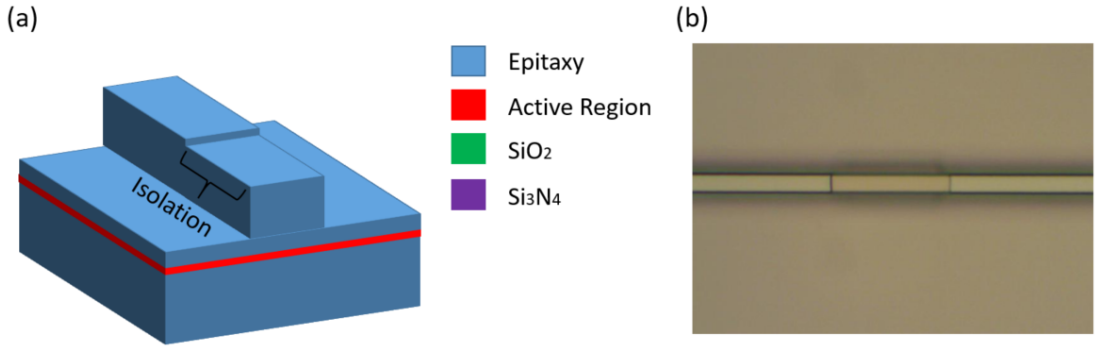


Figure 3.8: (a) Schematic showing the EPI wafer after the isolation etch. (b) Microscope View of isolation etch.

At this stage of the fabrication process, all the EPI etches are complete and the waveguides and features are exposed. HCl:H_3P_4 can be used to to ensure the sidewalls of the ridges and the surface are smooth. The sample is placed into this solution for 10 seconds. This short wet etch is sufficient to remove any of the rough or grassy regions that may have formed during the previous etches.

3.4.5 Oxide Open Lithography

The fourth lithography step is to define the oxide openings of the laser ridges. Using the PECVD 50 nm of SiO_2 is first deposited on the EPI wafer followed by 350 nm of Si_3N_4. As before, HMDS is deposited on the wafer, followed by S1828 at 4000 rpm for 50 seconds, and the wafer is baked at 115° for 180 seconds. The sample is aligned to the Oxide layer of the mask using the mask aligner and is exposed for 21 seconds using a vacuum contact. The EPI is then developed using MF319 for 50 seconds. The first exposed layer Si_3N_4 is removed using the SPTS Synapse Etcher exposing the 50 nm layer of SiO_2.

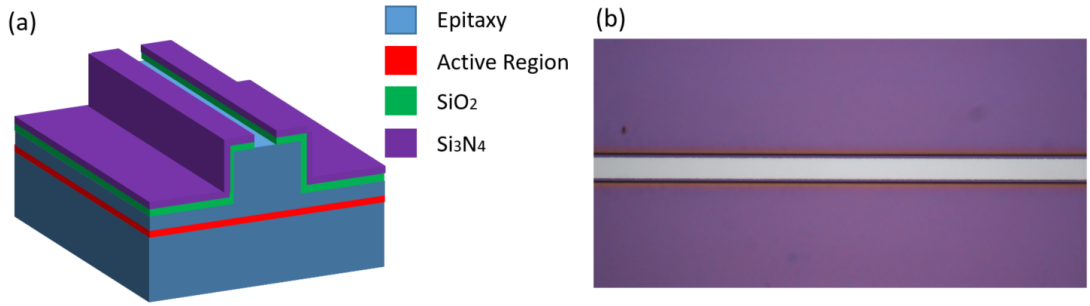


Figure 3.9: (a) Schematic showing the EPI wafer after the Oxide etch. (b) Microscope View of Oxide etch.

The purpose of these two layers is to passivate the side walls of the ridge to reduce current leakage and optical loss. The remaining SiO_2 needs to be etched away from the top of the ridge to allow metal contact pads to be added. A clean etch of the SiO_2 layer can be achieved by using BOE as it does not effect the EPI layers, however this carries a risk of under etching and could result in the BOE removing the SiO_2 from the side walls. The two layer approach of having 350 nm of Si_3N_4 on 50 nm of SiO_2 is used to reduce the rate of this under etch due to the viscosity of BOE and the thin layer of SiO_2. Therefore the EPI wafer can be held under BOE for long enough to ensure the exposed SiO_2 on the ridge is etched away while reducing the under etch of the SiO_2 and the etch of the SiO_2 on the sidewalls.

The EPI wafer is submerged in BOE for 10 seconds, which is sufficient to etch away the SiO_2 from the top of the ridges. This is illustrated in *Figure* 3.9.

3.4.6 Metal Lithography

The final lithography step is used to carry out the metal lift off to create the contact pads of the laser. HMDS is deposited onto the sample, however this time, two PRs are used. The first PR LOR10A is spun on the sample at 4000 rpm for 50 seconds and is baked at 160°C fro 180 seconds. This PR is is used as an undercut layer to assist with the liftoff. The second PR is S1828 which is spun on at 4000 rpm for 50 seconds and baked at 120°C fro 180 seconds. The sample is then aligned to the metal layer of the mask using the MA6 mask aligner and the sample was exposed at a hard contact for 21 seconds. The EPI wafer was then developed for 125 seconds exposing the regions where metal is desired. Depending on the length of time between this step and the deposition of the p-metal, it may be necessary to carry out a small BOE etch again, as the oxide layer could grow when exposed to oxygen.

Following this, p-metal consisting of 25 nm of titanium and 600 nm of gold are deposited on the surface. The EPI wafer is placed into a container of 1165 PR remover for approximately three hours which is sufficient for the LOR10A to be undercut. The metal is pealed off leaving the metal of the contact pads behind. This is illustrated in *Figure* 3.10.

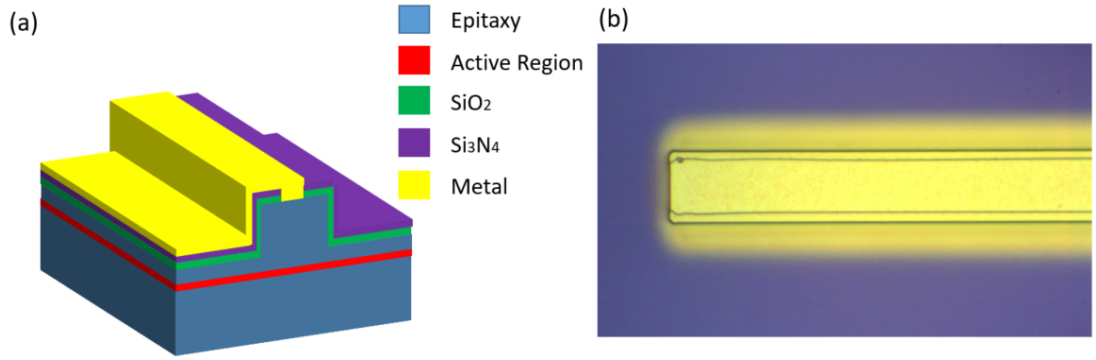


Figure 3.10: (a) Schematic showing the EPI wafer after the metal liftoff. (b) Microscope View of metal liftoff.

3.4.7 Final Steps

After the metal liftoff, a few final steps remain. First the InP substrate is thinned from 350 μm to 100 μm using a reacting bromine solution . The

thinning of the substrate allows for the EPI wafer to be cleaved with higher accuracy. Black wax is first melted on a glass plate and the surface of the EPI wafer is placed face down on this wax. This ensures the ridges are protected during the substrate etch. The substrate thinning is done by exposing the back of the sample to a reacting Bromine solution where the N_2 bubbles etch away the excess substrate.

After this process the n-metal is evaporated on the back side of the sample consisting of 20 nm of titanium and 250 nm of gold. The Wax is removed from the surface of the EPI wafer using Toluene as a solvent. To improve the contact resistivity of the device, the EPI wafer is annealed at 420°C for 10 minutes. Finally the EPI is cleaved into bars.

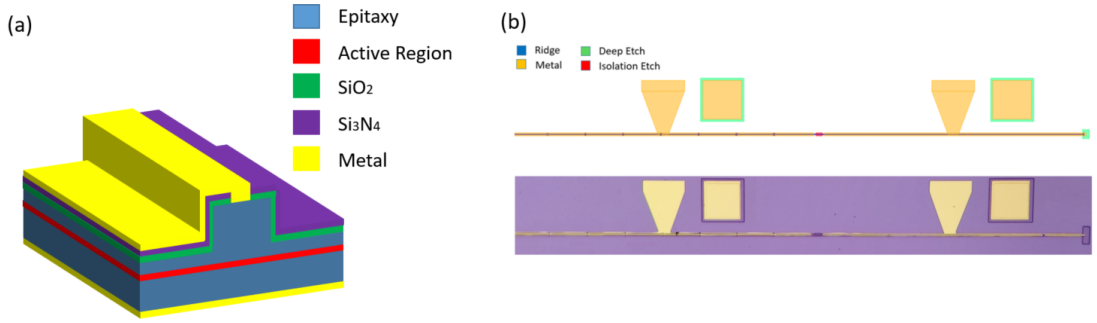


Figure 3.11: (a) Schematic showing finalised laser structure. (b) Microscope View of a laser.

3.5 Chapter Conclusion

This chapter describes the fabrication process used to create the lasers and PICs used in the following experimental chapters. The process uses different layers of a mask to develop each etch step and define each device feature. Starting with defining the ridges of the different devices, the lasers are shaped using three etch steps. A shallow etch which is an etch into the EPI that stops above the active region, a deep etch wich stops below the active region and an isolation etch that removes the top dopped layers of the EPI.

In Chapter 4, the experimental characterisation of these ridge lasers will be introduced, as well as the experimental effects of the different etches described in this chapter.

Chapter 4

Introduction to Device Characterisation and Features

4.1 Chapter Overview

This chapter is an introduction to device characterisation and different device features. The setup used for this project is described in detail along with the characterisation results for different devices. Starting with a Fabry–Pérot (FP) diode laser, this chapter demonstrated how shallow and deep etched FP lasers compare to each other. It is the goal for photonic integration to limit or eliminate the use of cleaved facets, and thus features like etched facets and metal etched facets are also introduced and characterised as an alternative to cleaved facets. The concept of curved lasers are also demonstrated and the lowest optimum radius of curvature is determined. Finally methods of generating single mode spectra are shown with reference to the simulations carried out in *Chapter 2*.

4.2 Characterisation

Devices are characterised on a setup that is custom built for the characterisation of PICs. Chips are placed on a thermally controlled brass chuck, multiple probe needles are used to bias the contact pads of the devices and optical fibers are used to collect the lasing light. A power meter is automated and is used to measure the power-curret (LI) curves of lasers and an ANDO AQ6317B optical spectrum analyser (OSA) is used to measure the

spectrum of the laser. A digital camera microscope is installed above the brass chuck to view the device while probing and fiber coupling. An image of this setup is shown below.

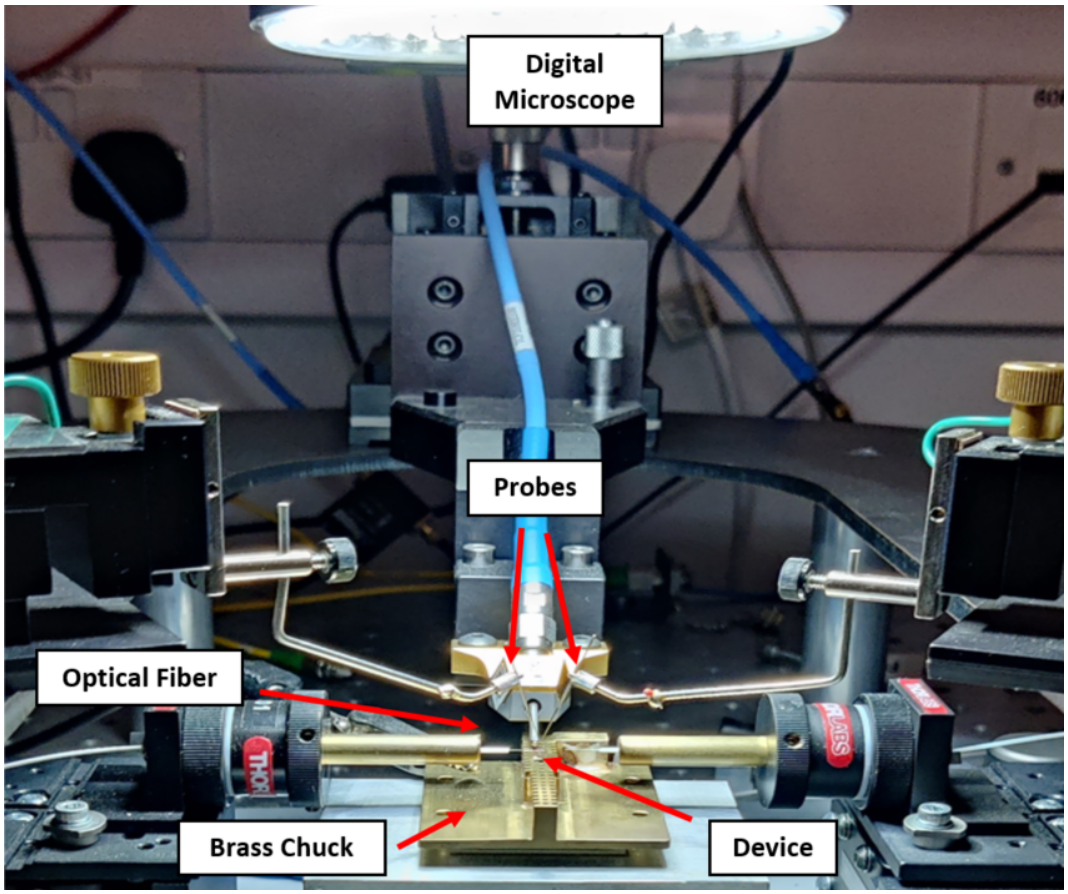


Figure 4.1: Image of characterisation setup.

4.3 Fabry Pérot Laser Diodes

Chapter 3 describes the fabrication process of the laser devices in this project and discusses ridge lasers with two different etch depths. These are a deep etch, where the EPI is etched to a layer below the active region and a shallow etch where the EPI is etched to a layer above the active region. This is illustrated in *Figure* 4.2.

A deep and shallow etched FP laser were fabricated using the fabrication process described in *Chapter 3*. Both of these devices were fabricated 750 μm in length and the cavity is confined by two cleaved facets. The mask image showing the different features of these devices is shown in *Figure* 4.3.

The contact pad of the laser is biased using a bias probe connected to a

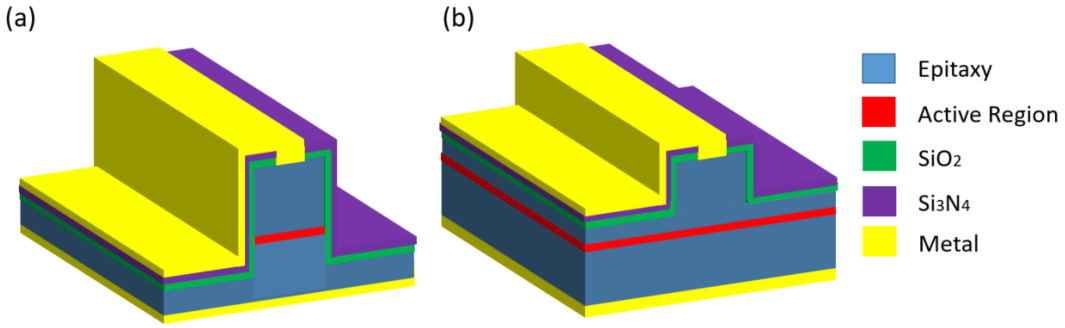


Figure 4.2: Illustration of deep and shallow etched waveguides.

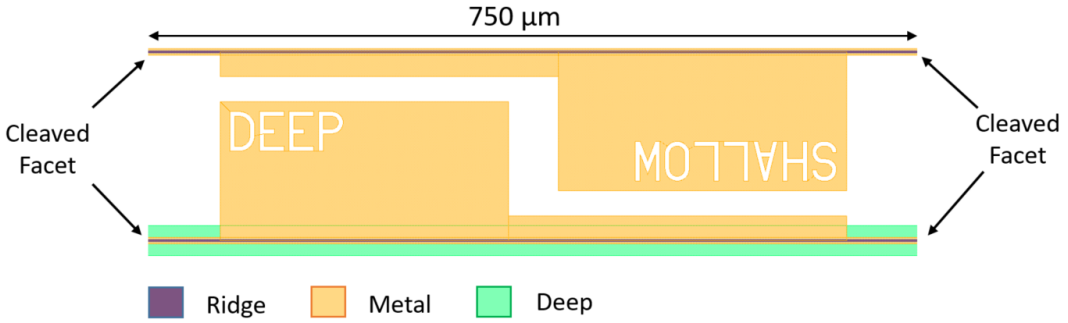


Figure 4.3: Illustration of the mask layout of a deep and shallow etched FP laser.

Keithley power source and current (I) was swept from 0 - 120 mA. The corresponding light power (L) and voltage (V) were measured and an LIV curve was attained via fiber coupling from both devices using the power meter (*Figure 4.4*(a)). The spectra of the device was measured using the OSA (*Figure 4.4* (b)).

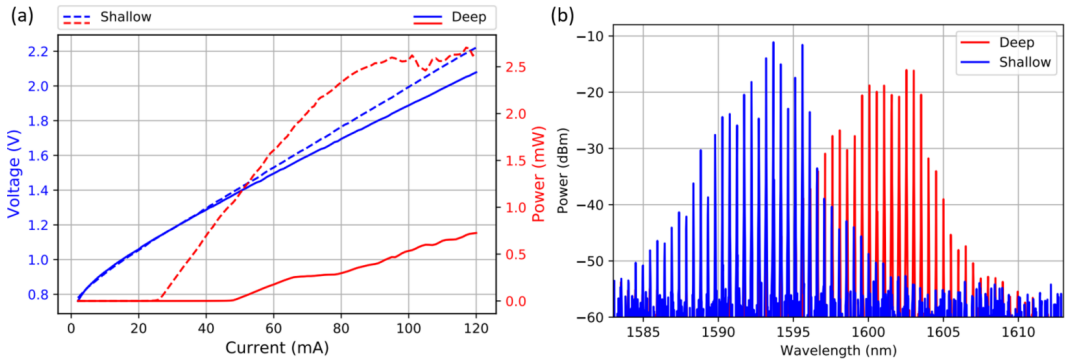


Figure 4.4: (a) Measured LIV curves and (b) measured spectra of a shallow and deep etched FP.

In terms of the measured LIV curve, the shallow etched FP performs better by achieving a threshold current of 26 mA and a lasing power of 2.5 mW at a bias current of 100 mA. In comparison, the deep etched FP achieves a threshold

current of 48 mA and a lasing power of 0.5 mW at a bias current of 100 mA. This result isn't unexpected, as lasers fabricated with deeper etched waveguides have been know to result in a reduced internal quantum efficiency and higher optical loss [46].

The spectra of both these FP lasers are also plotted in *Figure 4.4*. As there is no change in length of the device structure between the deep and shallow etched FP, the distance between lasing modes remains the same in both cases. This is consistent with the transmission matrix profiles for a FP demonstrated in *Chapter 2.2.1*. However, the position and power of the spectra is a result of the bias current through both the shallow and deep FP lasers which are 120 mA and 140 mA respectively. More current is required through the deep etch FP to give an almost equivalent power between the shallow and deep etch FPs which results in the deep etch spectra being measured at longer wavelengths in comparison to the shallow etch FP.

4.4 Etched Facets

As mentioned before, it is the goal for integrated photonics to reduce the use of cleaved facets. Etched facets and metal etched facets are typically used in place of a cleaved facet. Both of these consists of a deep etch through the quantum wells (QW), the purpose of this is to replicate a cleaved facet by creating this deep reflective defect, or in other words, an etched facet. A metal etched facet consists of the same deep etched facet but it is also subject to the following dielectric and metal depositions described in *Chapter 3* [47].

The top view of the mask layers and illustrations of the side view of these structures are shown in *Figure* 4.5.

Again, the contact pad of these lasers was biased and current was swept from 0 - 120 mA. The LIV from both devices was measured via fiber coupling using the power meter and the spectra of both lasers was measured using the OSA while both sections are biased at 80 mA. These plots are shown in *Figure* 4.6.

The LI measurements reveal a lower threshold current and higher power achieved from the metal etched facet compared to both the FP with an etched facet, and the FP laser with a cleaved facet in *Section* 4.3. Furthermore, the etched facet LI curve reveals that a lot of the light passes through the etched section compared to a cleave. The Spectra of both lasers are also shown in

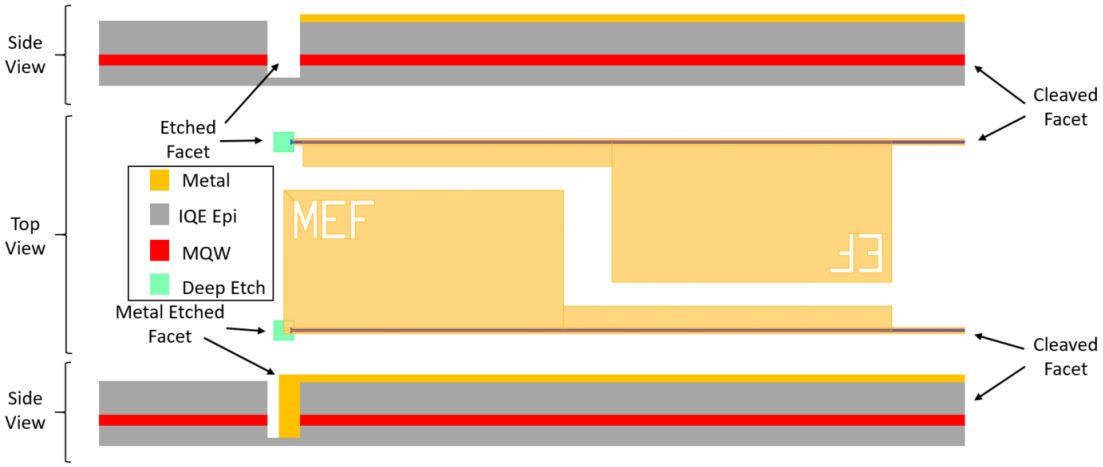


Figure 4.5: Top and side view schematics of a FP laser with an etched facet and a metal etched facet.

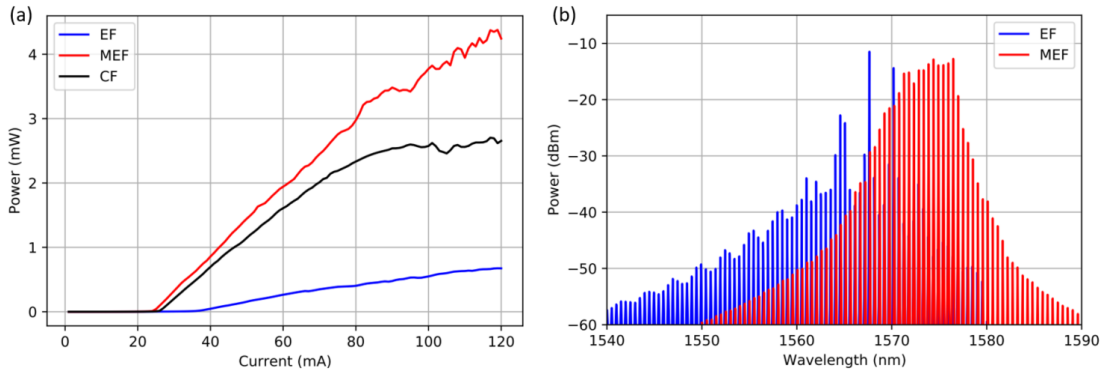


Figure 4.6: (a) LI curves of a FP laser with a cleaved facet, etched facet and metal etched facet. (b) Spectra of FP with etched facet and metal etched facet biased at 80 mA.

Figure 4.6 with comparable separation between lasing modes for both devices. The spectrum of the FP with the metal etched facet is visibly smoother with a higher power in comparison to the spectrum of the FP with the etched facet, which has a lower power and is more jagged in shape.

4.5 A FP laser with an added defect

In *Chapter 2.2.2* it simulated how adding reflective defects along the ridge of a laser effects the output spectra of the laser. Here, two examples are demonstrated, a single shallow slot etched into the ridge of the FP, and a single deep slot etched into the ridge of the FP. This slot is etched 1/3 of the distance along the ridge of both lasers and is illustrated in *Figure* 4.7.

The spectra of both of these lasers was measured using the OSA and plotted in

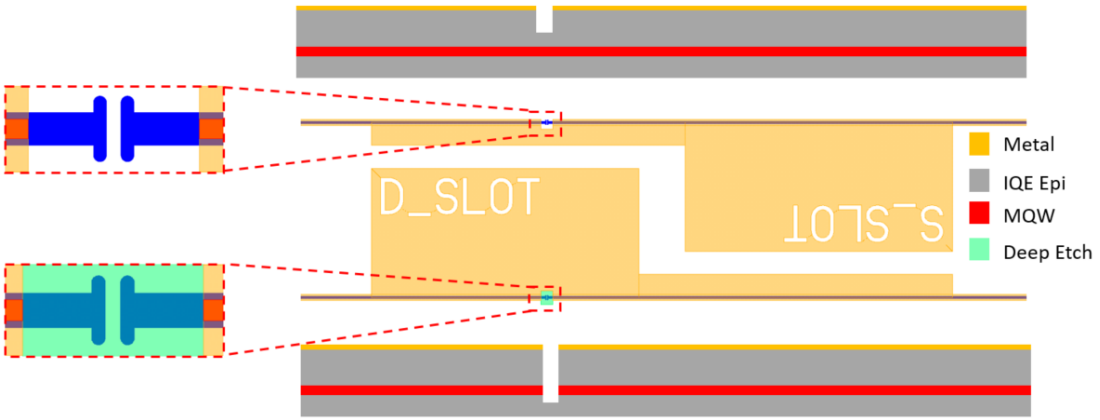


Figure 4.7: Top and side view schematics of a FP laser with a shallow and a deep slot etched into the ridge.

Figure 4.8. These spectra were achieved by biasing the deep and shallow slot FP lasers by 100 mA and 120 mA respectively.

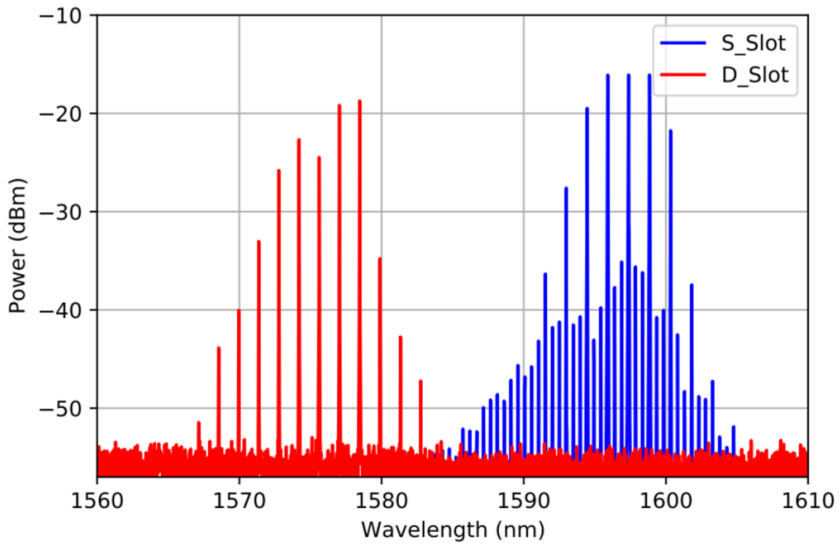


Figure 4.8: Lasing spectra of a FP with a single deep and shallow slot etched into the ridge.

The spectra of the FP with a single shallow slot shows the periodic suppression of of the FP lasing modes, specifically every second and third mode.

In comparison to this, the lasing spectra of the FP with a single deep slot etched into the ridge demonstrates the full suppression of these modes. This is because in the deep etch case, this is no longer a single cavity device, but instead is a lasing 250 μm FP being injected into a 500 μm FP and vice versa. Using the transmission matrix method described in *Chapter 2.2.1*, the transmission profile for a laser cavity of 250 μm, 500 μm and 750 μm can be simulated and is plotted in *Figure* 4.9.

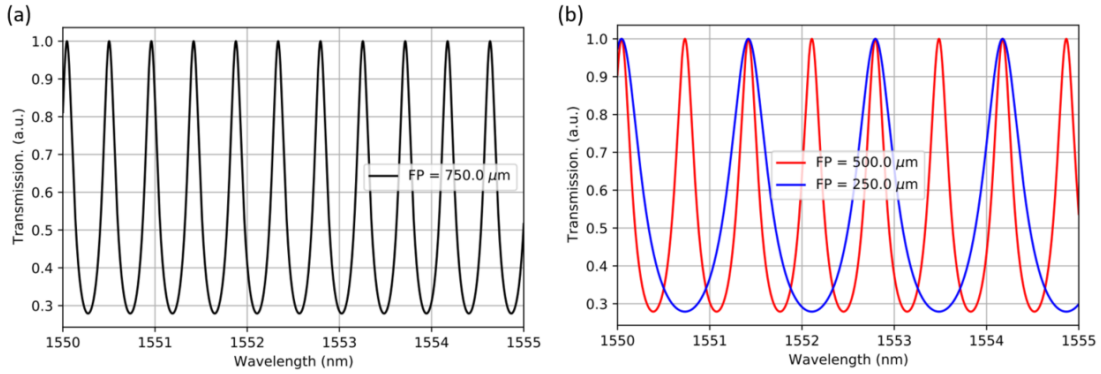


Figure 4.9: Transmission profile for a FP laser with a cavity length of (a) 750 μm and (b) 250 and 500 μm .

Because each cavity is an integer multiple of the other, the separation between lasing modes is also an integer multiple, with the 500 μm cavity producing two modes for very one of the 250 μm cavity, and the 750 μm micron cavity producing three modes for every one of the 250 μm cavity. *Figure* 4.9 demonstrates the case for a single cavity 750 μm in length as well as the case for the 250 μm and 500 μm cavity overlapping each other. It is clear from the overlap that every second mode of the 500 μm cavity laser matches every mode of the 250 μm cavity. Because this is the case for the deep slot device, where we have a 250 μm laser and a 500 μm laser injecting into each other, these overlapping modes result in a spectra with a mode spacing three times that of the 750 μm laser. However in the case of the shallow slot, because this slot is less reflective, the extra modes caused by the full cavity are still present, just partially suppressed.

The effects of these reflections can also be analysed by measuring the fast fourier transform (FFT) of the generated spectra [48]. The FFT of both lasing spectra was measured and plotted in *Figure* 4.10.

The FFT of the spectrum of the FP with a single shallow slot demonstrates a sharp peak at a cavity length of $L_3 = 750\ \mu m$ which is the overall cavity length of the FP. Additional smaller peaks were detected at $L_1 = 250\ \mu m$ and $L_2 = 500\ \mu m$ which is a reflection consistent with the shallow etched slot.

The FFT of the spectrum of the FP with a deep etched slot demonstrates sharp peaks at a cavity length of $L_1 = 250\ \mu m$ and $L_2 = 500\ \mu m$, which represent the two laser cavities confined by the etched facets and the deep etched slot. A sharp peak was measured at every distance of $L_3 = 250\ \mu m$ suggesting that the spectra is from a device that is effectively a FP with a cavity length of 250

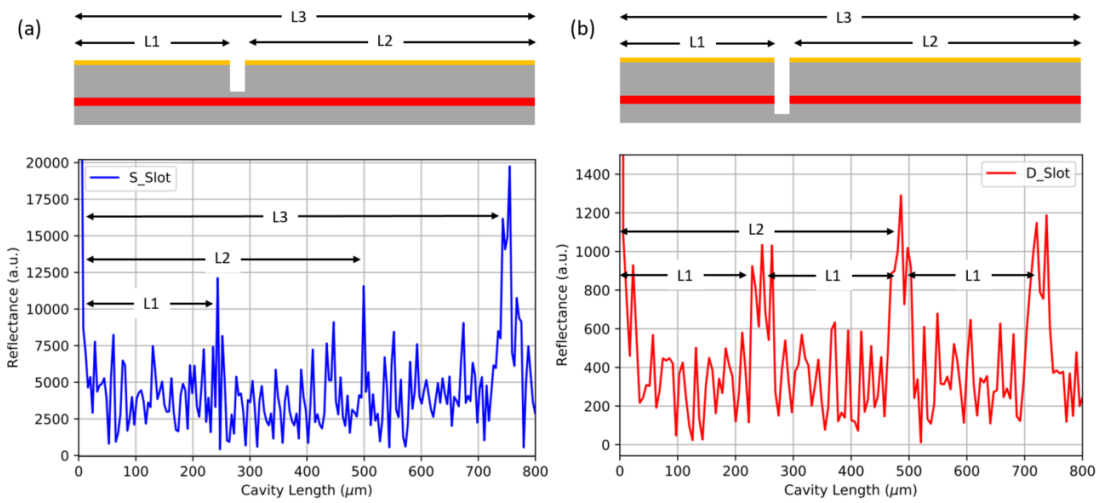


Figure 4.10: FFT of spectra attained for a FP laser with (a) a shallow slot etched into the ridge and (b) a deep slot etched into the ridge.

μm, which is consistent with the spectra in *Figure* 4.8 and the simulation in *Figure* 4.9.

4.6 U-bend Lasers

Curved waveguides on monolothically integrated circuits are notoriously lossy structures particularly with sharp bends. As the straight waveguide joins the curved waveguide the optical mode experiences a mode mismatch that results in radiation loss. Continuous curvature designs has been demonstrated as an effective method to allow the optical mode to evolve smoothly and continuously as it propagates through the bend [49].

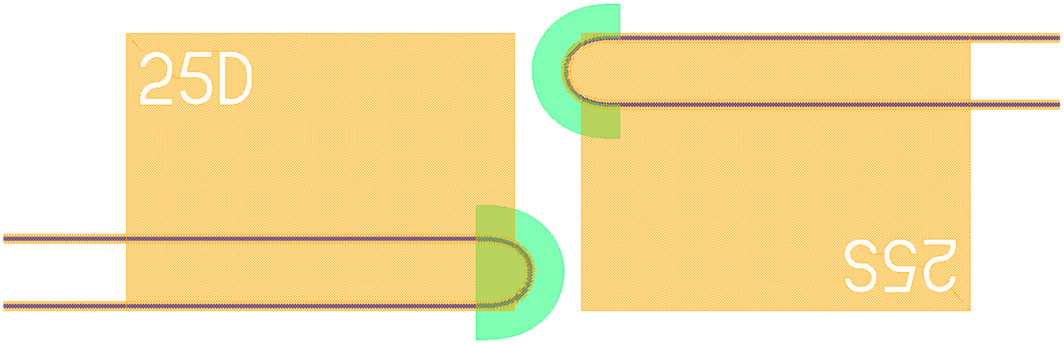


Figure 4.11: Single and double deep etched ubend lasers.

Figure 4.11 illustrates a mask image of two u-bend structures where both follows such a continuous curvature design. It is known that for curved structures with sharp bends a deep etch is required at the site of the bend to

support optical confinement. However in the examples shown, one could test whether a deep etch at both sides of the bending ridge or a deep etch on the outside curve of the bending ridge helps support the mode more effectively.

The effective radius of curvature of the ubend structures in *Figure* 4.11 is 25 μm. To test both structures, the contact pad was biased and LI curves and spectra were attained by fiber coupling through one of the two outputs. This is shown in *Figure* 4.12 where the spectra is attained at 100 mA.

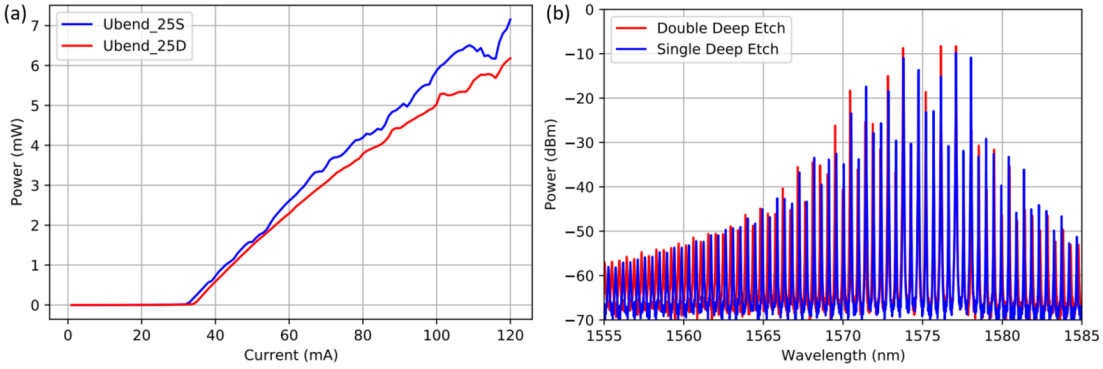


Figure 4.12: (a) LIV and (b) spectra of two Ubend lasers, one wih a deep etch at both sides of the bend and the other with a deep etch at one side of the bend.

While the LI curves of both structures are similar, the ubend with a single deep etch at the outside curve of the bend seems to generate a LI curve with a lower threshold current of 32.5 mA and a higher power of 5.95 mW at 100 mA, compared to a threshold current of 34 mA and a power of 5 mW at 100 mA attained from the other structure.

The spectra of both devices resembles that mostly of a FP which is expected as the cavity is confined by two cleaved facets. However, the slight suppression of FP modes suggests that there are partial reflections in the cavity. The FFT of both spectra is illustrated in *Figure* 4.13.

While the sharp peak attained at 700 μm demonstrates that the structure has a well defined cavity like that of a FP, the small additional peaks at 300 and 400 μm determines that there are still additional reflections. This is caused by the sudden change in effective refractive index as the modes transition from a shallow etched waveguide to a deep etched waveguide.

In integrated devices, reducing ones footprint is a desirable goal, and so multiple of these ubend structures were designed and fabricated at different radius of curvature to determine the smallest optimum radius that could be fabricated without sacrificing threshold current and lasing power. The results

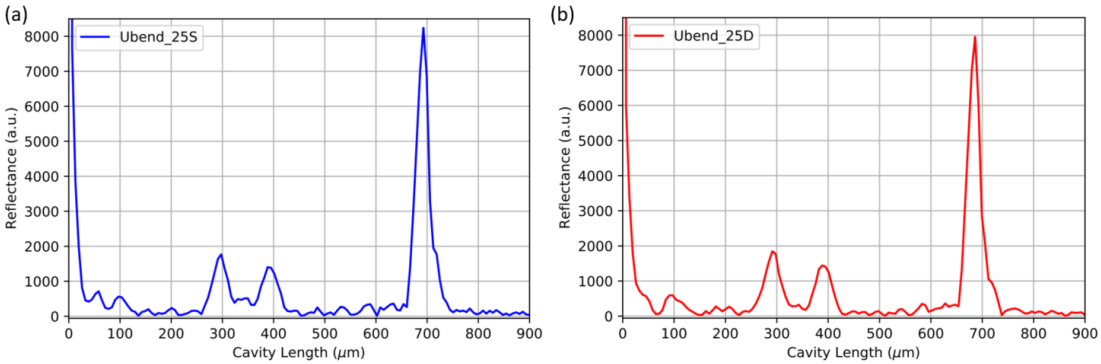


Figure 4.13: FFT of the spectra attained from a Ubend laser with a deep etch on (a) the outside of the bend and (b) both sides of the bend.

are as follows.

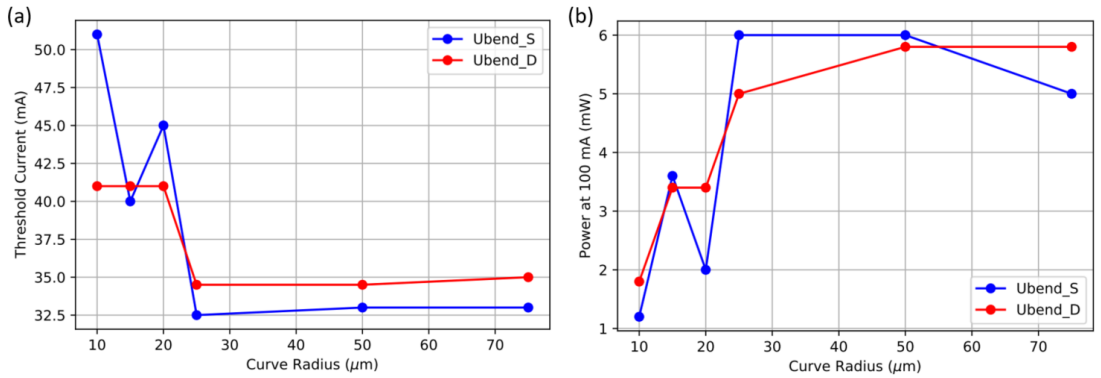


Figure 4.14: (a) Measured threshold current for both Ubend structures for different curvature of radius. (b) Measured power at 100 mA for both Ubend structures for different curvature of radius.

In terms of the devices with a single deep etch, the measured threshold current ranges from 32.5 - 51 mA with an apparent correlation between the threshold current and the radius of curvature, whereby the threshold current decreases as the radius increases. A similar correlation is evident on the double deep etched devices. In both cases the devices achieves optimum threshold current at a radius of 25 μm. There is also a correlation between the radius of curvature and the power measured. In both cases the power increases as the radius of curvature increases but doesn't improve much further after a radius of 25 μm.

4.7 Slotted Fabry Pérot Lasers

Section 5 of this chapter demonstrates how a single shallow slot can effect the lasing spectra of a FP laser, now we will look at how a series of such slots can

effect the lasing wavelengths. *Chapter 2.2.2* introduces the concept of etching reflective defects along the ridge of a laser as a method of creating a single mode spectrum. The example in *Chapter 2* refers to a FP laser cavity 1300 μm in length with a mirror section etched into a portion of the ridge. This mirror is made up of 7 slots with an interslot separation of 87 μm.

A mask schematic of such a device is illustrated in *Figure* 4.15. This schematic illustrates a two sectioned laser made up of a mirror section and gain section. The entire cavity of the structure is 1300 μm in length and is confined by a cleaved facet on the left and a metal etched facet on the right. The mirror section is made up of 7 shallow slots etched into the ridge of the laser and is electrically isolated from the gain section of the device via an isolation etch.

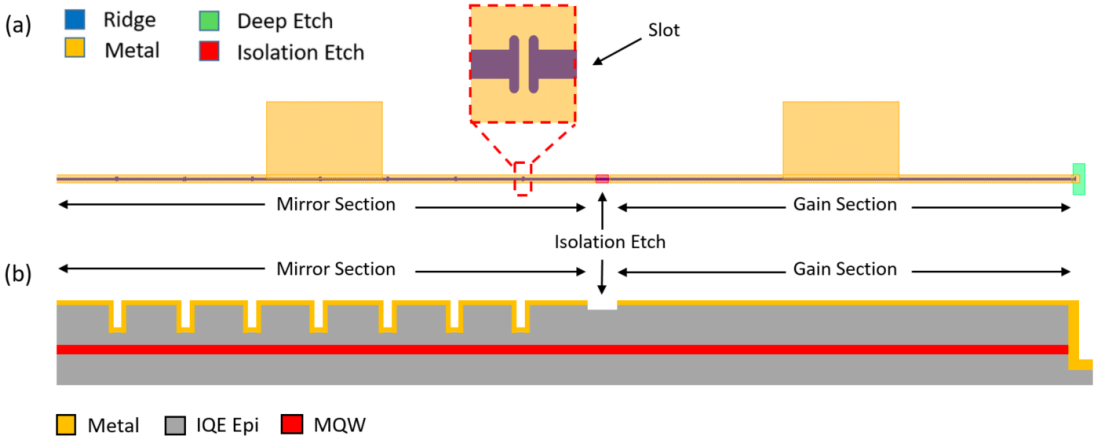


Figure 4.15: (a) Mask schematic and (b) side view illustration of a SFP laser.

The isolation etch allows both sections of the Slotted Fabry–Pérot (SFP) to be biased independently and so a larger tuning range can be creating by sweeping currents through both the gain and mirror sections. The LIV characteristics can be measured by sweeping the current through the gain section for different bias currents through the mirror section and both sections can be tuned to generate single mode spectra. Examples of these are plotted in *Figure* 4.16 where the light was collected via fiber coupling.

The results show that the threshold current of the device reduces and lasing power increases as the current across the mirror region is increased. The different single mode spectra are also plotted and demonstrats six different single mode spectra being generated at wavelengths 4.2 nm apart. This is consistent with the transmission profile determined in *Chapter 2, section 2.2.2* which is plotted here in black.

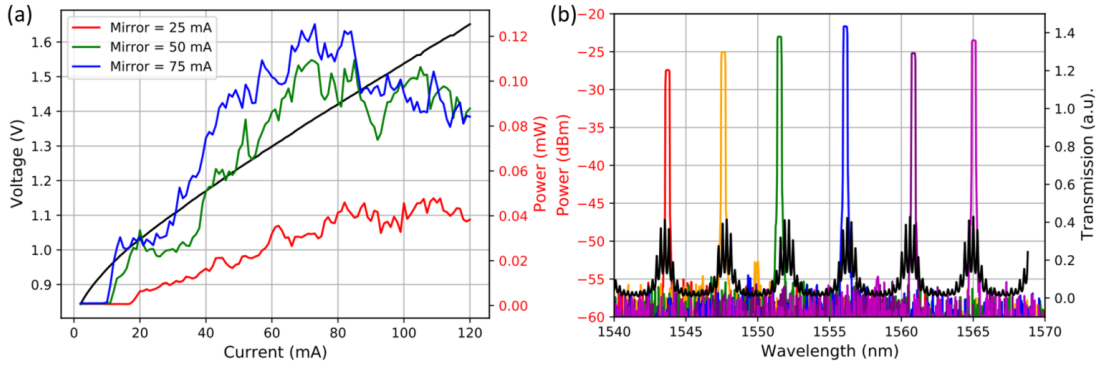


Figure 4.16: (a) LIV curves of a SFP laser. (b) Different single mode spectra attained from a SFP laser.

4.8 Pitted Fabry Pérot Lasers

An alternative method of generating a single mode spectra through reflective defects introduced in *Chapter 2, section 2.2.3* is by etching pits into the ridge of a FP. A schematic of this is illustrated in *Figure* 4.17.

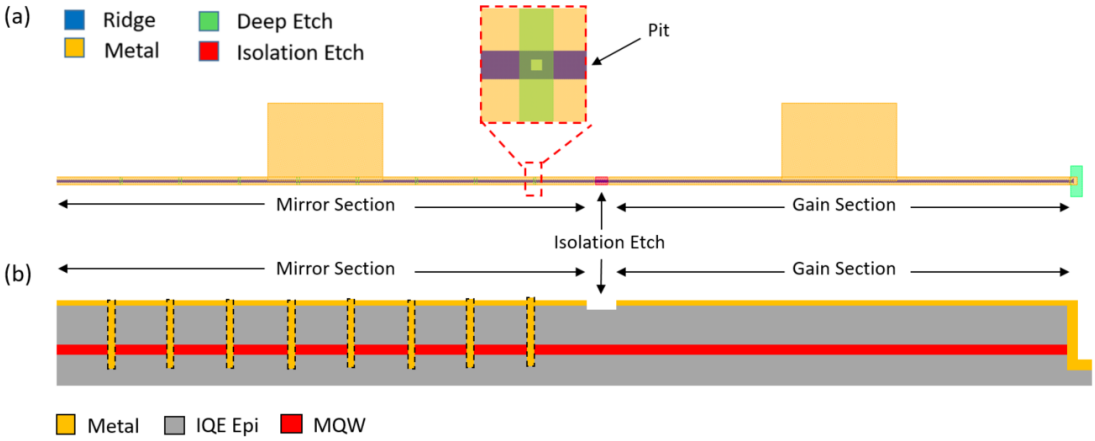


Figure 4.17: (a) Mask schematic and (b) side view illustration of a PFP laser.

Like the previous example, this laser is separated by an isolation slot into a gain and mirror section. The mirror section in this case is made up of 8 deep etched pits introduced into the ridge of the laser. The LIV characteristics can be measured by sweeping current through the gain section for different bias currents through the mirror section. Both sections can also be tuned to generate different wavelengths. These results are plotted in *Figure* 4.18 where the light was collected via fiber coupling.

Like the previous example, the threshold current decreased and lasing power increases as the current through the mirror section is increased. Seven different wavelengths are attained with a wavelength separation of 4.7 nm,

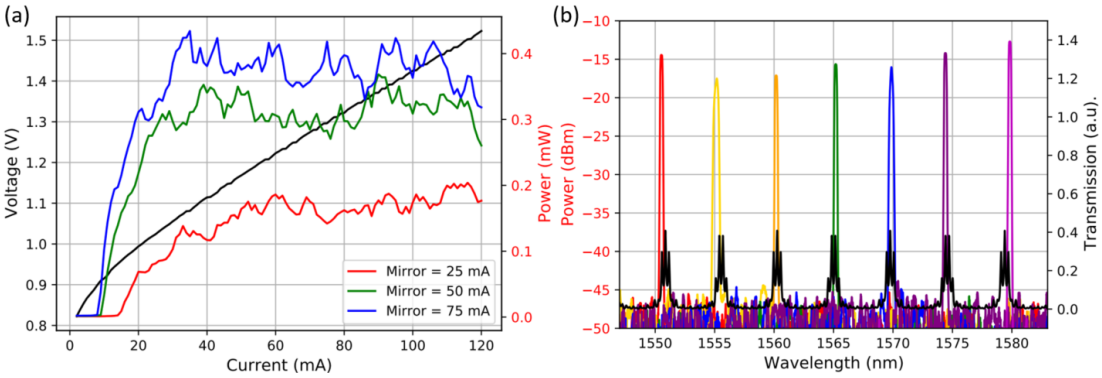


Figure 4.18: (a) LIV curves of a PFP laser. (b) Different single mode spectra attained from a PFP laser.

which is consistent with the transmission profile for this laser plotted in black.

4.9 Chapter Conclusion

This chapter introduces the characterisation setup used in this thesis as well as an introduction to the experimental effects of different features on ridge FP lasers. Beginning with a shallow and deep etched FP, the LIV curves and spectra were analysed with the shallow etch FP laser outperforming the deep etch FP in terms of threshold current and lasing power. Next, one of the cleaved facets of a shallow etch FP was replaced by an etched facet and a metal etched facet and the performance of the device was characterised. In this case the FP with the metal etched facet outperformed that with the etched facet, again achieving a higher optical power and a lower threshold current.

The concept of adding defects along the ridge of a FP to change the shape of the emission spectra was introduced in *Chapter 2*. This chapter demonstrates the effects of a single shallow and a single deep etched slot on the emission spectra of a FP. The shallow slot laser demonstrated the partial suppression of specific FP modes while the deep etch slot demonstrated the complete suppression of specific FP modes caused by the full laser cavity formed by the two cleaved facets. The technique of measuring the locations of reflections in a cavity was also introduced by taking the FFT of the emission spectrum.

U-bend lasers were introduced and the effects of the radius of curvature on the device's lasing power and threshold was characterised. The effects of fabricating these bends with a deep etch on the outside of the curved waveguide and on both sides of the curved waveguide, for optical

confinement, were demonstrated. Finally, the single mode devices using slots and pits simulated in *Chapter 2* were characterised. The singlemode wavelengths attained from both devices was compared with the equivalent simulations in *Chapter 2*, and good agreement was demonstrated in both cases.

Chapter 5

Comb Generation Techniques

5.1 Chapter Overview

Chapter 4 introduces different devices fabricated with cleaved facets, etched facets, metal etched facets, deep and shallow etched ridges, slots and pits. This chapter focuses on how these device features are utilised to design and create the photonic integrated circuits used to generate frequency combs. Gain switching is the technique used to generate combs in this project which involves modulating the bias current with a high power radio frequency (RF) signal, rapidly turning the laser on and off. This technique is typically achieved through some form of external injection [17] or on-chip injection locking [19] to maintain phase coherence allowing comb lines to be generated, and thus the integration of two different lasers is chosen as a starting point for this project. Beginning with traditional primary-secondary coupling techniques demonstrated in [19], on-chip injection locking is demonstrated as well as the resulting combs generated through gain switching. Furthermore, additional coupling techniques are introduced, demonstrating how stable combs can be generated through bidirectional coupling, and demonstrating how the traditional methods of [19] can be discarded in favour of mutual coupled lasers which greatly enhance the generated combs.

5.2 Combs through Primary-Secondary Coupling

On-chip coupling of monolithically integrated single mode lasers has been examined in [26] and [27] with very different configurations and design

types. Despite the lack of on-chip isolation, mutual phase locking was achieved in both cases improving several characteristics of the lasers and in particular, increasing the side mode suppression ratio (SMSR). The SMSR is the difference in power in dBm between the lasing mode of the laser and the secondary mode. In both cases mentioned above, the biasing of the lasers was highly asymmetric, thereby approximating a primary-secondary configuration.

A block diagram of the experimental setup used to generate combs in this fashion is demonstrated in *Figure* 5.1.

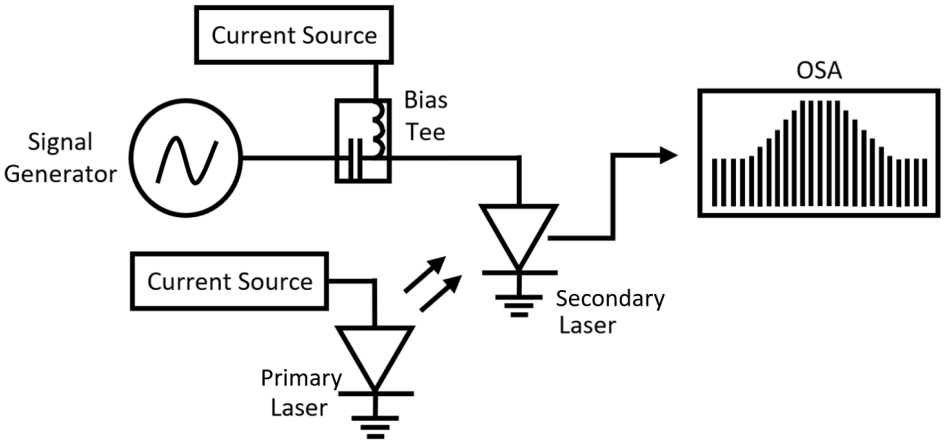


Figure 5.1: Block diagram of the experimental setup used to generate combs.

A current source is used to bias the primary laser which injects light into the secondary laser. Another current source is modulated with the RF signal from the signal generator via a bias tee creating a sinusoidal current which is used to bias and gain switch the secondary laser. The spectrum of the resulting system is measured using an OSA.

5.2.1 Example 1: Slotted Fabry Pérot Lasers

5.2.1.1 Device Design

A primary-secondary integrated device is fabricated using the fabrication process described in *Chapter 3* and is illustrated in *Figure* 5.2.

This PIC consists of a two sectioned single mode (SM) primary laser and a single section Fabry Pérot (FP) secondary laser. The single mode (SM) laser has a gain section 600 μm in length and a slotted mirror section consisting of 7 slots with an inter-slot separation of 108 μm. These slots act as reflective defects along the ridge by creating periodic regions of lower effective refractive index, effectively creating a laser that is both single mode and

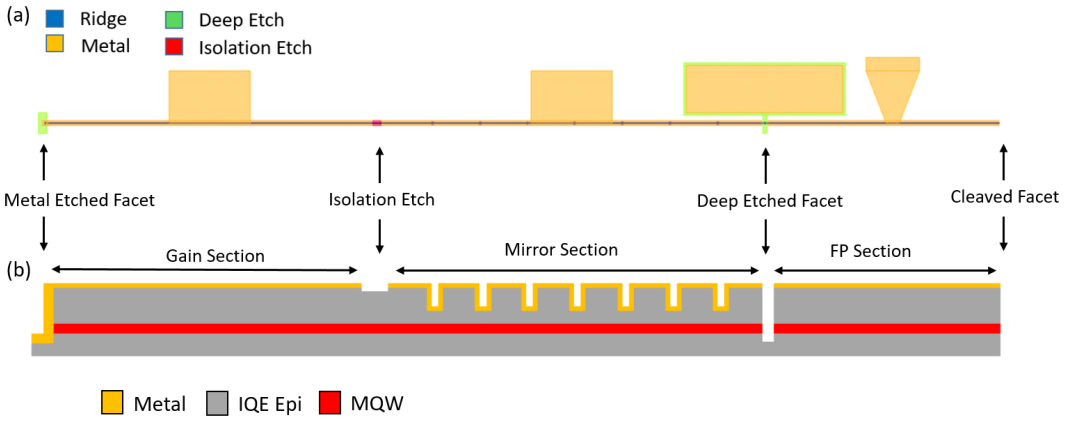


Figure 5.2: (a) Mask schematic and (b) side view illustration of the integrated primary-secondary laser.

tunable [32], [19], [50]. An isolation slot exists between these two sections for electrical isolation allowing both sections to be biased independently. The cavity of the SM laser is confined using a metal etched facet and a deep etched slot free of metal forming an etched facet. The cavity of the secondary Fabry–Pérot (FP) laser is 450 μm in length and is confined by the etched facet of the SM laser and a cleaved facet. Each of the three sections is fabricated with a contact pad to allow for biasing. A Ground Signal (GS) contact is added to the FP laser to allow for gain switching using a GS probe. The ground pad makes contact with the n-type substrate via a deep etch.

5.2.1.2 DC Characterisation

The LIV characteristics of the two lasers can be measured independently using fiber coupling through the cleaved facet. Starting with the SM laser, the mirror section was biased at 50 mA and the current across the gain section was swept from 0 - 120 mA. Simultaneously, the current across the FP laser was set to 10 mA which is large enough to make the laser passive but not large enough to allow the laser to lase. The lasing power (L) was measured using a power meter connected to the coupled fiber, and the voltage (V) and current (I) was measured and set using the Keithley power source. This was carried out for additional current values of 75, 100 and 125 mA across the mirror section. This is plotted in *Figure* 5.3.

The results resemble those discussed for Slotted Fabry–Pérot (SFP) lasers in *Chapter 4.7* as the threshold current of the device decreases and lasing power increases as the bias current of the mirror section increases.

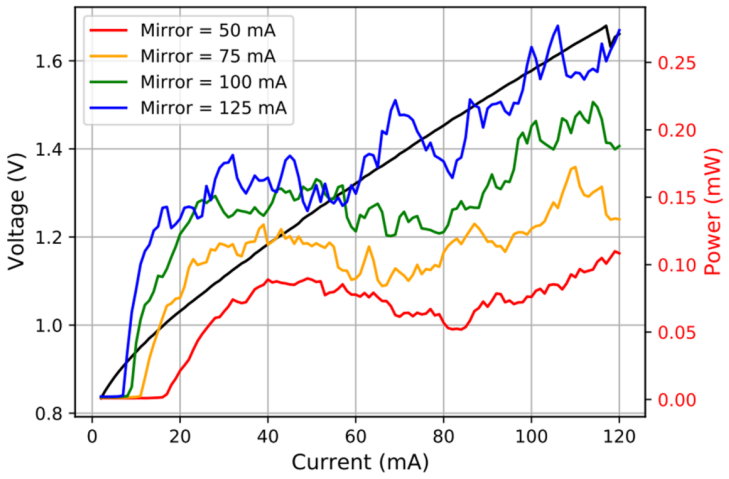


Figure 5.3: LIV characteristics of the primary laser as current is swept through the gain section.

To fully characterise the single mode nature of the laser, currents were swept across the gain and mirror sections. At each interval the optical spectrum of the laser was measured using the OSA and the lasers SMSR and lasing wavelength were measured and recorded. These results are plotted in *Figure* 5.4.

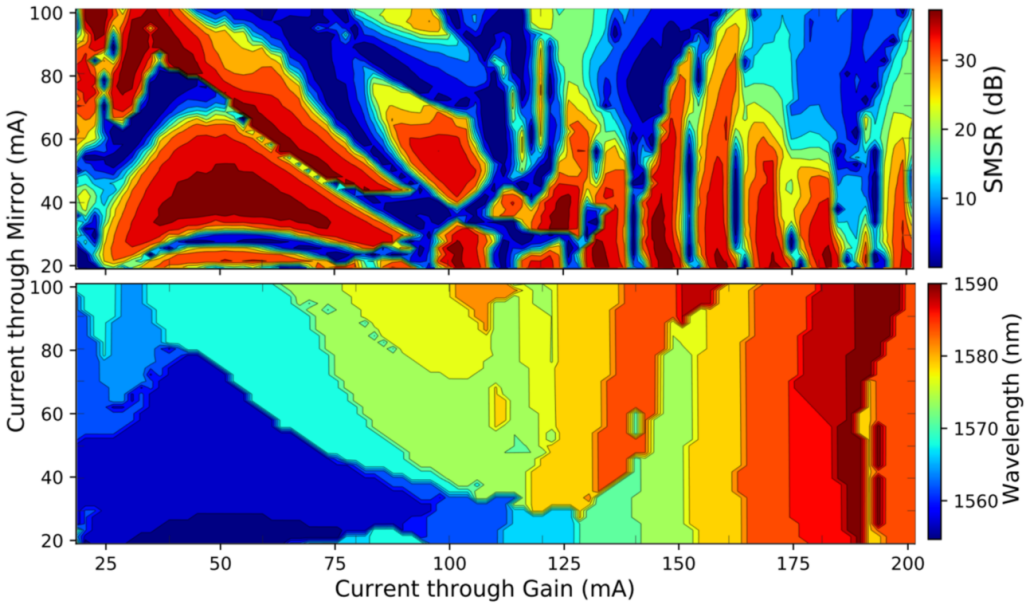


Figure 5.4: (top) SMSR and (bottom) lasing wavelength of the primary laser as current is swept across both laser sections.

This plot was attained by sweeping current from 20 - 200 mA across the gain section for different bias currents across the mirror section ranging from 20 - 100 mA. Again the secondary laser was biased at 10 mA. The colour plots in *Figure* 5.4 illustrated multiple different single mode regions where the SMSR

$>$ 30 dB. The plot also shows the wavelengths at which these single mode regions are achieved. An easy way to see the relation between these lasing wavelengths and the equivalent SMSR is by plotting both values together as done in *Figure* 5.5.

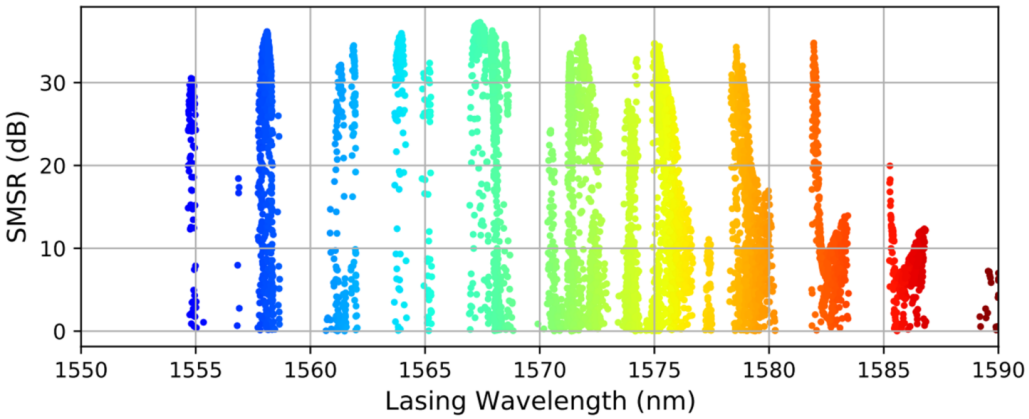


Figure 5.5: Plot of the SMSR of the primary laser achieved at different wavelengths.

This plot shows the different wavelengths defined by the mirror section at which a single mode spectrum could occur. In this case there are nine different single mode regions across a wavelength span of 27 nm ranging from 1555 - 1583 nm.

The LIV characteristics of the secondary laser are measured by sweeping the current across the FP laser from 0 - 100 mA as shown in *Figure* 5.6 and demonstrates a laser with a threshold current of 28 mA. This figure also shows the spectra of the laser at 30 mA (just above threshold current) which is the expected spectrum of a FP laser.

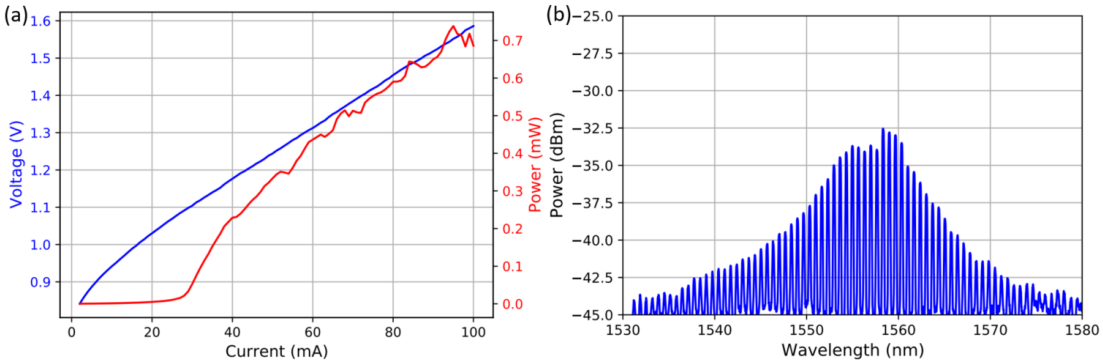


Figure 5.6: (a) LIV curves and (b) spectra of the FP secondary laser.

As described above, on-chip injection locking is achieved by operating the two lasers in an asymmetric bias regime whereby the primary laser is more heavily

biased than the secondary. The secondary laser is biased at 30 mA generating the spectrum plotted in *Figure* 5.6, the gain and mirror sections of the primary laser were biased at 120 mA and 20 mA respectively which generates a single mode spectrum at a wavelength of 1561 nm as defined by the colour plot attained in *Figure* 5.4. Injection locking occurs whereby the FP secondary laser is optically phase locked to the SM primary laser. This is demonstrated in *Figure* 5.7.

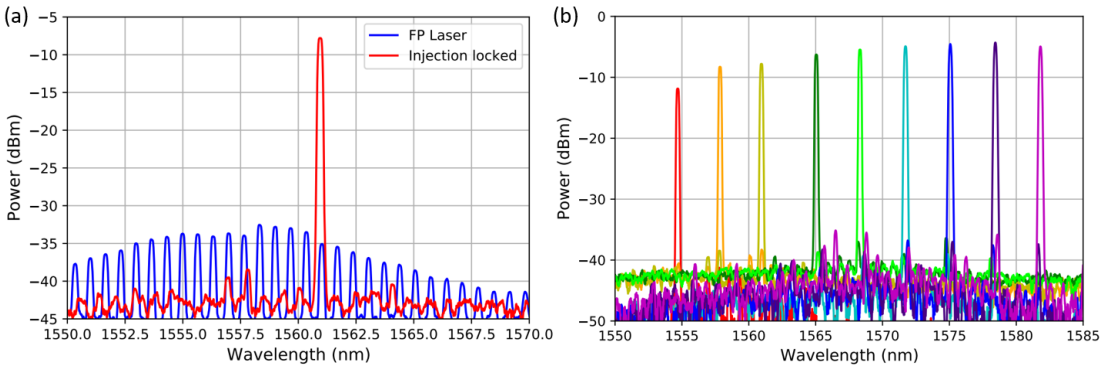


Figure 5.7: (a) Spectra of the secondary laser before and after the primary laser is biased and injection locking occurs. (b) Different injection locked spectra achieved at each lasing mode of the primary laser.

Figure 5.7 demonstrates the spectra of the secondary FP laser before and after the primary laser is turned on and injection locking occurs. What results is an injection locked single mode spectrum with an SMSR of 31 dB. This figure also demonstrates the different injection locked single mode spectra that can be achieved by adjusting the current through both sections of the primary laser to achieve the wavelengths determined in *Figure* 5.4. Again, these are nine different wavelengths across a wavelength span of 27 nm ranging from 1555 - 1582 nm.

5.2.1.3 Comb Generation

Once injection locking was achieved, the probe biasing the secondary FP laser was swapped for a GS probe, the signal generator was turned on and the FP was gain switched. Frequency combs were attained with a comb line frequency separation equivalent to the frequency determined by the RF signal. An example of a generated comb attained at 5 GHz is plotted in *Figure* 5.8.

Similar combs were achieved at each of the injection locked spectra demonstrated in *Figure* 5.7. An example of some of these are plotted in *Figure* 5.9.

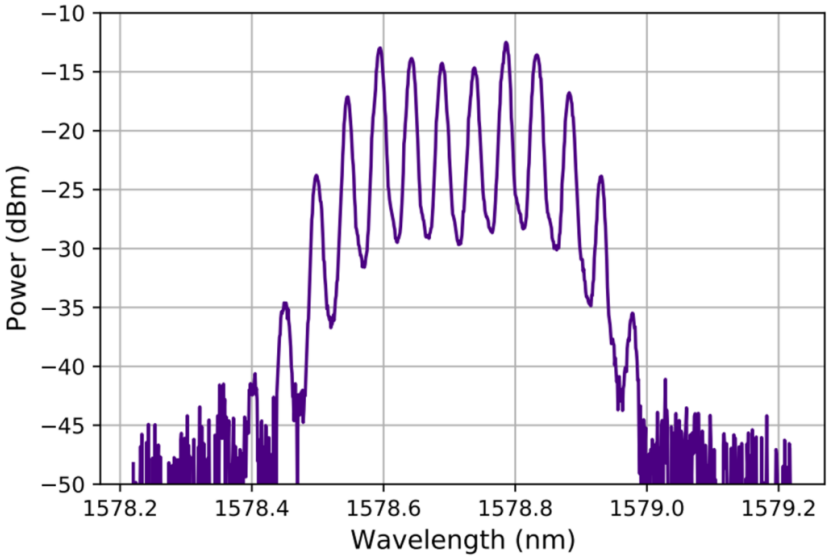


Figure 5.8: Frequency comb generated at an frequency of 5 GHz.

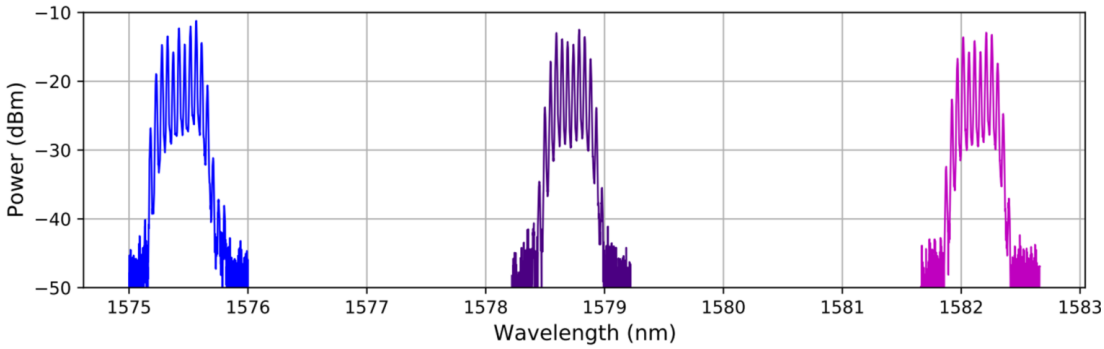


Figure 5.9: Example of frequency combs generated at an frequency of 5 GHz at different wavelengths.

5.2.2 Example 2: Pitted Fabry Pérot Lasers

Another example of this primary-secondary comb generation can be demonstrated through Pitted Fabry Pérot Lasers integrated with a gain switched secondary FP laser.

5.2.2.1 Device Design

Again this device is fabricated using the fabrication process described in *Chapter 3* and the schematic of the device is illustrated in *Figure* 5.10.

The design of this PIC is similar to that described in the previous example, however this time the mirror section is made up of 8 pits with an inter-pit separation of 77 μm etched into the ridge of the device. Again these features act as reflective defects along the ridge of the device. The primary laser was

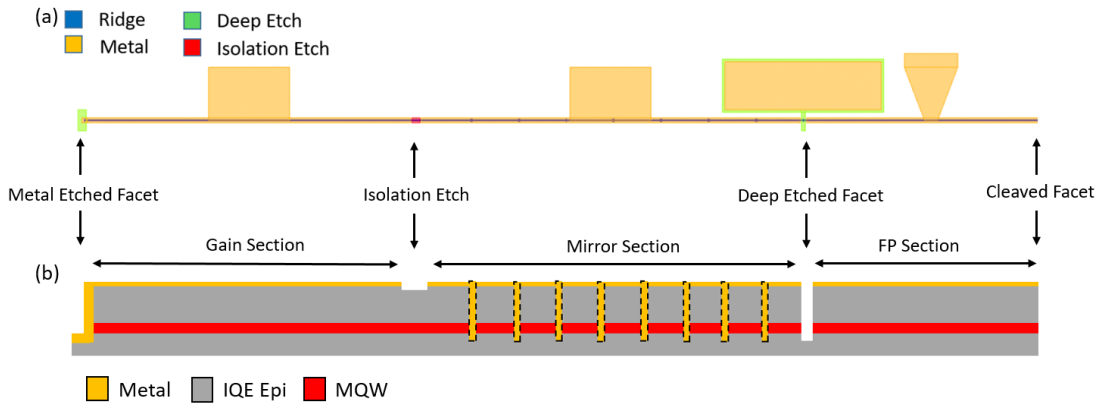


Figure 5.10: a) Mask schematic and (b) side view illustration of the integrated primary-secondary laser.

made up of this mirror section and a 600 μm long gain section and the cavity was confined by a metal etched facet and an etched facet. The secondary FP laser was integrated with the primary via the etched facet and had a cavity 450 μm in length confined by the etched facet and cleaved facet.

5.2.2.2 DC Characterisation

Like before, to measure the LIV characteristics of the primary laser, the secondary FP was biased at 10 mA to make that section passive but not lase. Current was swept across the gain section for different bias currents across the mirror section. These LIV curves are plotted in *Figure* 5.11. This was carried out for bias currents of 50, 75, 100 and 125 mA across the mirror section. The threshold current of the laser decreased, like before, for increasing currents through the mirror section. Also the power of the laser increased for higher bias currents across the mirror section.

The SMSR and lasing wavelengths of this primary laser were achieved again by sweeping currents across both sections of the primary and recording the spectra at specific intervals using the OSA. The SMSR and lasing wavelength for this primary laser are plotted in *Figure* 5.12.

The above plot was attained by sweeping the bias current from 20 - 400 mA across the gain section and 20 - 300 mA across the mirror section achieving multiple single mode regions (SMSR $>$ 30 dB) at multiple wavelengths. Like before, these lasing wavelengths can be illustrated by plotting the SMSR against the lasing wavelengths which is plotted in *Figure* 5.13.

This plot shows the different wavelengths defined by the mirror section at

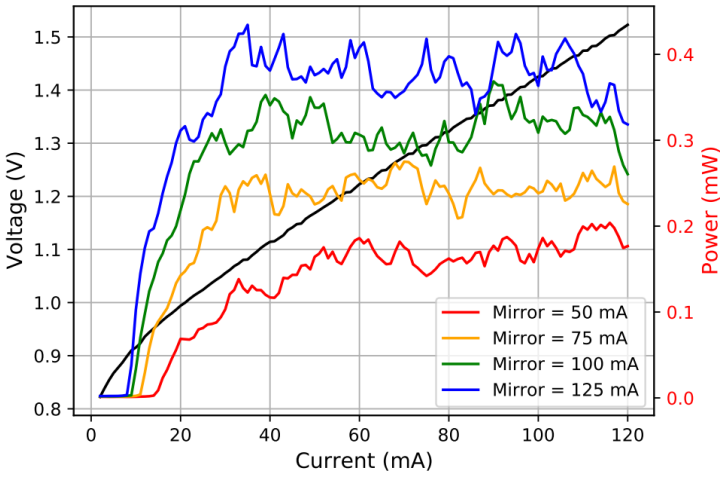


Figure 5.11: LIV characteristics of the primary laser as current is swept across the gain section for different bias currents through the mirror section.

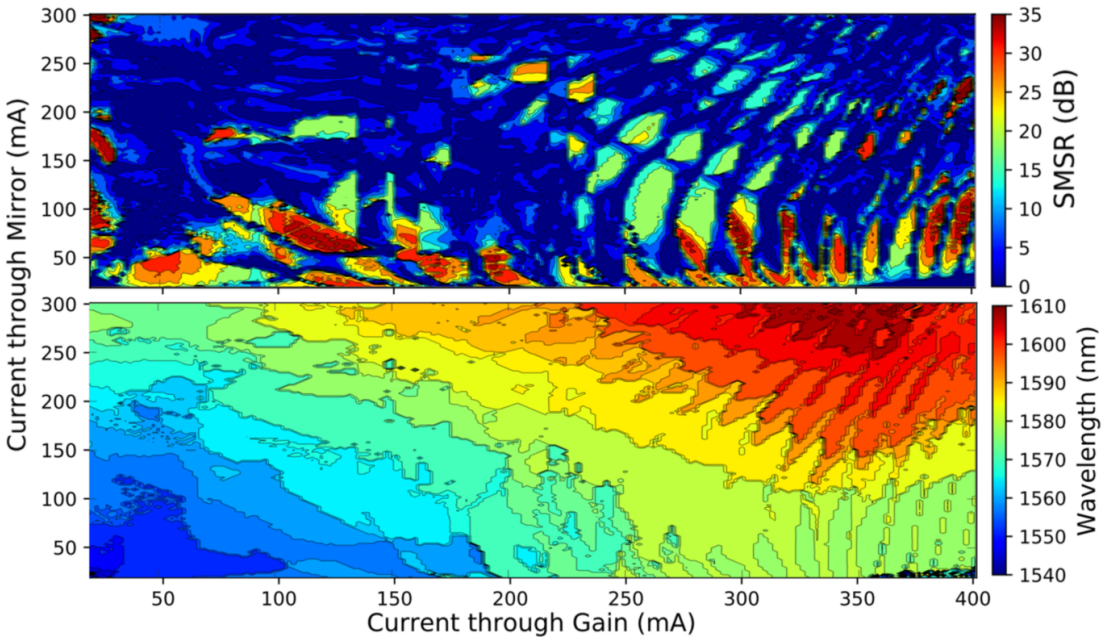


Figure 5.12: top) SMSR and (bottom) lasing wavelength of the primary laser as current is swept across both laser sections.

which a single mode spectrum occurs. This time 11 different lasing modes are achieved across a wavelength span of 50 nm ranging from 1550 - 1600 nm.

5.2.2.3 Comb Generation

Combs were generated by first injection locking the FP secondary laser to the single mode primary laser to attain a single mode injection locked spectra. Examples of injection locked spectra spectra are plotted in *Figure* 5.14 for different wavelengths defined by the primary laser.

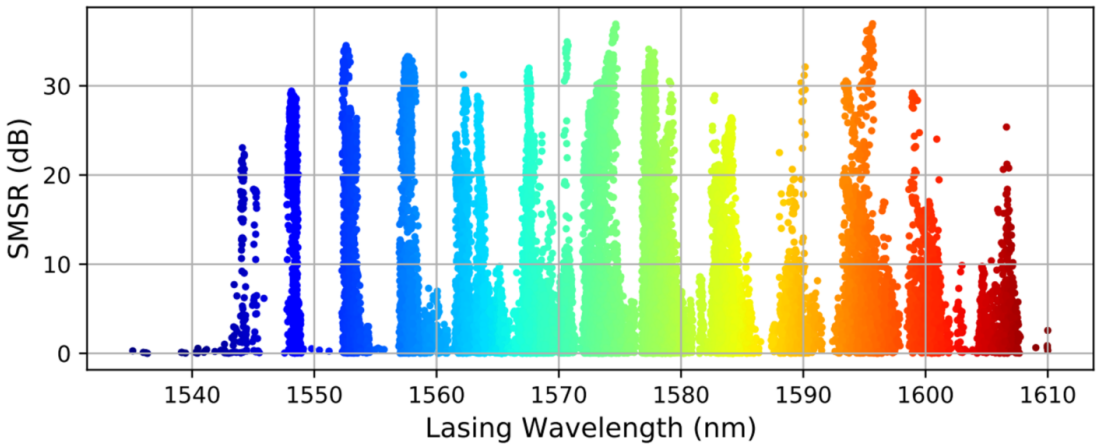


Figure 5.13: Plot of the SMSR of the primary laser achieved at each of the lasing wavelengths.

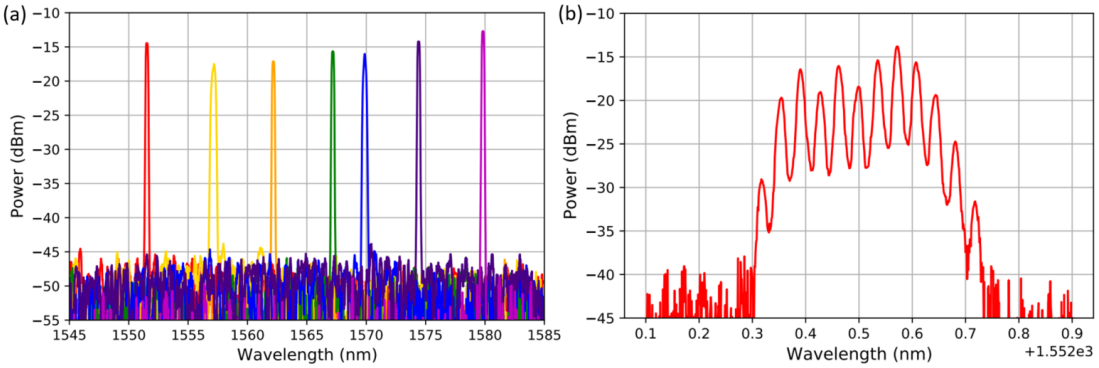


Figure 5.14: (a) Different injection locked spectra achieved at each lasing mode of the primary laser (b) Example of a comb generated at 1552nm at a gain switched frequency of 4.5 GHz.

Once the injection locking occurred, the secondary laser was biased using a GS probe which modulated the bias current with a high power RF signal allowing the FP to be gain switched. An example of a comb generated at 1552nm is also plotted in *Figure* 5.14 showing a comb with a frequency spacing of 4.5 nm.

Again, similar combs were attained at each of the injection locked wavelengths. An example of a few are plotted in *Figure* 5.15.

5.2.2.4 Frequency Response

In *Chapter 2* it is demonstrated theoretically that gain switching the laser at a frequency equivalent to the lasers Relaxation Oscillation (RO) frequency results in combs with a broader bandwidth. The experimental effects of the gain switched frequency on the quality of the comb can be determined by measuring the spectra of the generated comb for different gain switched

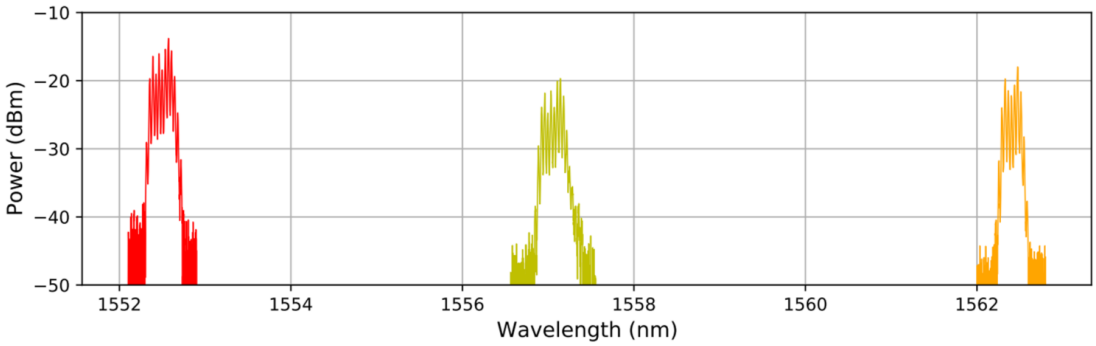


Figure 5.15: Example of frequency combs generated at an frequency of 4.5 GHz at different wavelengths.

frequencies and comparing the combs bandwidth. A comb was attained at 1552.5 nm by biasing the gain, mirror and FP sections at 50, 48 and 29 mA respectively. Multiple combs were measured for gain switched frequencies ranging from 3.8 - 8 GHz. The results are plotted in *Figure* 5.16.

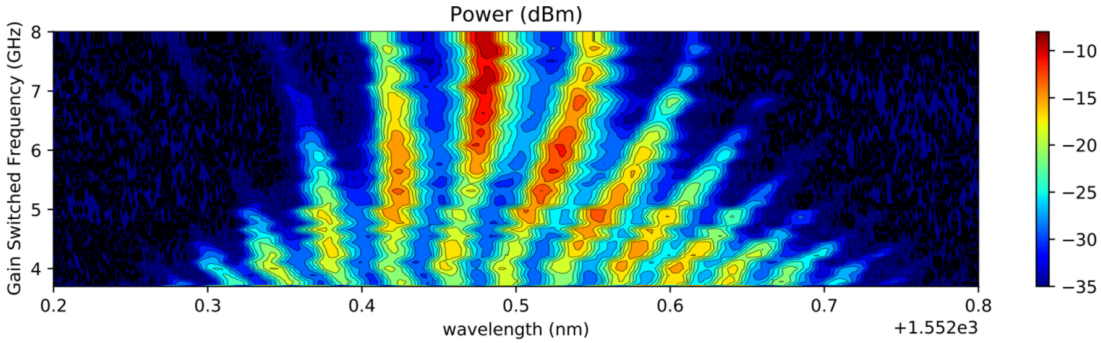


Figure 5.16: Combs generated at gain switched frequencies ranging from 3.8 - 8 GHz.

This image is comparable to the simulated frequency response demonstrated in *Chapter 2*. It is consistent with the simulated combs generated using a low bias current and thus a low RO frequency for the gain switched laser. In this case, the gain switched laser is the secondary FP which is biased at 29 mA.

To determine the RO of the secondary FP the secondary laser was biased and the spectrum was recorded using a high resolution APEX OSA which is plotted in *Figure* 5.17. This image shows the lasing modes of the FP laser and also the RO in the laser intensity which can be seen as sidebands to the lasing laser mode [51].

This is a spectrum attained from the secondary FP at a bias current of 45 mA, which allowed the laser to emit enough power so that the RO sidebands can be detected. The frequency difference between the lasing FP mode and these side

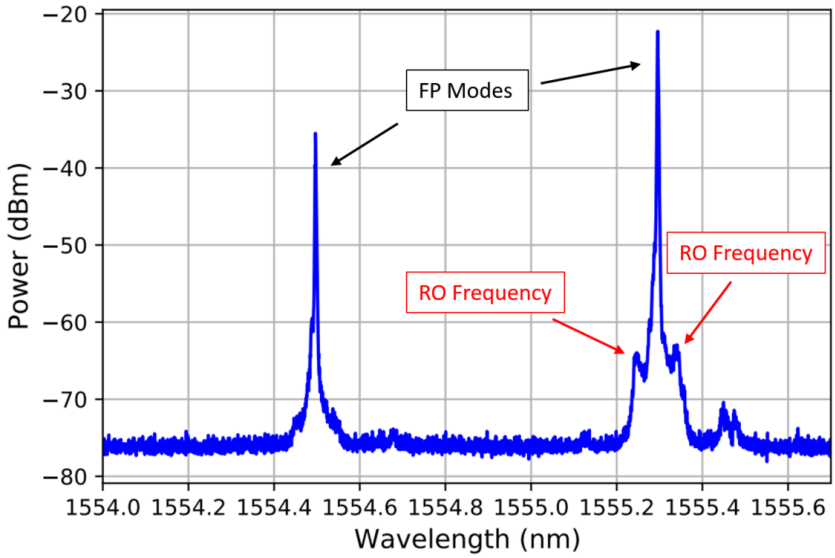


Figure 5.17: Spectrum of the FP laser biased at 45 mA illustrating the lasing modes and the sidebands caused by the lasers RO frequency.

bands was measured to be 4.8 GHz at 45 mA. We know from *Chapter 2.3.1* that the RO frequency of a laser increases with current, and so the RO of the secondary FP laser used to attain the combs in *Figure* 5.16, which is biased at 29 mA, has an RO $<$ 4.8 GHz. This is consistent with broader generated combs attained at 4 GHz.

The photonic integrated circuit used to generate these combs consists of two integrated lasers, a laser that is gain switched and a laser that isn't. We know the effect of gain switching the device at a frequency equivalent to the RO frequency of the gain switched laser, so it is logical to investigate the effects of gain switching the device at the RO frequency of the non-gain switched laser. To measure the RO of the SM laser, the secondary FP was biased at 10 mA, which again is a high enough current to make the section passive but not large enough to allow the section to lase. The gain and mirror sections were biased at 125 mA and 30 mA respectively generating a single mode wavelength at 1557 nm with detectable RO sidebands. This is plotted in *Figure* 5.18. The frequency separation between the lasing mode of the laser and the RO sidebands are measured to be approximately 2.5 GHz.

Next, the bias current across the secondary FP was increased to 30 mA allowing injection locking to occur. The secondary FP was gain switched at a frequency equivalent to the RO of the SM laser. Spectra were measured for gain switched frequencies of 2.3, 2.5 and 2.7 GHz using the high resolution OSA. These combs are plotted in *Figure* 5.19.

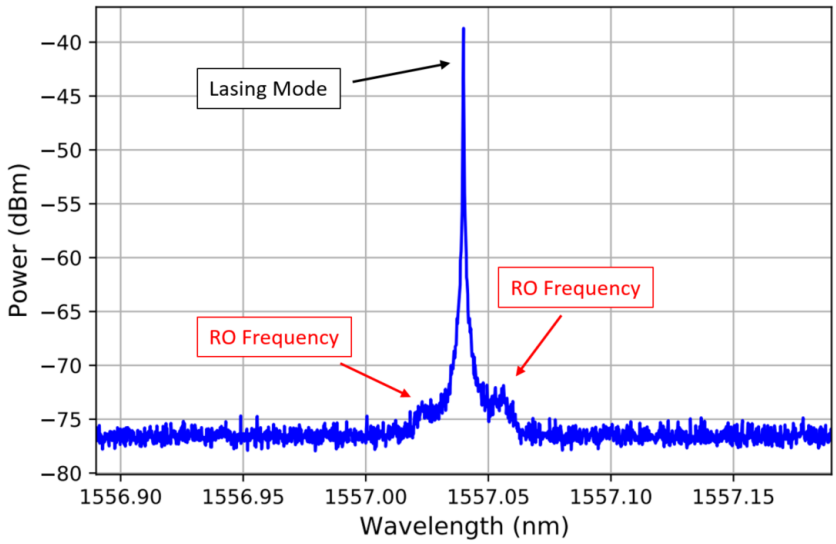


Figure 5.18: Spectra of the SM primary laser when the gain and mirror sections are biased at 125 and 30 mA respectively.

Figure 5.19 demonstrates how the generated combs change as the gain switched frequency passes through the RO frequency of the SM laser. Comb lines were generated at gain switched frequencies of 2.3 and 2.7 GHZ. However, as the gain switched frequency approached the RO frequency of the SM laser no such comb lines were generated. Instead, a broad lasing mode or spectral bulge is generated.

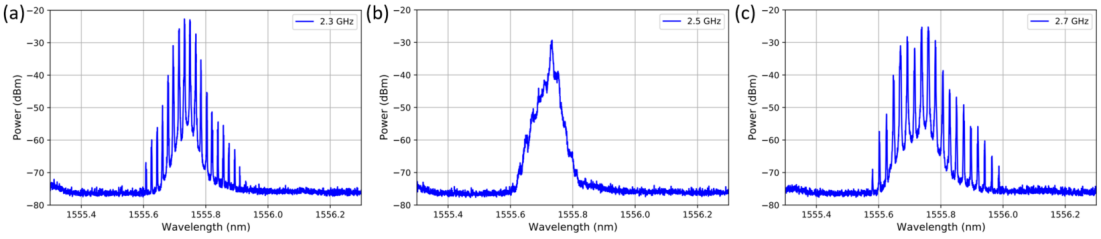


Figure 5.19: Combs measured at a gain switched frequency of 2.3, 2.5 and 2.7 GHz.

5.3 Combs through Bidirectional Coupling

As demonstrated in the previous section, a major benefit to generating combs through gain switching is the tunability allowed in the repetition rate of the periodic train of intensity pulses that results from periodically sweeping the laser from below to above threshold. In other words, gain switching allows for the tunability of the comb line spacing which is set by the modulation frequency. A downfall of this technique is the potential lack of coherence from

pulse to pulse as the laser is brought below threshold before each pulse. However, as shown in [52], by unidirectionally optically injecting a gain switched laser one can improve the coherence and generate optical frequency combs (OFCs) of excellent spectral purity.

Thus far, such configurations have been achieved off-chip only, in bench top like configurations. In such configurations, optical isolators can easily be employed to ensure unidirectional coupling. Ideally one would like to transfer this technique to PICs. However, the lack of on-chip isolators means that any optical coupling is necessarily bidirectional, a notoriously unstable configuration [53] for semiconductor lasers.

This section demonstrates how this bidirectional coupling does not in fact hamper the generation of on-chip comb sources. Such an integrated comb source allows combs to be propagated throughout the integrated circuit, allowing the comb to be detectable through multiple outputs without requiring more complicated designs.

5.3.1 Device Design

Like previous examples, this PIC takes the form of a primary-secondary configuration using a two sectioned, single mode primary laser and a FP secondary laser.

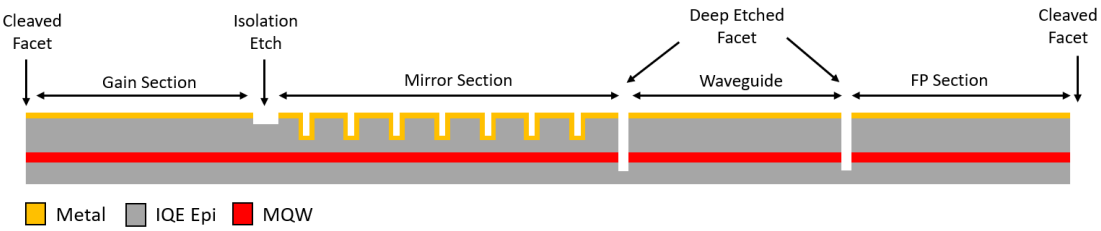


Figure 5.20: Side view illustration of device.

A schematic of the PIC used in this experiment is demonstrated in *Figure* 5.20. The PIC is fabricated using the fabrication process described in *Chapter 3*. The primary laser is a two section device made up of a 600 μm long gain section and a mirror section consisting of 8 slots with an inter-slot separation of 108 μm. Both sections are separated by an isolation etch and the cavity is confined by a cleaved facet and an etched facet. The secondary section is 450 μm in length and is confined by an etched facet and a cleaved facet. To extend the PIC to both cleaved facet of the fabricated bar, a deep etched waveguide 1100 μm in length is integrated between the primary and secondary lasers. The

design of the PIC allows for the primary and secondary laser to be characterised independently by using the left and right cleaved facet respectively. By biasing the gain and slotted sections, the left cleaved facet can be used to measure the SMSR and wavelength tunability of the primary laser. The right cleaved facet can be used to measure the spectrum of the secondary laser by biasing the secondary section, and it can be used to measure the injection locked spectra which occurs when the primary laser is optically phase locked to that of the secondary. Both cleaved facets can be used to measure the generated combs after gain switching the secondary laser due to bidirectional coupling.

5.3.2 Device Characterisation

To characterise the device, two optical fibers were coupled to both the left and right cleaved facets of the laser. The LIV characteristics of the primary laser is measured by sweeping current across the gain section for different bias currents of the mirror section and measuring the output through the left cleaved facet using a power meter. The LIV of the secondary laser was measured by sweeping current across the laser and measuring the output through the right cleaved facet. These Plots are shown in *Figure* 5.21.

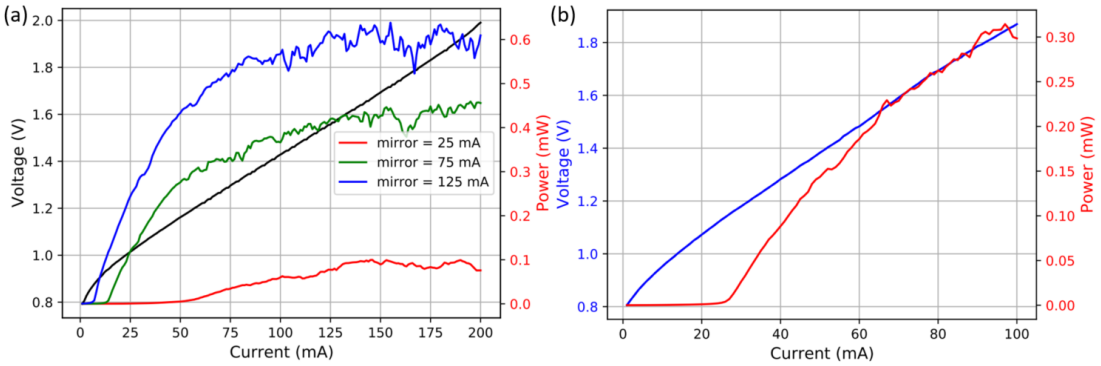


Figure 5.21: LIV curves measured from (a) the primary and (b) the secondary lasers.

The LIV curves of the primary laser demonstrates a decreasing threshold current and increasing lasing power as the bias current across the mirror section is increased. The LIV of the secondary laser gives a threshold current of 27 mA.

As described in previous sections, the primary laser is characterised by sweeping currents through both the gain and mirror section and measuring

the resulting spectra with an OSA through the left cleaved facet. The spectra of the secondary laser is measured at threshold current and double threshold current through the right cleaved facet. The spectra attained from the primary and secondary laser are plotted in *Figure* 5.22. The primary laser achieves six different single mode wavelengths ranging from 1557 - 1573 nm.

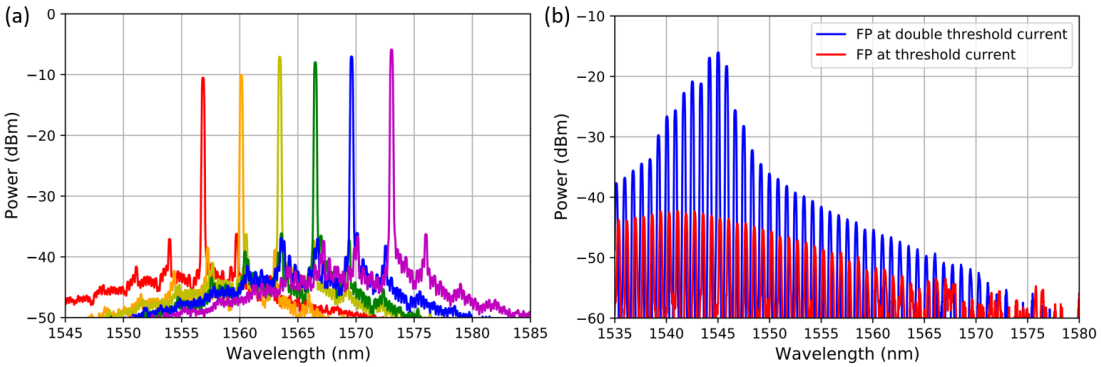


Figure 5.22: Spactra measured from (a) the primary laser and (b) the secondary laser.

To generate combs, the PIC was treated as a primary-secondary configuration and so the two lasers were asymmetrically biased, with the secondary laser being biased at 27 mA and the gain and mirror sections were biased at 179 mA and 28 mA respectively. This resulted in the injection locked spectrum plotted in *Figure* 5.23. Once this was achieved, the secondary laser was gain switched at 5 GHz generating a comb through the right cleaved facet with a frequency spacing of 5 GHz.

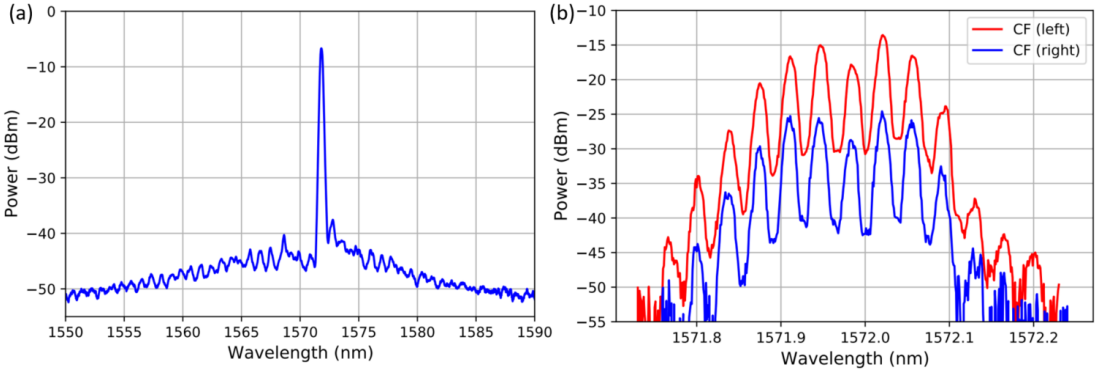


Figure 5.23: (a) Injection locked spectra and (b) Combs measured through the left and right cleaved facet.

Analysing the outputs of the device demonstrated that the comb generated by the secondary laser could be measured through both the left and right cleaved facet as shown in *Figure* 5.23. The bidirectional coupling is crucial to this

comb generation. Indeed it even results in almost identical combs in both devices generating 6 comb lines found within 4 dB of each other. The comb measured through the left cleaved facet achieved a higher power as it is amplified by the higher bias current of the primary laser. Despite this bidirectional coupling, the combs are coherent and stable [54].

5.4 Combs Through Mutual Coupling

Section 5.2 demonstrates how on-chip coupling of monolithically integrated single mode lasers can be achieved my approximating a primary-secondary configuration which occurs when the system operates in an asymmetric bias regime. On-chip coupling between integrated lasers has also been previously demonstrated in [26] and [27] with very different configurations and design types. In both of these cases, the biasing of the lasers was also highly asymmetric, thereby approximating a primary-secondary configuration.

In this section, a single mode (SM) laser is coupled to a FP laser on-chip, and it is demonstrated that this biasing asymmetry can be discarded while maintaining stable phase-locking. Furthermore, it is demonstrated that by gain-switching the FP laser, stable combs are produced and that the mutual coupling enhances the resulting OFCs by broadening the bandwith of the generated combs compared to traditional primary-secondary methods [19].

5.4.1 Device Design

The device in this section is fabricated using the fabrication process described in *Chapter 3*.

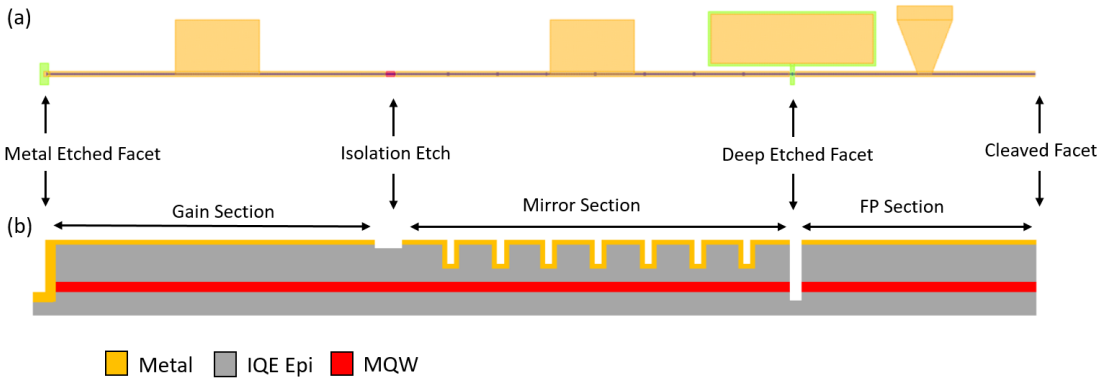


Figure 5.24: (a) Top view and (b) side view of the PIC schematic.

The PIC consists of a two section SM laser and a single section FP laser. The SM laser has a gain section 600 μm in length and a mirror section consisting of 7 slots with an inter-slot separation of 87 μm. These slots act as reflective defects along the ridge by creating regions of lower effective refractive index, effectively creating a laser that is both single mode and tunable [19] [50]. The last slot in the SM laser is deep etched thereby forming an etched facet, and is free of metal to allow for electrical isolation. The cavity of the SM laser is confined using this etched facet at one end of the mirror section and a metal etched facet at the opposite end of the gain section. The FP laser is 420 μm in length and the cavity is confined by the deep etched slot of the SM laser, and a cleaved facet. A Ground-Signal (GS) contact is added to the FP (as depicted in *Figure* 5.24) to allow for gain switching using the GS probe. The ground contact pad makes contact with the n-type substrate via the deep etch.

5.4.2 DC Characterisation

The LIV characteristics of the two lasers were measured independently using fiber coupling through the cleaved facet. Initially the FP laser was biased and current was swept from 0 - 100 mA, the corresponding voltage and optical power was measured and plotted in *Figure* 5.25. Similarly the LIV characteristics of the SM laser was measured by sweeping current through the gain section for different bias currents through the mirror section (*Figure* 5.25). Like before, the FP section was biased at 10 mA, which is high enough to make the section passive but not high enough to make the section lase, and so the SM laser could be measured independently through the same facet as the FP.

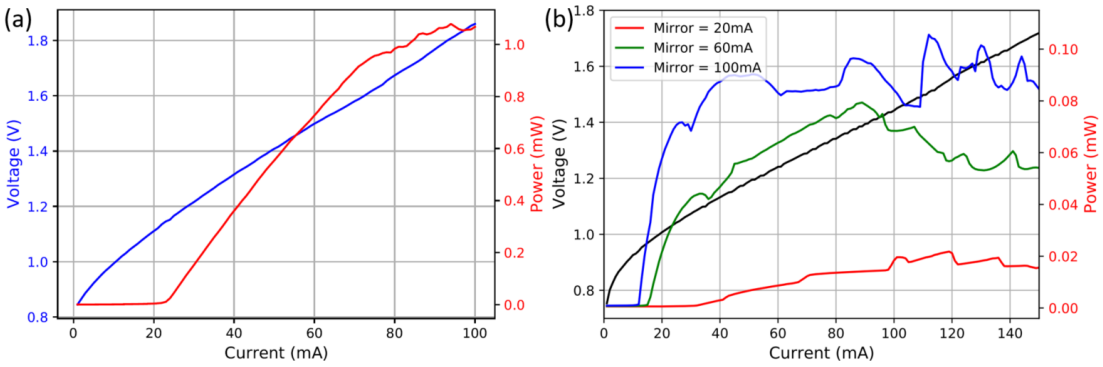


Figure 5.25: LIV characteristics of (a) the FP laser and (b) the SM laser as current is swept through the gain section for different bias currents through the slotted section.

The threshold current of the FP laser was measured to be 25 mA and the threshold current of the SM laser ranged from 12 - 35 mA depending on the bias current of the mirror section.

The spectra of the two lasers was also measured through fiber coupling using a high resolution APEX AP2061-A series OSA. The spectrum of the FP laser attained at a bias current of 50 mA and a single mode spectrum attained from the SM laser by biasing the gain and mirror sections at 75 and 100 mA respectively are both plotted in *Figure* 5.26.

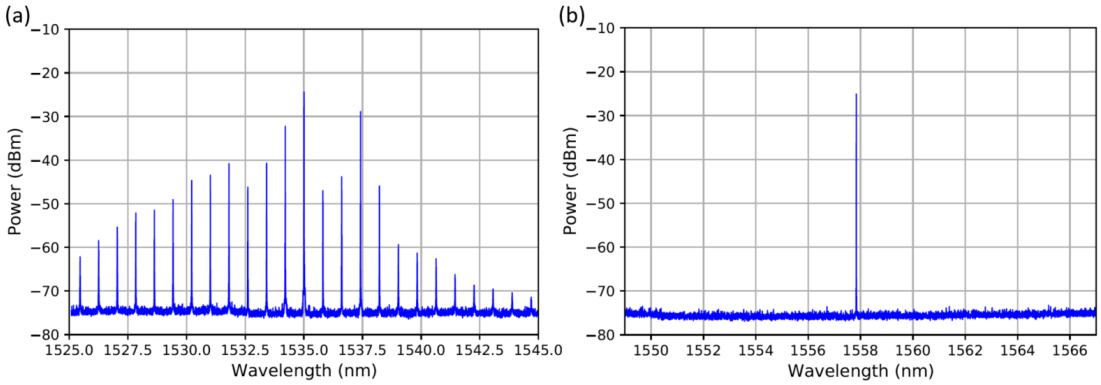


Figure 5.26: Spectra of (a) the FP laser biased at 50 mA and (b) the SM laser after biasing the gain and mirror sections at 75 and 100 mA respectively.

5.4.3 Comb Generation

To demonstrate the enhancement of combs in this section, combs were generated through the traditional primary-secondary coupling first and then they were generated by taking the system out of the asymmetric bias regime.

5.4.3.1 Primary-Secondary Coupling

As mentioned in *Section* 5.2, the traditional method of on-chip coupling involved biasing the integrated lasers asymmetrically in a strongly coupled primary-secondary configuration.

A single mode spectrum was achieved by biasing the gain, mirror and FP sections at 150, 40 and 25 mA respectively. The resulting spectrum is plotted in *Figure* 5.27 and has a lasing wavelength and SMSR of 1556.4 nm and 50 dB. A frequency comb was generated by biasing the FP laser with a GS probe and gain switching the FP. An example of a generated comb at a gain switched frequency of 6.8 GHz is plotted in *Figure* 5.27.

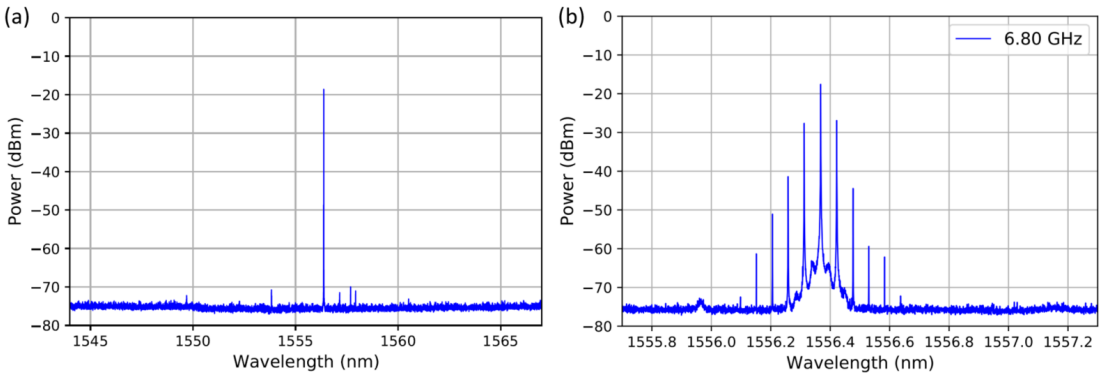


Figure 5.27: (a) Spectrum attained while the SM laser is injection locked to the FP laser while the laser are asymmetrically biased in a primary-secondary configuration. (b) Frequency comb generated at 6.80 GHz while the device is operating under this primary-secondary configuration.

5.4.3.2 Mutual Coupling

To demonstrate how mutual coupling can take the system outside of the asymmetric bias regime examined in [26] and [27], the mirror section was biased at 20 mA and current was swept across both the FP and gain sections. At each interval the optical spectrum was recorded from the cleaved facet using an optical fibre coupled to an ANDO AQ6317B OSA. The SMSR and peak lasing wavelength was recorded and plotted in *Figure* 5.28.

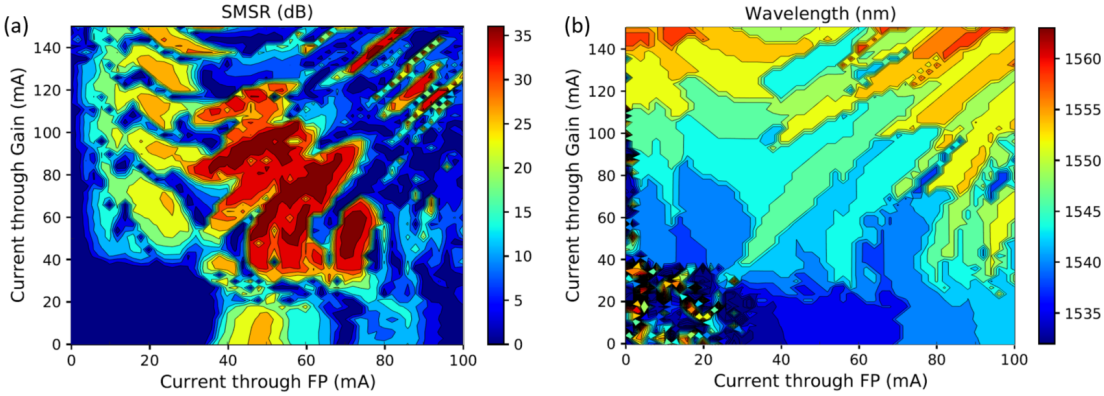


Figure 5.28: (a) SMSR and (b) lasing wavelength of the device as the current is varied through the gain and FP sections.

This coupled system generates six different single mode wavelengths ranging from 1537 - 1560 nm. A plot of the SMSR attained at each wavelength, as well as examples of single mode spectra are plotted in *Figure* 5.29.

The gain, mirror and FP sections were biased at 80, 20 and 50 mA respectively, attaining a single mode spectra at a wavelength 1547 nm. Analysing the spectra further with a the high resolution APEX OSA, this mutually coupled

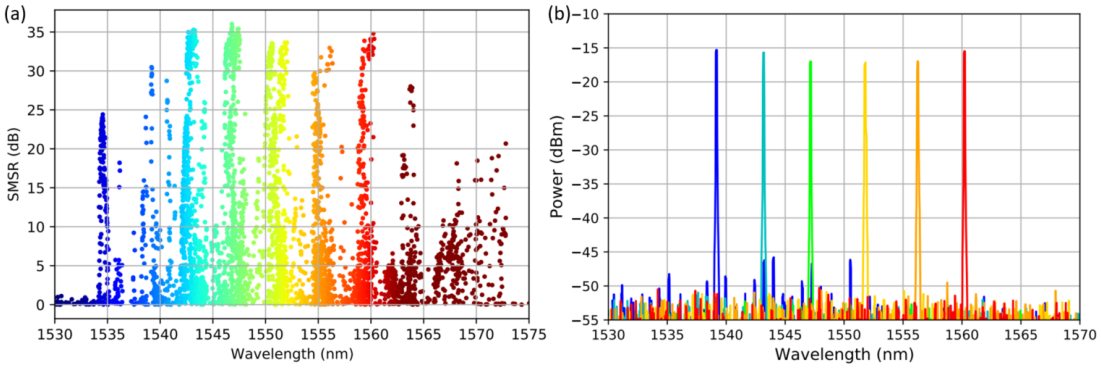


Figure 5.29: (a) Plot of the SMSR achieved at each lasing wavelength. (b) Examples of single mode spectra attained at six different wavelengths

system resulted in an increase in power and SMSR from -25 dBm and 50 dB (*Figure* 5.26) to -10 dBm and 60 dB respectively (*Figure* 5.30), and thus the biasing asymmetry can be discarded while maintaining stable phase-locking.

Once this single mode spectra was achieved, the FP section was once again biased using a GS probe and the device was gain switched. The corresponding comb is plotted in *Figure* 5.30 at a frequency of 6.8 GHz. What results is an enhanced frequency comb with a broader bandwidth and higher power compared to the frequency comb generated using the traditional primary-secondary configuration demonstrated in *Figure* 5.27.

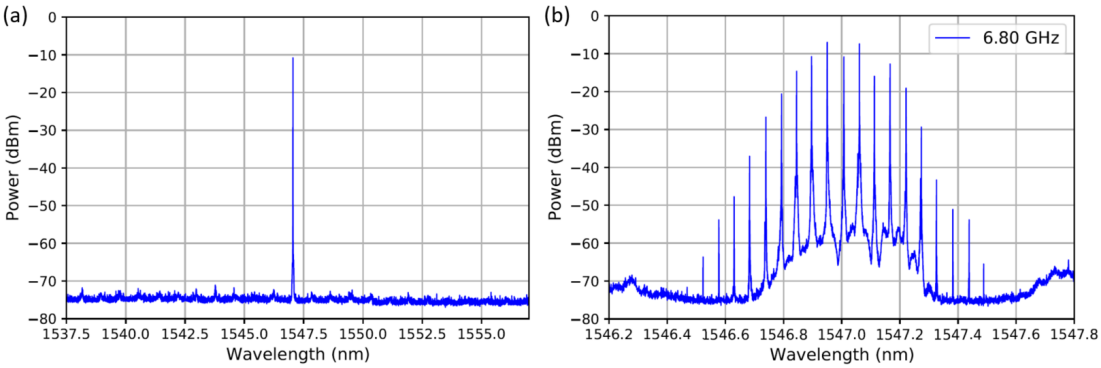


Figure 5.30: (a) Spectrum attained while the SM laser and FP laser are operating in a mutually coupled configuration. (b) Frequency comb generated at 6.80 GHz while the device is operating in this mutually coupled configuration.

Qualitatively similar results can also be found at different lasing wavelengths that could be generated from the mutually coupled system as demonstrated in *Figure* 5.28. More in-depth analysis into combs generated from this configuration is described in *chapter 6*.

Overall, this demonstrates how a three section PIC can be used to generate

and enhance gain switched combs. While traditional methods require operating the PIC in an asymmetrically biased primary-secondary configuration, here it is shown that this method can be discarded in favour of a mutually coupled system. The combs generated here from a mutually coupled system results in not only maintain stable phase locking, but the generated combs are enhanced to be detectable across a wider spectral range.

5.4.4 Comb Generation at RO Frequency

Section 2 of this chapter demonstrates how optimum combs are generated when the gain switched laser is modulated with a frequency equivalent to the lasers RO frequency. Using the high resolution APEX OSA as described in *Section 2.2.4*, the RO frequency of the FP laser in this PIC while biased at 50 mA is measured to be 3.6 GHz. To demonstrate the difference between combs generated at the lasers RO frequency in the case of primary-secondary coupling and mutual coupling, the RO frequency of the PIC while biased at 30 mA was also measured and found to be approximately 3.4 GHz. A single longitudinal mode was achieved from the PIC by biasing the gain, mirror and FP sections at 90, 24 and 30 mA respectively for primary-secondary coupling, and 48, 38 and 50 mA respectively for mutual coupling. The FP section was gain switched using a modulation frequency of 3.4 GHz for the primary-secondary coupling case, and 3.6 GHz for the mutual coupling case. The resulting combs are plotted on an x-axis scale of 2.5 nm in *Figure* 5.31 where the red comb represents that attained through primary-secondary coupling where the FP laser is gain switched at a modulation frequency of 3.4 GHz, and the blue comb represents that attained through mutual coupling where the FP laser is gain switched at a modulation frequency of 3.6 GHz.

Gain switching the FP laser of a primary-secondary coupled system results in a generated comb with a power of -38 dBm and 7 comb lines within 10 dB of each other. These 7 comb lines are generated across a bandwidth of Δf_{10} = 20.4 GHz. In contrast, gain switching the FP laser of the mutually coupled system results in a comb with a power of -18 dBm and 25 comb lines within 10 dB of each other. These 25 comb lines are generated across a bandwidth of Δf_{10} = 86.4 GHz, resulting in a much broader comb.

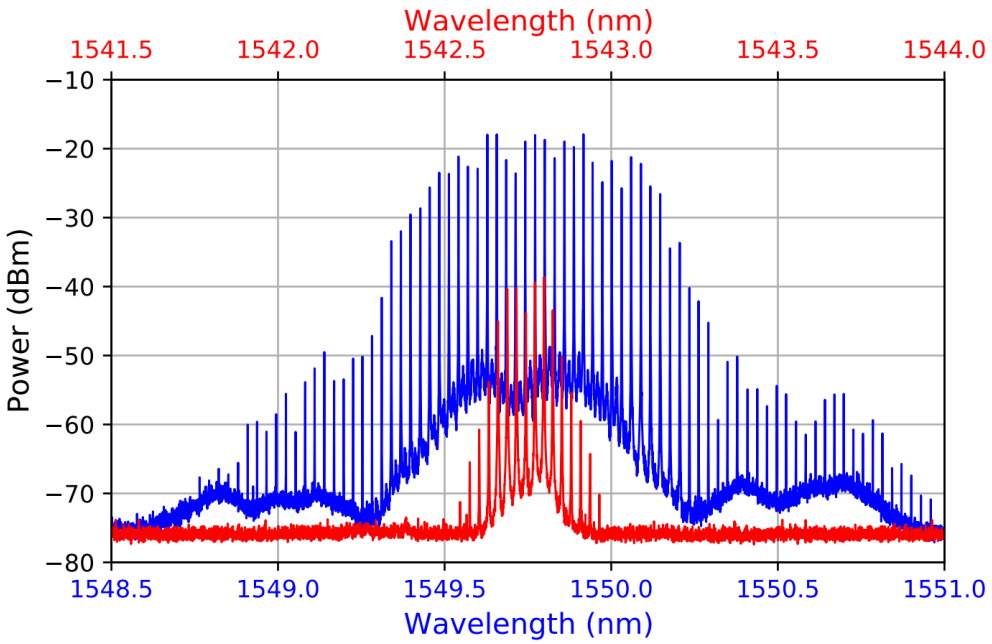


Figure 5.31: (Red) Comb attained through primary-secondary coupling with a modulation frequency equivalent to the FP laser's RO frequency. (Blue) Comb attained through mutual coupling with a modulation frequency equivalent to the FP laser's RO frequency.

5.5 Chapter Conclusion

This chapter introduces the different coupling techniques used to generate combs in this thesis. Beginning with traditional primary-secondary configurations, injection locking is used and the secondary laser is optically phase locked to the primary laser. Gain switching the secondary laser results in frequency combs being generated across a frequency range of 3.8 - 8 GHz with optimum combs generated at a frequency equivalent to the secondary laser's RO frequency. Gain switching the secondary laser at a frequency equivalent to the primary laser's RO frequency resulted in a broad lasing mode with no comb lines.

Combs generated through stable bidirectional coupling were also demonstrated in this chapter. Even though bidirectional coupling is a notoriously unstable configuration, the combs detected through this coupling were not only stable, but also benefited from the configuration. This is because the bidirectional coupled comb propagated through the heavily biased primary laser and was amplified as a result.

The final form of coupling introduced in this chapter is through mutual coupling which took the PIC outside the traditional asymmetrically biased,

primary-secondary configuration. This new form of on-chip coupling not only demonstrated stable phase locking with improved power and SMSR, but also enhanced the gain switched comb to be detectable across a wider spectral range. A comparison is carried out between gain switching the FP section of the primary-secondary PIC and the mutually coupled PIC at the FP laser's corresponding RO frequency. The result in both cases is the optimum comb for that coupled configuration. This features 7 comb lines across a bandwidth of 20.4 GHz that measure within 10 dB of each other for the primary-secondary configuration, and 25 comb lines across a bandwidth of 86.4 GHz that measure within 10 dB of each other for the mutually coupled configuration. A power difference between the different coupling methods is also observed with the primary-secondary coupled comb achieving a power of -38 dBm and the mutually coupled comb achieving a power of -18 dBm.

Chapter 6

Comb Frequency Response Through Asymmetric and Non-Asymmetric Gain Switching Techniques.

6.1 Chapter Overview

Chapter 5 demonstrated the enhancement of combs through the frequency response of primary-secondary gain switching and through gain switching mutually coupled lasers. This chapter focuses on a more in-depth analysis of gain switched combs formed from a mutually coupled system, in particular in relation to the frequency response of the combs. Starting with a general primary-secondary configuration the frequency response of the combs are compared to those attained from the mutually coupled configurations, demonstrating the conditions necessary to achieve a spectral bulge and the excitation of additional comb lines.

6.2 Device Design

Like previous examples, the device used in this chapter is a three section, two laser integrated circuit. One laser is designed to generate single mode spectra (single mode (SM) laser) and another laser is designed as a Fabry–Pérot (FP). The SM laser is made up of a gain and mirror section, where the gain section is 600 μm in length and the mirror section is made up of 7 slots with an inter-slot separation of 87 μm. An isolation etch separates the two sections to

allow for electrical isolation whereby both sections can be biased independently. The cavity of the laser is confined by a metal etched facet and an etched facet. The etched facet is used to integrate the SM laser with a FP 420 μm in length where the cavity of the FP laser is confined by the etched facet and a cleaved facet. Each section is fabricated with a metal contact pad to allow for biasing and the FP section is fabricated with a ground signal (GS) contact pad to allow for gain switching. The ground pad makes contact with the n-type substrate via the deep etch.

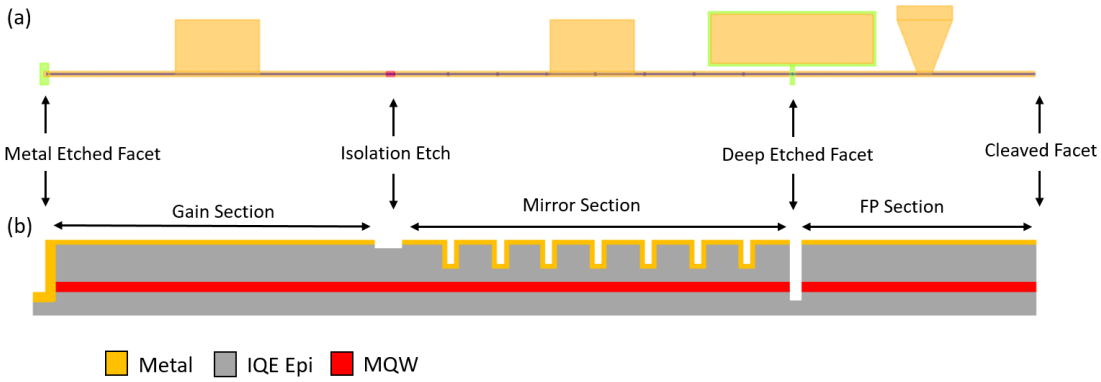


Figure 6.1: (a) Top view and (b) side view of the PIC schematic.

6.3 DC Characterisation

The LIV characteristics of the lasers in this PIC were measured via the cleaved facet using fiber coupling. The FP was biased and current was swept from 0 - 150 mA as shown in *Figure* 6.2. The gain section of the SM laser was swept from 0 - 150 mA for bias currents through the mirror section of 20, 100 and 180 mA, the FP was biased at 10 mA to allow the section to be passive but not lase. These results are plotted in *Figure* 6.2.

From the plot above, the FP laser has a threshold current of 26 mA. The threshold current of the SM laser decreases and the lasing power increases for increasing currents through the mirror section.

To demonstrate how the spectra of the FP laser changes with the bias current, the spectra of the FP is measured using an ANDO AQ6317B OSA at increments of 1 mA from 20 mA - 150 mA. *Figure* 6.3 illustrates the power in dBm of the laser at each wavelength for this current range.

Figure 6.3 illustrates the lasing modes of the FP laser and how they are effected by the bias current. The modes start to lase at the threshold current of

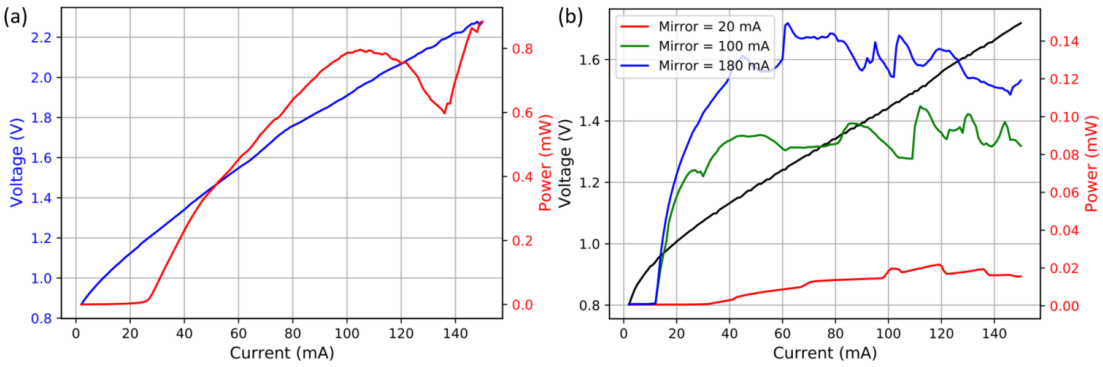


Figure 6.2: LIV curves of (a) FP laser and (b) SM laser as the current is swept across the gain section for different bias currents through the mirror section.

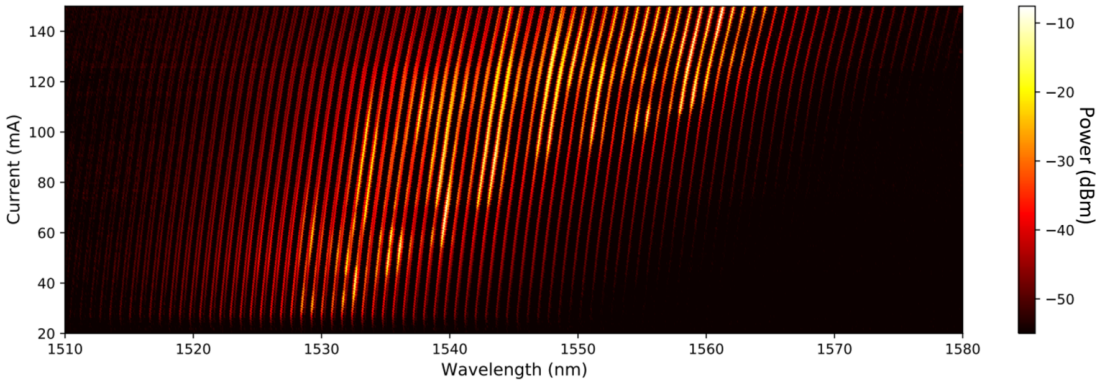


Figure 6.3: Spectra measured from the FP laser as current is swept from 20 - 150 mA.

the laser at 26 mA, and the increasing current allows the modes to shift along the wavelength domain as the optical path length of the device is increased and the gain shifts due to the increasing temperature.

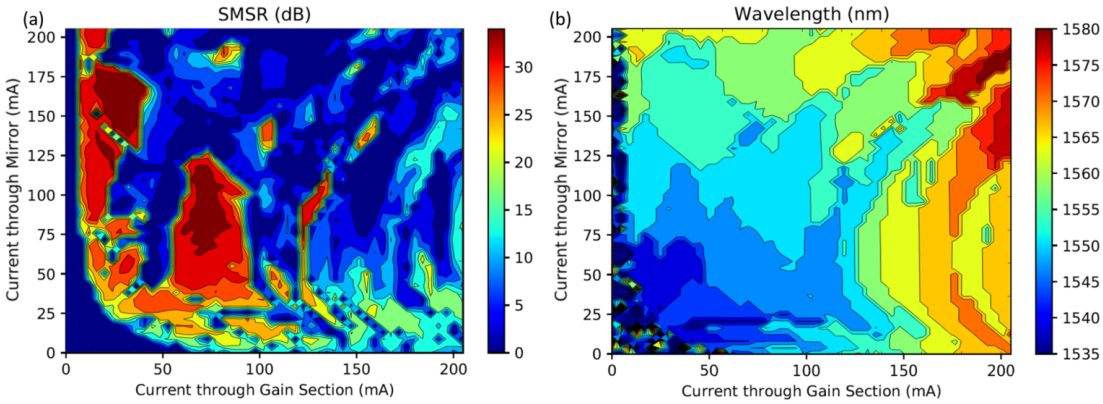


Figure 6.4: (a) SMSR and (b) lasing wavelength measured from the SM laser as current is swept from 0 - 200 mA across both the gain and mirror sections.

The SMSR and lasing wavelength of the SM laser was determined by biasing and sweeping current from 0 - 200 mA across both sections at intervals of 2

mA. At each interval the optical spectrum was recorded from the cleaved facet using an optical fiber coupled to an ANDO AQ6317B OSA. The SMSR and peak lasing wavelength were recorded and plotted in *figure* 6.4.

Figure 6.4 depicts the bias currents across the gain and mirror sections at which the SM laser generates a single mode spectra (SMSR >30 dB). The SM laser generates four single mode wavelengths between 1550 - 1565 at a wavelength spacing of 4 nm which is consistent with the design of the laser. These lasing wavelengths can more easily be demonstrated by plotting the SMSR of each spectra at each lasing wavelength of that spectra as demonstrated in *Figure* 6.5.

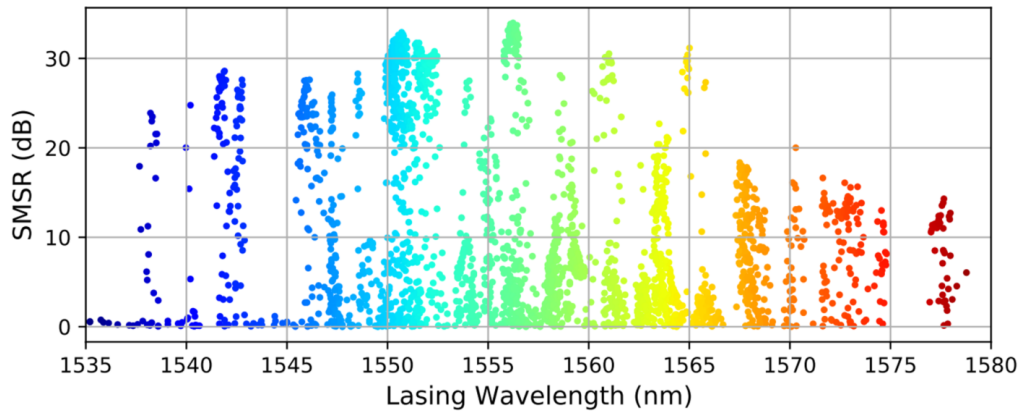


Figure 6.5: The SMSR achieved at each lasing wavelength of the SM laser.

This figure illustrates single mode spectra attained at approximate wavelengths of 1552, 1556, 1561 and 1565 nm.

6.4 Primary-Secondary Coupling

As mentioned in previous chapters, traditional methods of coupling two on-chip lasers requires operating the PIC in an asymmetric biasing regime, whereby one laser is more heavily biased than the other [26] and [27]. In terms of this PIC, the SM laser is more heavily biased than the FP, thereby generating a primary-secondary configuration where the FP secondary laser is optically phase locked to the SM primary laser. Despite the lack of on-chip isolation, mutual phase locking was achieved, improving several characteristics of the lasers and in particular, increasing the SMSR [19]. The effects of this form of coupling on the resulting spectra of the chip can be analysed by biasing the secondary FP laser at 26 mA (threshold current) and

sweeping the current across the two sections of the SM primary laser, measuring the spectra at each interval.

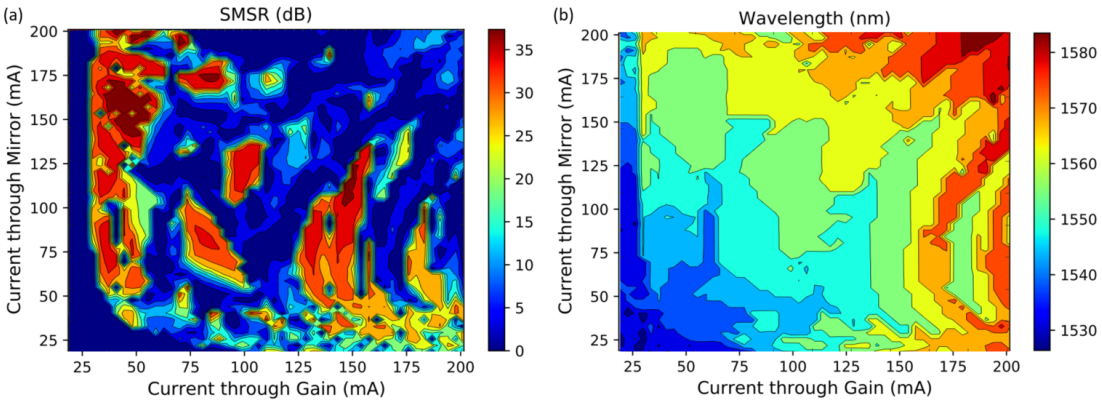


Figure 6.6: (a) SMSR and (b) lasing wavelength measured from the PIC as current is swept from 0 - 200 mA across both the gain and mirror sections, while the FP is biased at 26 mA.

The SMSR and lasing wavelength of this asymmetrically biased PIC was determined by biasing and sweeping current from 0 -200 mA across both sections of the SM primary laser at intervals of 2 mA. At each interval the optical spectrum was recorded from the cleaved facet using an optical fiber coupled to an ANDO AQ6317B OSA. The SMSR and peak lasing wavelength were recorded and plotted in *figure* 6.6. What is immediately evident in comparing the primary-secondary results in *Figure* 6.6 to the SM results in *Figure* 6.4 is that an overall higher SMSR of 37 dB was measured from the primary-secondary PIC as oppose to the SMSR of 33 dB measured from the SM laser. Additional regions of high SMSR was also measured from the primary-secondary PIC signifying additional single mode wavelengths being generated. This could be viewed more clearly by plotting the SMSR against the lasing wavelengths determined in *Figure* 6.6. This is demonstrated in *Figure* 6.7.

This time, the primary-secondary PIC achieves single mode spectra across a wavelength range of 1540 - 1565 nm as additional wavelengths achieve an SMSR $>$ 30 dB. This is as a result of this on-chip primary-secondary coupling in comparison to the wavelength range of 1550 - 1565 nm achieved by the solitary primary laser in *Section 3*. The single mode wavelengths that could be achieved before this coupling achieves a higher SMSR of 37 dB here compared to the previous 33 dB in *Figure* 6.5.

Figure 6.8 illustrates how the spectra of this primary-secondary PIC changes as

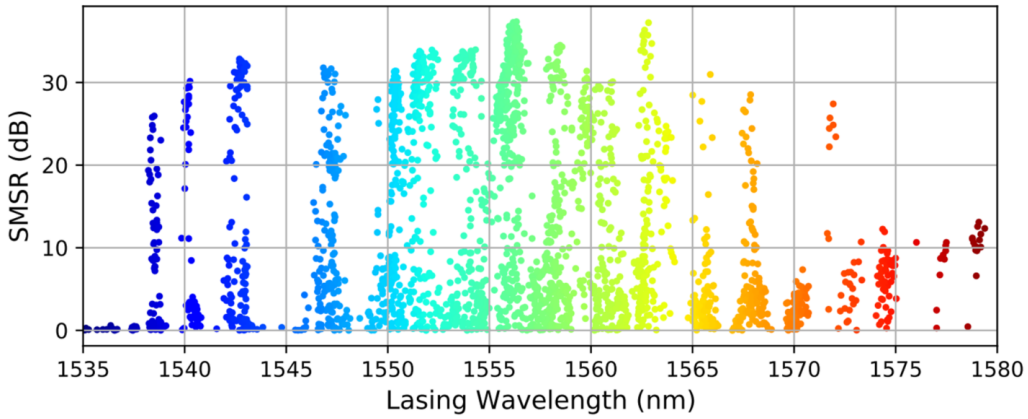


Figure 6.7: The SMSR achieved at each lasing wavelength of the primary-secondary PIC.

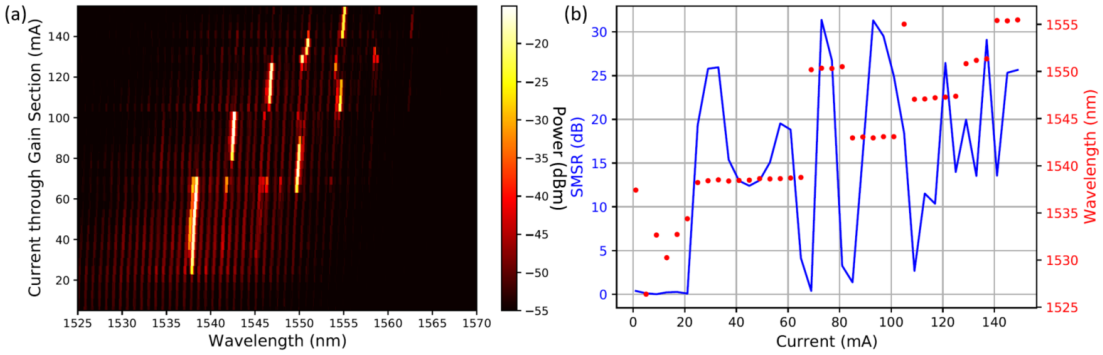


Figure 6.8: (a) A colour plot depicting the spectra of the device as current was swept through the gain section for bias currents of 35 and 26 mA through the mirror and FP sections respectively. (b) The equivalent SMSR and lasing wavelength.

the current across the gain section is swept from 1 - 150 mA for constant bias currents of 35 and 26 mA across the mirror and FP sections respectively. The corresponding SMSR and lasing wavelength is also plotted. This demonstrates the changes in the emission modes of the asymmetrically coupled PIC as the current through the gain section is adjusted. This is related to the changing mode simulations in *Chapter 2.2.2* where the lasing modes shift due to the increasing optical path length, which is what occurs during increasing current injection [33].

6.4.1 Comb Generation

A single mode spectrum was selected from this asymmetrically biased PIC by biasing the gain, mirror and FP sections at 92, 35 and 26 mA respectively. The FP section was biased using the a GS probe and undergoes gain switching to

generate combs. Stable phase locked combs were achieved for gain switched currents swept from 4.5 - 10.5 GHz at intervals of 0.05 GHz. A colour plot depicting how these combs change with gain switched frequency is depicted in *Figure* 6.9.

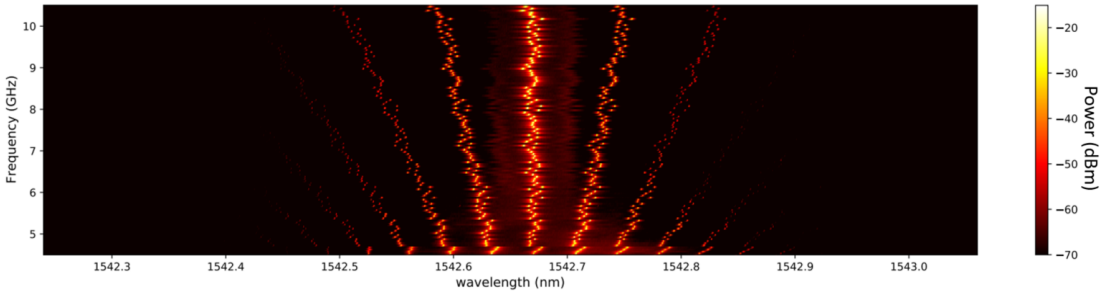


Figure 6.9: Colour plot depicting the generated combs as the gain switched frequency was swept from 4.5-10.5 GHz, while the PIC operates in an asymmetric bias regime.

These combs generate multiple comb lines with a frequency spacing equivalent to that of the gain switched current, and degrade in quality at higher frequencies as observed in *Chapters 2* and *5*. This degrade in quality is also illustrated in *Figure* 6.12.

As mentioned in previous chapters, the relaxation oscillation (RO) frequency of the laser could be measured using the high resolution OSA. Analysis of the spectra from the SM laser is measured while the gain and mirror sections are biased at 92 and 35 mA respectively. Again, the FP section was biased at 10 mA to make the section passive but not lase, and the resulting spectrum is plotted in *Figure* 6.10.

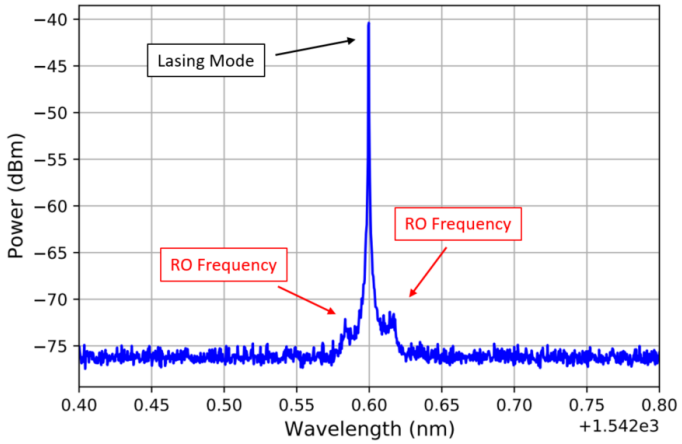


Figure 6.10: Plot of the lasing mode of the SM laser demonstrating the side peaks caused by the lasers RO frequency.

This image demonstrate the lasing mode of the laser as well as the side bands generated by the lasers RO frequency. Measuring the frequency separation between these sidebands and the SM laser, the RO frequency of the SM laser is measured to be approximately 2.5 GHz.

Chapter 5 demonstrated the effects of gain switching the secondary laser in a primary-secondary configuration at a frequency equivalent to the RO of the primary. The result was a spectral bulge where, instead of clear comb lines, a broad spectral bulge was measured.

This is demonstrated here in this example be gain switching the secondary FP laser at 2.5 GHz (*Figure* 6.11).

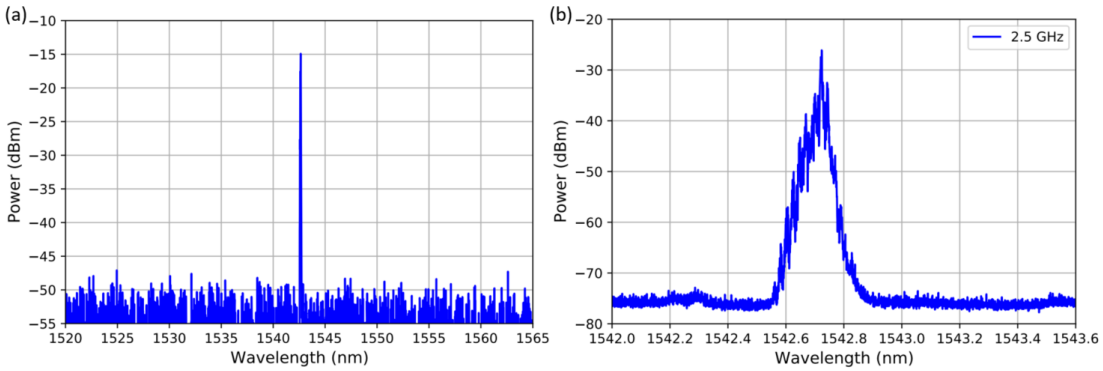


Figure 6.11: (a) Plot of the full spectra of the PIC while gain switched at 2.5 GHz using the low resolution ANDO OSA. (b) close up of the lasing spectra of the PIC while gain switched at 2.5 GHz using the high resolution APEX OSA.

The combs achieved from this configuration while gain switched at approximately 2×RO, 3×RO and 4×RO frequency are plotted in *Figure* 6.12. In each of these cases combs are generated with the generated combs reducing in quality as the gain switched frequency is increased. The measured Δf_{10} decreases from 15.15 GHz at a modulation frequency of 2×RO, to 7.35 GHz at 3×RO and 0 GHz at 4×RO.

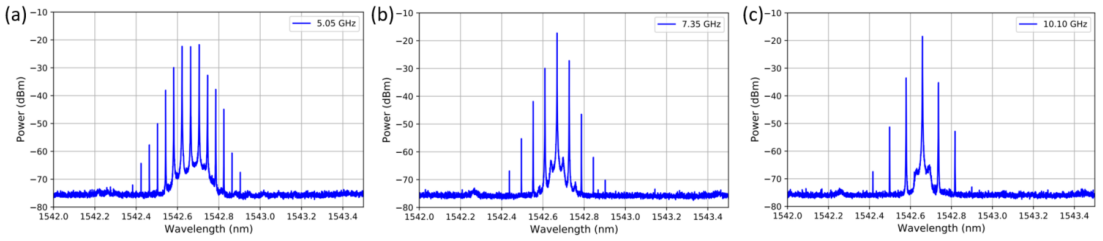


Figure 6.12: Combs generated through the asymmetric bias method at approximately (a) 2×RO Frequency, (b) 3×RO Frequency and (c) 4×RO Frequency of the SM laser.

6.4.2 ESA Analysis

The individual spectra that was generated at each frequency in *Figure* 6.9 was also analysed using an Electrical Spectrum Analyser (ESA). A colour plot depicting the ESA analysis is demonstrated in *Figure* 6.13.

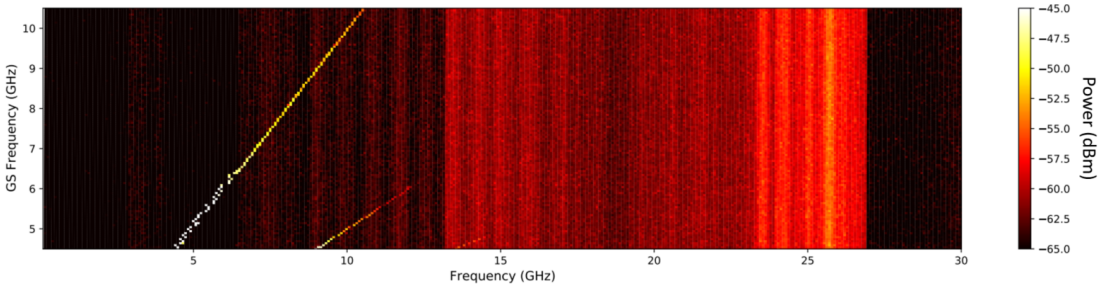


Figure 6.13: Colour plot depicting the measured ESA from the generated combs as the gain switched frequency was swept from 4.5-10.5 GHz.

Here the electrical spectrum is plotted against frequency (GHz) for different values of the gain switched frequency. As expected, with a gain switched value of 5 GHz, the ESA detects narrow peaks at 5 and 10 GHz, indicating a degree of coherence corresponding to the beat notes between comb lines.

The electrical spectra equivalent to the optical spectra plotted in *Figure* 6.12 are plotted below.

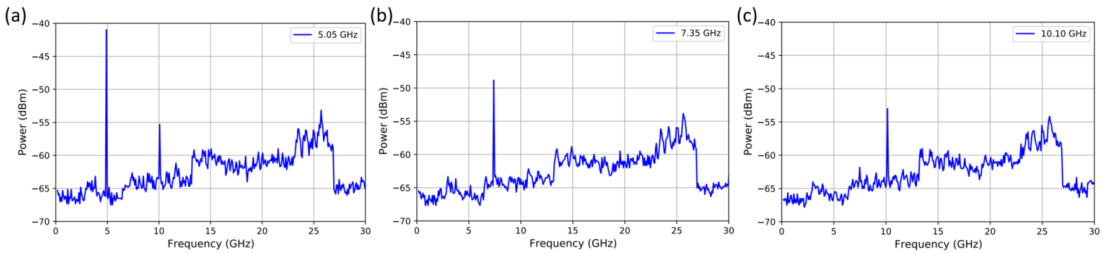


Figure 6.14: Electrical spectra corresponding to the generated combs gain switched at approximately (a) 2×RO Frequency, (b) 3×RO Frequency and (c) 4×RO Frequency of the SM laser.

From these plots, there is an evident decrease in the power of the detected peaks in the electrical spectra as the gain switched frequency is increased. This corresponds to the quality of the spectra measured through the high resolution OSA in *Figure* 6.12. *Chapter 2.3* demonstrates theoretically and *Chapter 5.2* demonstrates experimentally that the quality of the comb is optimum when the device is gain switched close to the RO Frequency of the secondary laser and decreases at frequencies further away from this RO Frequency. These ESA spectra were measured for gain switched frequencies of 5.05, 7.35 and 10.10

GHz and therefore degrade as the gain switched frequency is adjusted away from the lasers RO Frequency which is approximately 3.4 GHz.

6.5 Mutual Coupling

The concept of operating the PIC outside the asymmetric bias regime was demonstrated in *Chapter 5* and an enhanced gain switched comb was demonstrated by biasing the FP section at 50 mA. The Wavelengths achieved from the PIC while the FP section is biased at 50 mA could be determined by again sweeping current across the two sections of the SM laser and measuring the resulting SMSR and lasing wavelength.

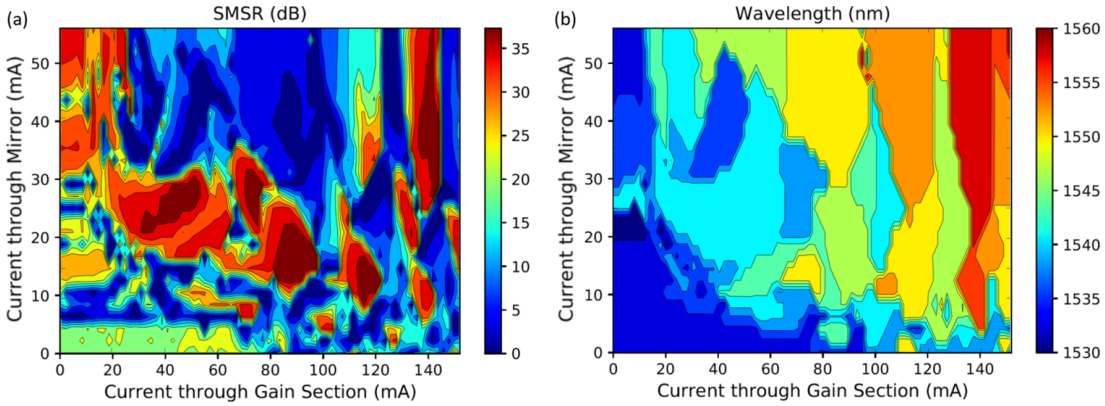


Figure 6.15: (a) SMSR and (b) lasing wavelength measured from the PIC as current is swept from 0 - 150 mA across the gain section and 0 - 55 mA across the mirror sections, while the FP is biased at 50 mA.

Once again, multiple single mode regions are attained, demonstrating that on-chip coupling could be achieved through non-asymmetric bias methods. The SMSR achieved at each lasing wavelength is plotted in *Figure* 6.16.

This data was attained through shorter spans of current being swept through the gain and mirror sections in comparison to the current sweeps carried out for the solitary primary laser in *Figure* 6.4 and the primary-secondary coupled system in *Figure* 6.6. However, single mode spectra are still achieved across a wavelength range of 1534 - 1559 nm while the FP section is biased at 50 mA.

6.5.1 Comb Generation: Example One

A single mode wavelength was selected by biasing the gain, mirror and FP sections at 110, 25 and 50 mA respectively. The FP laser was biased using a GS probe and was gain switched to generate a comb (*Figure* 6.17).

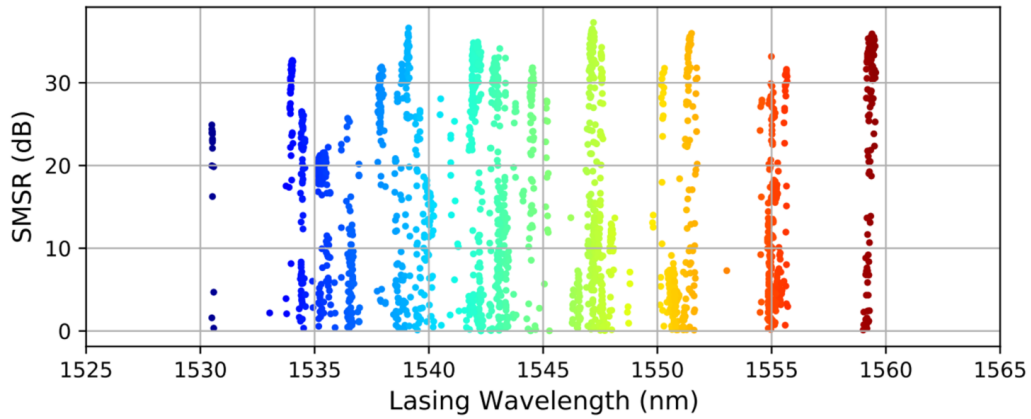


Figure 6.16: The SMSR achieved at each lasing wavelength of the mutually coupled PIC.

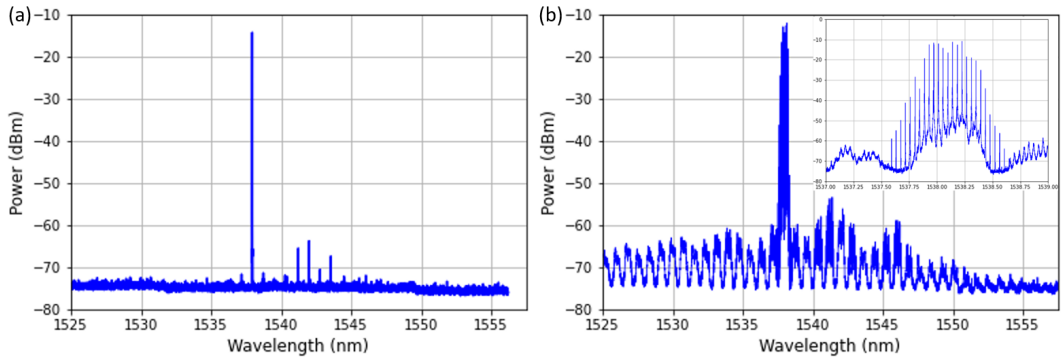


Figure 6.17: Spectra of the coupled system (a) before and (b) after the FP laser is gain switched at 5 GHz.

The system at this biasing was able to maintain stable phase locking at this wavelength for gain switched frequencies ranging from 5 - 7.5 GHz. The optical spectra of the combs generated for this frequency range is plotted in *Figure* 6.18.

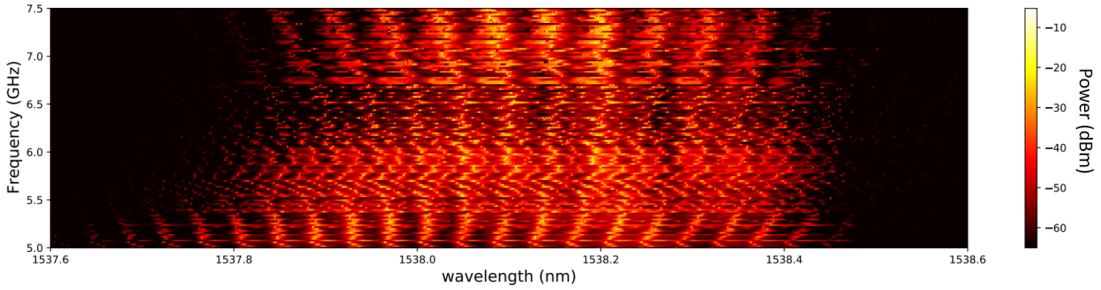


Figure 6.18: Combs measured through the high resolution APEX OSA as the gain switched frequency is swept from 5 - 7.5 GHz.

The frequency was swept at intervals of 0.02 GHz and mostly generated combs with a frequency spacing consistent with the frequency of the gain switched

current. However, across a specific frequency range, additional comb lines were generated at half the frequency of the gain switched current. Examples of this are shown in *Figure* 6.19. These periods of additional comb lines occurred from 5.4 - 6.2 GHz and then again from 6.7 - 7.3 GHz. These regions are consistent with twice the frequency of the RO frequency of the SM and FP laser, which were measured to be 2.8 and 3.6 GHz respectively using the APEX OSA at the specified bias currents.

Figure 6.19 demonstrates examples of these generated combs and how they change when they are gain switched at twice the RO frequency of the integrated lasers.

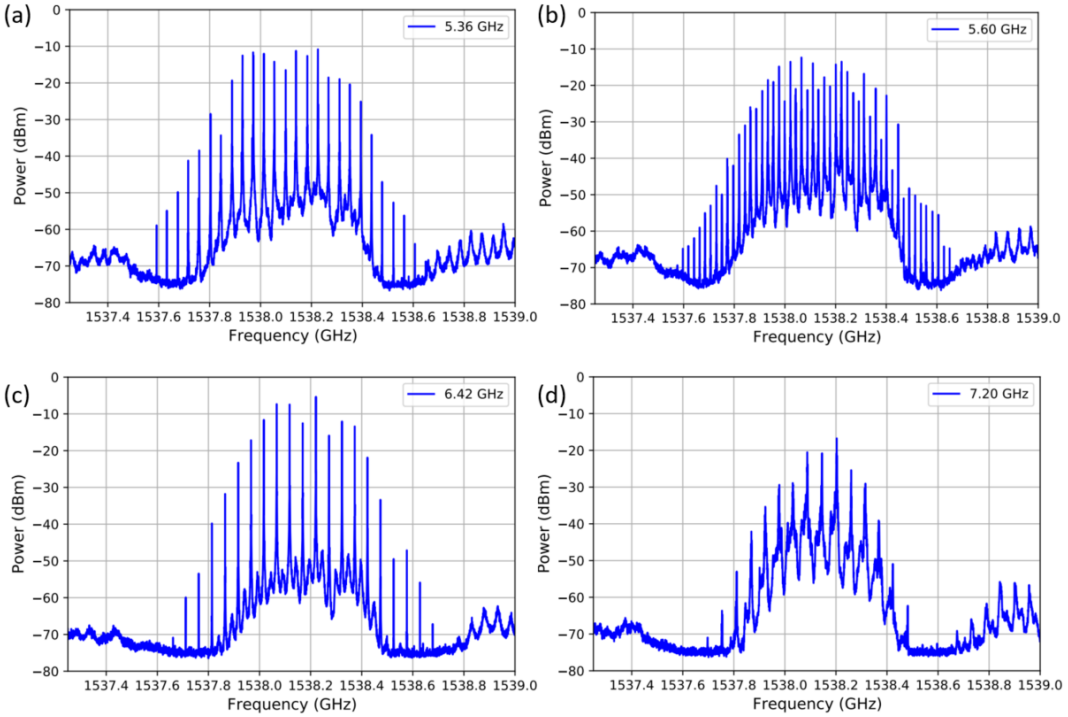


Figure 6.19: Combs generated at (a) 5.36 GHz, (b) 5.60 GHz, (c) 6.42 GHz and (d) 7.20 GHz.

The generated combs demonstrates the excitation of additional comb lines when sweeping the gain switched frequency while operating this PIC in a mutually coupled system. This suggests that gain switching the heavily biased FP laser in this mutually coupled system at twice the RO frequency of either the SM or FP laser, would result in additional comb lines being excited consistent with the RO frequency of that laser.

This phenomena has been demonstrated in [55], where an external comb laser was injected into an on-chip FP laser and additional comb lines were

generated corresponding to the RO frequency of the FP. The monolithically integrated device used here, not only allows this generation of extra comb lines corresponding to the RO frequency of the FP, but also the RO frequency of the SM laser. This is in part due to the strong, coherent bidirectional coupling between the two integrated lasers that was demonstrated in *Chapter 5*. Therefore, the comb propagates through both the laser cavities, each with it's own independent RO frequency, and therefore this extra comb line generation occurs for both lasers.

The individual spectra that was generated at each frequency was also analysed using the ESA. A colour plot depicting the ESA analysis is demonstrated in *Figure* 6.20. Here the electrical spectrum is plotted against Frequency (GHz) for different values of the gain Switched frequency. As expected, with a gain switched value of 5 GHz, the ESA detects narrow peaks at 5, 10, 15, 20 and 25 GHz, indicating a high degree of coherence corresponding to the beat notes between comb lines.

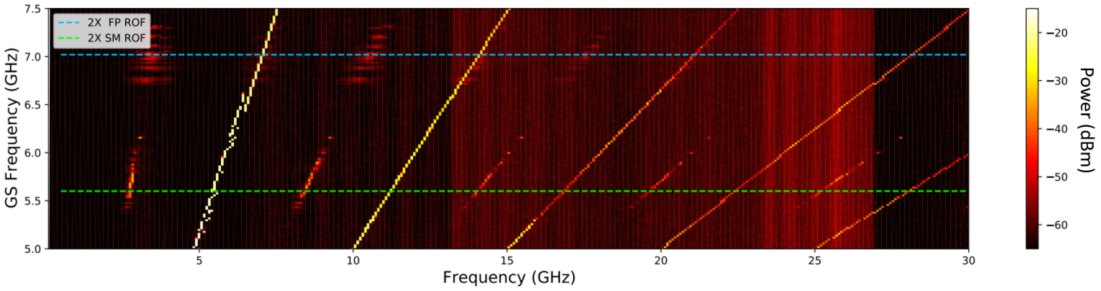


Figure 6.20: Colour plot demonstrating the ESA analysis of the PIC. The plot also measures extra narrow peaks at regions corresponding to the RO frequency of the single mode and Fabry-Pérot lasers.

Additional peaks are also measured at 5.4 - 6.2 GHz and then again from 6.7 - 7.3 GHz, which is consistent with twice the RO frequency of the SM and FP lasers respectively. As described in [55], these excited comb lines undergo a period of locking in a range around the RO frequency of the laser, which we demonstrate here at 5.4 - 6.2 GHz and again at 6.7 - 7.3 GHz.

The electrical spectra corresponding with the optical spectra in *Figure* 6.19 are plotted in 6.21.

6.5.2 Comb Generation: Example Two

The previous section demonstrates that while generating combs in a mutually coupled system, additional comb lines are generated with a frequency spacing

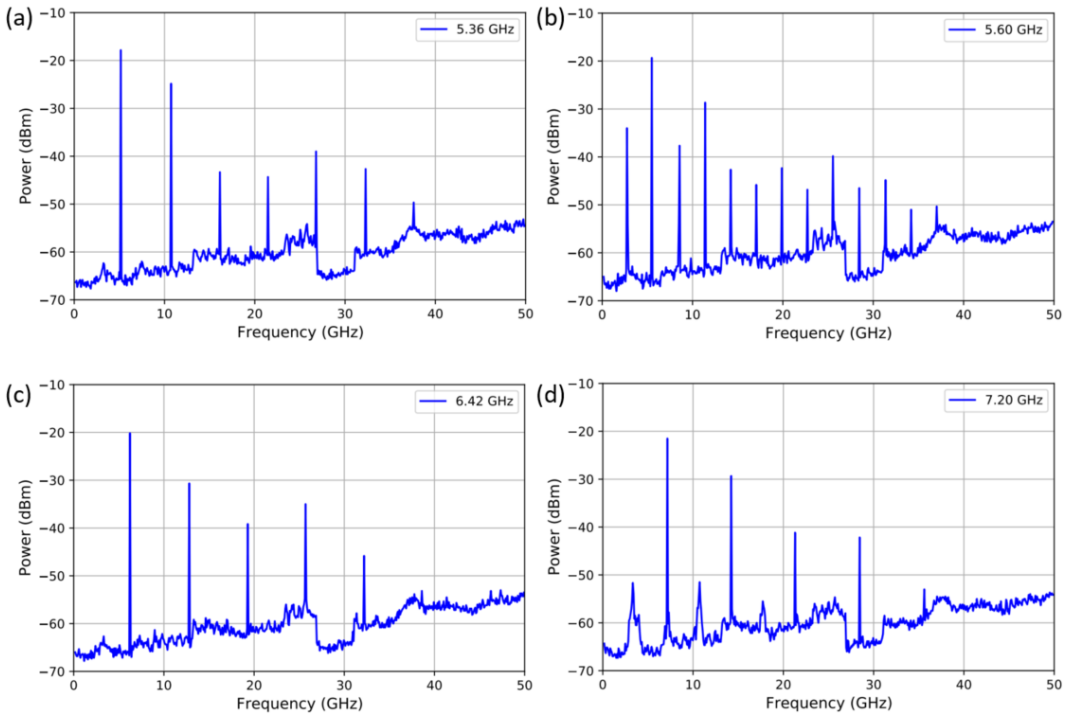


Figure 6.21: Electrical spectra of combs generated at (a) 5.36 GHz, (b) 5.60 GHz, (c) 6.42 GHz and (d) 7.20 GHz.

equivalent to the SM or FP's RO frequency when the FP is gain switched at a frequency that is twice the RO frequency of the SM of FP. The issue with the previous example is the short gain switched frequency range at which the PIC achieved stable phase locking. As a result, the effects of gain switching the FP at 3×RO or 4×RO frequency are unknown. In the off-chip example [55], where an external comb laser was injected into an on-chip FP, extra comb lines with a frequency separation equivalent to the lasers RO frequency, were not only excited when the gain switched frequency was double that of the lasers RO frequency, but also when the gain switched frequency was an integer multiple of the RO frequency. It stands to reason, that in a monolithically integrated system with a stable RO frequency, varying the gain switched frequency to integer multiples of the RO frequency would result in additional comb lines being excited with a frequency spacing equivalent to the laser's RO frequency. This is demonstrated in this section.

Stable phase locking of the mutually coupled system for a larger range of frequencies was achieved by biasing the gain, mirror and FP sections at 92, 35 and 47 mA respectively. The biasing currents of the SM laser is comparable to the primary-secondary example in *Section* 6.4.1, and so the RO frequency of the SM laser is approximately 2.5 GHz and the RO frequency of the FP is

approximately 3.4 GHz. The single mode spectra achieved by this mutually coupled system is plotted in *Figure* 6.22.

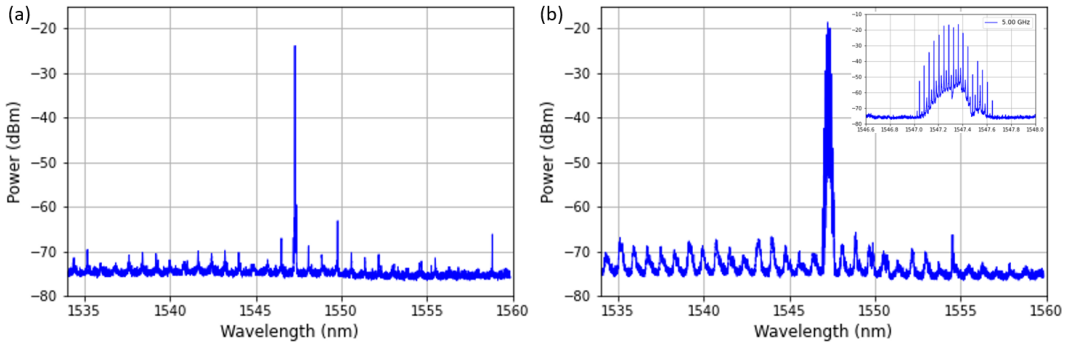


Figure 6.22: Spectra of the coupled system (a) before and (b) after the FP laser is gain switched at 5 GHz.

Once a comb was generated, the frequency of the gain switched current was swept from 5 - 11 GHz and the resulting combs were measured using a high resolution APEX OSA. The frequency was swept at intervals of 0.05 GHz and the results are plotted in *Figure* 6.23. Again combs are generated with a frequency spacing equivalent to the frequency of the gain switched current, however across specific frequency periods additional comb lines are also generated.

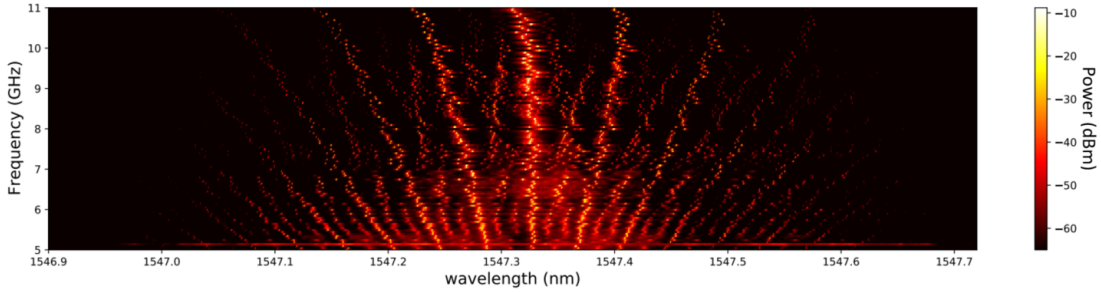


Figure 6.23: Combs measured as the gain switched frequency is swept from 5 - 11 GHz.

The excitation of extra comb lines and the number of excited comb lines depends on the frequency of the gain switched current. The RO frequency of the SM laser was measured to be 2.5 GHz and so *Figure* 6.24 shows the combs that were generated at 5.05, 7.35 and 10.10 GHz, approximately 2×RO, 3×RO and 4×RO frequency of the SM laser.

Each of these plots experiences the excitation of additional comb lines, all with a frequency separation equivalent to that of the RO frequency of the SM laser.

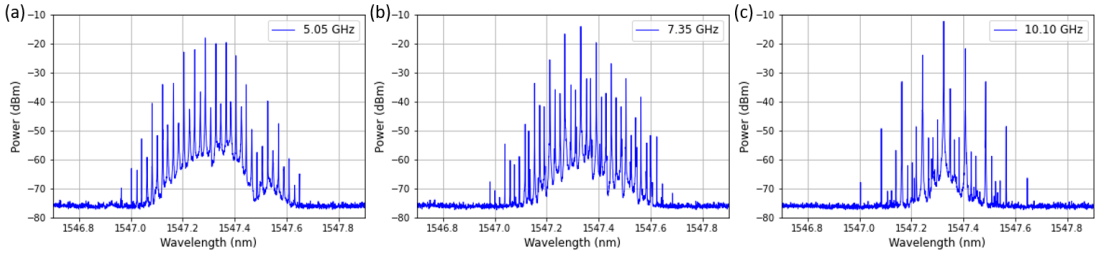


Figure 6.24: Combs generated through the non-asymmetric bias method at (a) 2×RO, (b) 3×RO and (c) 4×RO frequency of the SM laser.

These locking regions correspond to a harmonic locking to the frequency comb spacings at (a) $\frac{1}{2}$, (b) $\frac{1}{3}$, $\frac{2}{3}$, and (c) $\frac{1}{4}$, $\frac{1}{2}$, $\frac{3}{4}$ of the comb spacing.

This monolithically integrated device not only allows this generation of extra comb lines corresponding to the RO frequency of the SM laser, but also the RO frequency of the FP laser. Again, this is in part due to the strong, coherent bidirectional coupling between the two integrated lasers that was demonstrated in *Chapter 5*. Therefore, the comb propagates through both the laser cavities, each with it's own independent RO frequency, and therefore this extra comb line generation occurs for both lasers.

The RO frequency of the FP laser was measured to be approximately 3.4 GHz at 47 mA. The comb generated at 6.8 GHz is shown in *Figure* 6.25 and features a comb with a frequency spacing of 3.4 GHz, equivalent to the RO frequency of the FP laser.

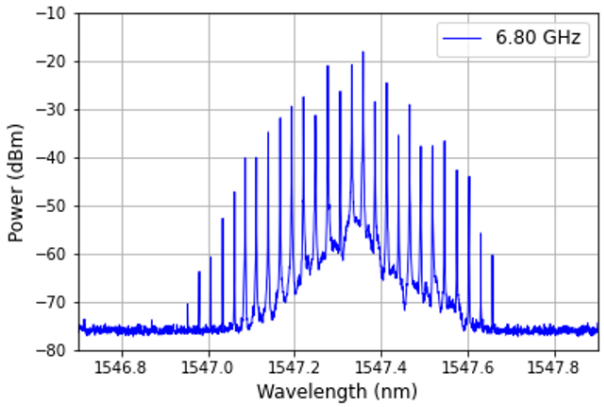


Figure 6.25: Comb generated through the non-asymmetric bias method at 2×ROF of the FP laser.

The individual spectra that was generated at each frequency was also analysed using an ESA. A colour plot depicting the ESA analysis is demonstrated in *Figure* 6.26.

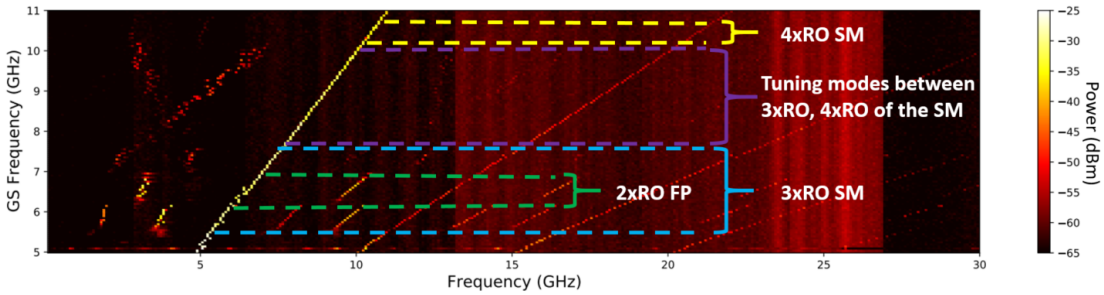


Figure 6.26: Colour plot demonstrating the ESA analysis of the PIC. The plot also measures extra narrow peaks at regions corresponding to the integer multiples of the RO frequency of the SM and FP lasers. Illustrations of the locking ranges are also included.

The additional peaks of the SM laser demonstrated a more elaborate locking pattern. From 5 - 5.1 GHz the end of the combs locking range for 2×RO frequency was detected by the excitation of an additional peak. The next locking range of 3×RO of the SM laser was detected from 5.65 - 7.45 GHz, here two extra peaks were excited but were extinguished when they conflicted with the 2×RO frequency of the FP laser. As the gain switched frequency is increased further, the two additional peaks excited by 3×RO frequency of the SM laser were present again, but decrease in power as they are forced out of this locking range. These two peaks drift until they reach a frequency $\frac{1}{4}$ and $\frac{3}{4}$ of the gain switched frequency where an additional peak is excited at $\frac{1}{2}$ the gain switched frequency. This occurs at a gain switched frequency of 10.10 GHz, equivalent to 4×RO frequency of the SM laser.

The equivalent electrical spectra to the optical spectra in *Figure* 6.24 are plotted in *Figure* 6.27. In each of these figures, the dominant peak is measured at a frequency equivalent to the gain switched frequency. However, the additional peaks are viewed in each at a frequency equivalent to the integer multiple of the RO frequency of the SM laser and are so located at (a) 2.525 GHz, (b) 2.45, 4.9 GHz and (c) 2.525, 5.05, 7.575 GHz.

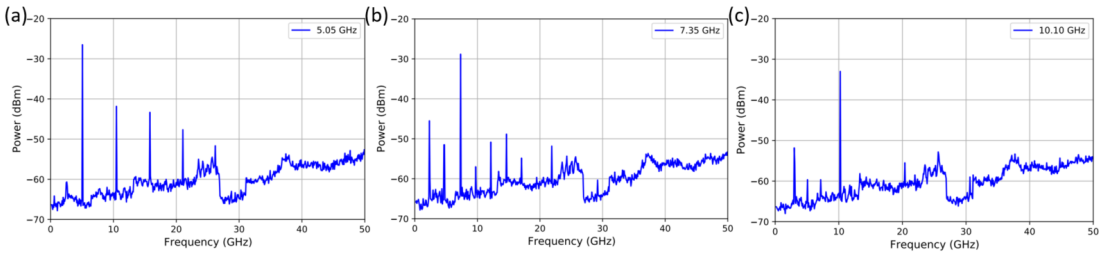


Figure 6.27: Electrical spectra of combs generated through the non-asymmetric bias method at (a) 2×RO, (b) 3×RO and (c) 4×RO frequency of the SM laser.

6.5.2.1 Induction of a Spectral Bulge

Both lasers in this configuration had their own independent RO frequency which was measured to be approximately 2.5 GHz for the SM laser and 3.4 GHz for the FP laser. However operating the PIC in this mutually coupled system and analysing the single mode spectra, this mutually coupled system appears to operate with its own independent RO frequency. A plot of the single mode peak is plotted in *Figure* 6.28.

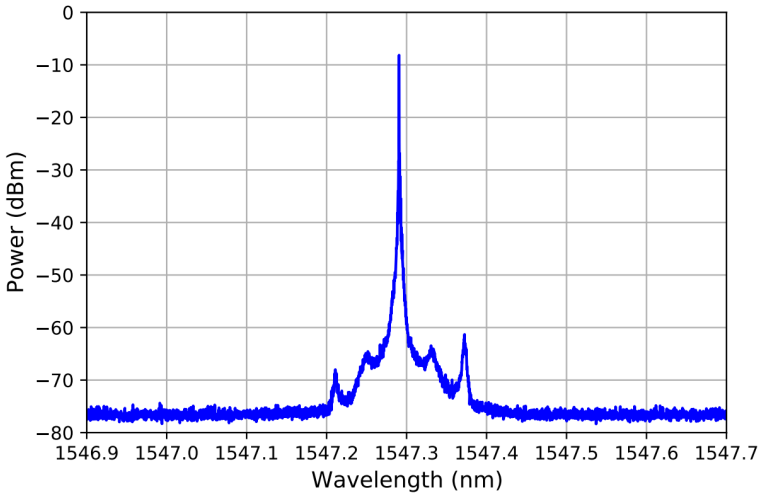


Figure 6.28: High resolution spectra of the mutually coupled system showing the side peaks caused by the PICs RO frequency.

Figure 6.28 illustrates the single mode wavelength achieved from the mutually coupled system while the gain, mirror and FP sections were biased at 92, 35 and 47 mA respectively. Two side bands are generated at both sides of the lasing mode with a frequency separation from the lasing mode of 5.15 and 10.30 GHz. Because these new sidebands are unique compared to both the RO sidebands of the SM and FP lasers, it is assumed that these side bands represents the RO and double RO frequency of the entire mutually coupled system. Both frequency values of these newly generated sidebands fall withing the gain switched frequency range analysed optically in *Figure* 6.23 and electrically in *Figure* 6.26. The high resolution optical spectra of the PIC gain switched at these frequencies are plotted in *Figure* 6.29.

No comb lines are generated when the mutually coupled system is biased at 5.15 GHz, but instead a broad spectra is generated where the comb should be. This is consistent with the spectral bulging demonstrated when the secondary FP laser is gain switched at the RO frequency of the SM primary laser in a primary-secondary configuration. Furthermore, gain switching the FP at twice

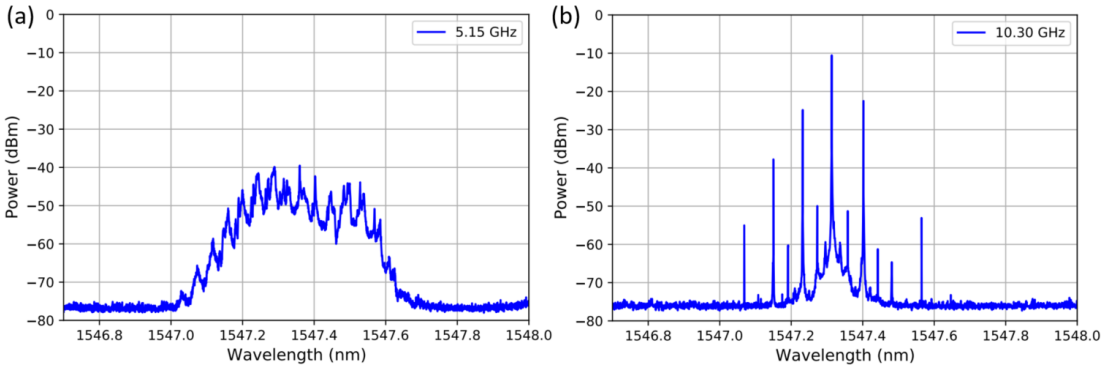


Figure 6.29: The gain switched optical spectra of the mutually coupled system when gain switched at the apparent RO and double RO frequency of the coupled system.

this frequency results in additional excited comb lines at $\frac{1}{2}$ the comb spacing, which is consistent with gain switching the FP at twice the RO frequency of a laser in a mutually coupled configuration. Therefore it is logical to assume that the full PIC of this mutually coupled system operates under its own separate RO frequency, whereby the asymmetric case doesn't. Therefore, gain switching the mutually coupled PIC is effected by the RO frequency of the coupled system, as well as the independent RO frequencies of the lasers in the PIC.

The corresponding electrical spectra of the optical combs measured in *Figure* 6.29 are plotted in *Figure* 6.30.

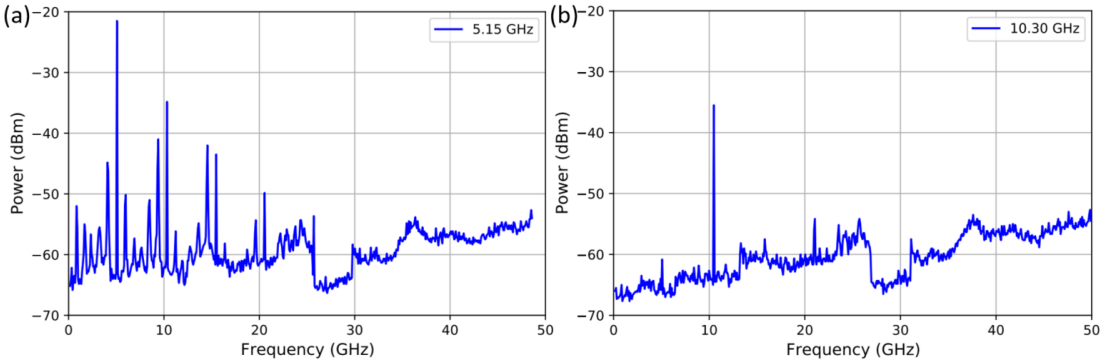


Figure 6.30: The gain switched electrical spectra of the mutually coupled system when gain switched at the apparent RO and double RO frequency of the coupled system.

The electrical spectrum of the spectral bulging generated at 5.15 GHz demonstrates a strong peak consistent with multiples of this frequency representing the beat notes between these comb lines, however additional peaks are also present between these beat notes. Unlike the additional one, two or three peaks that are generated when gain switching this mutually

coupled system at integer multiples of the lasers RO, this electrical spectrum illustrates the excitation of five additional peaks occurring at multiples of 850 MHz. The reason for this value is currently unknown. The electrical spectra of gain switching the mutually coupled system at double this frequency results in an additional peak being excited at $\frac{1}{2}$ the gain switched frequency, which is consistent with gain switching comb in *Figure* 6.29.

6.6 Analysis of Comb Quality

As demonstrated in *Section* 6.4.1, the combs generated using the primary-secondary configuration typically degrade in quality as the gain switched frequency is increased [19], with optimum combs being generated at a gain switched frequency corresponding to the gain switched laser's RO frequency [56]. The quality of the combs, in terms of number of comb lines and spectral range, improves while operating the PIC in a mutually coupled configuration, however, as depicted in *Figure* 6.19, the noise of the mutually coupled comb also increases across this regime.

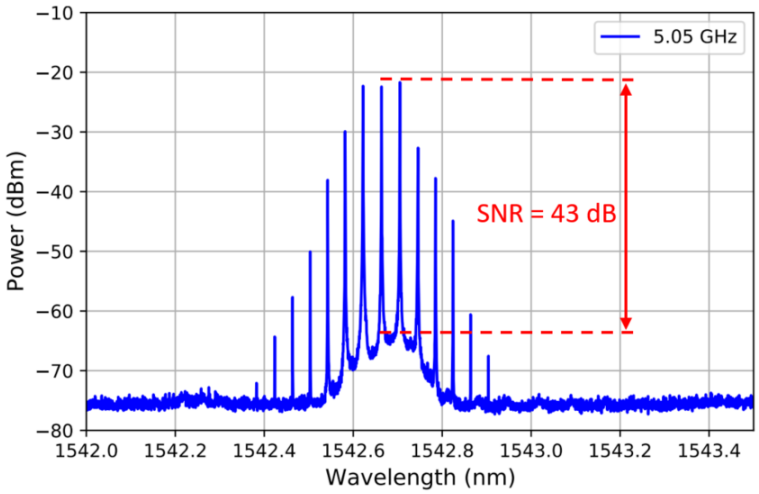


Figure 6.31: Measurement of the SNR of a generated comb. This is a measurement in dB between the maximum power of the comb and the maximum power of the noise level.

This quality parameter can be expressed by measuring the signal to noise ratio (SNR) of the generated combs. The SNR is the difference in dB between the maximum power of the comb and the maximum power of the induced noise in the comb. This is illustrated in *Figure* 6.31. This measurement was initially carried out for the primary-secondary combs plotted in *Figure* 6.9 which measured combs across a gain switched frequency range of 4.5 - 10.5 GHz.

This SNR is plotted in *Figure* 6.32 and demonstrates how the SNR of combs generated from a primary-secondary configuration changes as the gain switched frequency is swept from 4.5 - 10.5 GHz. The measured SNR ranges from 35 - 55 dB, and experiences a steady increase in SNR across a gain switched frequency of 4.5 - 6 GHz after which the SNR reaches a steady value.

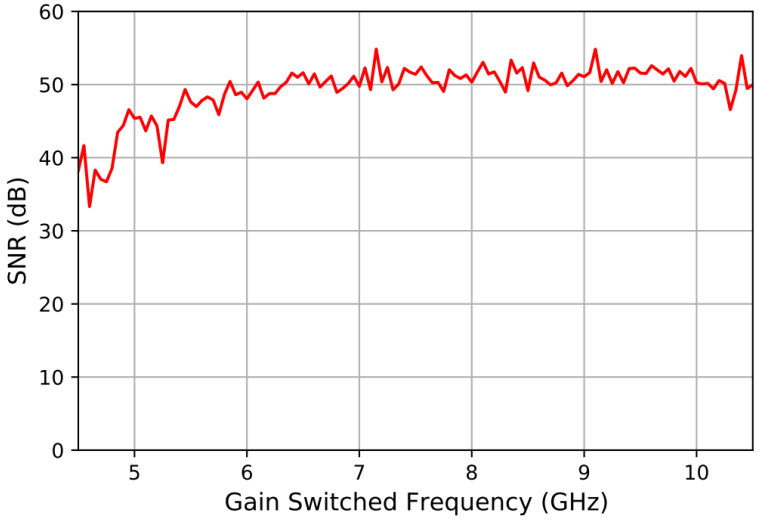


Figure 6.32: The measured SNR of combs generated from a primary-secondary configuration as the gain switched frequency is swept from 4.5 - 10.5 GHz.

The SNR measurements of the mutually coupled systems from *Sections* 6.5.1 and 6.5.2 are plotted in *Figure* 6.33.

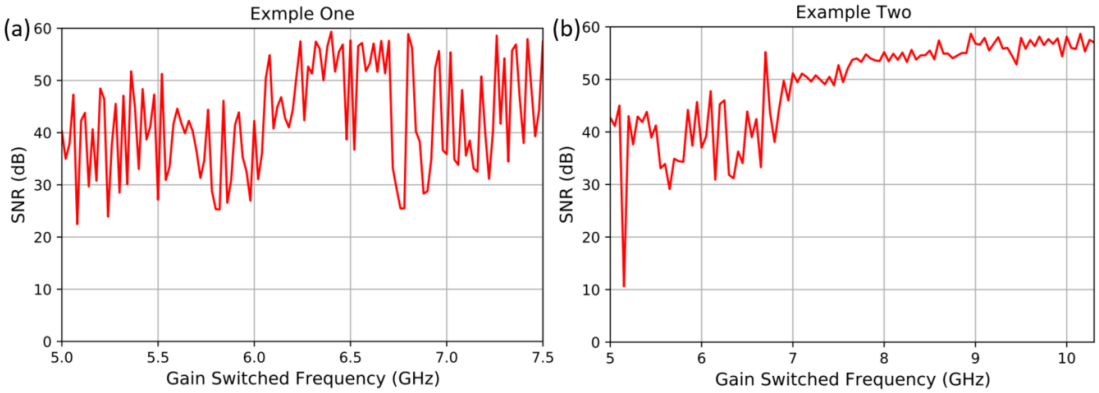


Figure 6.33: The measured SNR of the frequency combs generated through mutual coupling in *Sections* 6.5.1 and 6.5.2.

Example One illustrates the SNR measured from the combs generated in *Section* 6.5.1. Compared to the plot in *Figure* 6.32, this mutually coupled example demonstrates a more noisy SNR measurement across a frequency range of 5 - 7.5 GHz achieving an SNR ranging from 23 - 60 dB. The reduced SNR is more prevalent in regions effected by the additional generated comb

lines that occur while gain switching the PIC at a frequency equivalent to twice the RO frequency of an integrated laser in the PIC. However, 88% of the generated combs achieve an SNR $\geq$30 dB, with 18% of combs having a higher SNR than those achieved through the primary-secondary method, reaching as high as 60 dB.

Example Two illustrates the SNR measured from the combs generated in *Section* 6.5.2. This time the SNR ranges from 10 - 59 dB across a frequency range of 5 - 10.5 GHz. There is evident correlation between this plot and the ESA analysis demonstrated in *Figure* 6.26. The ESA analysis demonstrates the extra excited peaks with the highest power occurs across a frequency range of 5.5 - 7 GHz. Similarly, equivalent SNR plot demonstrates a noisy period across this frequency range with an SNR ranging from 30 - 50 dB. However, above this frequency range, the combs SNR achieves a higher SNR than those measured using the primary-secondary configuration in *Figure* 6.32. The sudden low SNR value of 10 dB occurs at 5.15 GHz where the spectral bulging in *Figure* 6.29 is generated.

6.7 Chapter Conclusion

This chapter demonstrates how the frequency of the gain switched current effects the generated combs for a PIC operating in the asymmetric and non-asymmetric biasing methods. In the case of the asymmetric bias method the combs are generated with a frequency spacing equivalent to the frequency of the gain switched current, with the quality of the combs deteriorating for higher frequencies as the comb frequency is no longer comparable with the RO frequency of the gain switched FP (*Chapter 5.2.2.4*). However, in both the asymmetric and non-asymmetric cases, when the frequency of the gain switched current is adjusted to the RO frequency of the SM laser, a broad spectra is achieved with no comb lines, indicating a spectral bulge.

In the case of the non-asymmetric biasing method, the combs generated were more elaborate as in many comb measurements, additional comb lines were excited. These additional comb lines were excited across regions equivalent to an integer multiple of the laser's RO frequency and resulted in combs with a frequency spacing equivalent to the laser's RO frequency. Examples of this are demonstrated by gain switching at 2$\times$RO frequency of the FP laser, and also by gain switching at 2$\times$RO, 3$\times$RO and 4$\times$RO frequency of the SM laser.

This phenomenon has previously been demonstrated off-chip with an external comb being injected into an on-chip FP laser [55]. The current across the FP laser was varied to vary the RO frequency of the FP laser, and when the RO frequency of the FP reached a frequency that was an integer division of the injected comb frequency, additional comb lines were excited with a frequency spacing equivalent to that of the RO of the FP. Here it can be achieved because of the strong, coherent bidirectional coupling between the two integrated lasers (*Chapter 5.3*). Therefore, the comb propagates through both laser cavities, each with it's own independent RO frequency, and therefore this extra comb line generation occurs for both lasers.

Chapter 7

Comb Line Filtering

7.1 Chapter Overview

In previous chapters, on-chip methods of gain switched comb generation and enhancement have been demonstrated through either traditional asymmetric biasing methods and the new non-asymmetric biasing techniques. A comb based super channel would require this optical source to be integrated with a de-multiplexer, which would divide the individual comb lines into waveguides with separate modulators before being recombined and transmitted. However, typical methods of on-chip de-multiplexing these narrow lines on a PIC have not been feasible [39], due to the difficulty of de-multiplexing the comb while retaining relative coherence between the optical carriers.

In this chapter, we focus on using an injection locked ring laser as a filter which is monolithically integrated with the tunable comb source. The concept of using a ring as a filter for comb lines has been introduced in *Chapter 2.4* where theoretically, a ring laser with a high Q-factor could be used as an integrated laser filter (ILF) where the ring laser locks to a comb line, transmitting that comb line and suppressing the others [40] [41] [42]. Because the integrated ring is also a laser, the position of the lasers transmission modes can also be adjusted through current injection which adjusts the lasers optical path length (*Chapter 2.4*), and therefore different comb lines can be transmitted while the others are suppressed, in other words filtered.

While the previous chapters demonstrate combs through different coupling techniques, for simplicity, the primary-secondary coupling technique was chosen for this chapter.

7.2 Device Design

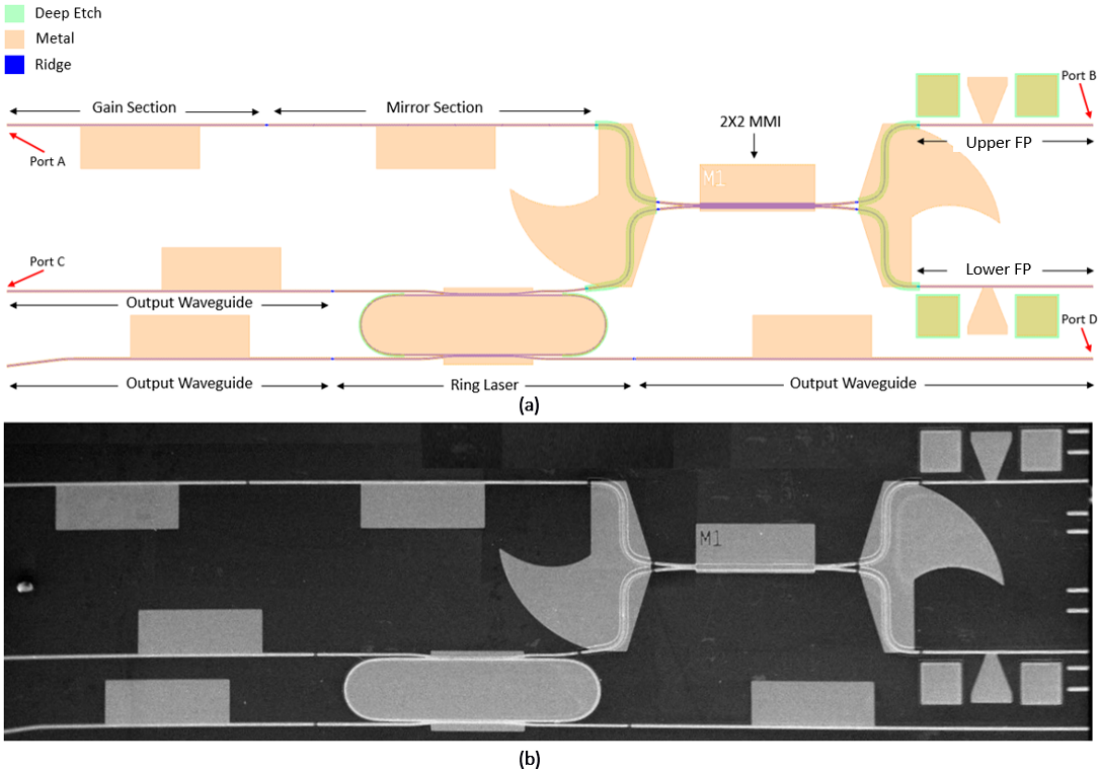


Figure 7.1: (a) Schematic of the PIC design and (b) SEM image of the fabricated PIC.

Like previous devices, this PIC was fabricated with commercially available material designed for the emission at 1550 nm, purchased from the company IQE and fabricated using the fabrication process described in *Chapter 3*.

The primary laser of the PIC is made up of the gain and mirror sections. The gain section is 600 μm in length and the mirror section is made up of 8 slots with an interslot separation of 108 μm. These slots act as reflective defects along the ridge by creating regions of lower effective refractive index, effectively creating a primary laser that is both single mode and tunable [19], [50]. The last slot in the mirror section of the device is deep etched to form an etched facet, and is free of metal to allow for electrical isolation. The primary laser couples into an S-shaped waveguide. This waveguide bends at an angle of 90° in a clockwise angle around a radius of 75 μm before bending again at an anticlockwise angle of 83° around a radius of 75 μm. This S-shaped waveguide is deep etched to increase the optical confinement and reduce bend loss [57], [58]. This S-shaped waveguide is used to integrate the primary laser with a multimode interferometer (MMI) by

coupling the light through a 7° isolation slot into the MMI arm. This slot is to allow for electrical isolation between the two sections and is so angled to reduce the reflection of the slot [59]. The input ridge of the arm of the MMI is tapered from 2.5 μm to 3.5 μm and bends at an angle of 7° anticlockwise with a length of 100 μm. The MMI itself is 290 μm long with a width of 14 μm. The 2×2 MMI was intended to split the light from the primary laser equally into two output arms [60]. Both of these output arms are tapered from 3.5 μm to 2.5 μm with a length of 100 μm and bend at an angle of 7°. However, the upper output arm bends anticlockwise and the lower output arm bends clockwise. Both of these outputs couple through a 7° angled isolation slot into an S-shaped waveguide with dimensions as described before and as shown in *Figure* 7.1. The waveguides couple through a deep etched isolation slot and are integrated with the upper and lower secondary Fabry–Pérot (FP) lasers, both of which are 420 μm in length.

These integrated Fabry Pérot (FP) lasers are fabricated with a ground-signal-ground (GSG) pad and can be probed with a GSG probe to gain switch the secondary laser by biasing the laser with the modulated RF current [19]. If the upper secondary laser is modulated, the optical comb can be measured at the output facet labelled B in *Figure* 7.1. Due to the strong bidirectional coupling described in *Chapter 5*, the comb will also be transmitted back through the MMI, with half the power going back to the primary laser and the other half going through the bottom left S-shaped waveguide. Again, this waveguide is deep etched to improve optical confinement, however this time it undergoes two 83° bends in the anticlockwise and clockwise directions, and has an angled slotted section at the end to reduce reflection. The next integrated waveguide is designed for the purpose of coupling with the ring laser. The waveguide first bends at an angle of 7° in the clockwise direction to make the waveguide parallel with the primary laser, MMI and secondary lasers. To create the coupling region the waveguide then bends 7° in the anticlockwise direction and then again in the clockwise direction. The waveguide is then fabricated straight for a length of 120 μm which is the coupling length between the waveguide and the ring laser. The waveguide bends again at a 7° angle in the clockwise direction and then again in the anticlockwise direction so that the waveguide is once again parallel to the primary laser waveguides. The waveguide is straight for another 215 μm where an angled slot is fabricated separating the ring laser coupling waveguide to the output waveguide which has a length of 770 μm.

The ridge separation between the coupling waveguide and the ring laser is 1.2 μm. The ring laser is made up of two 400 μm straight waveguides that are fabricated parallel to each other and the primary laser. These two straight waveguides are connected by a curved waveguide at each end, making a ring. The two curved waveguides are deep etched to improve optical confinement and bend at an angle of 180° around a radius of 75 μm. The ridge separation between the ring laser and the lower coupling waveguide is 1.2 μm and this coupling waveguide is fabricated with a similar geometry as the above coupling waveguide. This waveguide is fabricated with two angled etched facets at both ends to allow for electrical isolation and reduced reflection. This couples into a straight output waveguide to the right that has a length of 1130 μm from the ring laser coupling waveguide to the cleaved facet at *Port D*. This is the output where the filtered comb lines will be measured. To the left of the ring laser's coupling waveguide another output waveguide is fabricated. This is a straight waveguide for 645 μm before bending at an angle of 7° across a radius of 75 μm in the anticlockwise direction, and then is straight for another 75 μm before reaching the cleaved facet. This output waveguide is so angled to reduce reflections at the cleave to allow for the independent measuring of the ring laser spectra [59].

Each port acts as a different test section. Measuring the spectra through *Port A* determines the SMSR and wavelength tunability of the single mode (SM) primary section. The light generated from the primary section is split by the 2×2 multimode interferometer (MMI) into the secondary sections. Here either one of the secondary lasers could be used to generate the comb, in this chapter it is demonstrated how the upper secondary laser is used. Therefore, using the upper secondary laser, *Port B* can be used to measure the injection locked spectra. The upper secondary section undergoes gain switching by modulating the bias current with a high power RF signal, therefore generating a comb. *Port C* is used to test that the 2×2 MMI splitter is operational and splits the generated comb so that it can be measured through *Port A* and *Port C*. The final port (*Port D*) is used to measure the individual comb lines, filtered by the ring laser.

7.3 Theoretical Approach

The method to achieve filtering in this PIC is the use of an injection locked ring laser as an integrated laser filter (ILF). Using injection locked lasers as

coherent multiplexers has been previously demonstrated [39], while it has also been shown that further improvements in the mode suppression during de-multiplexing can be made with higher Q laser cavities [40] [41] [42]. Thus, the ring laser was used in this PIC due to its high Q factor. In the PIC, the comb is first injected into the ring laser and the bias current in the ring is adjusted to filter the individual comb lines. The dimensions of the ring laser results in a free spectral range of 66 GHz.

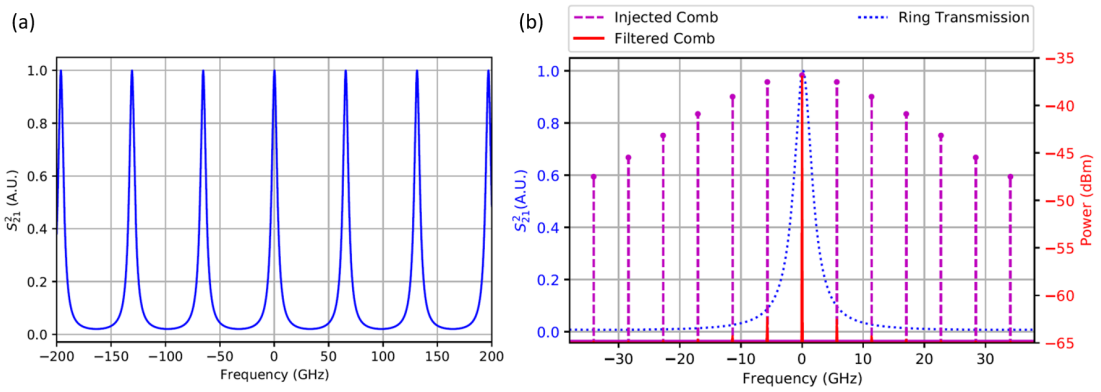


Figure 7.2: (a) Approximation of the transmission profile of a ring laser. (b) Simulation of the injected comb and transmission profile of the ring, and the filtered comb output of the ring laser.

The transmission profile of the ring laser ensures that the side peaks of the filtered comb are sufficiently suppressed when the comb passes through the ring. Using increasing current injection, the effective path length of the ring increases which allows the transmission profile of the ring laser to shift along the frequency (and spectral) domain. The high Q-Factor of the ring laser allows the previous comb line to be suppressed sufficiently before the next comb line is filtered.

7.4 Device Characterisation

7.4.1 DC Characterisation of the SM Laser

The LIV characteristics of the single mode (SM) primary laser in this PIC were measured via the cleaved facet at *Port A* using fiber coupling. The gain section of the SM laser was swept from 0 - 200 mA for bias currents through the mirror section of 25, 75 and 125 mA. These LIV curves are plotted in *Figure* 7.3 along with an example of a single mode spectrum attained from the SM laser.

Like examples in other chapters, the threshold current of the SM laser

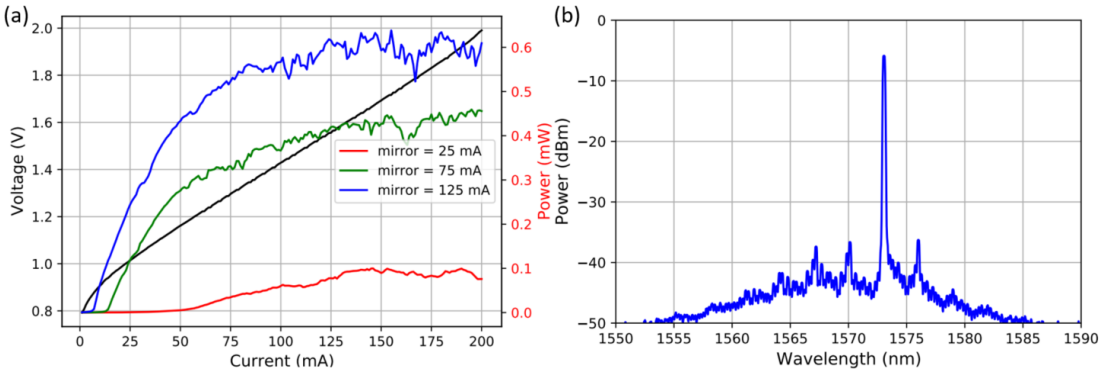


Figure 7.3: (a) LIV curves attained from the SM laser as current was swept across the gain section for different currents through the mirror section.

decreases and the lasing power increases for increasing currents through the mirror section. The single mode spectrum in *Figure* 7.3 was attained at 1573 nm for bias currents of 100 and 50 mA across the gain and mirror sections respectively. It has a SMSR of 30.5 dB indicating a single mode.

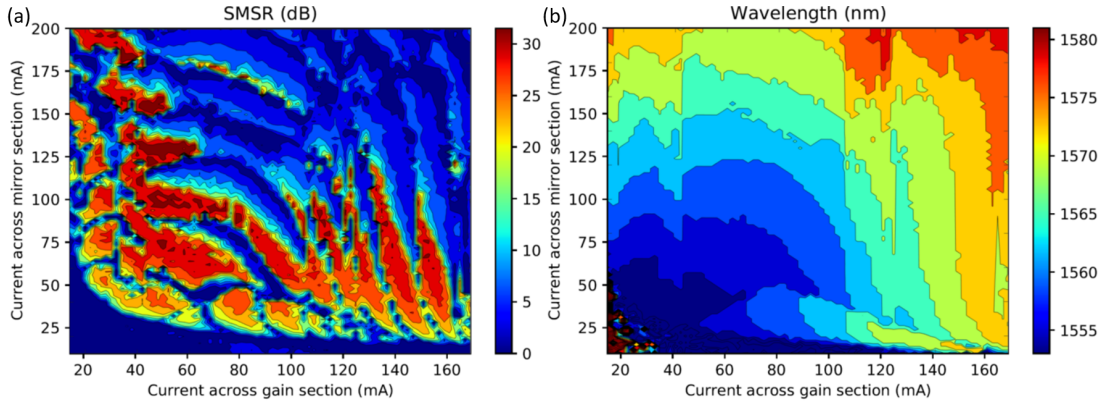


Figure 7.4: (a) SMSR and (b) lasing wavelength of the SM section of the device as the current is varied through the gain and mirror sections of the device.

To fully characterise the relation of the lasers SMSR and lasing wavelength to the currents pumped through the gain and slotted sections, current was swept through both sections with the spectra being analysed at specified intervals. These sections of the PIC were biased using currents ranging from 15 mA - 170 mA through the gain section and 15 mA - 200 mA through the mirror section. At each interval the optical spectrum was recorded from *Port A* using the ANDO AQ6317B OSA. The SMSR and peak lasing wavelength was recorded at each interval of 2 mA and are plotted in *Figure* 7.4.

The SM laser generates multiple single mode regions at different wavelengths across these biasing ranges. These wavelengths can be illustrated more clearly

by plotting the measured SMSR against the equivalent lasing wavelength. This is plotted in *Figure* 7.5

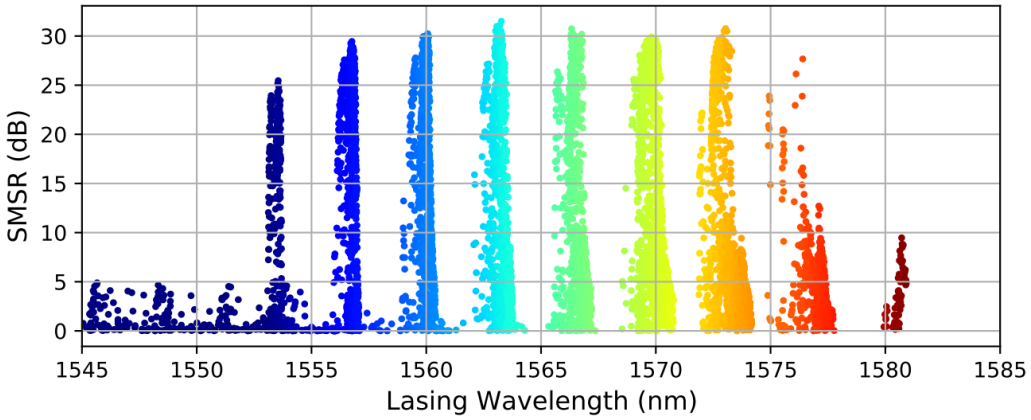


Figure 7.5: Plot illustrating the measured SMSR of the laser for each lasing wavelength.

From the plot above, the SM laser achieves six lasing wavelengths with an SMSR $>$ 30 dB across a wavelength range of 1557 - 1573 nm. These wavelengths are 3.5 nm apart which is consistent with the design of the laser.

7.4.2 DC Characterisation of the FP Laser and Injection Locking

The LIV curves of the FP laser were attained by sweeping current from 0 - 100 mA across the upper secondary FP and measuring the output through *Port B* via fiber coupling. The threshold current of the FP was measured to be 27 mA and examples of the FP laser's spectra at threshold and twice threshold current are plotted in *Figure* 7.6.

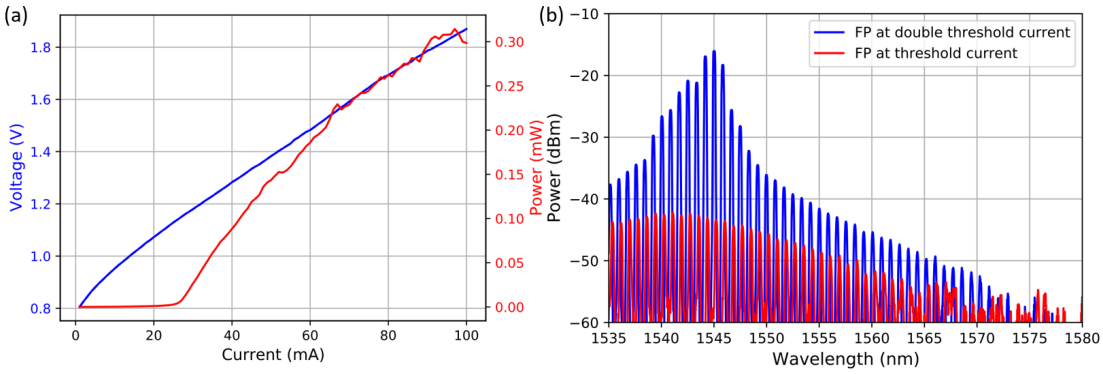


Figure 7.6: (a) LIV curve of the FP laser. (b) Spectra of the FP laser when biased at the lasers threshold current and at twice threshold current.

The shape of the measured spectra and the separation between the lasing modes is consistent with a FP laser 420 μm in length (*Chapter 2.2*).

To generate a single mode injection locked spectra between the SM primary laser and the FP secondary laser, the SM laser was biased to generate a single mode spectrum, the FP was biased at threshold current and the MMI coupler was biased at 180 mA and the S-shaped waveguides were biased at 75 mA. These bias currents were sufficient to allow the integrated MMI and the S-shaped waveguides to be passive. Examples of the single mode spectra measured through *Port B* when the secondary FP laser is optically phase locked to the primary SM laser are plotted in *Figure* 7.7.

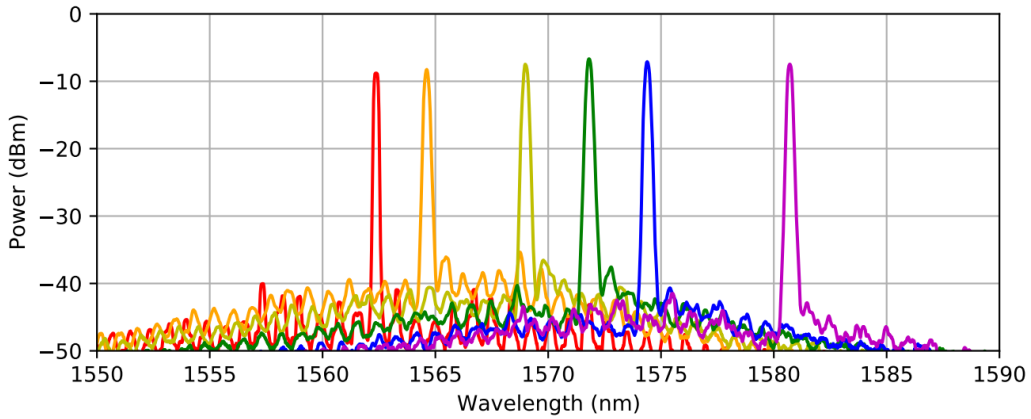


Figure 7.7: Examples of the injection locked spectra between the primary SM and secondary FP lasers measured through *Port B* via fiber coupling.

Different single mode, injection locked spectra were demonstrated for bias currents of 23 - 30 mA across the secondary FP, which was low enough to ensure the PIC was operating in the asymmetric bias regime to approximate a primary-secondary configuration [26] and [27]. Six single mode, injection locked spectra are demonstrated for a wavelength range of 1562 - 1581 nm.

7.5 Comb Generation

Once injection locking was achieved, the probe biasing the FP laser was swapped for a ground-signal (GS) probe, and a sinusoidal current was used to gain switch the secondary FP. Combs were detected through *Port B* with a comb line separation equivalent to the gain switched frequency of the bias current. However, because of the PIC's ability to support stable combs due to the bidirectional coupling demonstrated in *Chapter 5.3*, one would expect the

comb to propagate back into the passive MMI where the comb would be split between the upper SM laser and the lower output waveguide.

The output waveguide of *Port C* was biased at 25 mA to make the section passive but not lase and the outputs of *Port A* and *Port C* were measured using the ANDO OSA and were compared to the comb measured through *Port B*. These measured outputs are plotted in *Figure* 7.8.

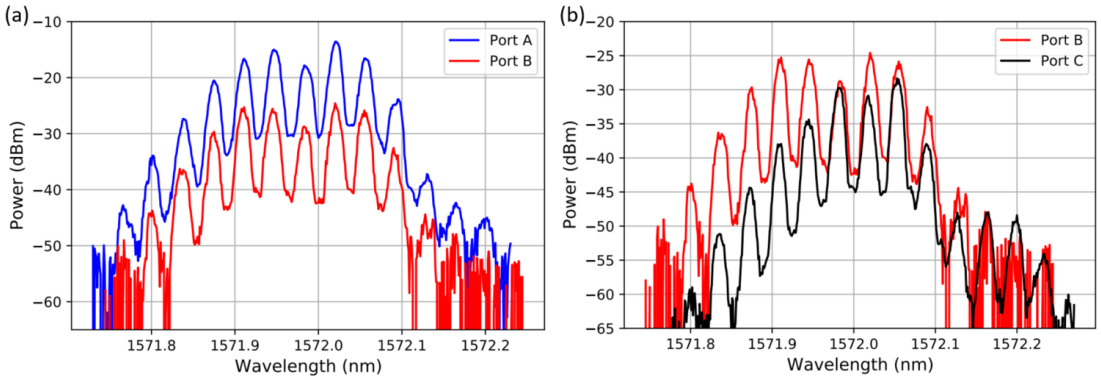


Figure 7.8: (a) Comb measured through *Port A* compared to *Port B*. (b) Comb measured through *Port C* compared to *Port B*.

The strong, coherent bidirectional coupling allows the comb generated by the secondary FP at *Port B* to be detected through *Port A* and *Port C*, both demonstrating a near identical comb to that generated and measured at *Port B*. The main obvious difference to the measured combs is the power of each and while this could be explained by poor fiber coupling, it can also be argued that the comb measured at *Port A* is amplified by the high bias currents through the SM laser, and the comb measured through *Port C* is lower due to the lossy nature of the length of the InP output waveguide.

This comb was generated by biasing the gain, mirror and FP sections at 179, 28 and 27 mA respectively and gain switching the FP section with a frequency of 5 GHz. The quality of the comb can be described as having six comb lines within 4 dB of each other.

7.6 Comb Filtering

Ring lasers are useful for on-chip ILFs because they are facet-less and due to their high Q-factor that makes optimal filtering possible [40]. Filtering occurs by injection locking the ring laser with the generated comb and varying the current across the the ring to injection lock the individual comb lines. The ring

laser was independently characterised using the angled waveguide fabricated at the lower left portion of the PIC illustrated in *Figure* 7.1. This allows the ring laser to be characterised while minimising the reflectance caused by the cleaved facet [59].

This time, due to the difficult nature of fiber coupling with an angled waveguide, an integrating sphere (IS) was used to measure the LIV curves. The ring laser was biased and current was swept from 0 - 500 mA, while the light was collected through the angled waveguide using the IS. This LIV curve is plotted in *Figure* 7.9. The ring laser demonstrates a threshold current of 85 mA and reaches a power of 1.6 mW at a bias current of 500 mA. A spectrum of the ring laser was measured via fiber coupling through the angled output waveguide at a bias current of 187 mA. As expected, the spectra of the ring laser resembles that of a FP.

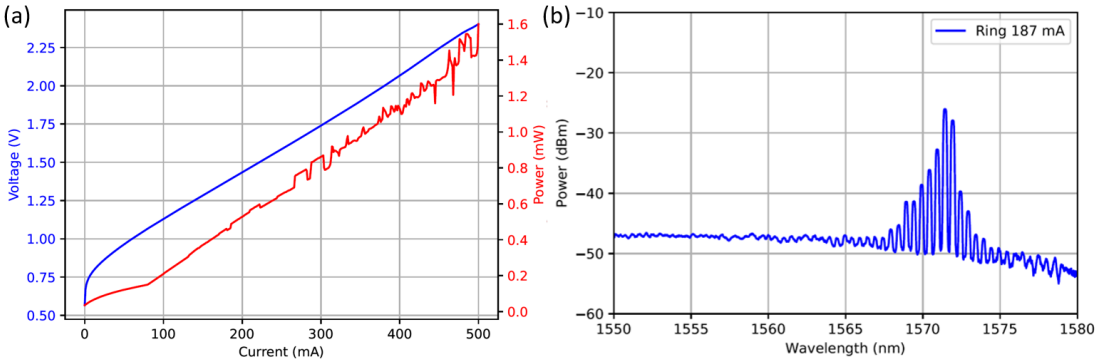


Figure 7.9: (a) LIV curves and (b) free running spectra of the ring laser.

Once the generated comb was detected through *Port C* it is known that the comb is propagating along the coupling waveguide above the ring laser. What is left to do is bias the ring and vary the current while measuring the output of *Port D*. The ring was initially biased at 80 mA and the wavelength span of the comb detected through *Port C* was monitored through *Port D*.

The first peak of the filtered comb was detected through *Port D* for a bias current of 169 mA through the ring laser. This current was increased by intervals of 1 mA and different peaks were detected at each interval of 3 mA. This was carried out for a bias current range of 169 - 199 mA across the ring laser. Eleven individual peaks were measured through *Port D* for this biasing range across the ring. These individual peaks are plotted and compared to the comb measured through *Port C* in *Figure* 7.10.

By plotting these peaks against the comb initially measured through *Port C*, it

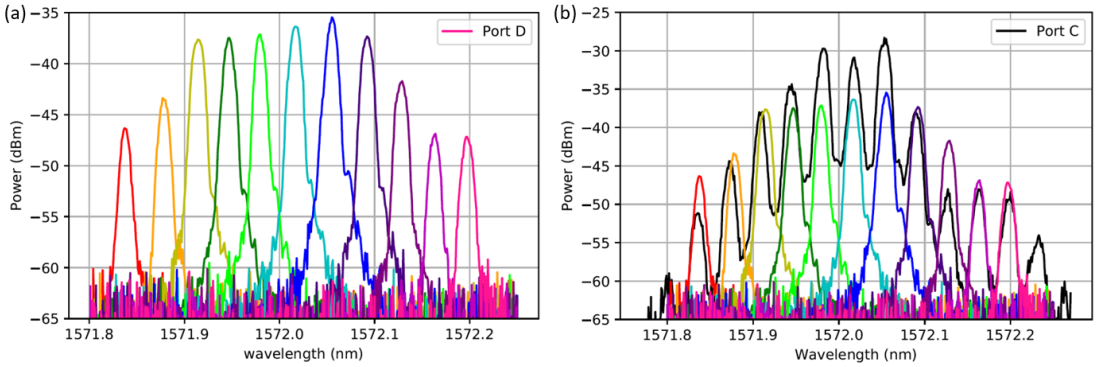


Figure 7.10: (a) Individual comb lines filtered by the ring laser and (b) plotted against the comb measured through *Port C*.

is evident that these individual peaks form as a result of the individual comb lines being filtered by the ring laser. The power of the filtered comb lines are lower than the combs measured through *Ports A, B and C* due to the loss from the ring and the length of the output waveguide.

A colour plot can be plotted to demonstrate how the measured spectra through *Port D* changes as the bias current across the ring laser is varied by 169 - 199 mA at intervals of 1 mA. This is plotted in *Figure* 7.11.

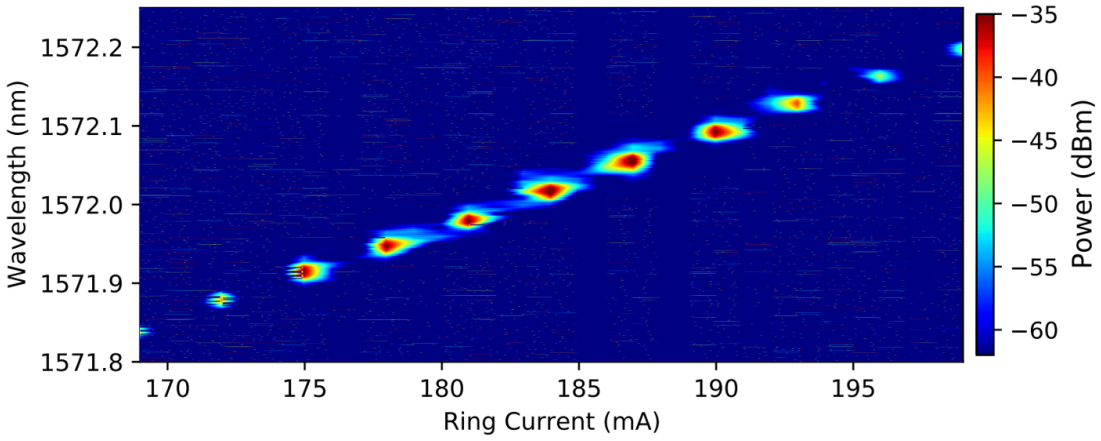


Figure 7.11: Colour plot illustrating the growth and suppression of individual comb lines as the current through the ring resonator is increased.

This colour plot illustrates the growth a comb line before it is suppressed and the next comb line is filtered.

7.7 Chapter Conclusion

This chapter demonstrates how a coherent optical comb can be created and filtered on a PIC. The comb was generated using the asymmetric biasing

method described in *Chapter 5*, however the primary-secondary lasers were integrated via a 2×2 MMI structure. This large structure complicates the PIC and future designs would be much simpler, however, it allows us to accurately measure the PIC by creating outputs at different ports where each is used as a separate test section. The PIC allows one to test the primary, secondary and ring lasers independently. Injection locking and bidirectional coupling (*Chapter 5*) can be measured, as well as the combs propagation throughout the PIC.

In this chapter, the PIC is capable of producing six single mode wavelengths from the primary laser across a range of 15 nm. Injection locking occurs between the single mode primary laser and the secondary FP, and combs can be generated through gain switching. Combs are generated with a frequency spacing equivalent to the frequency of the gain switched current, with the highest quality comb being measured at 5 GHz achieving six comb lines within 4 dB of each other. This generated comb is demonstrated to propagate throughout the PIC, being measured through *Port A*, *Port B* and *Port C*. This allows the comb to be coupled into the ring laser where the ring laser injection locks an individual comb line, and can select a comb line by varying the bias current through the ring laser.

This PIC demonstrates how a ring laser can be used to filter out comb lines. A full de-multiplexing network would utilise an array of these ring lasers, each filtering a different comb line into separate waveguides where data is incorporated and the comb lines are recombined and transmitted. This is illustrated in *Figure* 7.12.

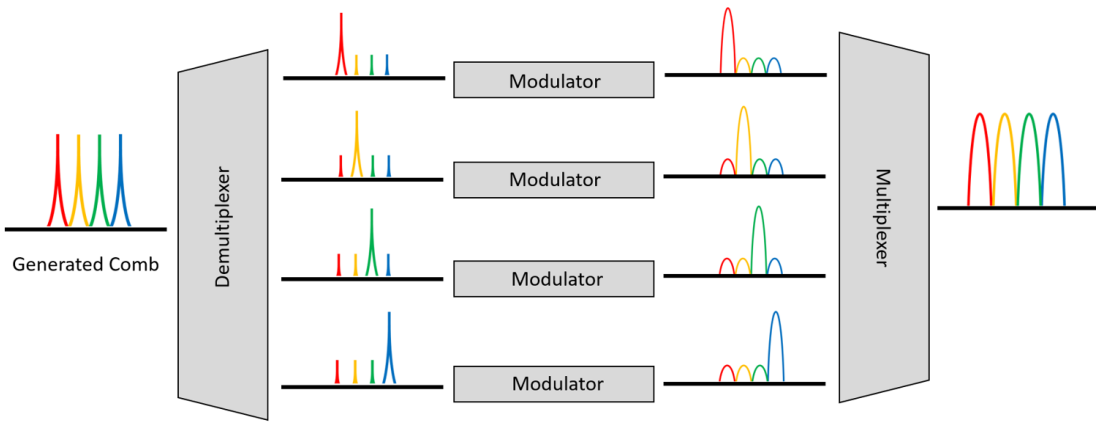


Figure 7.12: Schematic of a comb based optical network.

Chapter 8

Comb Generation Without Additional Optical Injection

8.1 Chapter Overview

Throughout this thesis, gain switched combs were generated using some form of coupling, primarily through primary-secondary coupling or mutual coupling. In all cases, more than one laser was integrated on a chip. In fact, up until now, flexible gain switching has only been achieved through some method of external injection [17], on-chip injection locking [19], or mutual coupling (*Chapters 5, 6*) which maintains phase coherence and allows combs to be generated. Less flexible forms of gain switching have been demonstrated without an additional form of injection by gain switching a single mode DFB at a frequency equivalent to the lasers relaxation oscillation frequency [12]. This method offers an enhanced comb but the frequency separation of the comb lines is limited to the lasers relaxation oscillation (RO) frequency.

This chapter focuses on using a two sectioned, single cavity laser to generate flexible frequency combs without using any of the fore mentioned methods to maintain the devices phase coherence. The two sectioned laser is similar to the single mode lasers used in earlier chapters as it is made up of a gain and mirror section, but electrically isolated from each other via an isolation etch. So while the device consists of two sections, they share the same cavity. Either of these sections can be gain switched while the other section is biased using a DC current. The device is demonstrated to generate single mode spectra at multiple wavelengths and combs are generated across a frequency range of 1 -

10 GHz, with the optimum combs being generated at a gain switched frequency equivalent to the RO frequency of the laser.

8.2 Device Design

Like previous devices, this PIC was fabricated with commercially available material designed for the emission at 1550 nm, purchased from the company IQE and fabricated using the fabrication process described in *Chapter 3*.

The laser of the PIC is made up of the gain and mirror sections. The gain section is 600 μm in length and the mirror section is made up of 7 slots with an interslot separation of 87 μm. These slots act as reflective defects along the ridge by creating regions of lower effective refractive index, effectively creating a single cavity laser that is both single mode and tunable [19], [50]. An isolation slot exists between both sections 15 μm in length with a depth of 0.25 μm to remove the surface GaInAs and GaInAsP layers to allow for electrical isolation between the two sections. The cavity of this laser is confined using a metal etched facet at one end of the gain section, and a cleaved facet at the opposite end of the mirror section. Ground Signal (GS) contacts were added to both sections to allow for each section to be gain switched using a GS probe. The ground pad made contact with the n-type substrate via the deep etch. A schematic of this device is shown in *Figure* 8.1.

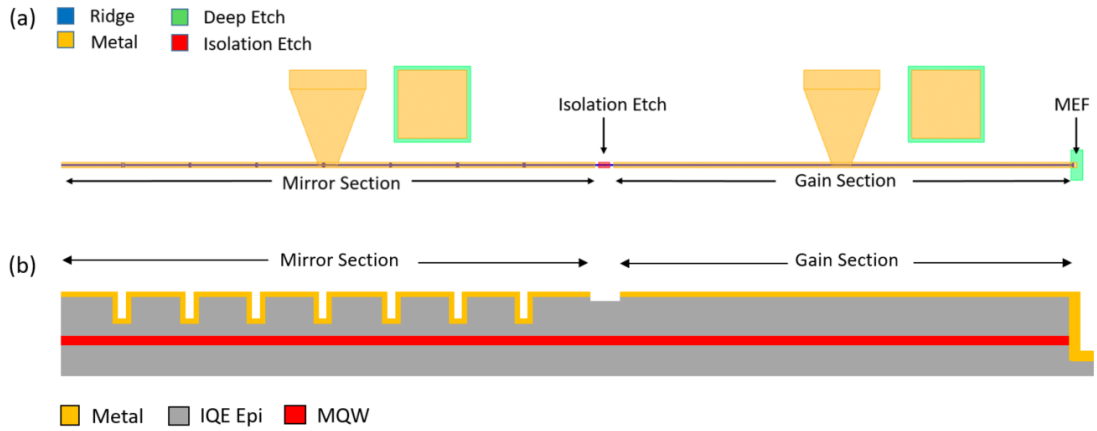


Figure 8.1: (a)Top view and (b) side view of device schematic.

8.3 Device characterisation

The LIV characteristics of the device was measured via the cleaved facet using an integrating sphere to avoid loss. Current was swept across the mirror section for different bias currents across the gain section (50, 60 and 70 mA). These results are depicted in *Figure* 8.2.

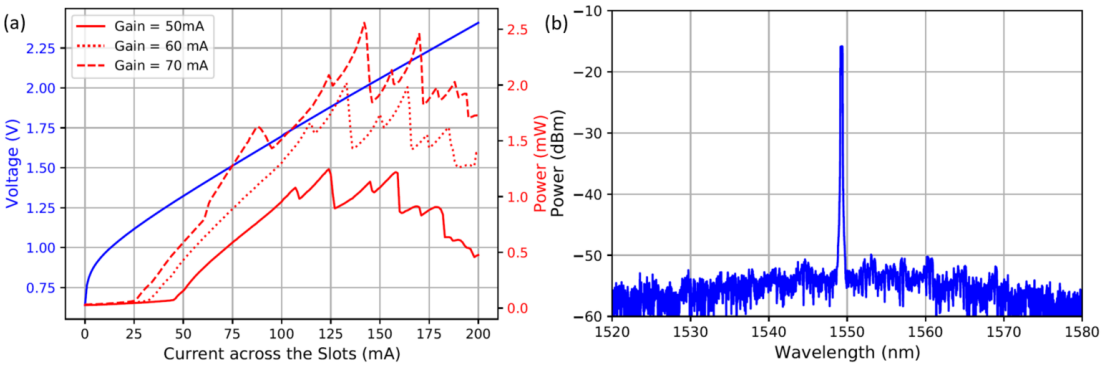


Figure 8.2: (a) LIV measurements as current is swept through the mirror section for different bias currents through the gain section (b) example of a single mode spectrum attained at 1549.5 nm.

The threshold current of the device ranged from 25 - 45 mA depending on the bias current of the gain section. The max power measured by the integrating sphere ranged from 1.5 - 2.4 mW, again depending on the bias current of the gain section. The trend follows that as the current through the gain section increased, the device experienced a decrease in threshold current and an increase in power.

The integrating sphere was replaced by an optical fiber and the spectra of the device was initially analysed using an ANDO AQ6317B OSA. The bias current across the two sections were varied until a single mode spectra was achieved at a bias current of 60 and 100 mA through the gain and mirror sections respectively. This spectra is plotted in *Figure* 8.2 and depicts a spectra with an SMSR of 34 dB at lasing wavelength of 1549.5 nm.

To fully characterise the single mode nature of the device, currents were swept across the gain and mirror sections of the device ranging from 40 - 86 mA through the gain section and 20 - 200 mA through the mirror section. At each interval the optical spectrum was recorded from the cleaved facet using an optical fiber coupled to the ANDO AQ6317B OSA. The SMSR and peak lasing wavelength was recorded and plotted in *Figure* 8.3.

From the plots attained, the laser produced multiple single mode regions

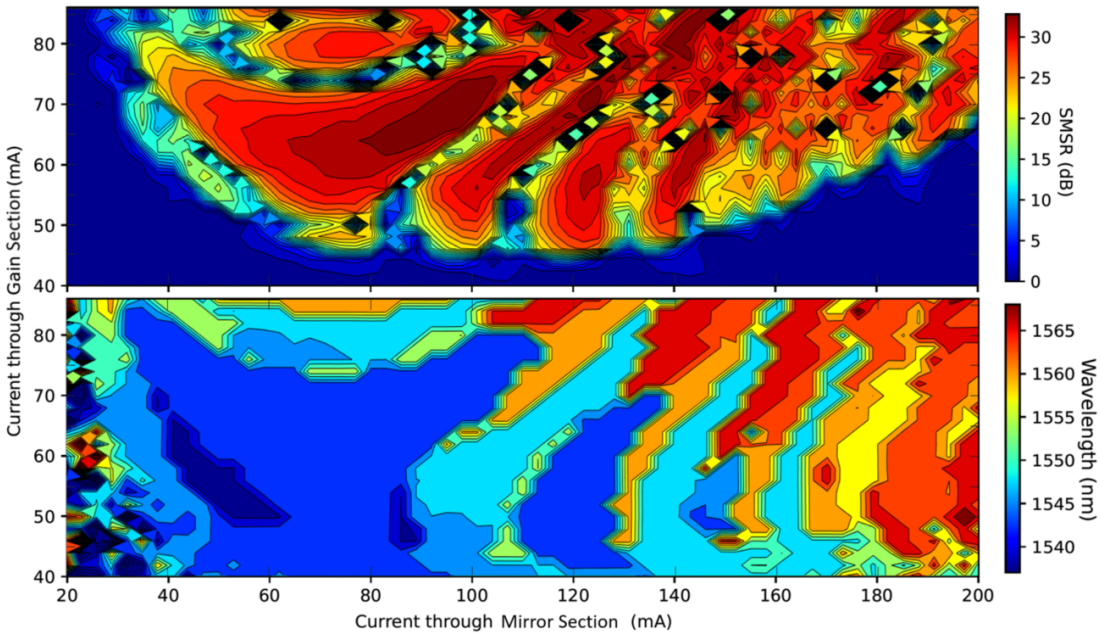


Figure 8.3: SMSR (top) and lasing wavelength (bottom) of the device as the current is varied through the gain and mirror sections.

within a wavelength range of 1543 - 1567 nm. These lasing wavelengths were approximately 4.5 nm apart which is consistent with the FSR due to the interslot separation in the device. All these lasing wavelengths appear as the current is swept across the mirror section while the bias current of the gain is constant at approximately 70 mA. Analysis of how the spectra changes across this period is plotted in *Figure* 8.4. Here we see how the lasing wavelengths of the spectra change from 1543 - 1567 nm as the bias current across the mirror section varies from 25 - 250 mA.

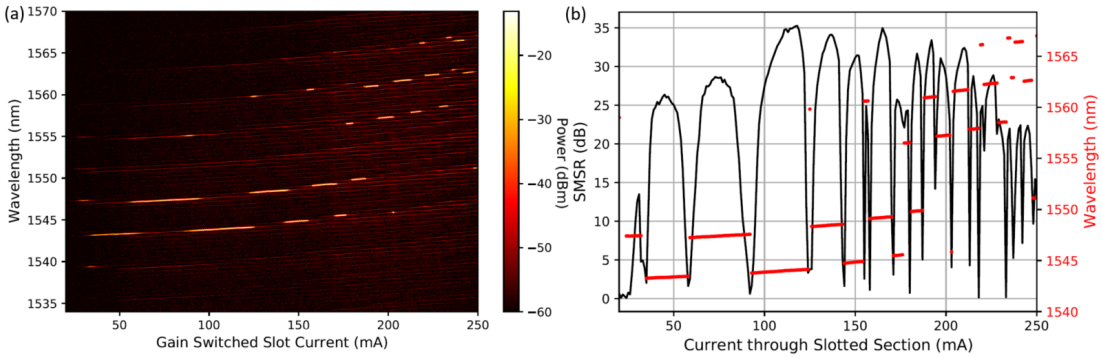


Figure 8.4: (a) Colour plot showing the power of the spectra as current was swept across the mirror section. (b) SMSR and lasing wavelength of the device as the current was swept across the mirror section.

8.3.1 RF Characterisation

Once the SMSR map (*Figure* 8.3) was developed, one of the DC probes was exchanged for a ground-signal RF probe and was used to gain switched either the gain or mirror section, while the other section is biased using a DC probe. Combs were generated by gain switching both the gain and mirror sections independently and are depicted in *Figure* 8.5. Both comb examples are generated at a gain switched frequency of 2 GHz and were measured using the high resolution APEX AP2061-A series OSA.

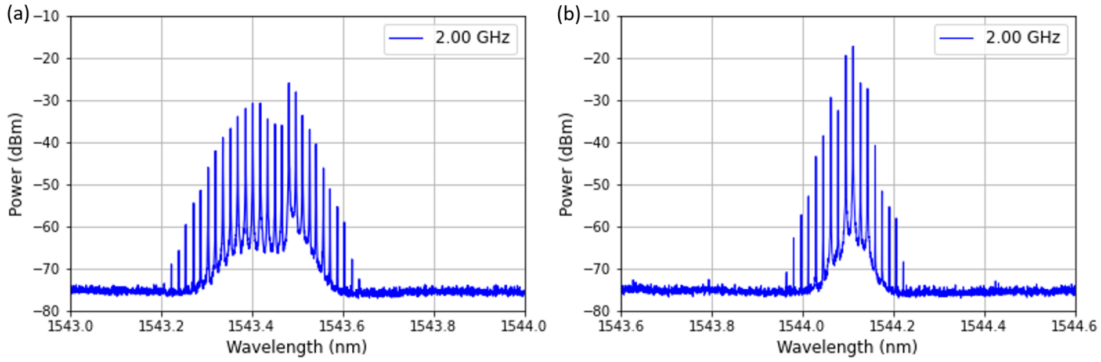


Figure 8.5: Comb attained through gain switching (a) the gain section and (b) the mirror section.

As mentioned in *Section* 8.1, achieving phase locked frequency combs through gain switching typically requires an additional form of optical injection, for example external injection [17], on-chip injection locking [19], or mutual coupling. However, here, combs were achieved without any of these conditions. Instead they were achieved by a two section, single cavity device, where one of the two sections was gain switched. The existence of comb lines suggests that the non-gain switched section of the single cavity device is sufficient to maintain the phase coherence of the device and thus combs are generated.

The frequency response of the combs was determined by biasing the gain and mirror sections at 70 and 100 mA respectively, gain switching the gain section and adjusting the gain switched frequency. The frequency was swept from 1 - 15 GHz at intervals of 1 GHz and the results are shown in *Figure* 8.6. The quality of the generated combs decreased as the gain switched frequency increased, which is consistent with previous on-chip gain switching techniques [19]. However, a broader comb is achieved at 3 GHz, generating 10 comb lines within 3 dB of each other.

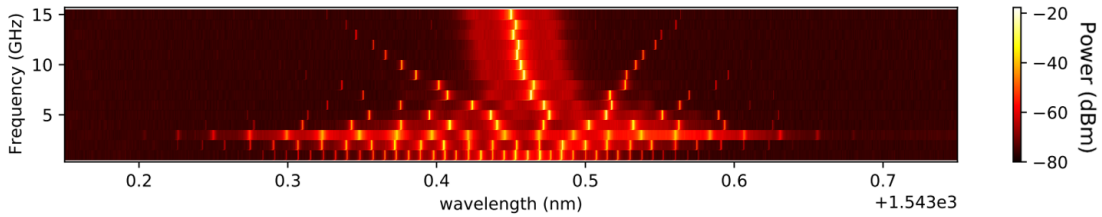


Figure 8.6: Frequency response of the generated combs.

Plots of the individual combs generated at 1, 5 and 10 GHz are plotted in *Figure* 8.7 which show the lower and upper limits of the gain switching frequency.

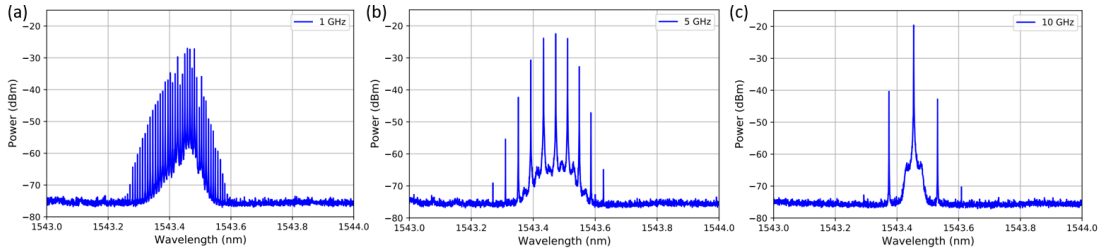


Figure 8.7: Comb attained through gain switching at (a) 1 GHz, (b) 5 GHz and (c) 10 GHz.

Based off of simulations in *Chapter 2*, and previously generated combs in *Chapter 5*, it can be assumed that this enhanced 3 GHz comb is a result of the laser having an RO frequency close to this frequency. The high resolution APEX OSA is used to determine the RO frequency of the laser when the gain and mirror sections are biased at 70 and 100 mA respectively. The side-bands of the peak lasing wavelength, that represent the laser's RO frequency [51], are shown in *Figure* 8.8.

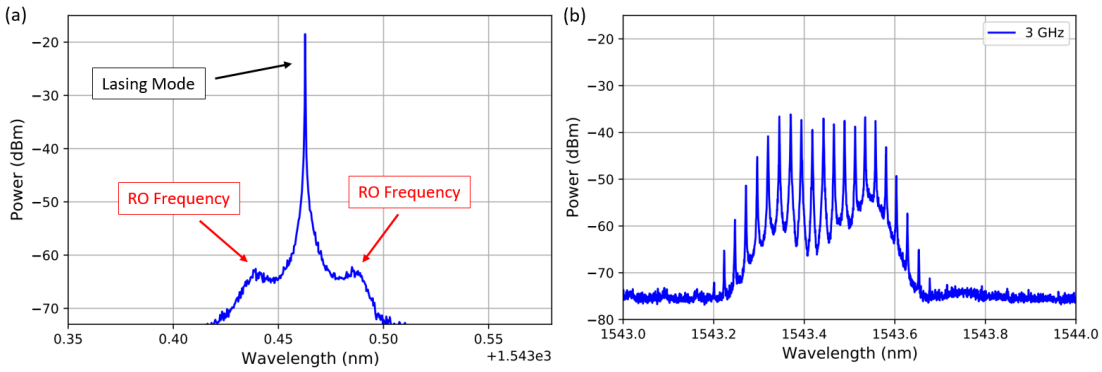


Figure 8.8: (a) High resolution image of the single mode spectrum with the RO sidebands. (b) The generated comb at a frequency equivalent to the RO frequency measured from the sidebands.

The RO frequency of the laser was measured by determining the frequency

separation between the lasing mode and these side bands. At these bias currents, this was measured to be 2.896 GHz, which is consistent with the optimum comb of 3 GHz plotted in *Figure* 8.8. This is also consistent with results attained in [12], where the quality of the comb could be enhanced by gain switching the device close to its RO frequency.

8.4 Effects of Bias Current

The basis of gain switching is to rapidly turn the laser, or in this case the laser section, on and off repeatedly using a high powered RF signal. So it is logical that the current itself would also effect the generated comb, specifically on the peak to peak separation of this sinusoidal current and its ability to turn the laser on and off. As demonstrated in *Figure* 8.4, the gain was biased at 70 mA and the current through the mirror section was swept from 25 - 250 mA achieving multiple single mode regions. Thus the effects of the bias current on the generated combs could be analysed by carrying out this sweep while the mirror section is gain switched.

An RF amplifier (JDS Uniphase Optical Modulator Driver H301-2310) is integrated with the experimental setup and so these current sweeps could be carried out at different amplifications of the gain switched current. The RF amplifier was powered using a standard voltage source and so the peak to peak of the RF signal could be adjusted by adjusting the voltage output of the voltage source. The RF amplifier had a maximum voltage input of 8 V, and so to analyse the effects of the RF peak to peak on the generated combs, the current sweeps were carried out for the RF amplifier being powered by 4 V and 8 V, to create a low and high RF peak to peak separation.

8.4.1 RF Amplifier at 4V

The RF amplifier was first powered by 4 V, the gain section was biased at 70 mA and the gain switched current through the mirror section was swept from 25 - 250 mA. The results of this are shown in *Figure* 8.9. The resulting spectra was mostly similar to the non-gain switched sweep in *Figure* 8.4, however, a slight reduction in SMSR was observed at bias currents $<$ 100 mA as the lower peak of the sinusoidal current approached 0 mA. This is consistent with a known phenomena where combs can't be generated when the lower peak of the gain switched current is approximately 0 mA [61].

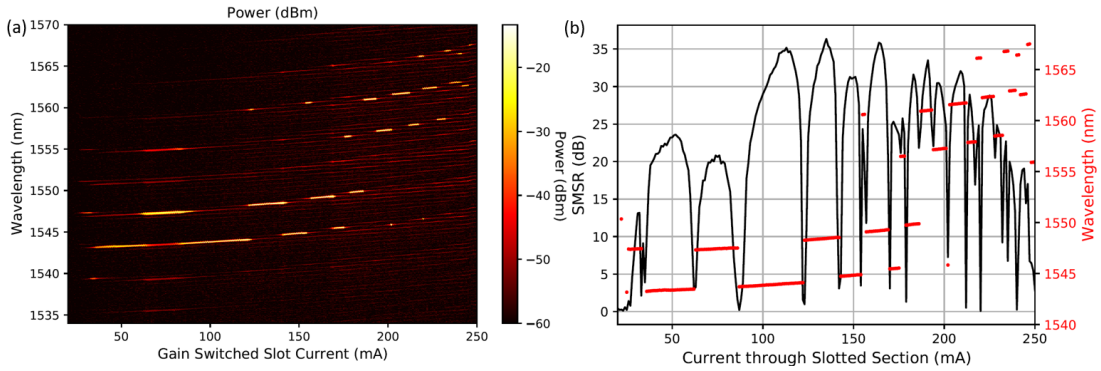


Figure 8.9: (a) Colour plot showing the power of the spectra as the gain switched current was swept across the mirror section. (b) SMSR and lasing wavelength of the device as the gain switched current was swept across the mirror section.

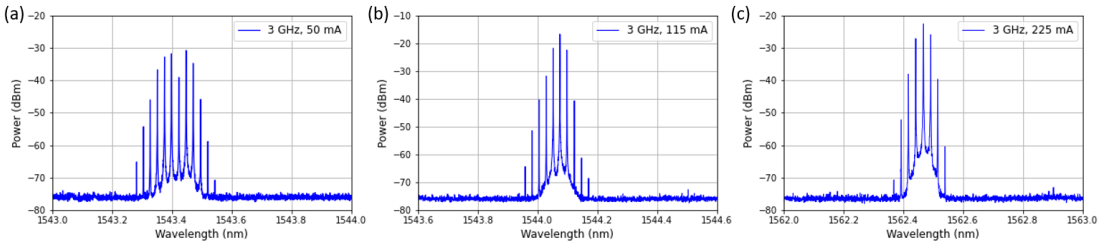


Figure 8.10: Analysis of the peak lasing wavelength while the gain switched current through the mirror section is (a) 50 mA, (b) 115 mA and (c) 225 mA.

The corresponding combs generated at a gain switched current of 50, 115, and 225 mA are plotted in *Figure* 8.10 and the quality of the combs degrade as the gain switched current increases. Since gain switching required the device to be continuously turned on and off, as the gain switched current increases there comes a point where gain switching is no longer possible, and so the quality of the combs degrade as the gain switched current increases. This directly relates to the theoretical analysis carried out in *Chapter 2.3.5*.

8.4.2 RF Amplifier at 8V

The analysis was carried out again, but this time the voltage powering the RF amplifier was set to 8 V to generate a high peak to peak separation sinusoidal current. The gain section was again biased at 70 mA and the gain switched mirror section was swept from 25 - 250 mA. The results are shown in *Figure* 8.11. This time a large reduction in the SMSR of the spectra was observed at bias currents $<$ 100 mA as the lower peak of the gain switched current reaches 0 mA.

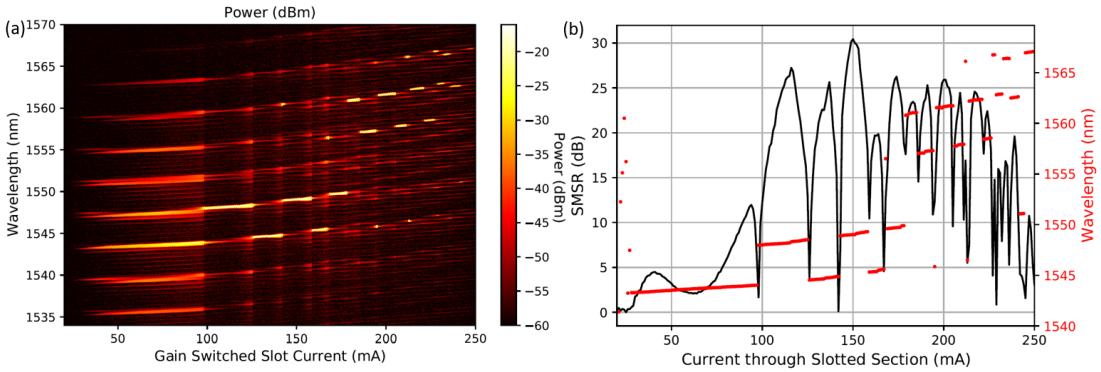


Figure 8.11: (a) Colour plot showing the power of the spectra as the gain switched current was swept across the mirror section. (b) SMSR and lasing wavelength of the device as the gain switched current was swept across the mirror section.

The corresponding combs generated at a gain switched current of 50, 150, and 186 mA are plotted in *Figure* 8.12.

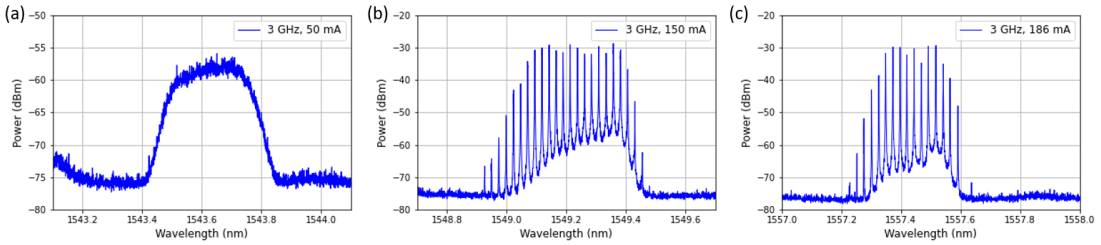


Figure 8.12: Analysis of the peak lasing wavelength while the RF current through the mirror section is (a) 50 mA, (b) 150 mA and (c) 186 mA.

From the above plots, what is generated in the first image cannot be considered an OFC as it contains no generated comb lines. This occurs when the modulation peak to peak separation is high enough to fully switch off the laser and therefore the resulting pulses are built up from spontaneously emitted photons and the coherence of the pulses are lost [61]. Increasing the gain switched current to 150 mA means that this high peak to peak sinusoidal current is no longer resulting in the device switching off completely and so the generated comb can benefit from the high peak to peak signal. This is demonstrated by the generated comb having 13 comb lines within 3 dB of each other, across a bandwidth of 36 GHz. Increasing the current further to 186 mA, the quality of the comb again starts to degrade for increasing gain switched currents as discussed in *Chapter 2.3.5*.

8.5 Chapter Conclusion

This chapter demonstrates how an on-chip gain switched laser doesn't need an additional form of injection to generate comb lines. Up until now, flexible gain switched comb lines have only been generated through some form of external injection [17], on-chip injection locking (*Chapter 5,7*) [19], or mutual coupling (*Chapters 5, 6*) which maintains the devices phase coherence. Alternative methods of gain switching without additional injection has been demonstrated by gain switching a DFB laser at a frequency equivalent to the lasers RO frequency. However this method generates combs limited to the RO frequency.

This chapter demonstrates a design that offers the same frequency flexibility demonstrated through the on-chip coupling techniques demonstrated in earlier chapters, but without a form of additional optical injection. The device is made up of a gain and mirror section that is separated by a small isolation etch to remove the top two contact layers of the EPI structure. So while the device itself has a single cavity, the two sections are electrically isolated to allow for independent biasing. Gain switching one of these sections while maintaining a constant bias through the other section has been demonstrated here to allow comb lines to be generated while the phase coherence is maintained.

This not only allows the length of the gain switched device to be reduced from the 1750 μm long primary-secondary/mutual coupled devices to 1300 μm, therefore reducing the devices footprint, but also the device can take advantage of gain switching at higher currents. By operating the gain switched laser at higher currents, the peak to peak separation of the sinusoidal current could be increased, which has been shown in this chapter to greatly improve the bandwidth and quality of the generated combs.

Chapter 9

Conclusion and Future Work

9.1 Chapter Overview

This chapter gives a recap and conclusions of the chapters of this thesis. Beginning with the traditional methods of on-chip gain switching, the asymmetric biasing technique is discarded in favour of non-asymmetric biased configurations. Methods of on-chip comb line filtering are demonstrated through the use of injection locked ring lasers. Finally, a technique to generate on-chip gain switched combs from a single mode laser without additional forms of coupling is developed. The next integration steps are also outlined to further enhance on-chip gain switched combs and to develop a comb based de-multiplexing optical network.

9.2 Thesis Conclusion

Chapters 1 and *2* introduces the concept and theory behind PICs and gain switched frequency combs. Gain switching is the technique that takes advantage of the relaxation oscillation phenomenon which occurs when a laser is biased abruptly where the laser experiences damped oscillations in the carrier and photon density before reaching a steady state. Gain switching involves modulating the bias current with a high power RF signal which rapidly turns the laser on and off, therefore continuously exciting the first pulse in the relaxation oscillations. This generates a continuous pulse train in the time domain and thus a frequency comb.

Chapter 3 illustrates the fabrication process used to develop the PICs used to

generate the frequency combs in this thesis. This chapter introduces the different etch depths carried out to fabricate the shallow, deep and isolation regions of the laser designs. *Chapter 4* introduces the characterisation setup and equipment used in this thesis, as well as the experimental effects of the fabricated features on a ridge laser. The effects of shallow and deep etched Fabry–Pérot (FP) lasers are characterised, as well as FP lasers with a metal etched facet, etched facet, shallow and deep etched slot, and U-bend FP lasers.

Previous methods of on-chip gain switching are introduced and demonstrated through gain switching an injection locked FP laser to maintain phase coherence [19]. This on-chip injection locking is achieved using asymmetric biasing where the single mode primary laser is more heavily biased than the FP secondary laser, therefore creating a primary-secondary configuration with stable phase locking. This traditional method is demonstrated in *Chapter 5.2* along with the range of frequencies that combs are generated through this method.

From here in *Chapter 5.3* the effects of bidirectional coupling are explored, a configuration known for its instabilities including chaos with semiconductor lasers [53]. However, it is demonstrated in this section how this bidirectional coupling doesn't in fact hamper the generation of combs but instead results in the comb also being propagated within the non-gain switched laser in the coupled system.

Chapter 5.4 demonstrates how the traditional asymmetric biasing method can be discarded in favour of a mutually coupled system which results in enhanced combs generated with a higher power detectable across a larger bandwidth. This bandwidth is dramatically increased when modulating the gain switched current to a frequency equivalent to the FP laser's relaxation oscillation (RO) frequency. In this chapter, a broad comb with 25 comb lines measured within 10 dB of each other are detected across a bandwidth of 86.4 GHz. This mutual coupling technique is analysed further in *Chapter 6* particularly in relation to the effects of the gain switched frequency on the generated combs. What is found is the frequency separation between the generated comb lines is, for the most part, equivalent to the frequency of the gain switched current. However when the gain switched frequency is comparable to an integer multiple of the RO frequency of one of the lasers in the integrated system, what is generated is a comb with a comb line separation equivalent to the RO frequency of that laser.

Chapter 7 introduces the concept of a comb based coherent super-channel which would require the optical comb source that was demonstrated in previous chapters to be integrated with a de-multiplexer. This de-multiplexer would divide the individual comb lines into waveguides with separate modulators, where data is incorporated before the comb lines are recombined and transmitted. This chapter demonstrates experimentally a method of filtering out individual comb lines on a monolithically integrated circuit. A gain switched comb is injected into an integrated ring laser which acts as an ILF with a high Q factor. Current injection is used to adjust the position of the rings modes and filter out the individual comb lines.

Finally, *Chapter 8* introduces a new technique of achieving gain switched combs. Up until now, flexible gain switching has only been achieved through some method of external injection [17] or on-chip injection locking [19] which maintains phase coherence and allows combs to be generated. Less flexible forms of gain switching have been demonstrated without an additional form of injection by gain switching a single mode DFB at a frequency equivalent to the lasers relaxation oscillation frequency [12]. This method results in a generated comb, but the frequency separation of the comb lines is limited to the lasers relaxation oscillation frequency. In this chapter, a single cavity, two sectioned laser is used to generate flexible combs. This is achieved by gain switching one section and biasing the second section to maintain the phase coherence of the combs. The quality of the combs were greatly enhanced while gain switched close to the relaxation oscillation frequency of the device. The combs were enhanced further by increasing the peak to peak separation of the gain switched current and biasing the device at a region where the lower limit of the sinusoidal current is low enough to generate good quality combs but not low enough as to completely switch the laser off. A flat comb was generated with 13 comb lines, 3 GHz apart across a bandwidth of 36 GHz.

These chapters demonstrates different methods and limitations of generating gain switched combs, either through primary-secondary coupling, mutual coupling or a two sectioned single cavity device. The overall conclusion of this thesis is that the quality of the comb, in relation to the combs general flatness and bandwidths are heavily dependent on the the RO frequency of the gain switched laser, as well as the value and peak to peak separation of the gain switched current. The general flatness of the gain switched combs is optimised when gain switching a laser with a frequency signal equivalent to the lasers RO frequency which is seen throughout this thesis and in previous gain

switched work using primary-secondary techniques [12], [19].

The bandwidth of the gain switched comb is also expanded when the gain switched signal is equivalent to the laser's RO but greater expansion is demonstrated by increasing the value and peak to peak separation of the gain switched current. *Chapter 6* demonstrates the effects that the gain switched current has on the generated comb for a low current primary-secondary configuration and a higher current mutually coupled configuration. The increased gain switched current of just 25 mA greatly increased the bandwidth of the resulting comb and number of comb lines generated. *Chapter 8* demonstrates the effects of the gain switched current's peak to peak separation on the generated combs. It is found that increasing the peak to peak separation of the gain switched current also effects the bandwidth of the generated comb, with optimum combs being generated at a high peak to peak while the minimum peak of the sinusoidal current remains above 0 mA.

Overall, one can conclude from this thesis that an optimum gain switched comb can be achieved by gain switching a laser with a high value, high peak to peak separation current where the minimum peak of the sinusoidal current is close to, but above, 0 mA. Also the frequency of the gain switched signal is equivalent to the RO frequency of the gain switched laser. The optimum combs generated through asymmetric coupling, non-asymmetric coupling and the two sectioned single cavity device are plotted in *Figure* 9.1. For comparison, the centre comb line for each example was set to 1550 nm.

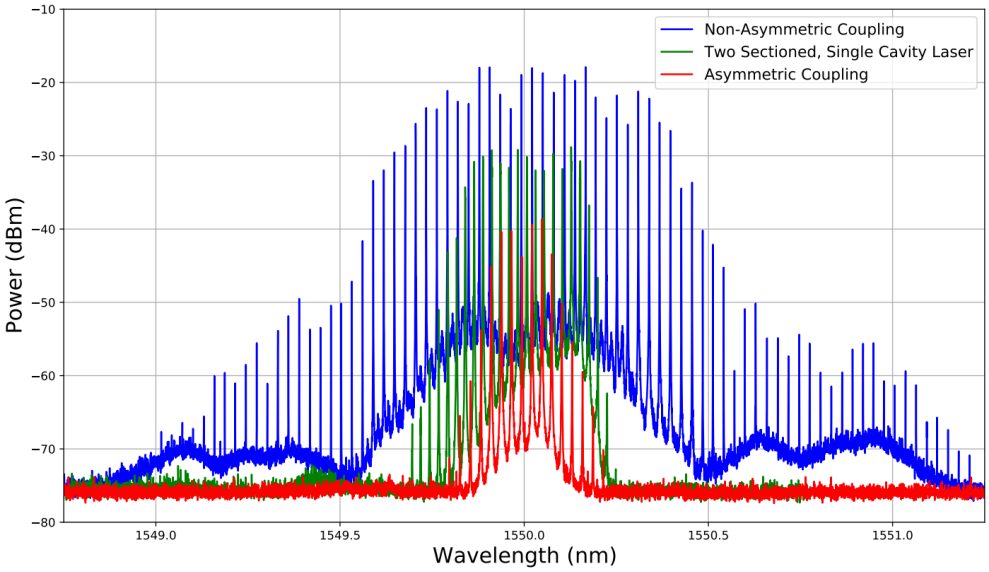


Figure 9.1: Optimum combs generated through different coupling techniques and devices.

9.3 Future Work

This thesis has demonstrated methods of enhancing the comb bandwidth to 86 GHz, however the power of the comb still remains in the negative dBm through fiber coupling. Naturally future work would focus on attempting to increase the output power in order for the comb source to be suitable for optical communications. Building on this, future designs of comb based optical super-channels would include a network of multiple ring lasers which would be used to fully de-multiplex the comb lines and separate them into different waveguides.

9.3.1 Power Enhancement: Example 1

Methods of power enhancement were demonstrated in *Chapter 5.4* through mutual coupling which enhanced the power of the generated comb from -20 dBm through asymmetric coupling, to - 10 dBm through non-asymmetric coupling. Therefore, it is logical to explore this method to further enhance the combs power. An example of such a PIC design is illustrated in *Figure* 9.2.

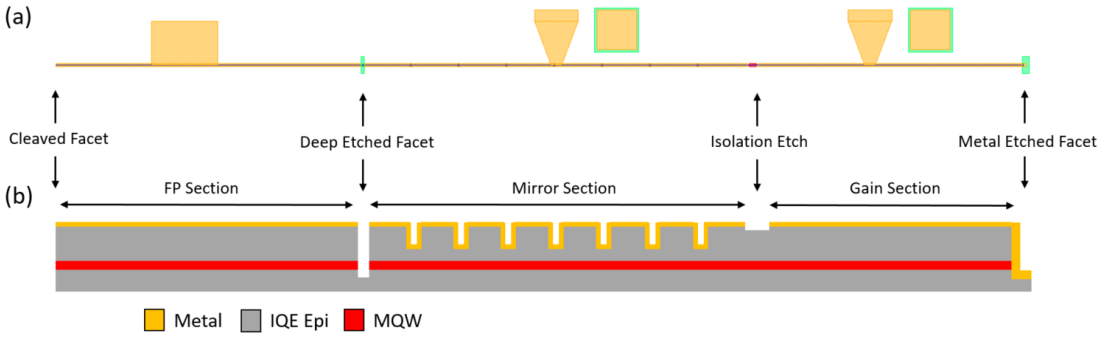


Figure 9.2: (a)Top view and (b) side view of device schematic.

This figure illustrates a two section, single cavity comb laser integrated with a FP laser. The two sectioned single mode laser is capable of generating a comb independent of the FP laser as demonstrated in *Chapter 8*. This generated comb can be greatly enhanced to be detectable across a larger bandwidth. The addition of the integrated FP laser offers the ability of the PIC to undergo mutual coupling, a technique which has been demonstrated in *Chapter 5.4* to improve the power and bandwidth of the generated comb. Devices could be designed with different FP lengths to investigate the relation between the FP length and the power of the mutually coupled comb.

This PIC design also allows one to characterise the effects of gain switching

both sections of the single mode laser simultaneously, while maintaining phase coherence by coupling the laser with the FP. Analysis of what form of comb can be generated from this PIC while stable phase locking is maintained and both sections of the single mode laser are gain switched at different frequencies.

9.3.2 Power Enhancement: Example 2

An additional method of enhancing the power of the generated comb is through the use of semiconductor optical amplifiers (SOAs). An SOA section between the comb source and the cleaved facet could be used to amplify the power of the generated comb. A tapered SOA section has been demonstrated to effectively amplify the power of a laser in [62]. Here the SOA sections were tapered from 2.5 μm to 3.6 μm for varying lengths with a length of 200 μm being determined to being the optimum length. At this length, the power of the laser is amplified without sacrificing the signal due to the gain saturation, which increases significantly for long SOAs.

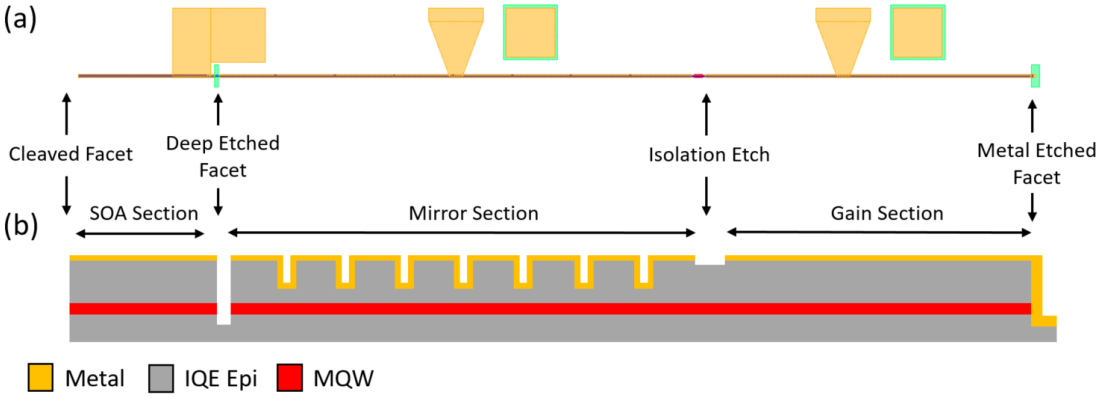


Figure 9.3: (a)Top view and (b) side view of device schematic.

PICs can be designed to investigate such SOA designs. Taking, for example, the two sectioned, single cavity device as the comb source and integrating a tapered waveguide as an SOA (*Figure* 9.3). This SOA section is integrated via a deep etched facet and confine the cavity of the comb source between the etched facet and the metal etched facet. This comb would be injected into this tapered waveguide which can be biased using a contact pad. An array of such devices can be designed with varying SOA taper widths and lengths to determine the optimum parameters of the SOA to amplify the comb but not to saturate the comb's signal.

9.3.3 Power Enhancement: Example 3

The final method that could be used to generate a comb with higher power is by increasing the power generated by the single mode primary laser before it is injected into the gain switched FP secondary laser in a primary-secondary configuration. The effects of this has been demonstrated off-chip in [63] showing an increase in the combs power and also an increase in the bandwidth of the generated comb. This could be attempted on-chip by integrating an SOA section between the single mode primary laser and the FP secondary laser.

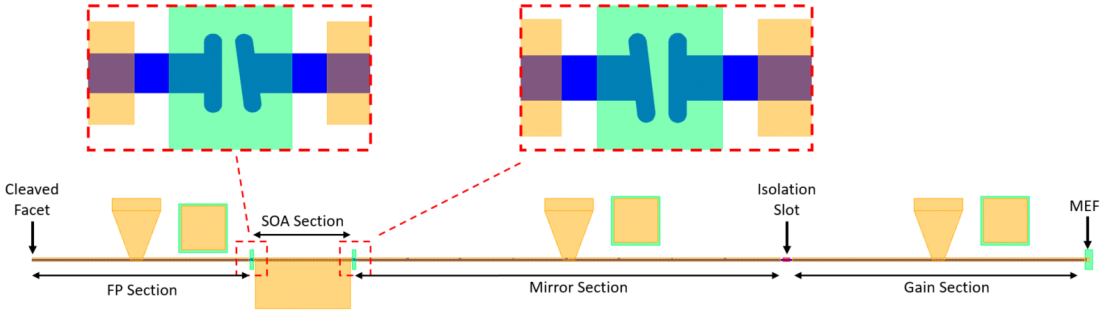


Figure 9.4: Top view of device schematic.

The primary and secondary lasers are similar to the designs used throughout this thesis. The primary laser is made up of a gain section 600 μm in length and a mirror section made up of seven slots with an interslot separation of 87 μm. The two sections are separated by an isolation slot to allow for electrical isolation, and the primary laser cavity is confined by a metal etched facet and an etched facet as illustrated in *Figure* 9.4. The secondary FP laser is 420 μm in length and is confined by an etched facet and a cleaved facet. The SOA section is integrated between these two lasers. This SOA section is fabricated with angled facets at both ends, this prevents lasing modes to be created by the SOA section as the angled facets reduce reflection [59]. To fully characterise the effects of this OSA section, and determine the optimum length at which the power of the laser is amplified but the signal isn't saturated by the length of the OSA [62], an array of these PICs can be fabricated with SOA lengths varying from 100 - 300 μm.

Injection locking the secondary FP laser with the amplified signal from the single mode primary laser and gain switching the secondary laser should ideally result in a generated comb with a higher power and an improved bandwidth [63].

9.3.4 De-Multiplexer

One utilisation of an optical comb source is to create an optical network with a de-multiplexer to separate the individual comb lines, modulators to incorporate data and a multiplexer to recombine the comb lines and transmit. a schematic of this is illustrated in *Figure* 9.5.

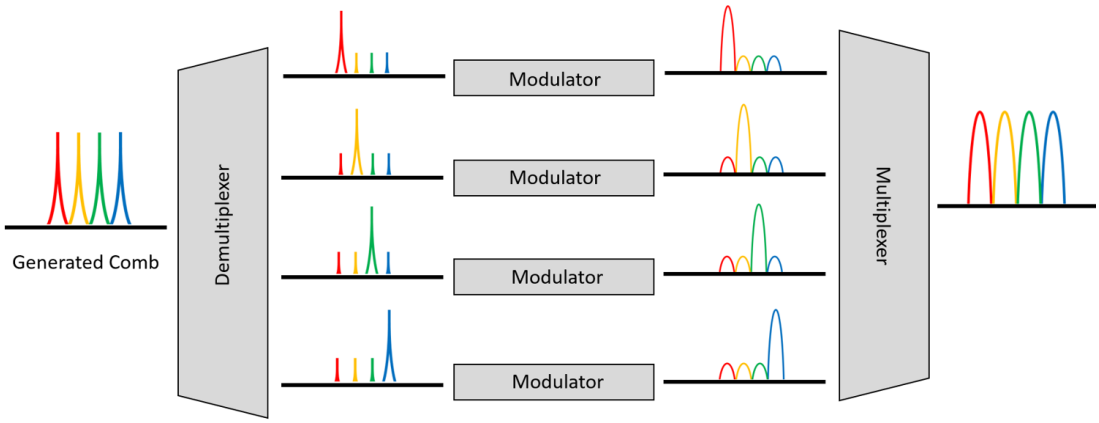


Figure 9.5: Schematic of a comb based optical network.

Chapter 7 experimentally demonstrates how a ring laser could be used to filter out the individual comb lines of an integrated comb source. De-multiplexing involves filtering out more than one comb line at one time and so a PIC with more than one ring laser is required. The PIC in *Chapter 7* is also unnecessarily large to allow for different test structures through each step of the PIC characterisation. A de-multiplexing PIC need not be so complex and an example of a PIC that could theoretically filter out two individual comb lines at once is illustrated in *Figure* 9.6.

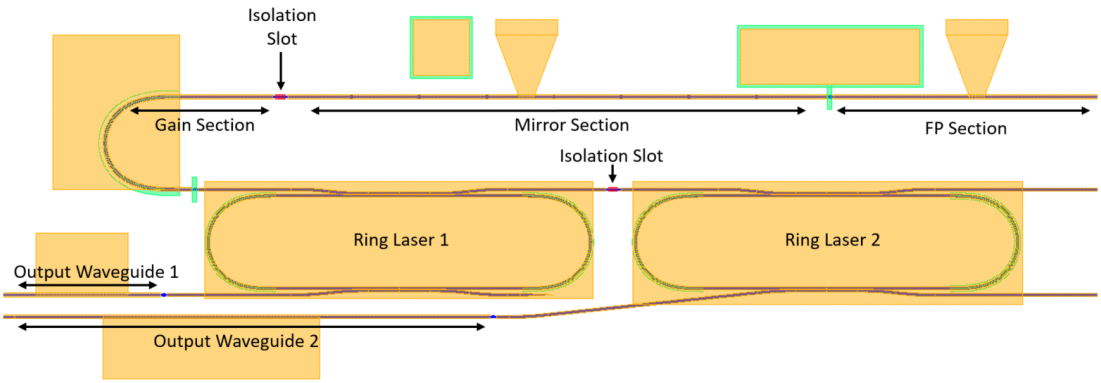


Figure 9.6: Schematic of a PIC that can generate combs and filter out two individual comb lines.

The comb source portion of the PIC is made up of a single mode laser and an

integrated FP laser, and so the combs can be generated through primary-secondary coupling or mutual coupling. The single mode laser is made up of a mirror and gain section separated by an isolation slot to allow for electrical isolation. To reduce the overall length of the laser, the gain is fabricated as a u-bend laser like those characterised in *Chapter 4* and based off these results, a u-bend section with a deep etch on the outer curve of the waveguide is selected with a radius of curvature of 25 μm or greater. It is known from *Chapter 5.3* that such a PIC design can support a comb in the non gain switched portion of the PIC through stable bi-directional coupling. The comb generated by gain switching the FP section would propagate along the single mode laser into the coupling waveguide that is integrated to the single mode laser via a deep etch. The two ring lasers can then be used to filter out different comb lines into output waveguide 1 and 2.

Alternatively, The two sectioned, single cavity comb source (*Chapter 8*) could be used in a similar PIC configuration as illustrated in *Figure* 9.7. In this configuration, the comb can be generated by gain switching either the gain or mirror section of the PIC. A deep etched curved waveguide is integrated with the comb source to transmit the comb from the single mode laser to the coupling waveguide. This curved waveguide is deep etched to allow for optical confinement and would be biased enough to make the section passive, but not high enough to allow the section to lase. Again, the two ring lasers are integrated with this coupling waveguide and would be used to filter out different comb lines into the two output waveguides.

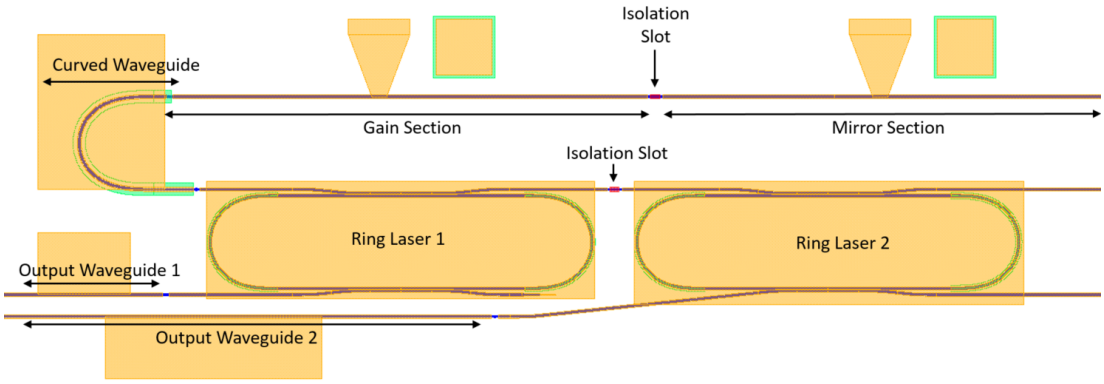


Figure 9.7: Schematic of a PIC that can generate combs and filter out two individual comb lines.

9.3.5 De-multiplexing Network

A more ambitious design would filter out even more comb lines at once. The previous designs could be altered by extending the curved waveguide in *Figure* 9.7 until another ring laser can be integrated with the coupling waveguide, however this would provide additional loss due to the lossy nature of InP waveguides [49]. One solution is to use the stable and coherent bidirectional coupling that is known to exist within the on-chip comb source (*Chapter 5.3*). Instead of having one curved waveguide integrating the comb source to the lower coupling waveguide, an additional curved waveguide could be used to integrate the comb source with an additional coupling waveguide that's coupled to two additional ring lasers (9.8).

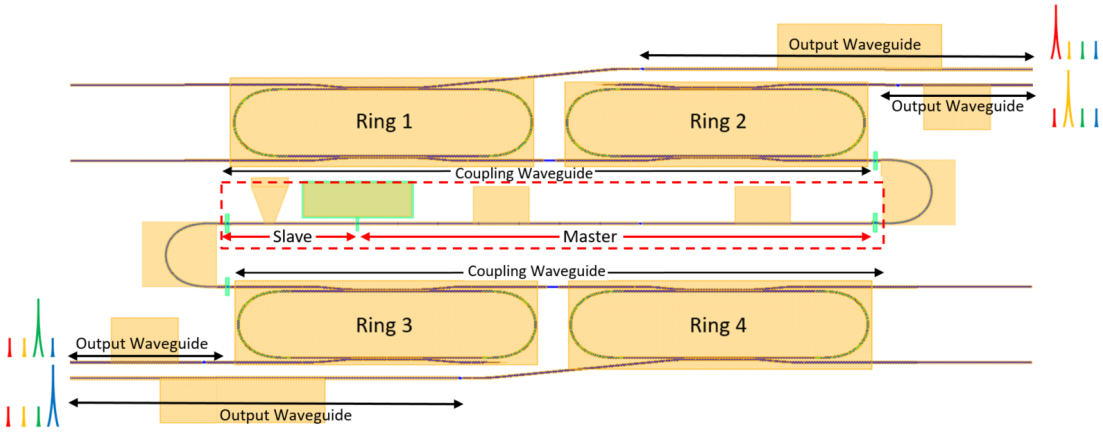


Figure 9.8: Schematic of a PIC that can generate combs and filter out four individual comb lines.

This configuration would allow for up to four individual comb lines to be filtered at once. The example here uses a primary-secondary configuration, however the comb source could be biased non-asymmetrically to generate enhanced combs through mutual coupling, or the PIC could be designed so that the comb source is a two sectioned, gain switched single mode laser (*Chapter 8*).

9.3.6 Comb Enhancement Through a High Speed Fabrication Process

In the comb examples demonstrated throughout this thesis, the frequency separation between comb lines was mostly limited to 1 - 10 GHz, with the quality of the comb being generally poor for higher frequencies. This performance is a limit caused by the capacitance of the device. The metal

contact pads used to bias the lasers results in a parallel plate capacitor type configuration and this capacitance, as well as the resistance of the device, inflicts what is known as the RC limit.

The corresponding frequency limit is given by [64]:

$$f_{RC} = \frac{1}{2\pi RC}, \text{ where } C = \frac{\epsilon_0 A}{d} \tag{9.1}$$

Where ϵ_0 is the dielectric constant, A is the area of the capacitance plate and d is the distance between plates. The capacitance of a laser is proportional to the materials dielectric constant, which in the case of InP is 12.35 [65] and is high enough to limit the performance of the laser to 10 GHz. Keeping in mind that the capacitance is proportional to the dielectric constant and inversely proportional to the distance between the capacitance plates, a logical solution would be to etch away the InP material under the contact pads and replace it with a polymer with a low dielectric constant. Benzocyclobutene (BCB) is one such polymer with a low dielectric of 2.65 [66] that has been demonstrated to increase the f_{RC} limit to beyond 10 GHz [67].

The fabrication process outlined in *Chapter 3* would remain largely unchanged for the lasers on the PIC that aren't undergoing gain switching. However, for the lasers that will be gain switched (an integrated FP laser for example), a deep etched ridge will be formed to remove the excess high dielectric InP layers before being deposited with SiO_2. This SIO_2 layer will help to promote adhesion of the BCB which will then be deposited onto the deep etched ridge laser.

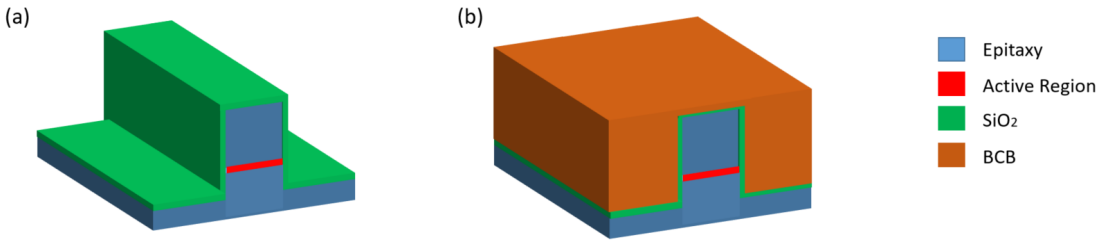


Figure 9.9: (a) Deep etched waveguide deposited with a layer of SiO_2. (b) BCB is deposited.

The layer of BCB would be etched back until the oxide layer at the top of the ridge is exposed. Because BCB also has relatively poor adhesion to metal, a layer of SiO_2 is deposited onto the BCB. From here the oxide open lithography would be carried out and a window open etch of the SiO_2 would be created on

the ridge and metal would be deposited as described in *Chapter 3*.

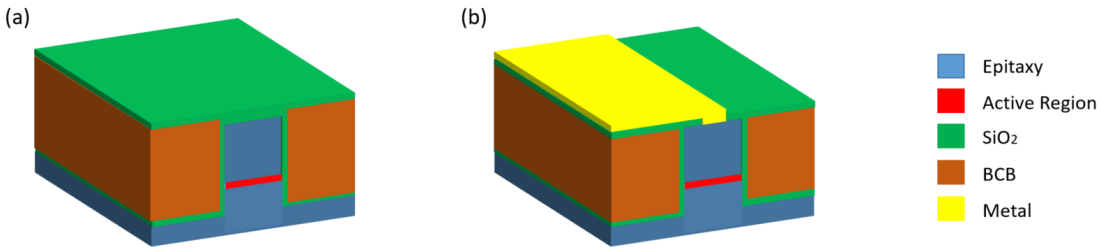


Figure 9.10: (a) BCB etched back and SiO_2 deposited. (b) Oxide open etch created and metal contact pad deposited.

A process run like this should result in high speed devices by reducing the capacitance caused by the dielectric constant of InP. A comb source capable of generating higher frequency combs across a larger bandwidth should ideally result, allowing the PIC to be more compatible with modern day comb source networks.

9.3.7 Micro-Transfer Printing

Throughout this thesis the issue of the lossy nature of InP waveguides has been mentioned and demonstrated. Attempts at biasing InP waveguides at a high enough current to make them passive but not lase was utilised throughout this thesis but ultimately resulted in a great loss of power. Due to its wide optical transparency range, Silicon Photonics has been recognised as a suitable candidate for waveguides in a PIC. Many methods over the last few years have been explored in integrating III-V lasers with Si waveguides, with flip chip bonding being mostly adopted in modern day industry. However, this process requires a high accuracy of alignment [68], [69] which in turn makes it difficult to reduce the cost and scale up production of the resulting chip.

Micro-transfer printing (μTP) is an integration technique that allows a micrometer sized device to be transferred from its native substrate to a target substrate. In other words, a comb source could be fabricated on an InP substrate before being transferred and printed to a Si PIC via evanescent coupling or butt coupling [70], [71]. With regards to the lasers designed in this thesis, the easiest method of integration with a Si PIC is through butt coupling as this requires fabricating the devices as they are, but replacing the cleaved facets with etched facets. The device would then be transfer printed into a Si circuit.

The primary difference between the epistructure for the fabrication process described in *Chapter 3* and for a μTP run is the inclusion of a release layer just above the substrate layer. Once the device is fabricated, additional etches are carried out into the sacrificial layer (release layer) surrounding the laser. The laser is encapsulated with a polymer which is etched into a grid shape in the region between the device itself and the native substrate.

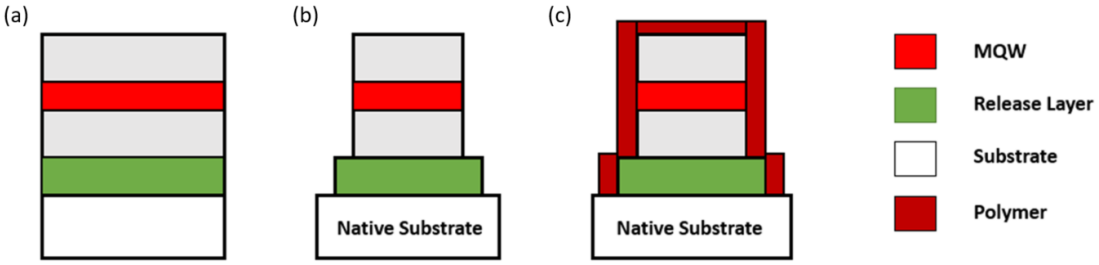


Figure 9.11: (a) Full μTP epistructure depicting the active region, the release layer and the Native substrate. (b) The fabricated device sitting on the release layer that has been etched down to the substrate. (c) The fabricated device and the release layer encapsulated in PR.

This grid shape allows the the release layer to be etched away (or undercut) while the device is fixed in position by the polymer's grid shape which now act as tethers. This is illustrated more clearly in *Figure* 9.12.

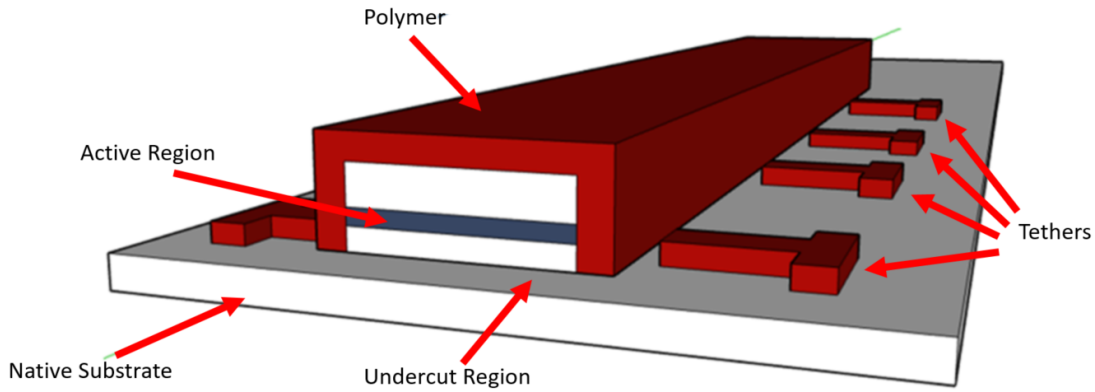


Figure 9.12: The encapsulated polymer is shaped into a grid like structure and the release layer is undercut. The grid polymer now acts as tethers holding the device in position.

Once the release layer is etched away, the encapsulated device is ready to be transfer printed. A polydimethylsiloxane (PDMS) stamp is aligned and laminated onto the device and is then pulled back at high velocity. This results in the tethers breaking and the device being picked up by the PDMS stamp. The device is then aligned and printed to the target by slowly pealing away the

PDMS stamp while the device is held in position either through van der Waals forces, or with an adhesive bonding agent [70].

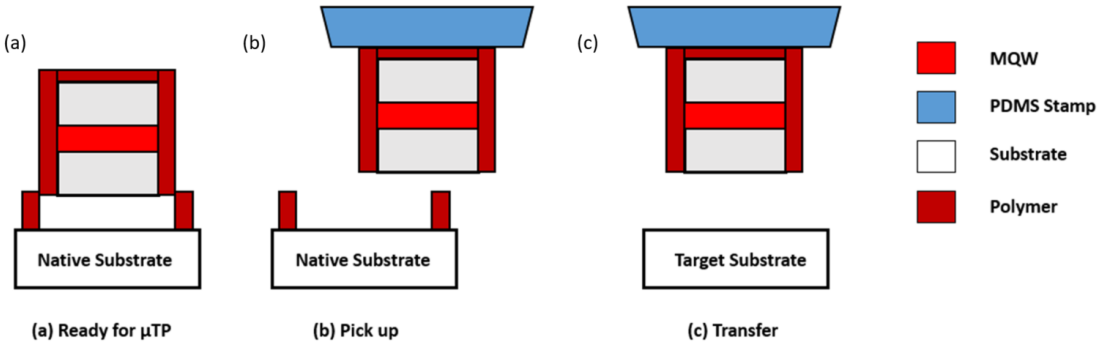


Figure 9.13: The encapsulated polymer is shaped into a grid like structure and the release layer is undercut. The grid polymer now acts as tethers holding the device in position.

As mentioned, a μTP device doesn't rely on the cleaved facets of the experiments described in this thesis, but would instead rely on etched facets. *Chapter 4* illustrated the experimental comparison between FP lasers where one end of the cavity is confined by a cleaved facet, an etched facet and a metal etched facet and the results are a relatively poorer performance in terms of threshold current and power for lasers with an etched facet. A PIC was designed to determine if the current comb PICs can generate a comb without being supported by a cleaved facet and this PIC is illustrated in *Figure* 9.14. This comb source takes the usual form of a single mode (SM) laser integrated with a gain switched FP laser. The cavity of the SM laser is confined by a metal etched facet and an etched facet and the cavity of the FP laser is confined by the etched facet of the SM laser, but also another etched facet instead of the usual cleaved facet.

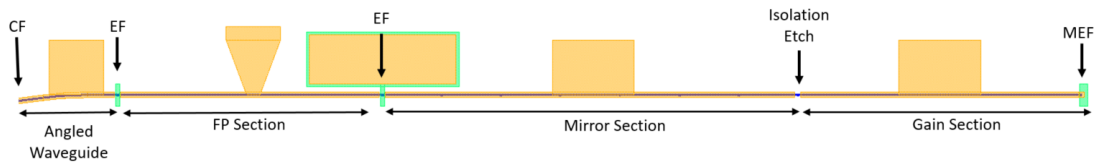


Figure 9.14: Schematic of device where the comb source is confined by a metal etched facet and an etched facet.

The device is integrated with an angled waveguide via this second etched facet which allows the generated light to be measured via a cleaved facet. The purpose of this angled waveguide is to minimise the reflection caused by the cleaved facet [59] and therefore ensuring the generated spectra and combs are

as a result of the cavities supported by the metal etched facet and etched facets.

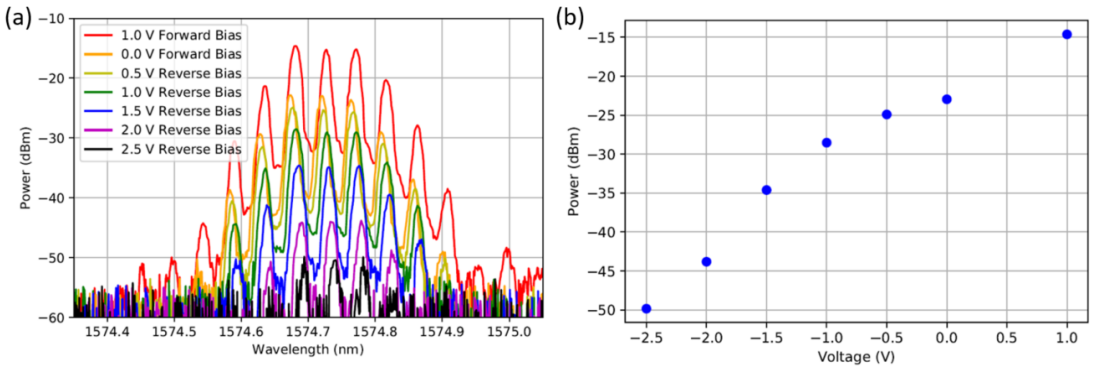


Figure 9.15: Plots of how the generated comb changes as the bias across the angled waveguide contact decreases.

Each section of the laser was biased to cause lasing and an optical fiber was coupled to the PIC's cleaved facet. The biasing of the SM laser was tuned until it generated a single mode spectra which was then injected into the FP laser where injection locking occurred. The FP laser was gain switched and a comb was measured through the cleaved facet while the angled waveguide was biased at 1 V to make that section passive. The generated comb was then measured for different biasing through the angled waveguide, where the voltage was reduced to 0 V and was then reverse biased until 2.5 V with the comb being measured at intervals of 0.5 V. The results of this are plotted in *Figure* 9.15.

The generated comb was detectable until a reverse bias across the angled waveguide of 2.5 V where the maximum power of the comb reached -55 dBm, the detectable limit of the ANDO OSA. These results demonstrate that a comb can be generated without cleaved facets and so this design is suitable for μTP processing.

References

[1] https://www.oberlo.com/statistics/how-many-people-use-internet.

[2] T. Maiman, *Stimulated Optical Radiation in Ruby*, Nature **187** (1960).

[3] d. B. Keck, *Optical Fiber Spans 30 years*, Lightwave **17**, 78–82 (2000).

[4] https://www.statista.com/statistics/617136/digital-population-worldwide/.

[5] https://www.internetlivestats.com/internet-users/.

[6] P. Dragic, C. Kucera, J. Furtick, J. Guerrier, T. Hawkins, and J. Ballato, *Brillouin Spectroscopy of a Novel Baria-Doped Silica Glass Optical Fiber*, Optics express **21**, 10924–41 (2013).

[7] M. Harrison, S. Kershaw, M. Burt, A. Rogach, A. Kornowski, A. Eychmüller, and H. Weller, *Colloidal nanocrystals for telecommunications. Complete coverage of the low-loss fiber windows by mercury telluride quantum dot*, Pure Appl. Chem.Pure Appl. Chem **72**, 295–307 (2000).

[8] B. Mukherjee, *Optical WDM Networks*, Springer Science Business Media (2006).

[9] A. Banerjee, Y. Park, F. Clarke, H. Song, S. Yang, G. Kramer, K. Kim, and B. Mukherjee, *Wavelength-division-multiplexed passive optical network (WDM-PON) technologiesfor broadband access: a review*, J. Opt. Netw. **4**, 737–758 (2005).

[10] E. Temprana, B.-P. Kuo, N. Alic, S. Radic, and S. Grubb. *400 Gb/s WDM DP-256-QAM transmission with 50 GHz channel separation*. In *2016 IEEE Photonics Conference (IPC)*, pages 1–2, (2016).

[11] H. Haus, *Mode-locking of lasers*, IEEE Journal of Selected Topics in Quantum Electronics **6**, 1173–1185 (2000).

[12] P. M. Anandarajah, S. P. Ó Dúill, R. Zhou, and L. P. Barry, *Enhanced Optical Comb Generation by Gain-Switching a Single-Mode Semiconductor Laser Close to Its Relaxation Oscillation Frequency*, IEEE Journal of Selected Topics in Quantum Electronics **21**, 592–600 (2015).

[13] Y. Takushima, H. Sotobayashi, M. Grein, E. Ippen, and H. Haus, *Linewidth of mode combs of passively and actively mode-locked semiconductor laser diodes*, Proc SPIE **5595**, 213 (2004).

[14] E. Sooudi, S. Sygletos, A. D. Ellis, G. Huyet, J. G. McInerney, F. Lelarge, K. Merghem, R. Rosales, A. Martinez, A. Ramdane, and S. P. Hegarty, *Optical Frequency Comb Generation Using Dual-Mode Injection-Locking of Quantum-Dash Mode-Locked Lasers: Properties and Applications*, IEEE Journal of Quantum Electronics **48**, 1327–1338 (2012).

[15] H. Ito, H. Yokoyama, S. Murata, and H. Inaba, *Picosecond optical pulse generation from an rf modulated AlGaAs dh diode laser*, Electronics Letters **23**, 738–740 (1979).

[16] S. Tarucha and K. Otsuka, *Response of semiconductor laser to deep sinusoidal injection current modulation*, IEEE Journal of Quantum Electronics **17**, 810–816 (1981).

[17] P. M. Anandarajah, R. Maher, Y. Q. Xu, S. Latkowski, J. O'Carroll, S. G. Murdoch, R. Phelan, J. O'Gorman, and L. P. Barry, *Generation of Coherent Multicarrier Signals by Gain Switching of Discrete Mode Lasers*, IEEE Photonics Journal **3**, 112–122 (2011).

[18] A. Weber, W. Ronghan, E. Bottcher, M. Schell, and D. Bimberg, *Measurement and simulation of the turn-on delay time jitter in gain-switched semiconductor lasers*, IEEE Journal of Quantum Electronics **28**, 441–446 (1992).

[19] J. K. Alexander, P. E. Morrissey, H. Yang, M. Yang, P. J. Marraccini, B. Corbett, and F. H. Peters, *Monolithically integrated low linewidth comb source using gain switched slotted Fabry-Perot lasers*, Opt. Express **24**, 7960–7965 (2016).

[20] J. G. Yoder. *Christiaan Huygens, book on the pendulum clock (1673)*. In *Landmark Writings in Western Mathematics 1640-1940*, pages 33–45. Elsevier, (2005).

[21] R. Pantell, *The laser oscillator with an external signal*, Proceedings of the IEEE **53**, 474–477 (1965).

[22] W. Steier and H. Stover, *Locking of laser oscillators by light injection*, IEEE Journal of Quantum Electronics **2**, 111–112 (1966).

[23] K. Iga. *Microoptics*. In R. A. Meyers, editor, *Encyclopedia of Physical Science and Technology (Third Edition)*, pages 735–754. Academic Press, New York, third edition edition, (2003).

[24] L. J. Aplet and J. W. Carson, *A Faraday Effect Optical Isolator*, Appl. Opt. **3**, 544–545 (1964).

[25] J. Fujita, M. Levy, R. Osgood, L. Wilkens, and H. Dotsch, *Polarization-independent waveguide optical isolator based on nonreciprocal phase shift*, IEEE Photonics Technology Letters **12**, 1510–1512 (2000).

[26] A. Tauke-Pedretti, G. A. Vawter, E. J. Skogen, G. Peake, M. Overberg, C. Alford, W. W. Chow, Z. S. Yang, D. Torres, and F. Cajas, *Mutual Injection Locking of Monolithically Integrated Coupled-Cavity DBR Lasers*, IEEE Photonics Technology Letters **23**, 908–910 (2011).

[27] A. Perrott, L. Caro, M. Dernaika, and F. Peters, *A Comparison between Off and On-Chip Injection Locking in a Photonic Integrated Circuit*, Photonics **6**, 103 (2019).

[28] F. M. Mogensen, H. L. Olesen, and G. Jacobsen, *FM noise suppression and linewidth reduction in an injection-locked semiconductor laser*, Electronics Letters **21**, 696–697 (1985).

[29] J. Wang, M. Haldar, L. Li, and F. Mendis, *Enhancement of modulation bandwidth of laser diodes by injection locking*, IEEE Photonics Technology Letters **8**, 34–36 (1996).

[30] S. W. C. L. A. Coldren and M. Mashanovitch, *Diode lasers and photonic integrated circuits* (2012).

[31] M. Chen, S. Xie, G. Zhou, D. Wei, H. Wu, S. Takahashi, H. Matsumoto, and K. Takamasu, *Absolute distance measurement based on spectral*

interferometer using the effect of the FSR of a Fabry–Perot etalon, Optics and Lasers in Engineering **123**, 20–27 (2019).

[32] Q. Lu, W.-H. Guo, D. Byrne, and J. Donegan, *Design of Slotted Single-Mode Lasers Suitable for Photonic Integration*, Photonics Technology Letters, IEEE **22**, 787 – 789 (2010).

[33] C. Png, S. Chan, S. Lim, and G. Reed, *Optical Phase Modulators for MHz and GHz Modulation in Silicon-On-Insulator (SOI)*, Lightwave Technology, Journal of **22**, 1573– 1582 (2004).

[34] M. Dernaika, N. Kelly, L. Caro, K. Shortiss, and F. Peters, *Regrowth-free single-mode semiconductor laser suitable for monolithic integration based on pits mirror*, Optical Engineering **56**, 1 (2017).

[35] A. Rosado, A. Pérez-Serrano, J. M. G. Tijero, A. V. Gutierrez, L. Pesquera, and I. Esquivias, *Numerical and Experimental Analysis of Optical Frequency Comb Generation in Gain-Switched Semiconductor Lasers*, IEEE Journal of Quantum Electronics **55**, 1–12 (2019).

[36] J. K. Alexander. *Low-linewidth optical comb sources based on gain-switched lasers*. PhD thesis, University College Cork, (2017).

[37] P. D. Lakshmijayasimha, A. Kaszubowska-Anandarajah, E. P. Martin, M. N. Hammad, P. Landais, and P. M. Anandarajah, *Characterization of a multifunctional active demultiplexer for optical frequency combs*, Optics & Laser Technology **134**, 106637 (2021).

[38] C. Pulikkaseril, *Filter Bandwidth Definition of the WaveShaper S-series Programmable Processor*, Finisar product whitepaper .

[39] W. Cotter, P. E. Morrissey, H. Yang, J. O'Callaghan, B. Roycroft, B. Corbett, and F. H. Peters, *Integrated demultiplexing and amplification of coherent optical combs*, Opt. Express **27**, 16012–16023 (2019).

[40] K. Shortiss, M. Shayesteh, W. Cotter, A. H. Perrott, M. Dernaika, and F. H. Peters, *Mode Suppression in Injection Locked Multi-Mode and Single-Mode Lasers for Optical Demultiplexing*, Photonics **6** (2019).

[41] D. Rabus, M. Hamacher, U. Troppenz, and H. Heidrich, *Optical filters based on ring resonators with integrated semiconductor optical amplifiers in GaInAsP-InP*, IEEE Journal of Selected Topics in Quantum Electronics **8**, 1405–1411 (2002).

[42] M. Hamacher, H. Heidrich, and D. G. Rabus. *Active ring resonators based on GaInAsP/InP*. In *Proc. SPIE*, pages 212–222, (2003).

[43] K. Shortiss. *Optical comb injection for optical demultiplexing and harmonic frequency locking*. PhD thesis, University College Cork, (2020).

[44] M. Dernaika. *Monolithically integrated coherent comb de-multiplexer using facetless semiconductor ring lasers*. PhD thesis, University College Cork, (2019).

[45] L. Caro. *Design and fabrication of single-mode tunable lasers for regrowth-free monolithically integrated photonic circuits*. PhD thesis, University College Cork, (2019).

[46] L. Bartolome, L. Cerutti, and E. Tournié, *Impact of the ridge etching [U+2010]depth on GaSb [U+2010]based laser diodes*, Electronics Letters **58** (2021).

[47] D. Liang, J. Wang, D. Hall, G. Peake, and Q. Hartmann, *High-index-contrast ridge waveguide lasers fabricated via oxygen-enhanced wet thermal oxidation*, Proceedings of SPIE - The International Society for Optical Engineering **6133** (2006).

[48] D. Hofstetter, L. T. Romano, R. L. Thornton, D. P. Bour, and N. Johnson, *Characterization of intra-cavity reflections by Fourier transforming spectral data of optically pumped InGaN lasers*, Applied physics letters **71**, 3200–3202 (1997).

[49] R. Sheehan, S. Horne, and F. Peters, *The design of low-loss curved waveguides*, Optical and Quantum Electronics **40**, 1211–1218 (2008).

[50] Q. Lu, W. Guo, R. Phelan, D. Byrne, J. Donegan, P. Lambkin, and B. Corbett, *Analysis of Slot Characteristics in Slotted Single-Mode Semiconductor Lasers Using the 2-D Scattering Matrix Method*, Photonics Technology Letters, IEEE **18**, 2605 – 2607 (2007).

[51] A. Baylón-Fuentes, P. Hernández Nava, A. Garcia-Juarez, I. Zaldivar-Huerta, J. Rodriguez-Asomoza, G. Aguayo-Rodríguez, and R. Gómez-Colín, *Modulation of Relaxation Oscillation Frequency of a DFB Laser by Using Direct Detection*, Proceedings of SPIE - The International Society for Optical Engineering **7958**, 12– (2011).

[52] L. Barry, P. Anandarajah, and A. Kaszubowska, *Optical pulse generation at frequencies up to 20 GHz using external-injection seeding of a gain-switched commercial Fabry-Perot laser*, IEEE Photonics Technology Letters **13**, 1014–1016 (2001).

[53] T. H. I. Fischer and W. Elsässer, *Chaos Synchronization and Spontaneous Symmetry-Breaking in Symmetrically Delay-Coupled Semiconductor Lasers*, Physical Review Letters **86**, 795–798 (2001).

[54] J. McCarthy, D. O'Sullivan, M. Shayesteh, M. Dernaika, F. H. Peters, and B. Kelleher, *Tunable, coherent optical comb source via on-chip bidirectional coupling*, Opt. Lett. **48**, 4137–4140 (2023).

[55] K. Shortiss, B. Lingnau, F. Dubois, B. Kelleher, and F. H. Peters, *Harmonic frequency locking and tuning of comb frequency spacing through optical injection*, Opt. Express **27**, 36976–36989 (2019).

[56] J. T. Verdeyen. *Laser Electronics*, pages 279–280. Prentice-Hall, 3 edition, (1989).

[57] R. Sheehan, S. Horne, and F. Peters, *The design of low-loss curved waveguides*, Optical and Quantum Electronics **40**, 1211–1218 (2008).

[58] M. Dernaika, N. Kelly, L. Caro, and F. Peters, *Single mode semiconductor laser based on coupled cavities of an active ring laser and Fabry Perot*, IET Optoelectronics **12** (2017).

[59] H. Yang, P. Morrissey, W. Cotter, C. L. M. Daunt, J. O'Callaghan, B. Roycroft, N. Ye, N. Kelly, B. Corbett, and F. H. Peters, *Monolithic Integration of Single Facet Slotted Laser, SOA, and MMI Coupler*, IEEE Photonics Technology Letters **25**, 257–260 (2013).

[60] L. Caro, N. P. Kelly, M. Dernaika, M. Shayesteh, P. E. Morrissey, J. K. Alexander, and F. H. Peters, *A facetless regrowth-free single mode laser based on MMI couplers*, Optics & Laser Technology **94**, 159–164 (2017).

[61] A. Rosado, A. Pérez-Serrano, J. M. G. Tijero, Ángel Valle, L. Pesquera, and I. Esquivias, *Experimental study of optical frequency comb generation in gain-switched semiconductor lasers*, Optics & Laser Technology **108**, 542–550 (2018).

[62] M. A. D. Theurer, *Electroabsorption Modulated Lasers and Hybridly Integrated Lasers for Communication and Sensing*, Journal **7** (2022).

[63] G. Jain, D. Gutierrez-Pascual, M. J. Wallace, J. F. Donegan, and P. M. Anandarajah, *Experimental investigation of external optical injection and its application in gain-switched wavelength tunable optical frequency comb generation*, Journal of Lightwave Technology **39**, 5884–5895 (2021).

[64] C. Sriprachuabwong, C. Srichan, T. Lomas, and A. Tuantranont. *Simple RC low pass filter circuit fabricated by unmodified desktop inkjet printer*. In *ECTI-CON2010: The 2010 ECTI International Confernce on Electrical Engineering/Electronics, Computer, Telecommunications and Information Technology*, pages 929–932, (2010).

[65] C. Hilsum, S. Fray, and C. Smith, *The optical frequencies and dielectric constants of InP*, Solid State Communications **7**, 1057–1059 (1969).

[66] DOW, *Processing Procedures for CYCLOTENE 4000 Series Photo BCB Resins*, CYCLOTENE Advanced Electronic Resins **7** (2005).

[67] T. Tanigawa, T. Onishi, S. Nagai, and T. Ueda. *High-speed 850 nm AlGaAs/GaAs vertical cavity surface emitting laser with low parasitic capacitance fabricated using BCB planarization technique*. In *(CLEO). Conference on Lasers and Electro-Optics, 2005.*, volume 2, pages 1381–1383 Vol. 2, (2005).

[68] H. Lu, J. S. Lee, Y. Zhao, C. Scarcella, P. Cardile, A. Daly, M. Ortsiefer, L. Carroll, and P. O'Brien, *Flip-chip integration of tilted VCSELs onto a silicon photonic integrated circuit*, Opt. Express **24**, 16258–16266 (2016).

[69] A. Moscoso-Mártir, F. Merget, J. Mueller, J. Hauck, S. Romero-García, B. Shen, F. Lelarge, R. Brenot, A. Garreau, E. Mentovich, A. Sandomirsky, A. Badihi, D. E. Rasmussen, R. Setter, and J. Witzens. *Hybrid silicon photonics flip-chip laser integration with vertical self-alignment*. In *2017 Conference on Lasers and Electro-Optics Pacific Rim (CLEO-PR)*, pages 1–4, (2017).

[70] J. Zhang, G. Muliuk, J. Juvert, S. Kumari, J. Goyvaerts, B. Haq, C. Op de Beeck, B. Kuyken, G. Morthier, D. Van Thourhout, et al., *III-V-on-Si photonic integrated circuits realized using micro-transfer-printing*, APL photonics **4** (2019).

[71] C. O. de Beeck, B. Haq, L. Elsinger, A. Gocalinska, E. Pelucchi, B. Corbett, G. Roelkens, and B. Kuyken, *Heterogeneous III-V on silicon nitride*

amplifiers and lasers via microtransfer printing, Optica **7**, 386–393 (2020).